

DISSERTATION

MAGMATISM, DEFORMATION, AND MINERALIZATION ALONG THE INTRA-ARC
ATACAMA FAULT SYSTEM, NORTHERN CHILE

Submitted by

Nikki M. Seymour

Department of Geosciences

In partial fulfillment of the requirements

For the Degree of Doctor of Philosophy

Colorado State University

Fort Collins, Colorado

Spring 2020

Doctoral Committee:

Advisor: John S. Singleton

John R. Ridley

Judith L. Hannah

Yvette D. Kuiper

Robert J. Wilson

Copyright by Nikki M. Seymour 2020

All Rights Reserved

ABSTRACT

MAGMATISM, DEFORMATION, AND MINERALIZATION ALONG THE INTRA-ARC ATACAMA FAULT SYSTEM, NORTHERN CHILE

Oblique plate motion is nearly universal across subduction margins, and the lateral component of motion produced by oblique subduction may be accommodated through distributed strain and/or along crustal-scale strike-slip faults in the overriding (upper) plate. Magmatic arcs, another fundamental features of the upper plate, have been suggested to play a key role in the initiation and development of localized intra-arc crustal-scale faults. Significant hydrothermal fluid flow derived from arc plutons has also produced world-class metal deposits along intra-arc faults, and may suggest the processes responsible for the initiation, continued deformation, and eventual abandonment of strike-slip faults may also play an important role in focusing economic mineralization. Here I study the sinistral Atacama fault system (AFS), a fossil intra-arc strike-slip fault that occurs within the Mesozoic Coastal Cordillera arc to better understand how oblique plate motion is accommodated in the upper plate and related to arc magmatism. Mapping along the northern ~70 km of the El Salado segment of the AFS documents the distribution of arc plutons and style of deformation. Petrology, geochemistry, and geo/thermochronology were used to characterize and correlate plutons, and structural data were analyzed to understand progressive changes in the style of deformation.

New zircon U-Pb dates document a major pulse of magmatism from 150–120 Ma, with the 135–119 Ma plutons most directly tied to AFS ductile deformation. Mylonitic fabrics along the AFS are uniquely associated with the margins of Early Cretaceous plutons, and are cut by late kinematic intrusions at 120–110 Ma. Steeply dipping N- to NE-striking mylonitic fabrics with sinistral shear sense indicators strike ~8–12° clockwise of the steeply dipping, N- to NW-striking AFS strands, indicating deformation occurred during progressive ductile to brittle sinistral strain.

The distinctive synkinematic Cerro del Pingo tonalite was mapped on both sides of the eastern branch of the El Salado segment. Petrography, geochemistry, and geochronology all overlap within error, and therefore I interpret two sinistrally separated exposures of the Cerro del Pingo Complex as an offset marker along the AFS. In addition, I correlate a chain of offset leucocratic granites and hypabyssal intrusions across the western branch of the El Salado segment. The sinistral slip magnitude across the entire the El Salado segment is $\sim 50 \pm 6$ km and occurred almost entirely between ~ 133 and ~ 110 Ma at an average slip rate of ~ 2.0 – 2.5 km/Myr. I postulate that thermal softening as a result of Early Cretaceous pluton intrusion into the shallow crust locally elevated geothermal gradients, allowing for ductile deformation at ~ 5 – 7 km depths. Spatially variable Early Cretaceous pluton emplacement set up a heterogeneous rheology that produced a segmented system that never evolved into a single regional-scale fault. Zircon (U-Th)/He dates record cooling through $\sim 180^\circ\text{C}$ by 116–99 Ma and relaxation of elevated gradients coeval with the end of slip along the El Salado segment.

Along the central El Salado segment ~ 150 – 200 km south of the offset Cerro del Pingo Complex tonalites, clear fault branches no longer define the AFS. The main branch of AFS in this region is defined by a ~ 200 – 500 -m-thick steeply NW-dipping shear zone that does not show evidence for brittle overprint. Zircon U-Pb dates document synkinematic emplacement of a tonalite in the shear zone at ~ 122 Ma. Kinematic indicators record oblique sinistral-reverse shear, but locally coaxial fabrics dominate, indicating an overall transpressional regime. Shear zone activity overlaps in age with other sections of the AFS. The tonalite records a synkinematic sodic-calcic assemblage of actinolite+epidote+titanite+plagioclase, but mylonitic microstructures are completely annealed. The shear zone is cut by an unstrained ~ 115 Ma diorite body that contains pervasive actinolite+epidote+andradite+plagioclase sodic-calcic mineralization. Similar hydrothermal alteration assemblages are also present ~ 20 km east of the AFS in the economic Punta del Cobre copper district near Copiapó. The absence of brittle faulting is likely related to continued magmatism associated with the Copiapó batholith complex, which is younger than most arc plutons in the

Coastal Cordillera. Postkinematic mineralization along the AFS is unique to the Copiapó area, and magmatic fluids responsible for alteration were most likely derived from the Copiapó batholith.

Together, these data document the development of the AFS as a highly segmented fault system that localized mineralization and slipped at a relatively slow rate over ~ 20 Myr, and was abandoned as plate motion vectors shifted in the middle Cretaceous and arc magmatism migrated eastward.

ACKNOWLEDGEMENTS

I would first like to thank my advisor, Dr. John Singleton, for his guidance throughout this process. His energy, creativity, and endless desire to know what's over the next ridge are traits I hope to emulate as I move forward in my career.

I received considerable support from my collaborators Drs. Rodrigo Gomila, Gert Heuser, Gloria Arancibia, Daniel Stockli, and Holly Stein, as well as my committee members, Drs. Judith Hannah, Yvette Kuiper, John Ridley, and Bob Wilson. Their feedback opened new avenues of exploration and pushed me beyond my comfort zone. This project was supported by the unparalleled laboratory resources and access provided by Drs. Jaime Barnes, Holly Stein, and Daniel Stockli. Rudra Chatterjee, Des Patterson, and Lisa Stockli are thanked for their analytical assistance at the UT-Chron facilities.

Financial support from the National Science Foundation and the Geological Society of America, Society of Economic Geology, and the AIRIE group enabled me to conduct field and analytical work, and I was supported by the E. Warner Research Assistantship, R. & L. Steininger Research Fellowship, CSU Vice President for Research Fellowship, McCallum Mineralogy & Petrology, Larry Kent Burns Memorial Scholarship, and Warner College of Natural Resources Graduate Student Success Scholarship during this dissertation.

Innumerable thanks go to the Singleton research group—Evan Strickland, Rachel Ruthven, Skyler Mavor, Stewart Williams, Emily Perman, and Dr. Michael Prior—and to both the CSU and UT-Austin graduate student communities.

Finally, I owe the greatest thanks to my family for their love and support.

DEDICATION

To my family.

TABLE OF CONTENTS

ABSTRACT	ii
ACKNOWLEDGEMENTS	v
DEDICATION	vi
LIST OF TABLES	ix
LIST OF FIGURES	x
 Introduction	 1
 Chapter 1 The Relationship between Magmatism and Deformation	 8
Summary	8
1.1 Introduction	9
1.2 Geologic Setting	10
1.2.1 Development of the Coastal Cordilleran Arc	12
1.2.2 Development of the Atacama fault system	13
1.3 Methods	14
1.3.1 Field Methods & Sampling Strategy	14
1.3.2 Compilation of geochronologic data	14
1.3.3 U-Pb Geochronology	16
1.3.4 (U-Th)/He Thermochronology	17
1.4 Results	20
1.4.1 Paposo Segment (24.6°S to 25°S)	20
1.4.2 Northern El Salado Segment (25.5°S to 26°S)	23
1.4.3 Central El Salado Segment (26.6°S to 27°S)	33
1.5 Discussion	40
1.5.1 Region-Specific Trends	40
1.5.2 The Relationship between Magmatism and Deformation	46
1.5.3 Thermal Weakening of the Crust due to Arc Magmatism	49
1.6 Conclusions	53
 Chapter 2 Early Cretaceous Magnitude, Timing, and Rate of Slip along the El Salado Segment	 55
Summary	55
2.1 Introduction	56
2.2 Geologic Setting	57
2.2.1 Atacama fault system	57
2.2.2 The El Salado Segment	60
2.3 Methods	63
2.3.1 Field Mapping & Petrography	63
2.3.2 Analytical Methods	64
2.4 Results	67
2.4.1 Eastern Branch	67

2.4.2	Western Branch	80
2.4.3	Brittle Fault Kinematics	85
2.5	Discussion	89
2.5.1	Correlation of Synkinematic Plutons and Mylonite Zones	89
2.5.2	Displacement Magnitude	90
2.5.3	Timing & Rate of Slip	94
2.5.4	Fault Scaling Relationships & Comparison to other Fault Systems	98
2.5.5	Implications for Mesozoic Slip Partitioning & Plate Convergence	100
2.6	Conclusions	103
Chapter 3	Sodic-calcic alteration along the ductile Atacama fault system near Copiapó	105
Summary	105
3.1	Introduction	106
3.2	Geologic Setting	109
3.2.1	Geology of the Copiapó Region	110
3.2.2	Mineralization in the Punta del Cobre District	114
3.3	Methods	117
3.3.1	Mapping & Structural Data	117
3.3.2	Geochronology	118
3.3.3	Geochemistry	122
3.4	Results	125
3.4.1	Map relationships	125
3.4.2	Geochemistry	136
3.4.3	Las Pintadas Andradite Vein	140
3.5	Discussion	145
3.5.1	Pluton Emplacement and Evolution of the Shear Zone	145
3.5.2	Comparison to Regional Magmatism & Deformation	148
3.5.3	Sodic-calcic Hydrothermal Alteration	151
3.5.4	Comparison to Las Pintadas & the Punta del Cobre District	155
3.6	Conclusions	160
Bibliography	162
Appendix	195

LIST OF TABLES

1.1	Summary of sample lithology and degree of strain	15
1.2	Summary of geo/thermochronometric data	19
2.1	Summary of U-Pb sample lithology and degree of strain	64
2.2	Summary of geo/thermochronometric data	66
2.3	Whole-rock geochemical data	66
2.4	Summary of brittle fault kinematic data	88
3.1	Summary of sample lithology	119
3.2	Summary of U-Pb and (U-Th)/He data	121
3.3	Summary of Re-Os data	121
3.4	Whole-rock geochemistry data	123
3.5	Oxygen stable isotope data	124
3.6	Garnet compositions from EDS data from the AFS Vein	141
3.7	Alteration facies	151

LIST OF FIGURES

1	Schematic model of slip partitioning during oblique convergence	2
2	Segments of the Atacama fault system (AFS)	4
1.1	Regional scale geometry of the AFS in northern Chile	11
1.2	Simplified map of the Paposo study area	21
1.3	U-Pb concordia diagrams for the southern Paposo segment	22
1.4	Simplified map of the northern El Salado segment	24
1.5	Stereograms of structural data from the northern El Salado segment	25
1.6	Inset maps and cross-sections of the Cerro del Pingo Complex	26
1.7	U-Pb concordia diagrams for the northern El Salado segment	28
1.8	Inset map of the andesitic dike that cuts the Atacama fault system	32
1.9	Simplified map of the central El Salado segment	34
1.10	New detailed mapping south of the Mantoverde mine	35
1.11	Field photographs along the central El Salado segment	38
1.12	U-Pb concordia diagrams for the central El Salado segment	39
1.13	Stereograms of structural data from the central El Salado segment	41
1.14	Time vs. N-S trend diagram summarizing deformation events along the AFS	43
1.15	Crustal strength profile showing thermal softening effects of magmatism	51
2.1	Regional map of the AFS showing the study area	58
2.2	Simplified map of the northern El Salado segment	68
2.3	Map of the northern mylonite zone	69
2.4	Stereograms of mylonitic foliations from the northern mylonite zone	71
2.5	Photomicrographs that correspond to the northern mylonite zone	72
2.6	Ternary diagram of pluton compositions	73
2.7	Map of the southern mylonite zone	75
2.8	U-Pb concordia diagrams for plutons associated with the southern mylonite zone	76
2.9	Stereograms from the southern mylonite zone	77
2.10	Photomicrographs from the southern mylonite zone	77
2.11	Maps of leucocratic igneous bodies	81
2.12	U-Pb concordia diagrams for the leucocratic plutons	83
2.13	Photomicrographs of the leucocratic igneous bodies	84
2.14	Stereograms of brittle faults along the northern El Salado segment	86
2.15	Correlation of offset markers along the AFS	92
2.16	Proposed slip history of the El Salado segment	97
3.1	Map of the AFS with Chilean Iron Belt deposits	107
3.2	Regional map of the Copiapó region	112
3.3	Detailed mapping along the AFS	126
3.4	Photomicrographs of the Copiapó shear zone	128
3.5	Stereograms of the Copiapó shear zone	130
3.6	Field photographs of the Copiapó shear zone	132

3.7	Zircon U-Pb concordia diagrams for the AFS shear zone	133
3.8	Whole-rock geochemical plots	137
3.9	Geochronology of the AFS andradite vein	141
3.10	Geochronology of the Las Pintadas vein	143
3.11	Temporal evolution of the shear zone and alteration	146
3.12	Time vs. N-S trend diagram summarizing magmatism, deformation, and alteration . . .	150
3.13	Stable isotope data from the AFS and Las Pintadas andradite veins	153

Introduction

Oblique plate motion dominates at nearly all subduction margins, and the trench-parallel component of motion may be partitioned between slab underthrusting and upper-plate lateral transport of the forearc. Lateral transport is accommodated through distributed strain and along crustal-scale strike-slip faults (Figure 1), with active faults dominating at margins where interplate coupling between a subducting oceanic plate and overriding continental plate is strong. Magmatic arcs are also fundamental features of subduction zones, and modern obliquely convergent margins including Sumatra, Philippines, and southern Chile have strike-slip faults running through the active arc that are linked to the main subduction zone thrust. The collocation of the arc and crustal-scale strike-slip fault point towards a relationship between the two features and suggest arcs may play a major role in the initiation and development of trench-linked systems. Evidence from the modern Sumatran fault system suggests intra-arc strike-slip faults are weak, potentially due to high geothermal gradients and intense hydrothermal fluid flow exsolving from subduction-related plutons, resulting in a shallow brittle-plastic transition.

The absolute motion of the overriding plate with respect to the trench—which includes the magnitude and rate of slip along trench-parallel strike-slip faults—must be known to understand subduction zone processes such as slip partitioning. Modern oblique margins with well-constrained geodetic data indicate intra-arc strike-slip faults accommodate a wide range of trench-parallel motion (25–66%), with the remaining motion primarily accommodated along the subduction interface. While direct slip rates on fossil fault systems cannot be gleaned from geodetic data, erosion to deeper levels in fossil strike-slip systems can expose piercing points that clearly preserve displacement magnitude, and crosscutting relationships can record the relative timing of slip and be used to estimate slip rates. These slip history constraints can be used to better understand the degree of slip partitioning across oblique margins in the ancient, and may yield insights into plate motion rates, vectors, and other processes such as fault linkage and subduction erosion.

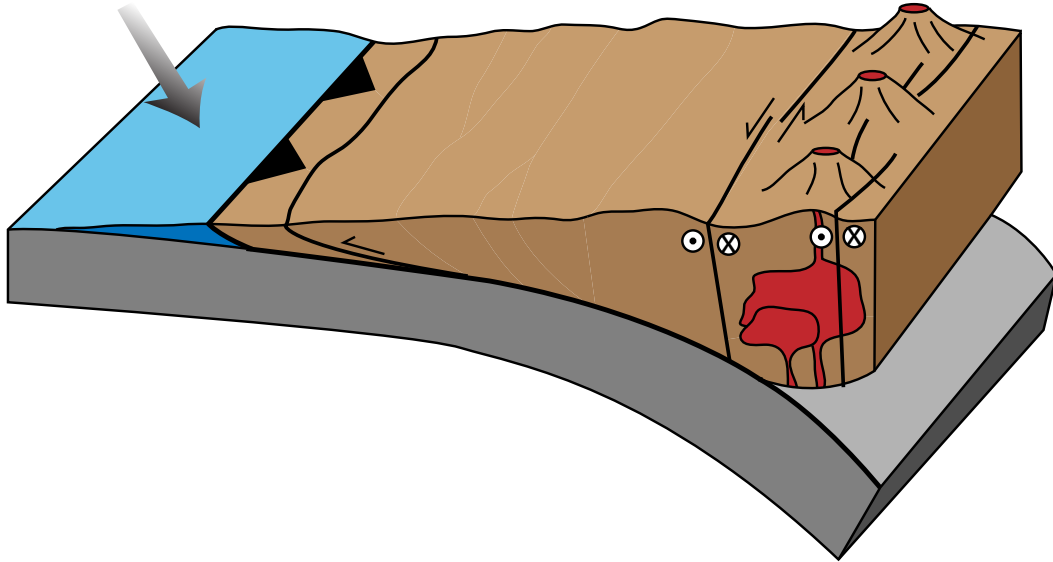


Figure 1: Schematic model during oblique convergence showing partitioning of trench-parallel motion between oblique underthrusting of the slab and crustal-scale strike-slip faults through the magmatic arc. Modified from Van der Pluijm and Marshak (2004).

Major faults localized through the magmatic arc above subduction zones often host world-class metal deposits, and may suggest the processes responsible for the initiation, continued deformation, and eventual abandonment of strike-slip faults may also play an important role in focusing economic mineralization. While some mineralization types such as porphyry-style deposits are well understood, significant uncertainty about the sources and processes responsible for others are still a source of debate. In particular, the mechanisms for the formation of iron oxide-copper-gold deposits remain controversial, and may be related to either magmatic-hydrothermal fluids or evaporite brines. Significant hydrothermal fluid flow derived from arc plutons is one of the proposed sources of this type of mineralization, and supporting or disproving a link to subduction-related magmatic arcs would greatly help future exploration efforts.

The central objective of this study is to improve our understanding of the relationship between arc magmatism and trench-linked strike-slip faulting during oblique subduction, with a particular focus on changes in rheology and implications for economic mineralization. I have addressed these topics through a detailed study of the Atacama fault system (AFS) in northern Chile, one of the best and most accessible examples of a major fossil trench-parallel, intra-arc strike-slip

fault system. This fault system accommodated lateral strain from the subducting Phoenix plate during Mesozoic oblique convergence and is exposed for $\sim 1,000$ km in the Late Jurassic to Early Cretaceous arc between Iquique and La Serena (Figure 2). The AFS is an ideal setting to study the structural evolution of an intra-arc strike-slip system because the hyperarid climate of the Atacama desert has resulted in unparalleled exposures of multiple generations of arc-related intrusions that are cut by ductile shear zones and/or brittle faults, providing an excellent opportunity to examine the relationship between magmatism and deformation and constrain the timing and magnitude of displacement. Brittle faults along this major regional structure provided a focused pathway for fluids exsolved from arc plutons at depth, giving rise to some of the largest iron oxide-copper-gold deposits in Chile.

The central objective of this study is to improve our understanding of the development of trench-linked strike-slip faults in magmatic arcs during oblique subduction. I addressed these topics through a series of focused questions in three chapters:

Chapter 1: How did magmatism affect deformation along the AFS?

Chapter 2: What was the magnitude and timing of slip along the AFS?

Chapter 3: How does AFS deformation relate to Chilean Iron Belt mineralization?

Results and interpretations presented in this dissertation are the result of an extensive field campaign over 5 seasons that mapped a ~ 5 km-wide swath along the northern ~ 70 km of the El Salado segment near Taltal, a ~ 70 km² area along the central El Salado segment near the Mantoverde mine, and a ~ 6 km² area near Copiapó. Field mapping was a team effort and included John Singleton, Skyler Mavor, Stewart Williams, Evan Strickland, Rachel Ruthven, and Micah Hernandez from Colorado State University and Rodrigo Gomila, Gert Heuser, and Gloria Arancibia from the Pontificia Universidad Católica de Chile in Santiago. Most geologic mapping focused on the exposed Coastal Cordilleran arc plutons and volcanics along the northern El Salado segment between Taltal and Copiapó. Mapping compiled at 1:25,000-scale by myself and S. Mavor. Structural data and samples for petrographic, microstructural, and geochemical analysis were collected from all three mapping areas.

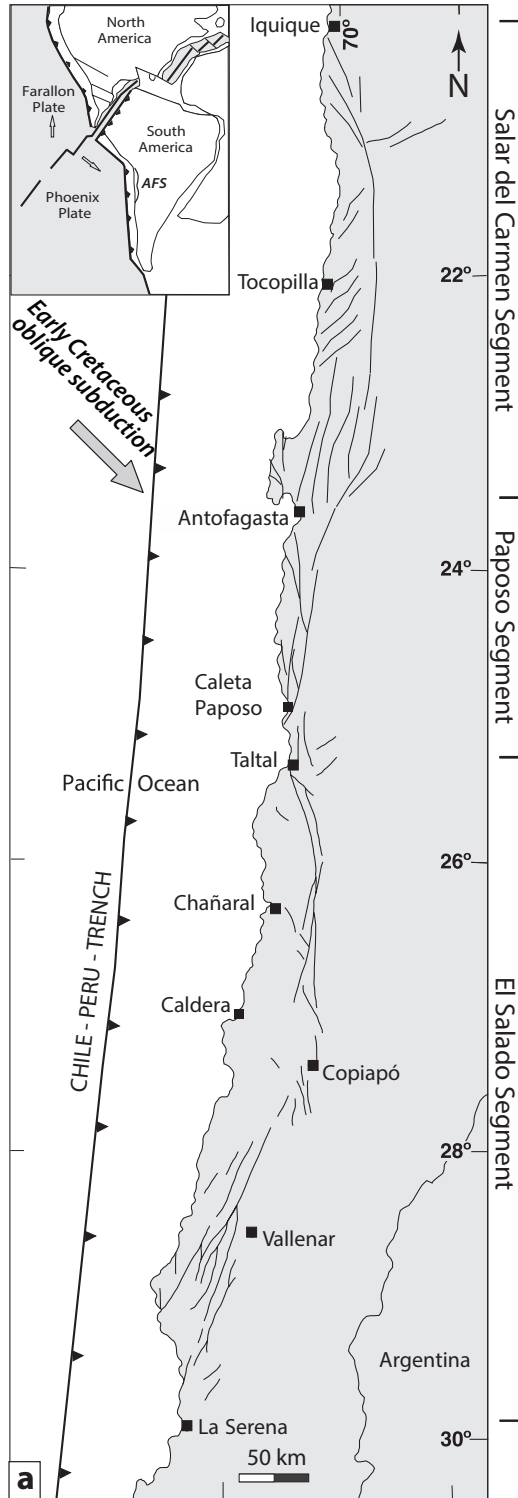


Figure 2: (a) Regional geometry of northern Chile showing the three segments of Atacama fault system (AFS) modified from Cembrano et al. (2005). Gray arrow shows the Mesozoic convergence vector from Jaillard et al. (1990).

Analytical methods including U-Pb geochronology and (U-Th)/He thermochronology in addition to oxygen stable isotope and whole-rock geochemistry supplemented mapping results, and here I present 25 new zircon U-Pb dates, 2 andradite U-Pb dates, 3 sulfide Re-Os dates, 10 zircon (U-Th)/He dates, 6 whole-rock geochemical analyses, and 8 bulk oxygen stable isotope analyses on mineral separates from 2 samples. I conducted all U-Pb and (U-Th)/He analyses at the University of Texas at Austin in the UT-Chron laboratory facilities. Daniel Stockli, Rudra Chatterjee, Megan Flansburg, Des Patterson, Margo Odlum, and Lisa Stockli assisted with laboratory analyses at UTChron. Re-Os analyses were conducted at the AIRIE laboratory at Colorado State University. Michelle Gevedon performed oxygen stable isotope analyses in Jaime Barnes' lab at UT-Austin. ALS Labs in Reno, NV and Activation Laboratories in Canada conducted whole-rock geochemistry. Geo/thermochronometric and geochemical data are available through the NSF-funded Geochron and EarthChem databases (https://www.geochron.org/dataset/html/geochron_dataset_2020_01_21_C9pPo).

All three chapters of this dissertation were written as extended versions of manuscripts that either have been or will be submitted to peer-reviewed journals. Chapter 1 addresses the relationship between Coastal Cordillera arc magmatism and AFS deformation using geologic mapping and geochronology (see also Seymour et al., 2020). Magmatic arcs are characterized by high geothermal gradients in the upper 10 km of the crust, providing an ideal thermally-weakened site to localize strike-slip motion. Brittle structures overprint a variety of kinematically compatible ductile fabrics along the AFS and clearly preserve the fossil brittle-plastic transition. New mapping in conjunction with zircon U-Pb data document two primary episodes of arc magmatism in the Jurassic and Early Cretaceous. The Early Cretaceous pulse is both temporally and spatially linked to deformation along the El Salado segment, and the presence of mylonites only along the margins of the Early Cretaceous plutons and the surrounding Chañaral Complex metasedimentary rocks further indicates pluton emplacement facilitated sinistral slip by providing a thermally-weakened zone to initiate deformation which then propagated out into the surrounding lithologies as a brittle fault. These along-strike rheological changes indicate elevated geothermal gradients around Early

Cretaceous plutons locally raised the brittle-plastic transition to shallow ($\sim 5\text{--}7$ km) crustal depths. Zircon U-Pb and (U-Th)/He data document the end of magmatic activity coeval with the end of brittle slip and subsequent regional cooling, indicating cooling of the arc is linked to abandonment of the AFS.

Chapter 2 builds on the results of Chapter 1 and evaluates the correlation of pre-, syn-, and post-tectonic intrusions along the El Salado segment to determine the timing, magnitude, and rate of slip during Mesozoic convergence. The regional tectonic history of an area provides key insights into how intra-arc strike-slip fault systems accommodated oblique strain and slip partitioning. Previous estimates of slip along the AFS are poorly constrained because no clear piercing points have been identified across the fault system. New mapping presented here documents offset markers across the eastern and western branches of the El Salado segment that allows me to reconstruct the slip history and determine the magnitude, timing, and rate of slip along the AFS: a pair of synkinematic plutons and associated metasedimentary mylonites across the eastern branch and a chain of leucocratic granites across the western branch. These results provide the first full estimate of displacement across two major branches the El Salado segment of the Atacama fault system during Early Cretaceous convergence based on offset geological markers: 32–38 km on the eastern branch and $\sim 14\text{--}18$ km on the western branch. Cross-cutting relationships constrain the timing of slip to $\sim 133\text{--}110$ Ma, yielding a slip rate of $\sim 2.0\text{--}2.5$ km/Myr over the ~ 23 Myr duration of deformation. Compared to other trench-linked intra-arc strike-slip systems such as the Sumatran, Philippine, and Liquiñe-Ofqui faults, these rates are relatively low, which suggests: (a) plate convergence rates or obliquity may have been significantly lower than previously modeled, (b) the vast majority of trench-parallel slip was accommodated along the slab interface or within the forearc, and/or (c) soft-linkage of the fault system prevented effective lateral transport of the forearc sliver.

Finally, Chapter 3 expands upon the relationships explored in Chapter 1 and investigates the presence of hydrothermal alteration along the El Salado segment near Copiapó. The El Salado segment has played an important role in controlling mineralization along the Chilean Iron Belt, which hosts some of the largest copper reserves in Chile including the Mantoverde and Candelaria

deposits. This study uses a combination of geologic mapping, geochronology, and geochemistry to relate the ductile shear zone to the broader history of Coastal Cordillera arc magmatism and AFS deformation. I also incorporate whole-rock and stable isotope geochemistry to compare hydrothermal alteration along the AFS to the Punta del Cobre mining district to understand how ore-forming plutons and IOCG mineralization are related to AFS deformation.

Chapter 1

The Relationship between Magmatism and Deformation

Summary

Magmatic arcs may play a major role in the initiation, behavior, and abandonment of intra-arc strike-slip systems. Here we present zircon U-Pb and (U-Th)/He geo-/thermochronology with new mapping to relate Coastal Cordillera arc magmatism to sinistral shear along the Atacama fault system (AFS) in northern Chile. New dates from 18 intrusions along the AFS between 24.6–27° S compiled with published data record a minor Early Jurassic magmatic pulse (185–175 Ma), broad latest Jurassic to Early Cretaceous (150–120 Ma) pulse, and a minor younger (120–105 Ma) pulse. Mylonitization occurred only along the margins of Early Cretaceous plutons and surrounding Paleozoic metasedimentary rock, whereas Jurassic plutons and metasedimentary rocks away from Early Cretaceous plutons lack mylonitic fabrics. Early Cretaceous magmatism facilitated AFS deformation by thermally weakening the crust with elevated geothermal gradients that enabled mylonitization to take place at ~5-7 km depths and low stresses. Spatial variability of pluton emplacement produced significant rheological heterogeneity, giving rise to a highly segmented fault system that did not originate as a regional-scale shear zone. Synkinematic dikes (~120–117 Ma) cut mylonitic fabrics, and a post-kinematic dike (~110 Ma) records the end stages of slip. The cessation of slip coincided with cooling below ~180°C at ~116–99 Ma as arc magmatism migrated eastward and geothermal gradients relaxed, coeval with a major reorganization in plate motion and the onset of seafloor spreading in the south Atlantic.

1.1 Introduction

Trench-parallel intra-arc faults directly accommodate oblique plate convergence and facilitate large-magnitude forearc block and exotic terrane translation (Beck, 1991; Jarrard, 1986; Avé Lallemant and Oldow, 1988)¹. Magmatic arcs are fundamental features of most subduction zones, and may play a major role in the initiation, development, and eventual abandonment of intra-arc strike-slip systems. The importance of these systems has been recognized for over 30 years (Jarrard, 1986; Woodcock et al., 1986), and many arcs and batholiths have prominent faults running the length of the arc (e.g., Busby-Spera and Saleeby, 1990; Barrier et al., 1991; Cembrano et al., 1996; Quebral et al., 1996; McCarthy and Elders, 1997; Sieh and Natawidjaja, 2000; Tabei et al., 2003; Cembrano et al., 2005; Sato et al., 2015). The rheological behavior and magnitude of displacement on these faults has implications for the tectonics of terrane translation, slab-upper plate coupling, crustal strength, and relationship between magmatism and fault displacement.

Several studies have discussed potential genetic relationships between magmatism and deformation, with some authors suggesting magmatism is necessary for the initiation of intra-arc deformation during oblique subduction (e.g., Beck, 1983; de Saint Blanquat et al., 1998; Scheuber and Reutter, 1992; Cao et al., 2015), while others suggest the presence of active intra-arc strike-slip structures provides pathways for magma emplacement (e.g., Glazner, 1991; de Saint Blanquat et al., 1998; Grocott and Taylor, 2002; Cembrano and Lara, 2009). Spatial and temporal pulses of arc magmatism are expected to have an important effect on strain localization in the upper plate. Magmatic arcs are characterized by high geothermal gradients in the upper 15 km of the crust (up to 40°C/km in Japan, Uyeda and Hôrai (1964); ~45–65°C/km in the Cascades, Blackwell et al. (1982, 1990); and ~40°C/km in the eastern Peninsular Ranges, Rothstein and Manning (2003)), providing an ideal thermally weakened site to localize strike-slip motion (Beck, 1983; Jaquet and Schmalholz, 2018). High geothermal gradients within the arc compared to the surrounding country rock can result in a locally elevated brittle-plastic transition, allowing for ductile deformation

¹This chapter is published: Seymour, N.M., Singleton, J.S., Mavor, S.P., Gomila, R., Stockli, D.F., Heuser, G. and Arancibia, G., 2020, The relationship between magmatism and deformation along the intra-arc strike-slip Atacama fault system, northern Chile. *Tectonics*, p.e2019TC005702.

at shallower crustal levels and lower deviatoric stress magnitudes. Furthermore, a heterogeneous distribution of intrusions in the shallow crust would produce variations in the degree of thermal softening, which would in turn produce a range of ductile shear versus brittle behavior at similar crustal levels. The duration of arc magmatism may also play a key role in the development of these structures, as a large volume of magma and continued intrusions would be needed in order to maintain a consistently elevated geothermal gradient while cooling of the arc has been suggested to coincide with abandonment of intra-arc fault systems (Busby-Spera and Saleeby, 1990; Brown et al., 1993; Dallmeyer et al., 1996; Scheuber and Gonzalez, 1999; Andronicos et al., 2003; Nadin et al., 2008), underlining the importance of this relationship.

The Atacama fault system (AFS), located within the Mesozoic Coastal Cordillera arc, is a classic example of an intra-arc strike-slip system that accommodated oblique convergence along the Peru-Chile trench (e.g., Scheuber and Andriessen, 1990, Figure 1.1). The AFS is an ideal setting for studying the structural and rheological evolution of an intra-arc strike-slip system because the hyperarid climate of the Atacama Desert has resulted in excellent exposures of arc-related intrusions and brittle structures that overprint ductile fabrics. Here we integrate geologic mapping and structural measurements along the AFS with new zircon U-Pb and (U-Th)/He dates on syn- and post-kinematic intrusions and existing literature data to document the deformational, magmatic, and cooling history of this intra-arc strike-slip system. Together, these new data allow us to relate pulses of magmatism and subsequent cooling of the arc to the behavior and abandonment of the AFS, providing a clear picture of the spatial and temporal relationships between arc activity and deformation in the Coastal Cordillera.

1.2 Geologic Setting

Subduction beneath the western margin of South America from ~ 200 Ma to the present day has resulted in an extended period of arc magmatism and forearc deformation (Mpodozis and Kay, 1992; Parada et al., 2007; Charrier et al., 2007, 2015). Until the Late Permian, subduction and terrane accretion associated with the assembly of Gondwana dominated the tectonic development

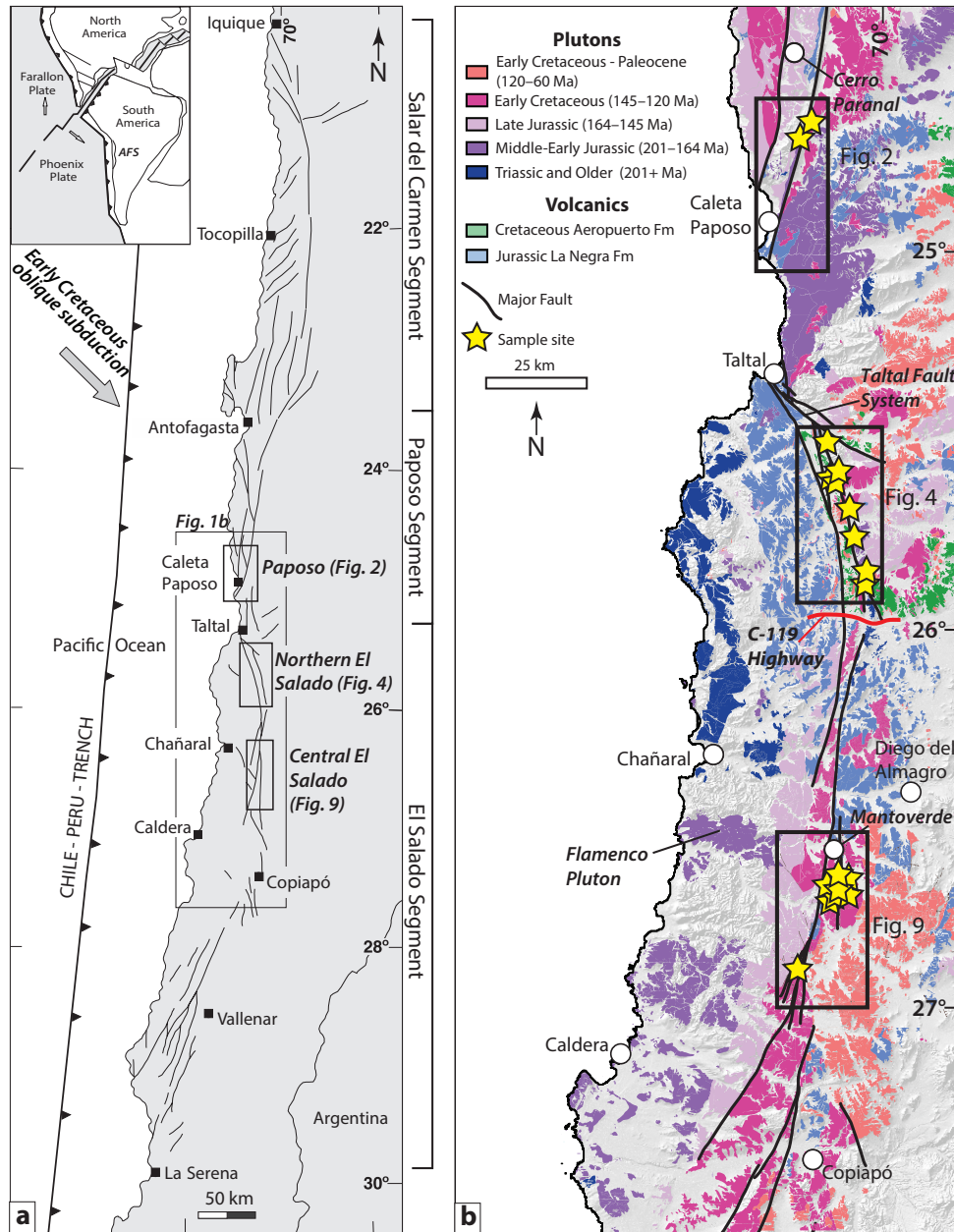


Figure 1.1: (a) Regional scale geometry of northern Chile showing the three segments of Atacama fault system (AFS) modified from Cembrano et al. (2005). Gray arrow shows the Mesozoic convergence vector from Jaillard et al. (1990). Boxes show the location and name of the three areas studied in this work. Inset map shows approximate plate configuration coeval with Mesozoic sinistral strike-slip deformation along the AFS from Jaillard et al. (1990). (b) Map of igneous lithologies color-coded by age. Note the west to east younging of pluton age and the spatial association of major AFS faults with Early Cretaceous plutons (pink). Data were compiled and simplified from SERNAGEOMIN quadrangle maps (Álvarez et al., 2016; Escribano et al., 2013; Contreras et al., 2013; Espinoza et al., 2014; Godoy and Lara, 1998, 1999; Lara and Godoy, 1998; Godoy et al., 2003; Arévalo, 2005a). Stars indicate sample locations for new dates presented in this study.

of northern Chile. Late Permian–Triassic granitic to syenogranitic S-type magmatism that lacks a calc-alkaline signature documents a ~55 Myr subduction hiatus during the final assembly of Gondwana (Berg and Baumann, 1985; Charrier et al., 2007). Early Jurassic calc-alkaline plutonism records the renewal of subduction along the northern Chilean margin as the Phoenix (Aluk) plate subducted obliquely southeastward below the South American plate along the N-S trending Peru-Chile trench (Coira et al., 1982). The SE-directed convergence vector has been attributed to spreading across a Farallon-Phoenix ridge, which Jaillard et al. (1990) suggest was kinematically related to Tethyan rifting in the North Atlantic and Western Mediterranean. Sinistral forearc translation was accommodated along the Atacama fault system, which extends from Iquique (20.5°S) to La Serena, Chile (30°S) (Figure 1.1a).

1.2.1 Development of the Coastal Cordilleran Arc

Coastal Cordillera plutons are elongate, tabular bodies intruded into metasedimentary rocks of the Carboniferous Chañaral Complex at middle to upper crustal levels along a N-S trend (Figure 1.1b, Godoy and Lara, 1998). Permian, Triassic, and Jurassic mafic diorite and tonalite are found along the coast and Cretaceous quartz diorite, tonalite, and granodiorite were emplaced progressively inboard (eastward) of the margin (Naranjo and Puig, 1984; Dallmeyer et al., 1996; Parada et al., 2007; Oliveros et al., 2010). The earliest magmatism associated with the renewal of subduction and development of the Coastal Cordilleran arc is the Early Jurassic Flamenco pluton near Chañaral (Figure 1.1b, Grocott et al., 1994; Dallmeyer et al., 1996; Rodríguez et al., 2019). Magmatism was dominantly calc-alkaline I-type with $^{86}\text{Sr}/^{87}\text{Sr}$ and ϵNd values indicative of a mantle or deep crustal source with little to no crustal contamination (Berg and Breitzkreuz, 1983; Rogers and Hawkesworth, 1989; Lucassen and Thirlwall, 1998). Jurassic calc-alkaline to alkaline andesitic lava flows of the La Negra Formation also record low $^{86}\text{Sr}/^{87}\text{Sr}$ ratios and overlie Late Triassic-earliest Jurassic extensional basin sequences (Oliveros et al., 2010).

Mesozoic magmatic activity peaked between the Middle Jurassic-Early Cretaceous (160–120 Ma; Boric et al. (1990) in Scheuber and Gonzalez (1999)) and postdated La Negra volcanism. Up-

lift of the Coastal Cordillera has been interpreted from Albian (113–100 Ma) apatite fission track dates (Maksaev, 1990; Gana and Zentilli, 2000) and correlates with a major regional unconformity between backarc sedimentary units and overlying Late Cretaceous units (Scheuber et al., 1994). Both the Albian fission track dates and a regional unconformity are temporally associated with erosion of the continental margin, eastern migration of the magmatic arc, and development of both a wide forearc and continental foreland basin (Coira et al., 1982; Emparan and Pineda, 2000, 2005).

1.2.2 Development of the Atacama fault system

Deformation accommodating the trench-parallel component of southeast-directed oblique convergence below the N-S trending Gondwanan margin localized along the intra-arc AFS. Three major segments of the fault system (the Salar del Carmen, Paposo, and El Salado segments) are composed of several parallel branches rather than a single through-going fault plane and together comprise the ~1,000 km fault system (Figure 1.1a). Motion along the AFS was dominantly sinistral strike-slip with periods that also included margin-perpendicular extension or shortening (Grocott and Taylor, 2002; Scheuber and Andriessen, 1990; Stern, 2011; Ruthven et al., 2020). The NW-striking Taltal fault system cuts the AFS (Arabasz, 1971; Mavor et al., 2020).

Several studies present evidence that the AFS has been active intermittently since the Jurassic, with the oldest middle-crustal mylonites hosted in and temporally related to Middle to Late Jurassic arc plutons along the Salar del Carmen and Paposo segments (Scheuber and Andriessen, 1990; Scheuber and Reutter, 1992; Scheuber et al., 1994). A compilation of hornblende and biotite K-Ar and $^{40}\text{Ar}/^{39}\text{Ar}$ data shows a peak in ductile deformation associated with growth of synkinematic biotite in mylonites between 160–120 Ma (Scheuber and Gonzalez, 1999). Kinematically compatible brittle faults are superimposed on ductile shear zones along the AFS, suggesting the structure evolved from ductile to brittle behavior during slip in the Cretaceous based on K-Ar dates of mineralization associated with faulting (Zentilli, 1974; Brown et al., 1993; Vila et al., 1996; Scheuber et al., 1995). Neogene to Quaternary E-side-down dip-slip motion recorded along the main strand of the Paposo segment (Hervé, 1987a; Naranjo, 1987; González and Carrizo, 2003;

González et al., 2006; Allmendinger and González, 2010) did not significantly overprint or alter the Cretaceous structures.

1.3 Methods

1.3.1 Field Methods & Sampling Strategy

Three primary regions were chosen that feature mylonite zones overprinted by brittle structures: the Paposo segment, northern El Salado segment, and central El Salado segment. We incorporated recent mapping along the southern Paposo segment along a 5 km-wide swath stretching ~ 27 km from Cerro Paranal to Caleta Paposo and completed new mapping along both a 5 km-wide swath ~ 40 km from the Taltal fault system to the C-119 highway and a ~ 70 km² area just south of the Mantoverde mine (Figure 1.1a). Sites located between these study regions typically lack well-developed mylonite zones.

Lithologies in each area were examined for ductile and/or magmatic fabrics including quartz recrystallization, aligned minerals, asymmetric porphyroclasts, and S-C fabrics. We collected samples for thin section petrography and geo/thermochronometric analyses, including a range of syn- and post-kinematic plutons with a variety of compositions and degrees of alteration (Table 1.1). We collected orientation data on brittle fault planes and slickenlines. Slip sense was determined using offset features, Riedel shears, lunate steps, T-fractures, and mineral growth steps (e.g., Petit, 1987). Structural data were plotted and analyzed with Stereonet and FaultKin (Marrett and Allmendinger, 1990; Allmendinger et al., 2011; Cardozo and Allmendinger, 2013). Average structural orientations were determined using maximum eigenvectors.

1.3.2 Compilation of geochronologic data

We compiled published Coastal Cordillera age data within 10 km of the AFS to provide a context for our new geo/thermochronometric data. Published age data from Servicio Nacional de Geología y Minería (SERNAGEOMIN) quadrangle maps, theses/dissertations, and previous studies were classified by mineral and method type (U-Pb, K-Ar, ⁴⁰Ar/³⁹Ar, etc.) and plotted

Table 1.1: Summary of sample lithology and degree of strain.

Sample	UTM Coordinates ¹		Lithology	Deformation
	Easting (m)	Northing (m)		
161-29	360554	7255860	Hbl Tonalite	Protomylonitic
171-P118	358915	7253026	Tonalite	Unstrained
171-N235	373065	7146532	Bt Granodiorite	Altered; Brittle Fracture
171-J250	375552	7132552	Granodiorite	Altered; Brittle Fracture
171-N225	375029	7134850	Tonalite	Altered; Brittle Fracture
181-S55	368531	7163402	Hbl Granodiorite	Protomylonitic
188-S158	368815	7161392	Hbl-Bt Granodiorite	Protomylonitic
181-S228	368352	7163483	Boudin – Granodiorite	Unstrained
161-62	370930	7152474	Bt-Hbl Tonalite	Unstrained
161-43	364950	7171489	Andesitic Dike	Unstrained; Cut by Fault
181-N44	369801	7049130	Granite	Discrete Shear Zones
181-N76	368261	7045339	Hbl Qz Diorite	Unstrained
161-89	369238	7049392	Hbl Granodiorite	Mylonitic
171-G200	371743	7046186	Andesitic Dike	Unstrained; Cut by Fault
171-G229	370304	7050021	Dacitic Dike	Unstrained; Cut by Fault
161-87	368999	7049417	Bt-Hbl Tonalite	Unstrained
181-N67	368130	7046175	Bt-Hbl Tonalite	Unstrained
181-N103	362644	7028496	Hbl Qz Diorite	Unstrained

¹Coordinates in Universal Transverse Mercator (UTM) World Geodetic System 1984 (WGS84)

using DensityPlotter (Vermeesch, 2012) with a bandwidth of 3 and bin width of 5 Myr to identify age peaks. Peaks are defined by visual inspection; taller ($n \geq 5$ dates) peaks were defined as major pulses and shorter ($5 > n > 1$) peaks defined as minor or subpulses. We combine K-Ar and $^{40}\text{Ar}/^{39}\text{Ar}$ dates of volcanic rocks and zircon U-Pb dates on both plutonic and volcanic lithologies in order to capture the timing of both intrusive and extrusive magma emplacement and compare zircon U-Pb to K-Ar and $^{40}\text{Ar}/^{39}\text{Ar}$ dates of plutonic rocks to evaluate differences in emplacement versus cooling dates. Data classified as mineralization, alteration, or deformation dates were excluded. A full list of data and publications included in the compilation is included in the Data Repository (Appendix 3.6).

1.3.3 U-Pb Geochronology

Previous geochronologic studies of the Coastal Cordillera have primarily utilized hornblende and biotite K-Ar and $^{40}\text{Ar}/^{39}\text{Ar}$ data (e.g., Zentilli, 1974; Hervé and Marinovic, 1989; Dallmeyer et al., 1996; Kurth, 2002); however, these systems record high-temperature cooling dates rather than crystallization dates and are more susceptible to disturbance by thermal perturbations or hydrothermal alteration (e.g., Harrison, 1982; Harrison et al., 1985; Grove and Harrison, 1996; Dahl, 1996). Older plutons are commonly hydrothermally altered with replacement of magmatic biotite and hornblende by chlorite and actinolite, so age compilations using these data are inherently biased towards younger, fresher rocks. Here we use zircon U-Pb geochronology, which typically does not experience post-crystallization resetting and has been applied worldwide to understand the timing of pluton emplacement.

Zircons from samples 171-P118, 171-N235, 171-N225, 171-J250, 188-S55, and 161-62 were mounted in epoxy, polished to expose the center of the grains, and imaged using cathodoluminescence (CL) to document internal zoning patterns (Appendix 3.6). We depth-profiled euhedral, unpolished grains for samples 161-29, 171-P118, 181-S228, 188-S158, 161-62, 161-43, 181-N44, 181-N76, 161-89, 161-87, 181-N67, 181-N103, 171-G200, and 171-G229 to capture potential core-and-rim relationships that are too thin to resolve by spot analysis on polished mounts (e.g.,

Marsh and Stockli, 2015). Depth-profiled zircons were mounted parallel to the c-axis on double-sided tape. Both sample preparation styles were ablated with a Photon Machines Analyte G.2 Excimer laser. Approximately 30 zircon grains per sample were ablated using a 30 μm diameter spot with a repetition rate of 10 Hz for 30 seconds and analyzed on a ThermoScientific Element II high-resolution magnetic sector inductively coupled plasma mass spectrometer (HR-ICP-MS). Sample analyses were interspersed 5:1 with primary standard GJ1 (600 Ma, Jackson et al., 2004; Elhlou et al., 2006) to correct for elemental and downhole fractionation. Secondary standards Pak1 (43 Ma, unpublished thermal ionization mass spectrometry data), Plesovice (337 Ma, Sláma et al., 2008), and 91500 (1065 Ma, Wiedenbeck et al., 1995) were interspersed with unknowns to monitor date accuracy. Raw $^{206}\text{Pb}/^{238}\text{U}$ data were reduced in Iolite using VizualAgeDRS and plotted with Isoplot 4.15 (Ludwig, 2003; Jackson et al., 2004; Petrus and Kamber, 2012). The U decay constant of Jaffey et al. (1971) was used for all date calculations. The uncertainty reported for individual grains represents the combined internal and external error (Appendix 3.6). Reduced data were filtered to <10% discordance to eliminate grains with either inheritance or significant Pb loss. Weighted averages of concordant $^{206}\text{Pb}/^{238}\text{U}$ dates are reported with 2σ error.

1.3.4 (U-Th)/He Thermochronology

Zircon (U-Th)/He (ZHe) thermochronology records thermal histories of rocks via the retention of radiogenically-produced ^4He and can be used to understand cooling and exhumation of a region or particular structure (e.g., Ehlers and Farley, 2003; Reiners et al., 2003; Stockli, 2005). For rapidly cooled grains, He is lost from the zircon crystal lattice via thermally-activated volume diffusion at temperatures in excess of $\sim 180^\circ\text{C}$ (Reiners et al., 2004; Wolfe and Stockli, 2010). Below $\sim 180^\circ\text{C}$, He is retained, thereby recording the time since the grain passed through this closure temperature (Dodson, 1973).

Four to five unbroken, euhedral, inclusion-free zircons $>70 \mu\text{m}$ in width picked from each sample and measured for standard geometric alpha particle ejection correction (FT, Farley et al., 1996). Single-grain aliquots were packed in Pt tubes, laser heated to extract ^4He , and analyzed

on a Balzers Prisma QMS-200 quadrupole mass spectrometer. Aliquots were reheated until completely degassed (<1% He on second heating). Fish Canyon Tuff zircon grains were analyzed as standards. After complete degassing, aliquots were unpacked and dissolved in hydrofluoric and nitric acid in high-pressure digestion vessels, spiked with a 7N nitric solution enriched in ^{235}U , ^{230}Th , and ^{149}Sm , and analyzed for ^{238}U , ^{235}U , ^{230}Th , and ^{147}Sm on a Thermo Element2 HR-ICP-MS operated in solution mode. A standard analytical error of 8% is applied to each aliquot based on the internal laboratory reproducibility of the Fish Canyon Tuff standard (Reiners et al., 2002, 2004, Appendix 3.6). Average dates are reported for each sample. Error is reported as the larger of either the standard error of the average (n/standard deviation of dates) or the alternative standard error ($1/n \times \sqrt{\sum_i \sigma_{xi}^2}$, where n is the number of aliquots included in the average date and σ_{xi} is the error on each aliquot).

Table 1.2: Summary of geo/thermochronometric data.

Sample	Date Range	U-Pb			(U-Th)/He				
		Mean Date $\pm 2\sigma$ (Ma)	n ¹	MSWD	Mean Date $\pm 1\sigma$ (Ma)	n	SE ⁴	Alt SE	Max SE
161-29	118.8–141.2	130.3 \pm 1.7	21/23	3.7	106.7 \pm 2.8	5/6	1.3	3.5	7
171-P118	177.7–197.4	182.7 \pm 0.8	33/33	1.4	116.2 \pm 6.6	5/5	3	3	6
171-N235	188.2–219.4	196.4 \pm 2.2	27/29	4.1	107.9 \pm 5.4	5/5	3.4	2.9	5.8
171-J250	183.2–207.9	195.6 \pm 1.0	38/43	4.4	103 \pm 16	4/5	8	2.9	16
171-N225	175.8–524.4	188.6 \pm 0.8	32/35	1.7	-	-	-	-	-
181-S55	123.0–143.4	132.6 \pm 0.9	55/58	5.5	-	-	-	-	-
188-S158	128.1–155.0	132.3 \pm 1.3	23/26	3.5	-	-	-	-	-
181-S228	146.3–336.4	153.3 \pm 1.3	21/22	3.9	-	-	-	-	-
161-62 - cores	114.8–136.9	128.1 \pm 0.5	59	1.8	100.2 \pm 14.4	5/6	6.5	3.5	12.9
161-62 - rims	114.8–136.9	118.6 \pm 2.1	11	3.5	100.2 \pm 14.4	5/7	6.5	3.5	12.9
161-43	108.8–1339	119 \pm 6.6	8	70	-	-	-	-	-
161-43 ²	108.8–111.7	109.9 \pm 4.0	3						
181-N44	231.6–255.6	245.4 \pm 1.8	31/32	4.6	-	-	-	-	-
181-N76	130.1–142.7	135.6 \pm 1.5	15/15	5.9	-	-	-	-	-
161-89	120.3–157.3	132.1 \pm 1.9	19/21	5.3	98.2 \pm 4.3	4/6	2.2	2.8	4.3
171-G200	111.7–124.4	119.7 \pm 0.9	35/37	2.8	-	-	-	-	-
171-G229	111.6–123.6	117.1 \pm 0.9	37/38	3.2	-	-	-	-	-
161-87 ³	106.7–120.2	108.8 \pm 2.8	14/14	3.6	-	-	-	-	-
181-N67 ³	103.1–145.6	104.1 \pm 2.9	17/23	1.5	-	-	-	-	-
181-N103	103.5–111.9	107.1 \pm 0.9	26/27	4.5	-	-	-	-	-

¹Number of grains used to calculate average date. ²Date provided by youngest 3 grains. ³Date determined from lower Tera-Wasserburg Intercept. ⁴SE denotes Standard Error and is the larger of the normal Standard Error or the Alternative Standard Error. See text for details.

1.4 Results

Here we present results by study region, moving systematically from the southern Paposito segment near Cerro Paranal (24.6°S) to the southern margin of the central El Salado segment (27°S; Figure 1). In total, we present 18 zircon U-Pb dates and 6 zircon (U-Th)/He (ZHe) dates from intrusions along the Atacama fault system (Table 1.2).

1.4.1 Paposito Segment (24.6°S to 25°S)

The Paposito segment of the AFS is continuous for >160 km from Caleta Paposito to Antofagasta and is defined by the Paposito fault, the Izcuña fault, and a series of subsidiary structures (Figure 1.1, Figure 1.2; Naranjo, 1987; Cembrano et al., 2005; Jensen et al., 2011; Álvarez et al., 2016). Between Cerro Paranal to Caleta Paposito, the Paposito fault is the dominant structure and is lined entirely by the Jurassic Yumbes Tonalite on the west and the Latest Jurassic-Early Cretaceous Matancilla and Remiendos Plutonic Complexes on the east (Figure 1.2). South of Caleta Paposito, the fault is hosted entirely within the La Negra Formation and splits from one master fault into several parallel strands (Escribano et al., 2013). A mylonitic shear zone up to ~2 km wide is present along the southern ~37 km length of the eastern margin of the Paposito fault (Scheuber and Andriessen, 1990; Álvarez et al., 2016). A brittle fault gouge core (up to ~50 m wide) derived from the Jurassic Yumbes tonalite defines the trace of the Paposito fault between Caleta Paposito and Pacific Ocean (Ruthven et al., 2020).

Intrusions along the southern Paposito segment are predominantly tonalite and granodiorite with hornblende and biotite (Figure 1.2, Figure 1.3). Near Cerro Paranal on the western side of the Paposito fault, sample 171-P118 is an unstrained, coarse-grained hornblende biotite diorite mapped as the Yumbes tonalite (Álvarez et al., 2016). The pluton lacks dynamic recrystallization, and aligned hornblende and chloritized biotite define a weak magmatic fabric (Figure 1.3). Zircons yield U-Pb date of 182.7 ± 0.8 Ma ($n = 33/33$; MSWD = 1.4) and a ZHe date of 116.2 ± 6.0 Ma (Figure 1.3). CL imagery of zircon shows igneous textures such as oscillatory zoning with no evidence of overgrowth development (Appendix 3.6). Chlorite and actinolite replacement of

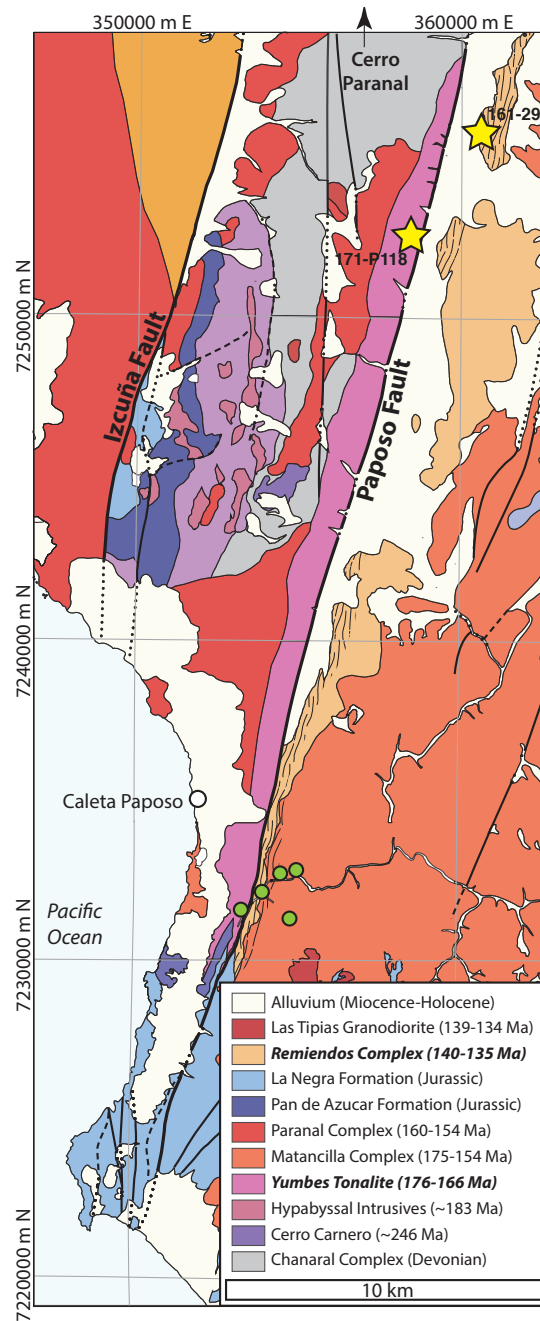


Figure 1.2: Simplified map of the Paposo study area compiled from Escribano et al. (2013), Álvarez et al. (2016), and Ruthven et al. (2020). The Yumbes tonalite is shown in light purple and the Remiendos Plutonic Complex is shown in shades of red and orange. Bold black lines show the Paposo and Izcuña Faults and mylonites are shown by the wavy pattern. Yellow stars show new U-Pb samples from this study and green circles show location of U-Pb data from Ruthven et al. (2020).

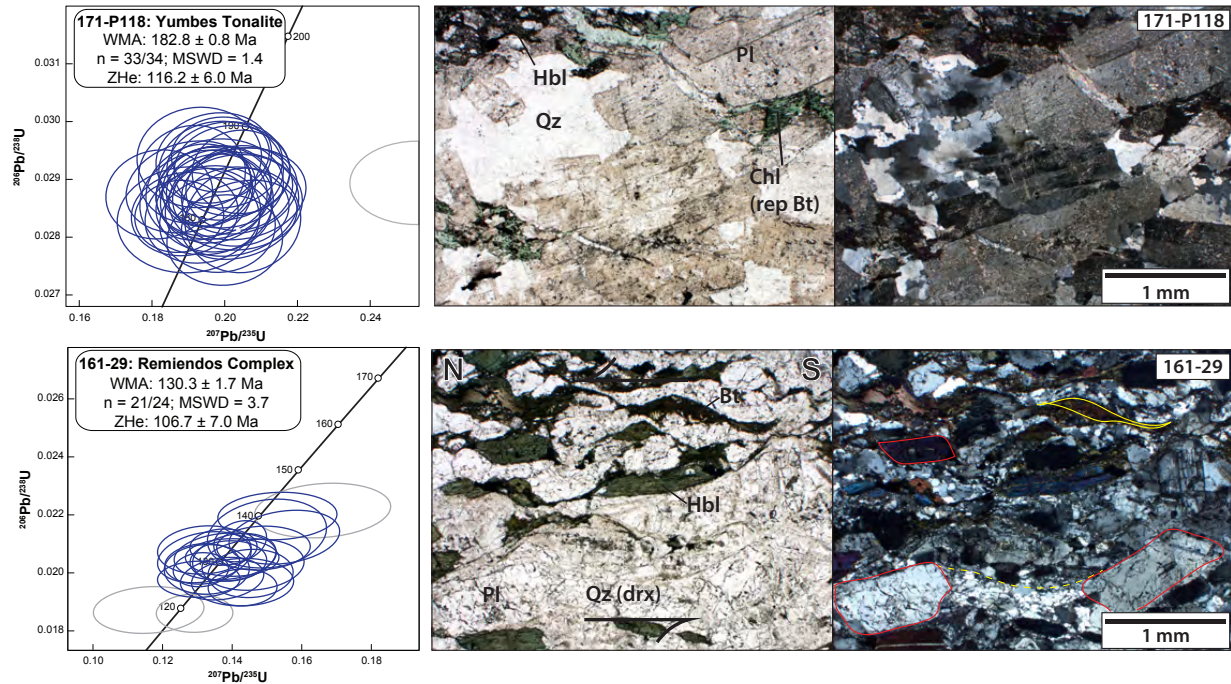


Figure 1.3: Left column: U-Pb concordia diagrams for the Yumbes tonalite and the Remiendos Plutonic Complex. Grains with >10% discordance are shown in gray. Uncertainties are reported at 2σ . Right column: Photomicrographs in plane-polarized and cross-polarized light of the altered but unstrained Yumbes tonalite (171-P118) and the mylonitized Remiendos Plutonic Complex (161-29). Yellow polygon outlines an asymmetric Bt showing sinistral shear, dashed yellow line indicates foliation defined by recrystallized Qz, and red polygons indicate internally undeformed Hbl and Pl crystals. Abbreviations are as follows: Bt = biotite; Chl = chlorite; drx = dynamically recrystallized; Hbl = hornblende; Qz = quartz; Pl = plagioclase; rep = replaced.

mafic phases generally increases with spatial proximity to the AFS, and fault gouge (up to ~ 50 m wide) derived from the Jurassic Yumbes tonalite defines the core of the Paposo fault between Caleta Paposo and Pacific Ocean (Ruthven et al., 2020).

The Early Cretaceous Remiendos Plutonic Complex (sample 161-29) records ductile strain and is a fresh, slightly protomylonitic hornblende tonalite just east of the Paposo fault near Cerro Paranal. The Remiendos tonalite has a U-Pb date of 130.3 ± 1.7 Ma (n = 21/24; MSWD = 3.7) and ZHe date of 106.7 ± 7.0 Ma (Figure 1.3). A mylonitic shear zone up to ~ 2 km wide is developed in this pluton and an adjacent Late Jurassic/Early Cretaceous granodiorite complex east of the Paposo fault (Figure 1.2, Scheuber and Andriessen, 1990; Álvarez et al., 2016; Ruthven et al., 2020). Plagioclase and hornblende grains are weakly aligned but internally undeformed.

Biotite-lined shear bands recording sinistral shear and quartz ribbons with minor bulging recrystallization define the foliation (Figure 1.3). Mylonitic fabrics record sinistral shear with an average foliation orientation of 032, 84 E, slightly clockwise of the trend of the Paposo fault at this latitude (015–195°) and compatible with kinematic data from ultramylonites near Cerro Paranal and Cerro Yumbes (Scheuber and Andriessen, 1990).

1.4.2 Northern El Salado Segment (25.5°S to 26°S)

The AFS is composed of two major strands along the northern El Salado segment, defined as the western branch and the eastern branch. The western branch is mapped for ~130 km from the coast at Taltal to the C-209 highway, ~55 km northwest of the town of Diego del Almagro and the eastern branch is mapped as a discontinuous trace for ~180 km from the coast north of Taltal to its termination 6 km south of the C-119 highway, ~45 km north of the city of Copiapó (~26°S; Figure 1.1, Figure 1.4; Escribano et al., 2013; Espinoza et al., 2014; Godoy and Lara, 1999; Lara and Godoy, 1998). Within the mapped area shown in Figure 1.4, the western branch is largely covered by alluvium. La Negra volcanics occur west of the fault, and Early Cretaceous volcanic and clastic strata of the Aeropuerto Formation crops out between the western and eastern branches. The eastern branch is mapped as a discontinuous trace for ~180 km from the coast north of Taltal to its termination 6 km south of the C-319 highway, ~45 km north of the city of Copiapó (Escribano et al., 2013; Espinoza et al., 2014; Godoy and Lara, 1999; Lara and Godoy, 1998). The eastern branch is mapped as two main strands and a series of subsidiary structures (Figure 1.4; Espinoza et al., 2014). Along the 40 km length of the eastern branch through this map area, Early Cretaceous plutons are found for 12–14 km on the eastern side and 7–8 km on the western side, thereby accounting for ~30% and ~18–20% of the exposure along the eastern and western margins, respectively. The remaining ~13.7 km along the eastern margin are Chañaral Complex metasedimentary rocks (~35%), and 22 km of exposed rock on the western margin of the eastern branch is Aeropuerto volcanics. Jurassic plutons are along the eastern margin of the eastern branch for 11 km (~28%; Espinoza et al., 2014, this work).

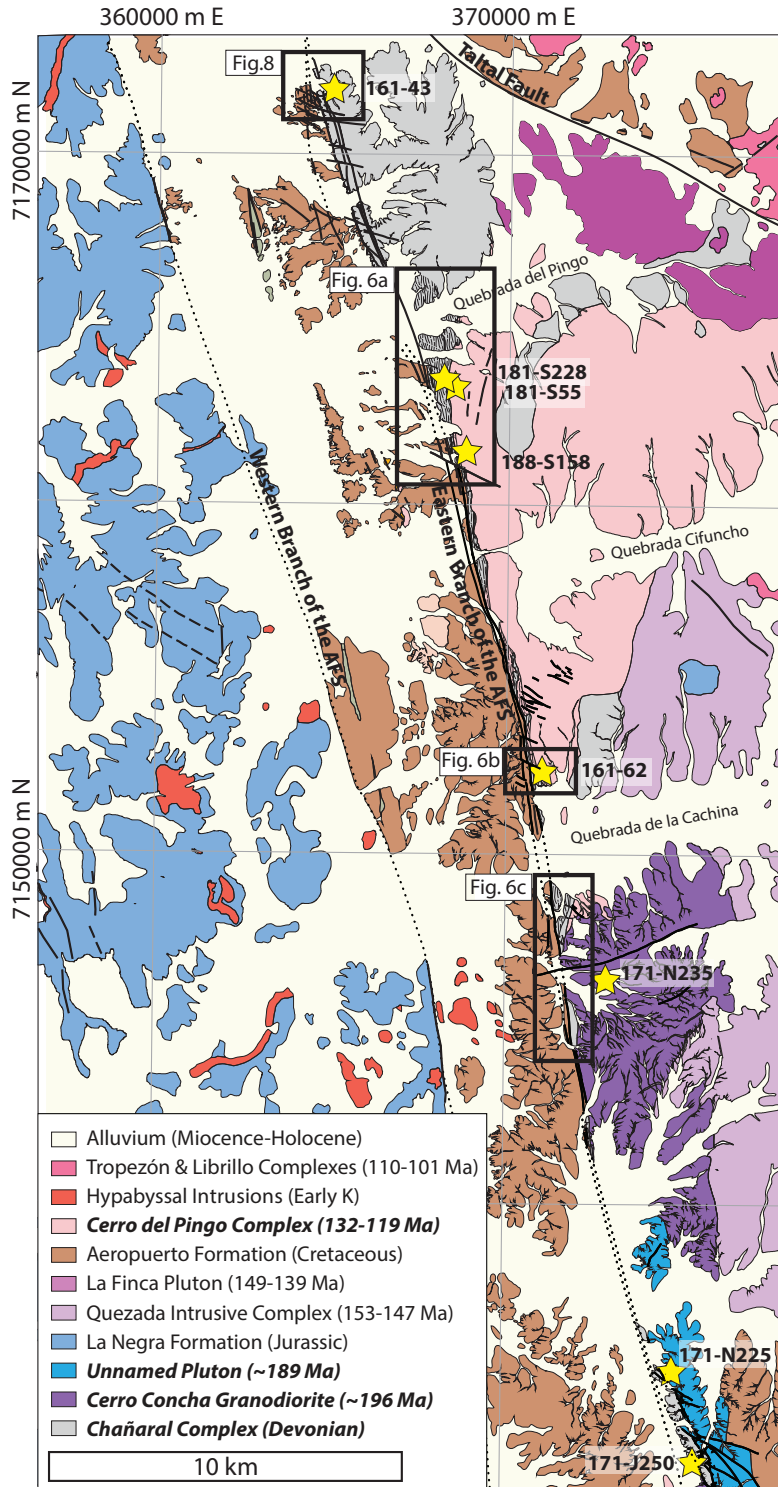


Figure 1.4: Simplified map of the northern El Salado segment study area compiled from our new mapping and Espinoza et al. (2014). The Cerro del Pingo Complex is shown in pink, the Jurassic plutons are shown in purple and blue, and the Chañaral Complex is shown in gray. Bold black lines show the major strands of the AFS and mylonites are shown by the wavy pattern. Yellow stars show new U-Pb samples from this study. Black boxes show the location of the inset maps in Figure 1.6 and Figure 1.8.

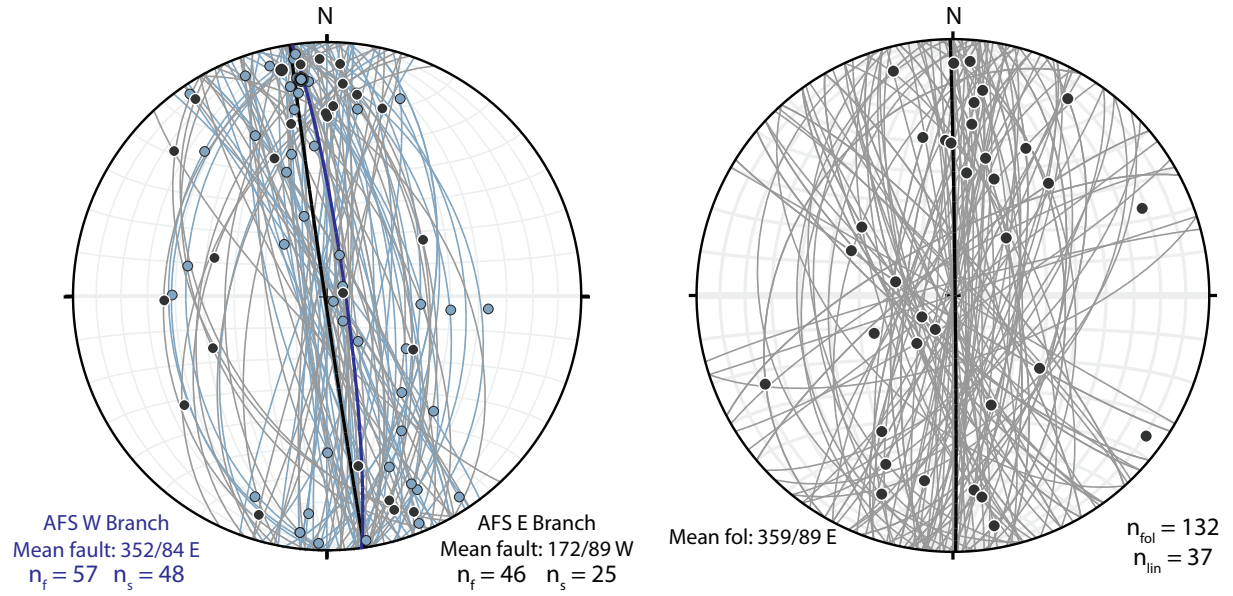


Figure 1.5: Equal-area stereograms of brittle faults (left) and mylonitic foliations (right) from the northern El Salado segment. Individual measurements are shown with great circles (faults, foliations) and dots (slickenlines, lineations). Average orientations are given by bold great circle (faults, foliations).

The trend of the AFS along the northern El Salado segment ranges between $\sim 345^\circ$ to 357° . The average orientation of principal slip surfaces on the western branch is 352, 84 E with an average slickenline trend of 349/10, whereas the average orientation of the eastern branch is 172, 89 W with an average slickenline orientation of 353/14 (Figure 1.5). These orientations are $\sim 7^\circ$ counterclockwise of the average orientation of mylonitic fabrics (359, 89 E) along the eastern branch. The width of the damage zone correlates to the presence or absence of variably mylonitized quartzites and Early Cretaceous tonalites: where these mylonitic lithologies are present the brittle damage zone is narrow (<10 m) compared to the mylonite zone (up to 800 m), and where Early Cretaceous tonalites are absent the damage zone is entirely brittle and up to ~ 200 – 300 m wide.

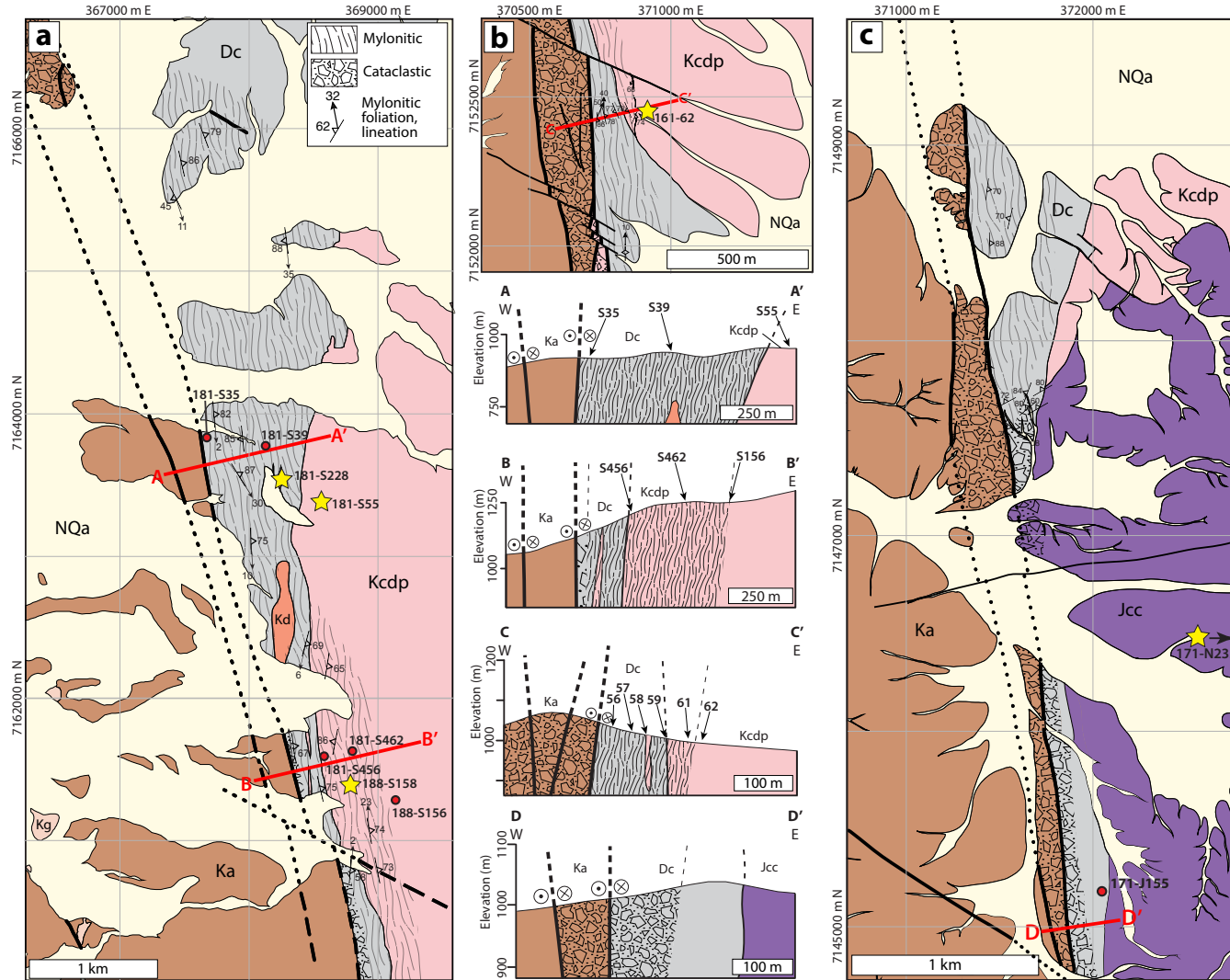


Figure 1.6: Left: Inset map of the northern and central region Cerro del Pingo Complex, Center: Inset map of the southern region Cerro del Pingo Complex, and Right: Inset map of Jurassic plutons adjacent to the AFS south of the Cerro del Pingo Complex. Cross-sections correspond to the lines indicated in each map.

Along the northern El Salado segment, both the Jurassic La Negra and Early Cretaceous Aeropuerto formations are highly fractured with cataclasite zones up to ~ 200 m thick. Jurassic and Early Cretaceous plutons intrude the Chañaral Complex along the eastern strand of the AFS. Jurassic plutons primarily record brittle deformation with local mylonitization concentrated in discrete shear zones. Discontinuous screens of Chañaral Complex metasedimentary rocks along the AFS adjacent to Jurassic plutons are up to ~ 400 m thick and deformed by cataclasis (Figure 1.6c). Chañaral Complex metasedimentary rocks are composed of variably metamorphosed decimeter-scale phyllite and quartzite interbeds. Phyllites are dominated by sericite with lesser biotite, chlorite, and fine-grained quartz. Quartzites are medium- to fine-grained quartz arenite and arkose: quartz arenites are generally monocrystalline quartz with undulatory extinction and scarce fine interstitial sericite, and arkoses have sub-rounded to subangular quartz and plagioclase. These outcrops retain detrital or statically recrystallized textures even within the damage zone of the eastern branch near 171-J250, a highly altered granodiorite with a zircon U-Pb date of 196.2 ± 2.2 Ma ($n = 27/29$; MSWD = 4.1) and ZHe date of 103.0 ± 16.0 Ma (Figure 1.7). Along Quebrada de La Cachina (Figure 1.4), an unstrained biotite granodiorite mapped as the Cerro Concha granodiorite (~ 177 Ma biotite $^{40}\text{Ar}/^{39}\text{Ar}$, Espinoza et al., 2014) has a zircon U-Pb date of 195.6 ± 1.0 Ma (sample 171-N235, $n = 38/43$; MSWD = 4.4) and ZHe date of 107.9 ± 5.4 Ma (Figure 1.7), and is relatively fresh away from contacts with other units. These dates overlap within error of the Cerro Concha sample 171-J250 (Figure 1.7). Locally the fresh Cerro Concha pluton is altered along faults and its southern margin, where it is intruded by a 188.6 ± 0.8 Ma ($n = 32/35$; MSWD = 1.7) unstrained, altered tonalite with plagioclase grains largely replaced by fine white mica and mafic minerals replaced by chlorite (sample 171-N225; Figure 1.4, Figure 1.7). Relict igneous textures are clearly preserved despite this high degree of alteration. None of the Jurassic plutons are foliated nor do they preserve any evidence of ductile strain (Figure 1.7).

The volumetrically largest plutonic complex in contact with the eastern branch of the northern El Salado segment is the Cerro del Pingo Plutonic Complex, a fresh, medium-grained lithology that ranges in composition from hornblende granodiorite to hornblende biotite tonalite and has

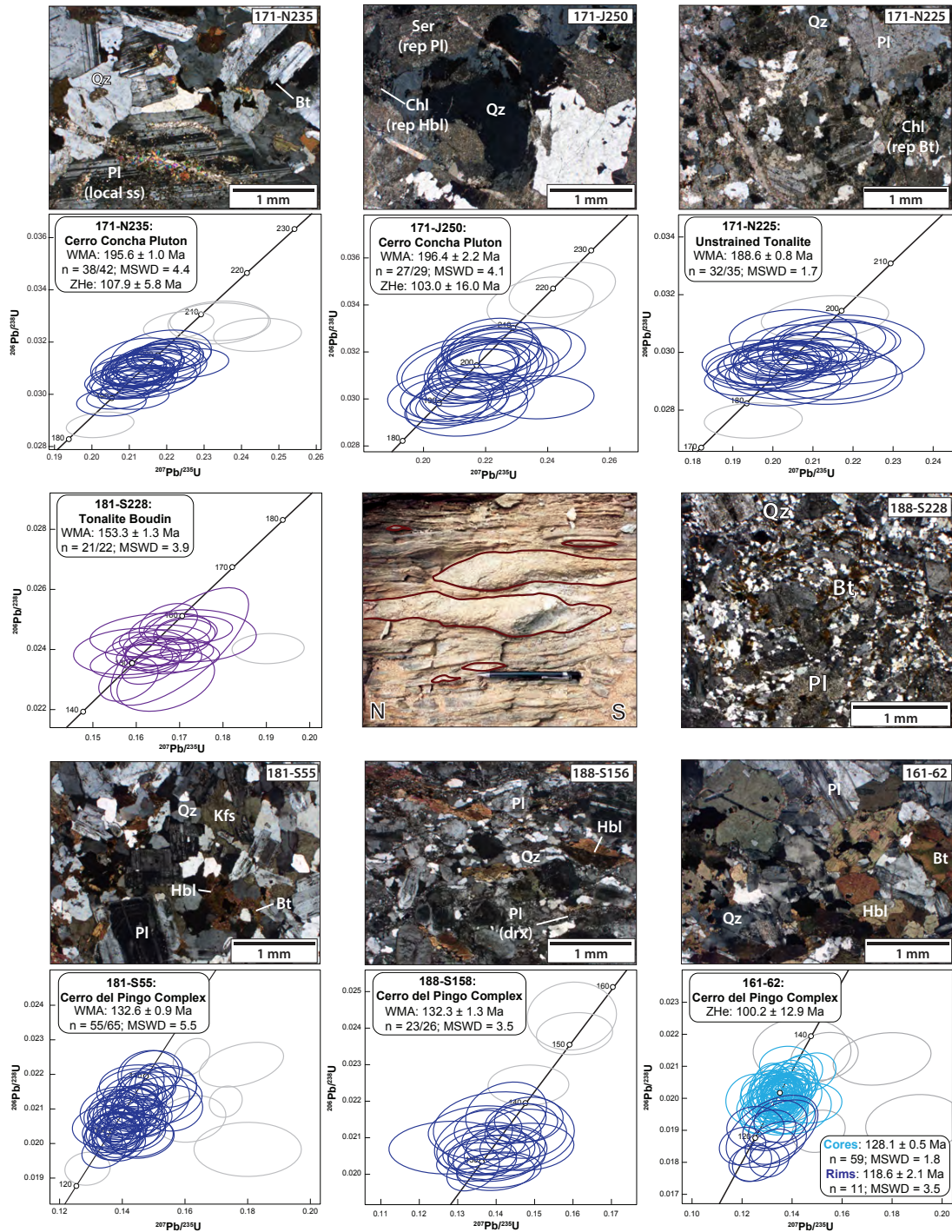


Figure 1.7: U-Pb concordia diagrams for prekinematic tonalite boudins (purple) and plutons (blue) along the northern El Salado segment. Grains with >10% discordance are shown in gray. Uncertainties are reported at 2σ . Pre-kinematic quartz diorite boudins (sample 181-S228) hosted in metasedimentary mylonites outlined in brown. Photomicrographs for plutons are in cross-polarized light. Abbreviations are as follows: Bt = biotite; Chl = chlorite; drx = dynamically recrystallized; Hbl = hornblende; Qz = quartz; Pl = plagioclase; rep = replaced; Ser = sericite.

zircon U-Pb dates 132.6 ± 0.9 Ma (sample 181-S55, $n = 55/58$; MSWD = 5.5) and 132.3 ± 1.3 Ma (sample 181-S158, $n = 23/26$; MSWD = 3.5; Figure 1.7). The ~ 132 Ma Cerro del Pingo tonalite and neighboring lithologies record variable degrees of ductile strain. Mylonitic fabrics, best developed in the ~ 14 km along-strike length of Chañaral Complex metasedimentary rocks adjacent to the Cerro del Pingo Complex, grade from mylonitic to unstrained ~ 1.5 – 2 km north and south of the plutonic complex, resulting in a total AFS-parallel shear zone length of ~ 18 km (Figure 1.4, Figure 1.6a). The degree of mylonitization correlates with the distance between the metasedimentary-Cerro del Pingo Complex intrusive contact and the eastern branch: where the contact is >2 km from the AFS, there is contact metamorphism but no mylonite in either unit (near point 181-S432; Figure 1.4); where the contact is between 500–1300 m from the AFS, the metasedimentary rocks are mylonitized but the pluton is not (sample 181-S55); and where the contact is <500 m from the AFS, both the metasedimentary rocks and pluton are mylonitic (sample 188-S158).

To the north and immediate south of Quebrada del Pingo at the northern boundary of the Cerro del Pingo Complex, an ~ 1.2 – 1.3 km wide zone of interlayered quartzites and phyllites spatially adjacent to the fault is intruded by the northern margin of the Cerro del Pingo pluton. Near point 181-S55, quartzites not adjacent to the AFS appear statically recrystallized but unstrained, whereas phyllitic layers are mylonitic with sinistral S-C fabrics and asymmetric porphyroclasts (Figure 1.6a). The exposure of metasedimentary rocks thins southward to ~ 100 m, due to the irregular nature of the Cerro del Pingo intrusive contact. Mylonitic shear zones vary in width from ~ 200 – 800 m thick near the central part of the Cerro del Pingo Complex, including up to ~ 300 – 400 m into the pluton itself. Near the center of Cerro del Pingo Complex, the shear zone is up to ~ 800 m wide and extends up to ~ 300 – 400 m into the tonalite (Figure 1.6a). Shear strain is primarily localized in the metasedimentary rocks with well-developed foliation and lineation in both quartz-rich and phyllosilicate-rich lithologies. Quartz within decimeter-scale granodiorite and tonalite boudins within the metasedimentary mylonites such as sample 181-S228 are entirely statically recrystallized and show no evidence of penetrative strain. One of these boudins yielded a

zircon U-Pb date of 153.3 ± 1.3 Ma ($n = 21/22$; MSWD = 3.9; Figure 1.7). Differing proportions of amphibole, biotite, and alkali feldspar make these nonmylonitic boudins lithologically distinct from the Cerro del Pingo Complex, pointing towards a pre-kinematic emplacement within the Chañaral Complex metasedimentary rocks prior to the intrusion of the Cerro del Pingo Complex (Figure 1.7).

Across Quebrada Cifuncho, the southern end of the ~ 132 Ma Cerro del Pingo Complex is intruded by a distinctive medium-grained mesocratic biotite hornblende tonalite with common mafic enclaves (sample 161-62). The zircon U-Pb date for this phase of the Cerro del Pingo is complex. Individual zircon dates range from 114.8–136.9 Ma, and weighted mean dates for <10%, <5%, and <2% discordance have high MSWD values. High MSWD values are typically related to zircon growth and recycling during the assembly of large arc pluton complexes, which may span several million years (e.g., Miller et al., 2007; de Saint Blanquat et al., 2011). CL imagery (Appendix 3.6) shows evidence of zircon recycling with cores with igneous textures and medium-gray overgrowths. Polished-mount analyses of cores give a weighted mean date of 128.1 ± 0.5 Ma ($n = 59$; MSWD = 1.8). Depth-profile analyses capture the core population and overgrowths, which most likely of magmatic origin based on Th/U values of 0.68–1.89 (e.g., Kirkland et al., 2015). Here we report the weighted mean date of the overgrowth population as the crystallization age: 118.6 ± 2.1 Ma ($n = 11$; MSWD = 3.5; Figure 1.7). The ZHe date is 100.2 ± 14.4 Ma. The contact between the metasedimentary rocks and the pluton is ~ 130 – 170 m east of the eastern branch of the AFS and protomylonitic fabrics locally extend ~ 50 m into the tonalite. Unstrained sample 161-62 was collected ~ 200 m from the fault, outside of the shear zone (Figure 1.6b). Moving west towards the fault, the tonalite becomes protomylonitic with C' planes defined by biotite and foliation planes defined by finely recrystallized quartz and fractured feldspar porphyroclasts (Figure 1.6b). The mylonitic foliation in the tonalite has a subvertical, NNE-striking foliation. Quartzites near the contact with the mylonitic tonalite show bulging and subgrain rotation recrystallization of quartz grains and biotite fish indicative of sinistral shear. The degree of strain increases towards the fault, with quartz grain sizes decreasing and the development of clear oblique grain shape fabrics.

Mica-rich phyllitic intervals locally record sinistral shear in the form of asymmetric intrafolial folds. A >1 m wide tonalite sill within the metasedimentary rocks has a protomylonitic fabric with aligned biotite and hornblende, dynamically recrystallized quartz seams, and minor recrystallization around the margins of plagioclase porphyroclasts.

The southern strain gradient along the AFS eastern branch occurs across Quebrada de La Cachina, where the ~119 Ma tonalite intrudes the ~196 Ma Jurassic Cerro Concha granodiorite (Figure 1.4). Quartzites grade from platy ultramylonite and protomylonite within ~500 m of the eastern branch to undeformed metasedimentary rocks with rounded detrital grains >620 m from the eastern branch. Roughly 1400 m east of the fault along the eastern margin of the ~119 Ma tonalite, Chañaral nonmylonitic quartzite within an isolated ~2.7 km² roof pendant is statically recrystallized and disharmonically folded (Figure 1.4).

Along the AFS ~6 km south of the intersection with the Taltal fault, an undeformed ~10-m-wide andesitic dike (sample 161-43) clearly cuts across the main eastern branch of the AFS, a coherent Chañaral Complex slate with gently-dipping bedding-parallel cleavage, 200 m of AFS-related black cataclasite locally derived from quartzite and highly altered granitoid, and andesitic volcanic rocks of the Aeropuerto Formation (Figure 1.8). However, this dike is sinistrally offset ~148 m along a fault parallel to the eastern branch, suggesting that the dike was emplaced at the very end of slip, after the vast majority of displacement had occurred. The age of the dike is complicated by low zircon yield and a large spread in dates (108 Ma to 1339 Ma), many of which overlap with nearby plutons and feature a high degree of discordance. Filtering grains to a higher discordance threshold only slightly reduces the spread in dates and does not significantly change with weighted mean date (119.0 ± 6.6 Ma, $n = 8$ at <10% discordance and 117.4 ± 8.6 Ma, $n = 6$ at <2% discordance). There is a gap in dates between the three youngest grains (~108 Ma, ~111 Ma, and ~112 Ma) and older grains (~127–115 Ma) that are most likely xenocrysts from nearby plutons. As such, we report the weighted average average of the youngest three concordant grains: 109.9 ± 4.0 Ma (Figure 1.8). Both the dike and the AFS are cut by NW-striking sinistral faults parallel to the younger Taltal fault system (Mavor et al., 2020).

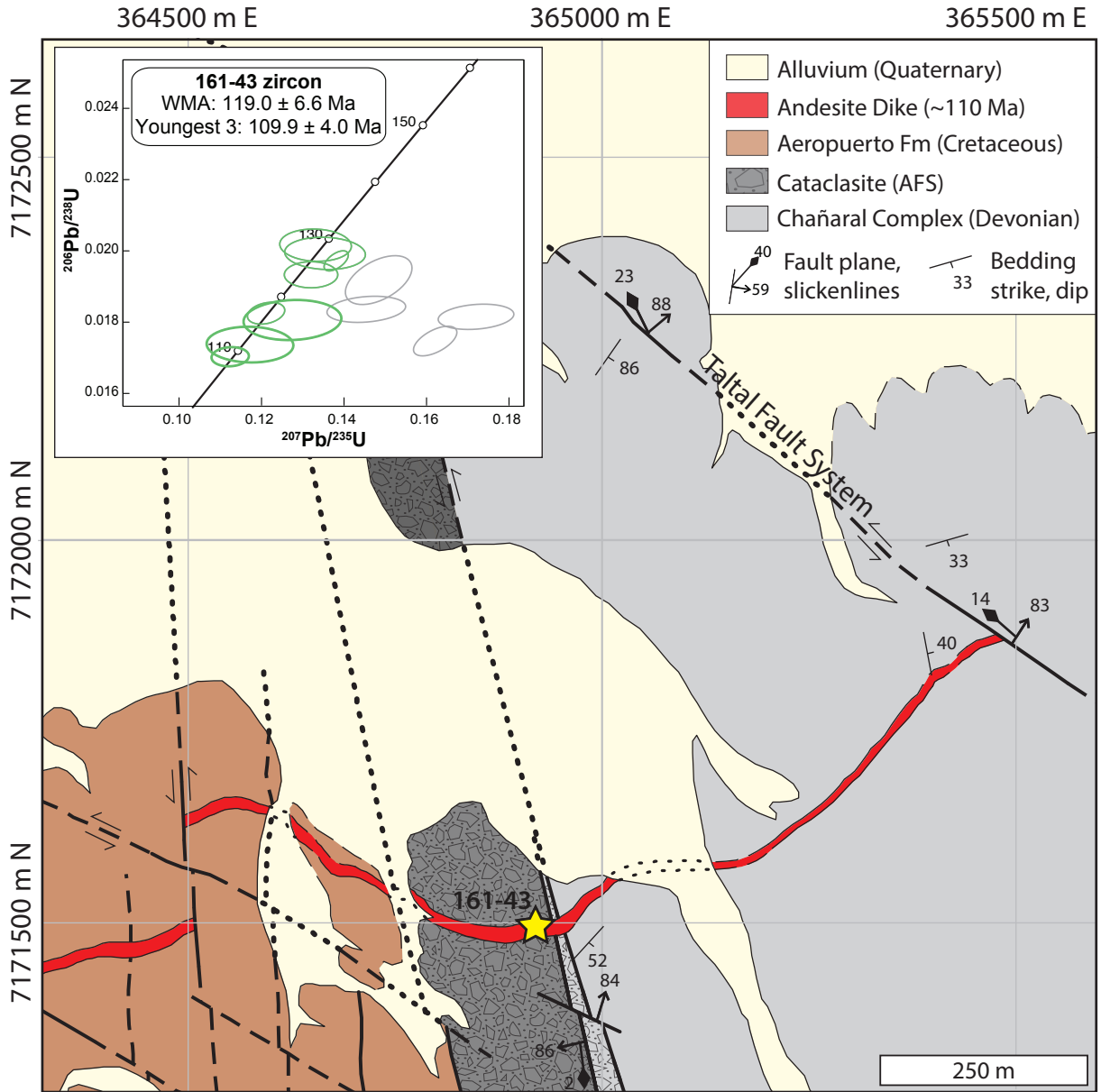


Figure 1.8: Inset map of the andesitic dike that cuts the Atacama fault system. The dike is sinistrally offset ~ 147 m by the westernmost strand, suggesting intrusion during the end stages of brittle deformation. The dike and the AFS are cut and displaced sinistrally by a NW-SE striking fault parallel to the Taltal fault that displaces the AFS further north. Location of the zircon U-Pb sample (161-43) is shown by the yellow star. Inset shows U-Pb concordia with $>10\%$ discordant grains shown in gray.

1.4.3 Central El Salado Segment (26.6°S to 27°S)

The central El Salado segment near the Mantoverde mine is defined by the southern extent of the eastern branch extending down from the northern El Salado map region and a fault east of the eastern branch, here called the Salitrosa branch. The Salitrosa branch is clearly exposed through the area (Figure 1.9). The volume of Early Cretaceous plutons exposed along the central El Salado segment is much larger than the exposure of Early Cretaceous plutons along the northern El Salado segment, and the width of the mylonite zone along the Salitrosa branch is correspondingly much wider (Figure 1.9, Figure 1.10). The eastern branch is mapped as a single structure that juxtaposes Early Cretaceous plutons for ~67 km (64%) of its exposed length, including the Las Animas, Cerro Moradito, and Las Tazas plutons on the west against La Negra volcanics, Cerro Morado pluton, and Chañaral Complex metasedimentary rocks between the two branches (Godoy and Lara, 1998; Lara and Godoy, 1998, this work). Large stretches of the eastern branch are covered by alluvium (Figure 1.9, Figure 1.10). The Salitrosa branch has an ~30 km long map trace and juxtaposes the previously mentioned lithologies against Chañaral Complex metasedimentary rocks, La Negra volcanics, and the Early Cretaceous Sierra Dieciocho pluton (~127 Ma, Dallmeyer et al., 1996, Figure 1.9). Early Cretaceous plutons are exposed along the Salitrosa branch for 23 km (76%) on the eastern side and 17 km (57%) on the western side (Lara and Godoy, 1998, this work).

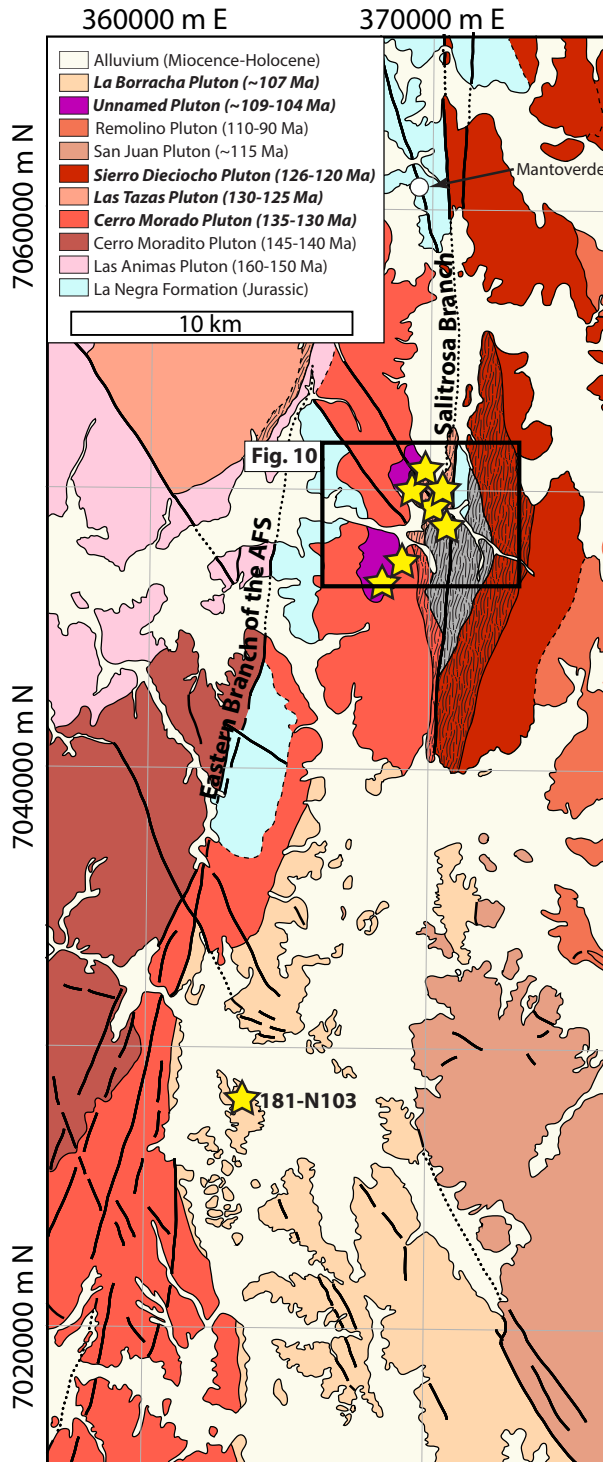


Figure 1.9: Simplified map of the central El Salado segment compiled from our new mapping and Lara & Godoy, 1998. The Early Cretaceous plutons are shown in shades of red and the La Borracha pluton is shown in light tan. Bold black lines show the major strands of the AFS and mylonites are shown by the pattern. Yellow stars show new U-Pb samples from this study; sample labels are given in Figure 1.10 (black box).

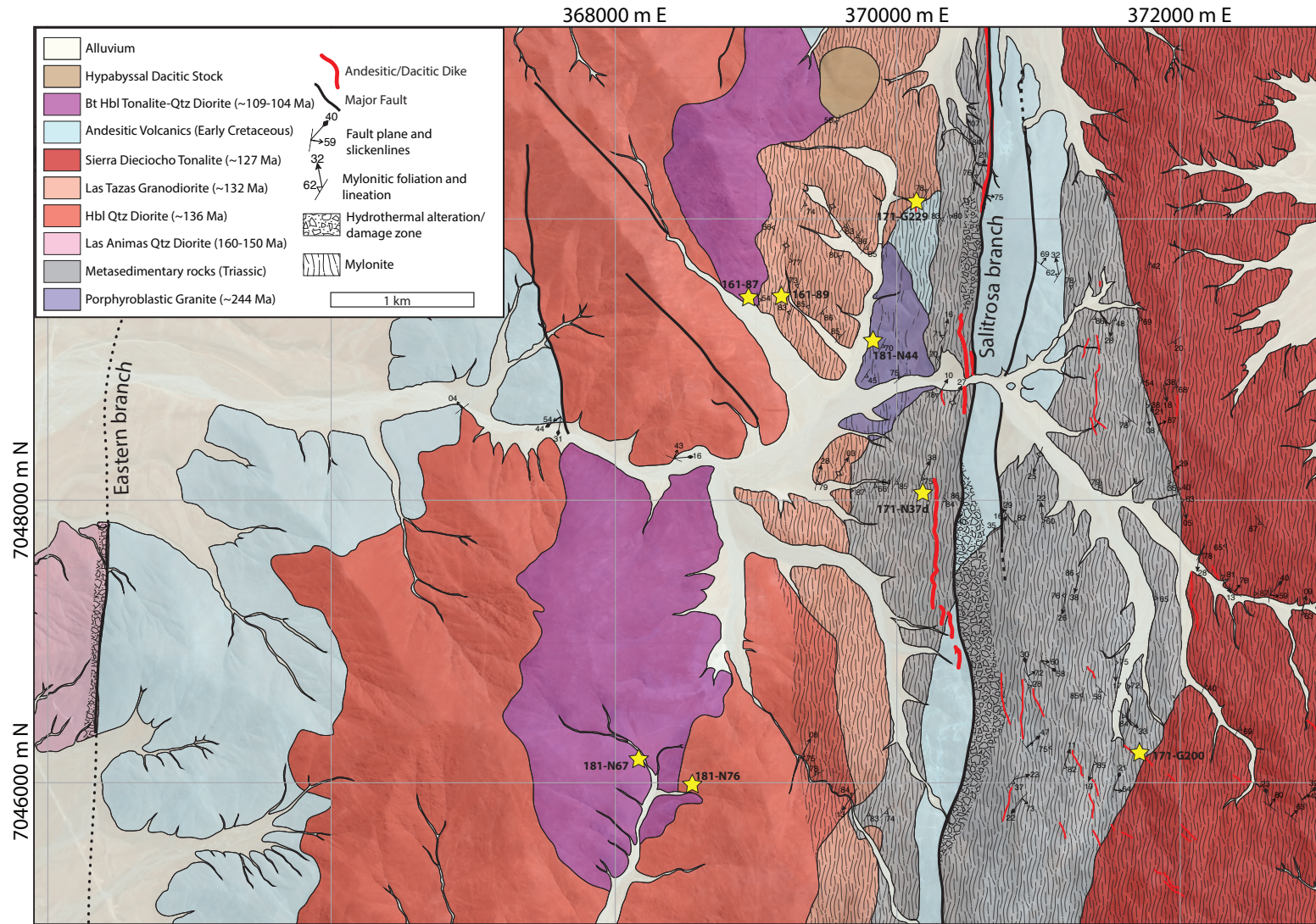


Figure 1.10: New detailed mapping south of the Mantoverde mine. Note the extent of the mylonitic shear zone surrounding the Salitrosa branch. Yellow stars show new U-Pb samples from this study. See Plate 1 for 1:20,000-scale version.

A well-foliated mylonitic biotite quartzofeldspathic schist (sample 171-N37d; Figure 1.11b) previously mapped as a part of the Las Tazas pluton along the western margin of the Salitrosa branch (Lara & Godoy, 1998) yielded zircon U-Pb data with a wide spread of concordant dates ($\sim 238\text{--}2564$ Ma) rather than a single coherent population (Appendix 3.6). This date spectrum is consistent with a sedimentary protolith rather than an igneous protolith. These data do not include a population of three young grains overlapping at 2σ error, so we do not report a maximum depositional age for this unit.

Pre-Cretaceous plutons along the central El Salado segment are either entirely unstrained or protomylonitic with discrete high-strain zones. The oldest pluton is a porphyritic granite (sample 181-N44) with a zircon U-Pb date of 245.4 ± 1.8 Ma (Figure 1.12, $n = 31/32$; MSWD = 4.6) located just west of the cataclastic zone along the Salitrosa branch. The deformation in this granite varies from unstrained to protomylonitic with large, rounded plagioclase grains aligned in a biotite-rich matrix that defines a steeply ESE-dipping foliation (Figure 1.12, Figure 1.13). Locally bleached discrete high strain zones are present. In contrast, Early Cretaceous plutons are pervasively strained (Figure 1.12). Volumetrically, the most important plutons east of the Salitrosa branch of the AFS are hornblende quartz diorite (sample 181-N76), high-strain tonalite (sample 161-89), and the Sierra Dieciocho pluton (Figure 1.9). 181-N76 is a coarse-grained quartz diorite with euhedral plagioclase and hornblende that becomes protomylonitic as it approaches the AFS. This sample has a number of zircon grains that plot along a common-Pb array and has a lower intercept date of 134.5 ± 2.0 Ma (MSWD = 6.8; Figure 1.12) and weighted mean date of 135.6 ± 1.5 Ma ($n = 15/15$; MSWD = 5.9). North of this pluton, a high-strain mylonitic to ultramylonitic hornblende granodiorite represented by sample 161-89 has a zircon U-Pb date of 132.1 ± 1.9 Ma ($n = 19/21$; MSWD = 5.3) and a ZHe date of 96.2 ± 5.7 Ma (Figure 1.9, Figure 1.10, Figure 1.12) that matches the emplacement age of the Las Tazas granodiorite (132–130 Ma; Berg and Breiterkreuz, 1983; Dallmeyer et al., 1996). Asymmetric porphyroclasts, S-C fabrics, and dynamically recrystallized oblique quartz grain shape fabrics record solid-state, sinistral shear strain in the Las Tazas pluton (sample 161-89; Figure 1.12). On the eastern margin of the Salitrosa branch, sinistral

shear is recorded in the protomylonitic Sierra Dieciocho pluton (~ 127 Ma; Dallmeyer et al., 1996) by S-C-C' fabrics, asymmetric porphyroclasts, and antithetic domino rotation of brittle feldspar (Figure 1.10a). In addition to these plutons, mylonites are well developed in metasedimentary rocks located along either side of the brittle core of the AFS. The average orientation of mylonitic foliations across all units in this study area is 018, 81 E with an average lineation of 016/04 (Figure 1.13). Lineations west of the fault generally plunge NNE and lineations east of the fault generally plunge SSW. 20% of lineations on either side of the fault plunge $20\text{--}30^\circ$ and 20% plunge $>30^\circ$, which implies a minor component of dip-slip motion during ductile deformation. The difference in plunge directions across the Salitrosa branch and preservation of Early Cretaceous volcanics on both sides of the fault indicate dip-slip motion was minor, and suggests a similar structural level across the fault.

Several dacitic and andesitic dikes cut mylonitic fabrics, including a $\sim 12\text{--}20$ m wide dacite dike that lines the western side of the fault for ~ 3 km (Figure 1.11d), and are in turn cut by the $\sim 005^\circ$ -trending brittle core of the Salitrosa branch, located near the central axis of the ~ 6 km-wide mylonite zone (Figure 1.10). The dacitic and andesitic dikes are represented by sample 171-G200 with a zircon U-Pb date of 119.7 ± 0.9 Ma ($n = 35/37$; MSWD = 2.8) and sample 171-G229 with a zircon U-Pb date of 117.1 ± 0.9 Ma ($n = 37/38$; MSWD = 3.2; Figure 1.12). These crosscutting relationships indicate that the dikes were emplaced after the cessation of AFS mylonitization but prior to the cessation of brittle slip. The average orientation of the principal slip surface of the Salitrosa branch is 006, 80 E with slickenlines oriented 176/25 (Figure 1.13). Small-scale faults parallel to the main traces of the AFS (strike $345\text{--}015^\circ$) are steeply dipping (average 78 E) with an average slickenline orientation of 019/27. NW-trending structures (strike $315\text{--}345^\circ$) also have steep dips (average 87 E) and shallow slickenlines with an average orientation of 349/06. These faults parallel the Mantoverde fault, interpreted as a relay between branches of the AFS (Figure 1.9; Vila et al., 1996).

The ~ 109 Ma to 104 Ma plutons in this area are entirely unstrained. Samples 161-87 and 181-N67 are both fresh biotite-hornblende tonalite to quartz diorite with clear intrusive contacts with

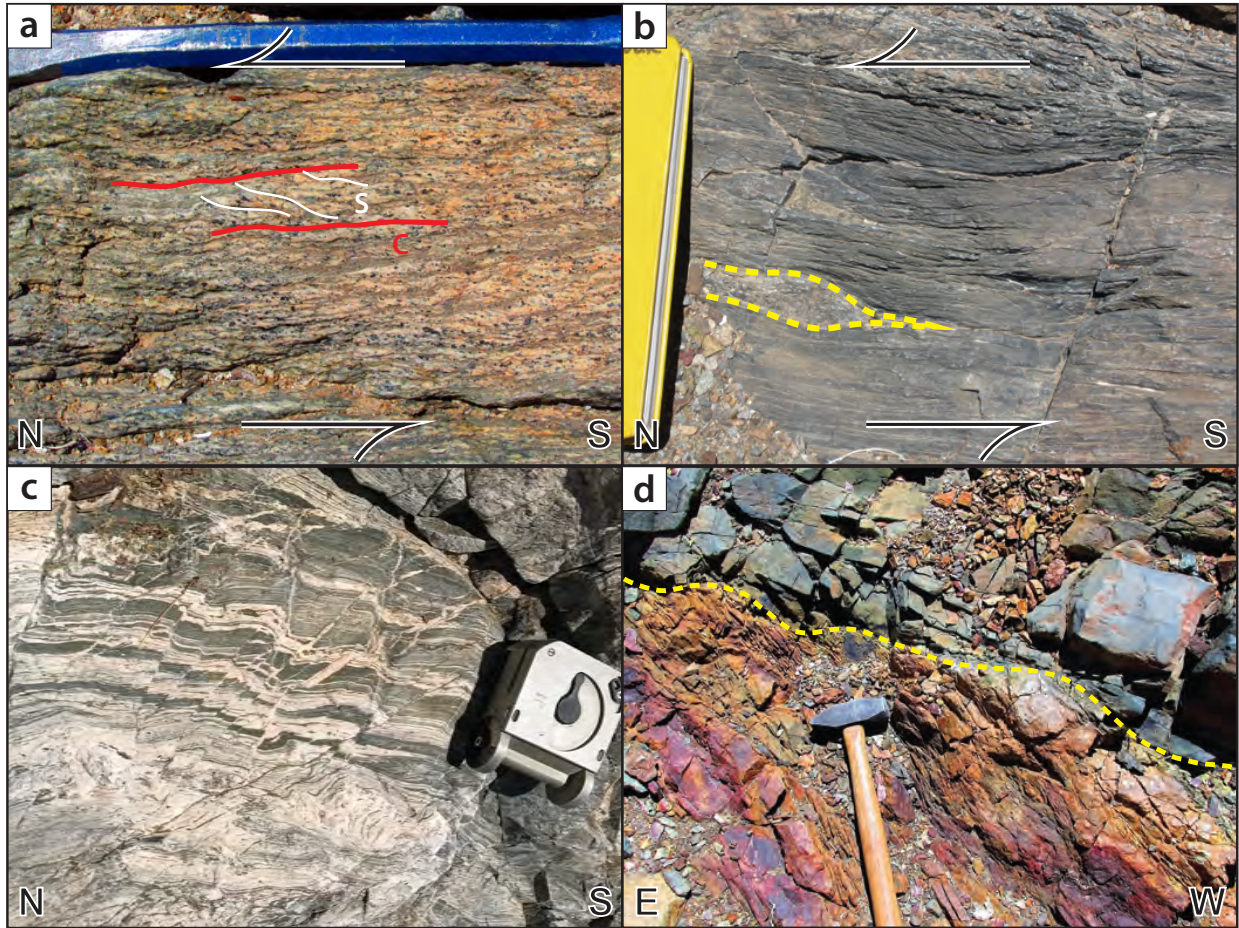


Figure 1.11: Field photographs of (a) sinistral shear sense defined by S (white) and C (red) planes in the Las Tazas pluton, (b) sinistral shear sense in the metasedimentary rocks adjacent to the Salitrosa branch, (c) brittle faults cutting mylonitic fabrics, and (d) an andesite dike cutting mylonitic fabrics. Contacts are shown in with a dashed yellow line.

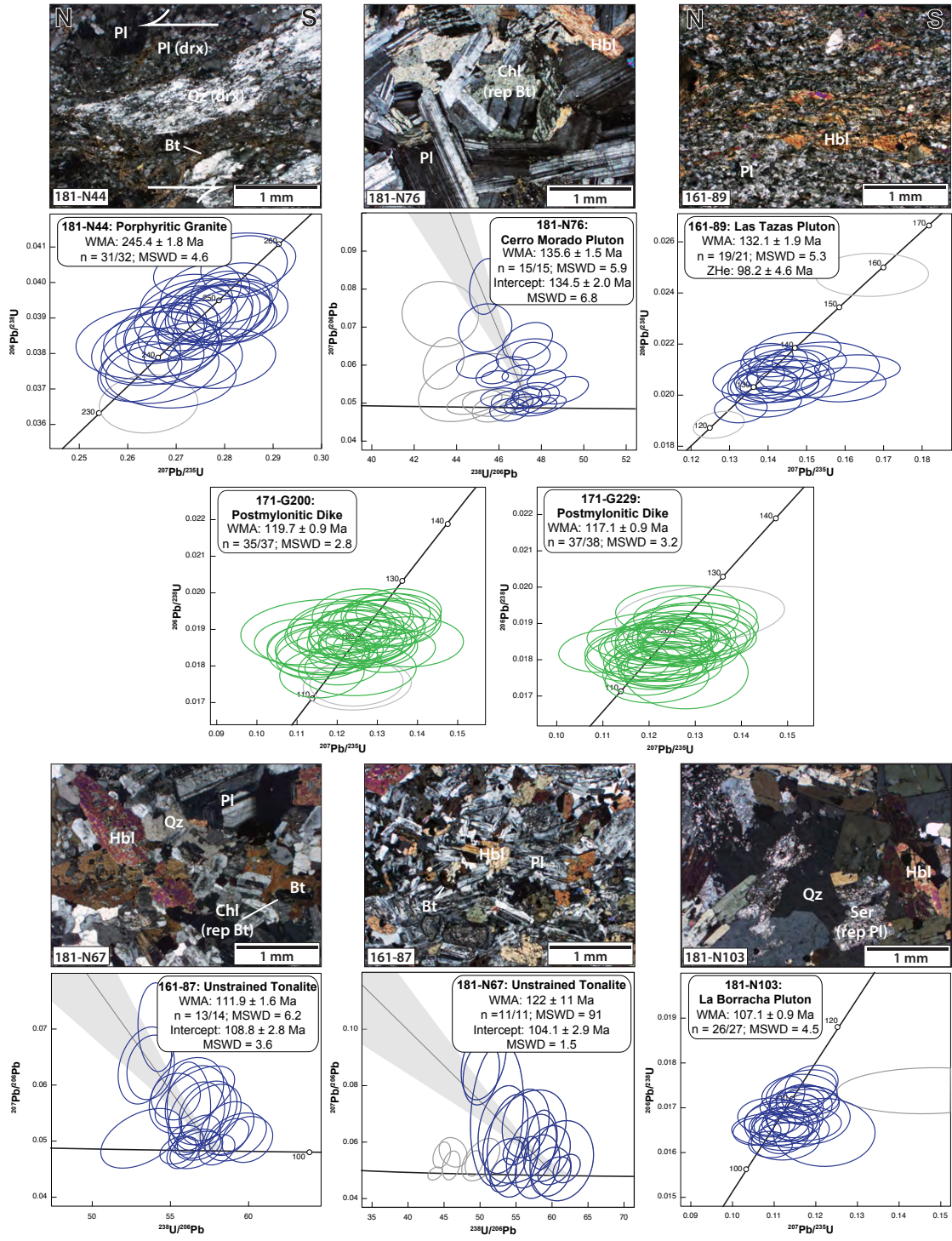


Figure 1.12: U-Pb concordia diagrams for plutons (blue) and post-mylonitic dikes (green) along the central El Salado segment. Grains with >10% discordance are shown in gray. Uncertainties are reported at 2σ . Photomicrographs for plutons are in cross-polarized light. Abbreviations are as follows: Bt = biotite; Chl = chlorite; drx = dynamically recrystallized; Hbl = hornblende; Qz = quartz; Pl = plagioclase; rep = replaced; Ser = sericite.

neighboring plutons and retain an equigranular texture (Figure 1.12). An unstrained, fresh biotite-hornblende tonalite with Tera-Wasserburg lower intercept dates 108.8 ± 2.8 Ma (sample 161-87; $n = 23$; $MSWD = 3.6$) and 104.1 ± 2.9 Ma (sample 181-N67; $n = 17$; $MSWD = 1.5$; Figure 1.12) clearly cuts mylonitic fabrics, but does not directly interact with the Salitrosa branch of the AFS. The La Borracha pluton (sample 181-N103) south of the Mantoverde mine is unstrained, preserving equigranular textures and randomly oriented hornblende. The La Borracha pluton has a U-Pb date of 107.1 ± 0.9 Ma (Figure 1.12, $n = 26/27$; $MSWD = 4.5$). The western margin of the La Borracha pluton is mapped as a 350–500-m wide mylonite zone for ~ 32 km along the eastern branch AFS (Lara and Godoy, 1998); however, our mapping documents biotite and plagioclase-rich hypabyssal intrusive or subvolcanic rocks along a ~ 6 -km long, ~ 2.1 -km wide zone with subvertical NNE-striking foliation with a lineation plunging steeply south (Figure 1.9, Figure 1.13). These fabrics are magmatic foliations rather than mylonites and are cut by the unstrained La Borracha pluton. Mylonites derived from a plutonic protolith are only found on the western margin of the shear zone, and petrographic analysis suggests they are derived from the older Early Cretaceous Cerro Morado pluton rather than the La Borracha pluton.

1.5 Discussion

1.5.1 Region-Specific Trends

Paposo Segment

A compilation of plutonic and volcanic K-Ar, $^{40}\text{Ar}/^{39}\text{Ar}$, and U-Pb geochronologic data along the southern Paposo segment records two peaks of magmatic activity (Figure 1.14): minor peaks at 235–220 Ma and 180–170 Ma and a broad peak from 155–125 Ma with individual peaks centered on ~ 147 Ma and ~ 130 Ma. Most of the data that comprise the peak centered at ~ 147 Ma are concentrated in the Desplazado plutonic complex (151–142 Ma) and Izcuña quartz diorite (144–140 Ma) located between the Pacific coast and AFS, whereas the ~ 130 Ma centered peak is comprised of the Remiendos Plutonic Complex located along the eastern margin of the AFS. These plutons

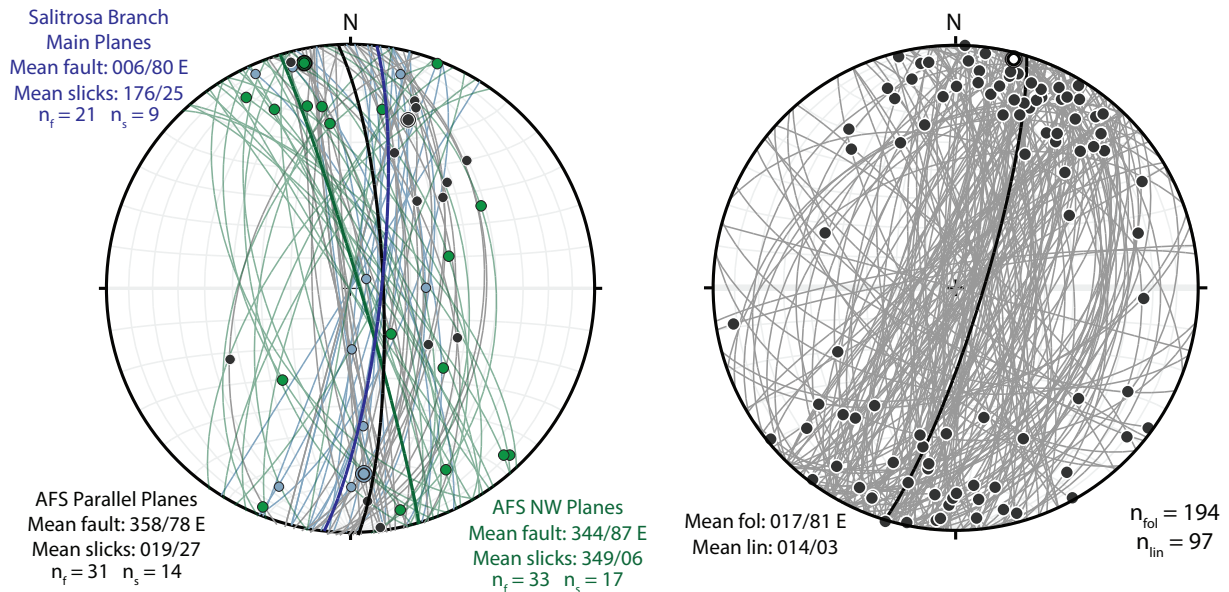


Figure 1.13: Equal-area stereograms of brittle faults (left) and mylonitic foliations (right) from the central El Salado segment. Individual measurements are shown with great circles (faults, foliations) and dots (slickenlines, lineations). Average orientations are given by bold great circle (faults, foliations) and larger composite dots (slickenlines, lineations).

are voluminous along the Paposo segment and constitute the majority of exposed rock in the Puerto Posallaves 1:100,000-scale quadrangle (Álvarez et al., 2016).

Near Caleta Paposo, the western side of the Paposo fault is dominated by a pervasively fractured and chlorite-altered but otherwise unstrained ~ 178 Ma Yumbes tonalite and a sinistral shear zone is developed on the eastern side in the protomylonitic ~ 136 Ma Remiendos hornblende tonalite and a mylonitic granodiorite complex. Ruthven et al. (2020) document the onset of ductile deformation ~ 139 Ma based on mylonitization and hydrothermal alteration of a ~ 148 – 139 Ma granodiorite complex. A ~ 136 Ma protomylonitic tonalite unit located within the shear zone between the brittle fault core and high-strain zone lacks mafic dikes and intense hydrothermal alteration (Figure 1.2, this study; Figure 2a of Ruthven et al., 2020), indicating that most shear zone development occurred between ~ 139 and 136 Ma (Figure 1.14). Mylonitization locally continued until Early Cretaceous plutons cooled below biotite Ar closure (~ 133 – 128 Ma; Hervé and Marinovic, 1989; Álvarez et al., 2016) and progressed from oblique sinistral-reverse shear and local coaxial strain in mylonites east of the Paposo fault to brittle sinistral and sinistral-reverse slip along the

fault between 139 Ma and 116 Ma, and illite-rich gouge most likely developed along the Paposo fault by ~ 116 Ma based on ZHe data (Ruthven et al., 2020). The youngest plutons in this region were emplaced at ~ 125 Ma and ZHe dates indicate cooling below $\sim 180^\circ\text{C}$ between ~ 116 – 107 Ma (Figure 1.14). The duration of AFS deformation, bracketed by the initiation of ductile deformation and the transition to brittle slip by ZHe dates, was ≥ 23 Myr and spanned two phases of pluton emplacement. The similarity of ZHe dates between the Yumbes tonalite and Remiendos Complex both near Cerro Paranal and Caleta Paposo (~ 116 Ma and ~ 107 Ma; Figure 1.14) and absence of ductile fabrics in the Yumbes tonalite suggests that while the two plutons were likely in contact during the Early Cretaceous, ductile conditions were not realized in the older, colder, and stronger Yumbes tonalite and were concentrated in the younger, hotter and therefore weaker eastern plutonic complexes. Alternatively, Ruthven et al. (2020) document a minor E-side up component of reverse slip on the Paposo segment, suggesting the east side was structurally deeper during mylonitization and thus may have been hotter due to its position at a deeper structural level. Neogene E-side down reactivation (e.g., González et al., 2006) would have restored some—but probably not all—of this difference in structural level.

Northern El Salado Segment

The new dates obtained along the northern El Salado segment fall into two broad groups: an older ~ 200 – 185 Ma peak and a broad peak from 150 – 120 Ma with individual peaks centered at ~ 140 Ma and ~ 130 Ma, and a minor peak from 115 – 100 Ma (Figure 1.14). Jurassic plutons including the Cerro Concha Granodiorite (~ 196 Ma) comprise the oldest peak and occur along the eastern flank of the AFS. The broad 150 – 120 Ma peak includes the Quezada Intrusive Complex (153 – 147 Ma), Goyenechea Granodiorite (~ 140 Ma), and Cerro del Pingo Complex (132 – 119 Ma). The youngest plutons are the Tropezón Plutonic Complex (~ 110 Ma), and Librillo Intrusive Complex (106 – 101 Ma), which occur largely along the Taltal fault system ≥ 10 km east of the AFS.

Along the northern El Salado segment, Jurassic tonalite boudins such as sample 181-S228 (Figure 1.7) lack mylonitic and magmatic fabrics, indicating mylonitic deformation of Chañaral Complex metasedimentary rocks occurred after 154 Ma. U-Pb zircon dates of mylonitic and non-

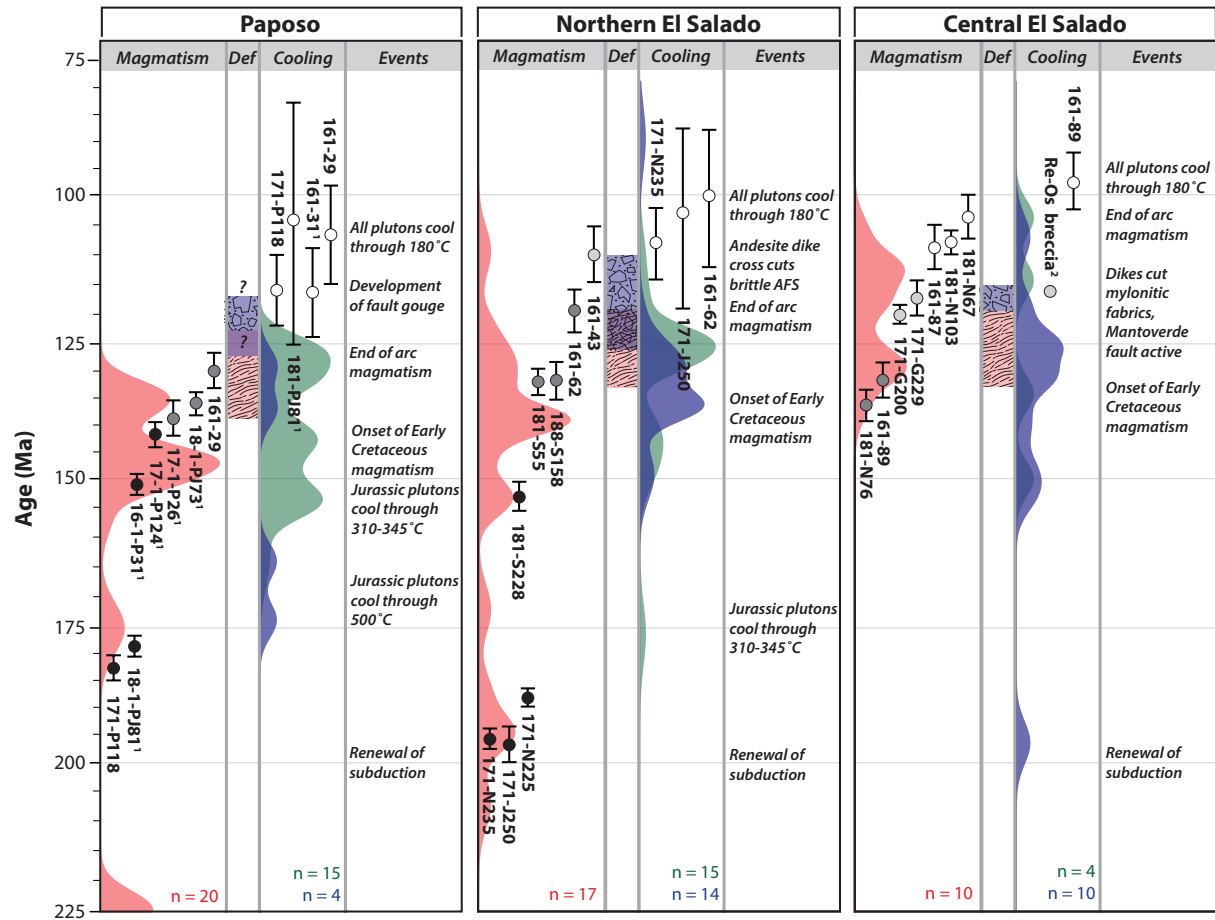


Figure 1.14: Time (vertical axis) vs. N-S trend (horizontal axis) diagram summarizing geochronologic data, thermochronologic data, deformation, and tectonic events along the southern Paposo, northern El Salado, and central El Salado segments. In the Magmatic column, kernel density estimate plots of our new dates compiled with published plutonic and volcanic zircon U-Pb data are shown in red. Plots were constructed with a bandwidth of 3 and a bin width of 5. Curves with $n \geq 5$ dates are considered major peaks and curves with $1 < n < 5$ are considered minor peaks. Individual data points in the Magmatic column are zircon U-Pb dates with 2σ error bars. Black points are pre-kinematic, medium gray points are synkinematic in the ductile regime, light gray points are synkinematic in the brittle regime, and white points are post-kinematic. In the Deformation column, duration of deformation determined by field relationships is shown in the red bar, with ductile deformation noted by the wavy pattern and brittle deformation noted by the block pattern. In the Cooling column, curves are hornblende K-Ar and $^{40}\text{Ar}/^{39}\text{Ar}$ (blue) and biotite K-Ar and $^{40}\text{Ar}/^{39}\text{Ar}$ dates (green) from published literature. Individual data points in the Cooling column are zircon (U-Th)/He dates with 2σ error bars. Sources of published data are given in Appendix 3.6. Individual data point sources: 1-Ruthven et al. (2020); 2-Mathur et al. (2002).

mylonitic tonalite (samples 188-S158 and 181-S55, respectively; Figure 1.7, Figure 1.14) indicate that ductile conditions initiated and localized along the AFS by ~ 132 Ma and continued locally as late as ~ 119 Ma. The onset of ductile deformation is younger here compared to the Paposo segment, likely due to the lack of a voluminous ~ 139 – 136 Ma magmatic pulse along the northern El Salado segment. Al-in-hbl barometry on the Cerro del Pingo pluton records emplacement depths at 6–10 km (Kurth, 2002). Recent studies show these estimates should be treated as maximum values rather than true emplacement depths (e.g., Memeti et al., 2009; Putirka, 2016), supporting intrusion of Early Cretaceous plutons at shallow crustal levels. Mylonitic shear zones vary in width from ~ 200 – 800 m thick near the center of the Cerro del Pingo Complex, including up to ~ 400 m into the pluton itself, and are continuous along the northern El Salado segment for ~ 18 km. Strain gradients preserved along the Cerro del Pingo Complex in both the Early Cretaceous plutons and Paleozoic metasedimentary rocks are especially clear in the quartzites, which retain rounded detrital grains or have undergone static recrystallization everywhere except along the margins of Early Cretaceous plutons suggesting the background temperature prior to intrusion of the Cerro del Pingo Complex was below the threshold for quartz crystal plastic deformation. Metasedimentary rocks intruded by Early Cretaceous plutons but not located adjacent to the AFS are statically recrystallized but not mylonitized, suggesting both the heat brought in by the emplacement of these plutons and proximity to the actively shearing AFS were necessary for mylonitization. Variable zircon U-Pb, hornblende $^{40}\text{Ar}/^{39}\text{Ar}$, and biotite K-Ar dates in plutons that all have ZHe dates in the range of 107–99 Ma suggest the entire northern el Salado segment was below $\sim 300^\circ\text{C}$ but above $\sim 180^\circ\text{C}$ prior to Early Cretaceous magmatism. Adjacent to and within the plutons, the temperature exceeded the lower limit of quartz plasticity (~ 280 – 310°C in strike-slip regimes; Stöckhert et al., 1999; Stipp et al., 2002) during the Early Cretaceous and then cooled through $\sim 180^\circ\text{C}$ by ~ 100 Ma (Figure 1.14). The age of the transition from ductile to brittle deformation along the northern El Salado segment is not well constrained, but the similarity of closure temperatures for biotite $^{40}\text{Ar}/^{39}\text{Ar}$ thermochronometers (310 – 345°C ; Harrison et al., 1985) to the brittle-plastic transition temperature in quartzofeldspathic rocks approximates cooling to brittle conditions in the mylonitic

granitoids at 130–127 Ma (Espinoza et al., 2014), though the ~ 119 Ma date described above indicates mylonitic deformation continued locally after that time where younger magmatism occurred. Cataclastic deformation along strike of the AFS but away from this plutonic complex was likely coeval with ductile deformation. Kinematic similarity between sinistral mylonitic fabrics and brittle faults including an $\sim 7^\circ$ clockwise angle between the average mylonitic fabric (359, 89 E) and average eastern branch brittle fault orientation (172, 89 W) supports synkinematic emplacement of the Cerro del Pingo pluton during progressive sinistral strike-slip strain (Figure 1.5). ZHe dates of ~ 107 – 99 Ma indicate cooling below 180°C ~ 17 – 25 Myr after the intrusion of the youngest pluton (Figure 14) and the latest-kinematic andesite dike near Taltal clearly documents the ending stages of brittle slip on the AFS by ~ 110 Ma (Figure 1.8). The duration of deformation in the area is thus ~ 23 Myr.

Central El Salado Segment

Magmatism along the central El Salado segment includes a minor pulse centered at ~ 150 Ma, and a broad pulse from ~ 140 – 105 Ma with individual peaks centered at ~ 130 Ma and ~ 117 Ma (Figure 1.14). The Las Animas pluton makes up the ~ 150 Ma peak and is mapped along the western margin of the AFS (Lara & Godoy, 1998). Early Cretaceous plutonism is associated with an ~ 6 -km-wide mylonite zone. The ~ 136 Ma hornblende quartz diorite is largely unstrained, although it has a protomylonitic margin where it comes into contact with the high-strain Las Tazas granodiorite and surrounding metasedimentary rocks, suggesting it may be either (a) pre-kinematic or (b) earliest synkinematic with a narrow strain gradient due to its relatively strong rheology. Other synkinematic plutons include the Cerro Morado (135–130 Ma; Arévalo, 1995) and Las Tazas (132–130 Ma; Grocott and Taylor, 2002), both mapped along the eastern branch of the AFS through this region. Grocott and Taylor (2002) interpret the mylonitic eastern margin of the Las Tazas pluton to record emplacement during AFS deformation. The development of mylonites in this pluton suggests that the Las Tazas records most of the duration of AFS displacement, whereas the protomylonitic Sierra Dieciocho pluton (~ 127 Ma; Dallmeyer et al., 1996) is less strained despite its similar mineralogy and inferred rheology, suggesting that the Sierra Dieciocho records a shorter

duration of mylonitization. The consistent sinistral shear sense indicators and 11° clockwise angle between the average mylonitic fabric and average brittle fault orientations are kinematically compatible with a continuous evolution from ductile to brittle behavior during progressive strain (Figure 1.13).

The second pulse of Early Cretaceous magmatism was post-mylonitic. Younger ~ 119 – 117 Ma andesite dikes cut mylonitic fabrics and are in turn cut by AFS-related brittle faults, indicating a shift to brittle deformation after ~ 13 Myr of mylonitization (Figure 1.14). The age of the brittle core of the central El Salado segment is constrained by a ~ 116 Ma Re-Os date of mineralized breccias located along the Mantoverde fault (Mathur et al., 2002), a relay structure that connects the eastern and Salitrosa branches of the AFS (Vila et al., 1996). The youngest plutons in the area—the La Borracha, San Juan, Chivato, Remolino, and Sierra Merceditas plutons (115–107 Ma)—intruded to the east of the Salitrosa branch. These plutons lack pervasive strain and do not interact with the main AFS core, so while slip along the eastern branch in the northern El Salado segment ended by ~ 110 Ma, the relationship between intrusion of the young plutons and the end of slip along the brittle Salitrosa branch is not clear. Regional cooling through 180°C did not occur until ~ 96 Ma (Figure 1.14), after the emplacement of the La Borracha pluton (~ 107 Ma) and cessation of slip along the El Salado segment (~ 110 Ma).

1.5.2 The Relationship between Magmatism and Deformation

Overall, the deformation timing and duration strongly support a coupled evolution of magmatism and deformation. Our new dates and analysis of published data indicate three pulses of Coastal Cordillera magmatism: a minor pulse at 195–175 Ma, a broad pulse of magmatism along the central ~ 300 km of the AFS at 150–120 Ma, and a minor younger pulse from 120–104 Ma (Figure 1.14). Along both the Paposo and El Salado segments, zircon U-Pb dates are typically ~ 12 – 18 Myr older than Ar system dates for Jurassic plutons. Differences between zircon U-Pb and Ar system dates may be a product of post-emplacement cooling or alteration, which disturbs the Ar system. Extensive hydrothermal alteration may average that Jurassic plutons are underrepre-

sented along the AFS; however, fresh Jurassic plutons such as the Cerro Concha granodiorite near sample 171-N235 also record a younger Ar system date (~ 177 Ma, biotite $^{40}\text{Ar}/^{39}\text{Ar}$; Espinoza et al., 2014) than zircon U-Pb date (~ 196 Ma; this work). Thus, we interpret zircon U-Pb dates in Jurassic plutons to record emplacement and Ar system dates to record cooling through the hornblende and biotite closure temperatures of $\sim 500^\circ\text{C}$ and $310\text{--}345^\circ\text{C}$, respectively, for cooling rates of $10\text{--}100^\circ\text{C}/\text{Myr}$ (Harrison, 1982; Harrison et al., 1985; Dahl, 1996; Grove and Harrison, 1996; McDougall and Harrison, 1999). As both systems yield dates older than the Early Cretaceous plutons, these cooling dates indicate that the background temperature of the Coastal Cordillera crust was $<350^\circ\text{C}$ prior to Early Cretaceous arc magmatism. Jurassic plutons lack pervasive mylonitic fabrics along the southern Paposo and northern El Salado segments. Ruthven et al. (2020) document mylonitic fabrics in a Latest Jurassic-Early Cretaceous ($\sim 148\text{--}139$ Ma) plutonic complex; however, field relationships and zircon U-Pb geochronology indicate that the hydrothermal alteration and deformation occurred in the Early Cretaceous. Along the northern El Salado segment, contact aureoles with discrete shear zones are present in Jurassic plutons and the metasedimentary rocks they intrude. Given the sensitivity of metasedimentary lithologies to penetrative strain documented along Early Cretaceous plutons, the lack of well-developed mylonite zones in and along the margins of Jurassic plutons indicates AFS-related deformation occurred after the intrusion and cooling of Jurassic plutons. Thus, when the Early Cretaceous plutons did intrude, the increase in geothermal gradient and resultant crustal weakening was localized around the plutons, while the surrounding Jurassic and metasedimentary rocks experienced a lower geothermal gradient, as evidenced by the preserved older Ar system dates. On average, Jurassic plutons also have older ZHe cooling dates than Early Cretaceous plutons (e.g., ~ 110 Ma versus ~ 100 Ma, Table 1.2; Figure 1.14), suggesting that the along-strike thermal gradients persisted through the end of AFS activity.

Hornblende Ar system dates in both Jurassic and Early Cretaceous plutons overlap with or are within a few million years of the zircon U-Pb date, suggesting cooling through $\sim 500^\circ\text{C}$ (Harrison, 1982) shortly after pluton emplacement at shallow crustal levels. Biotite Ar system dates show

a greater difference between the zircon U-Pb and hornblende Ar system dates indicating slower cooling between $\sim 500^{\circ}\text{C}$ and $\sim 310^{\circ}\text{C}$ most likely due to elevated geothermal gradients in the arc. In the Remiendos Complex along the Paposo segment, biotite Ar system dates are uniformly ~ 129 Ma while the zircon U-Pb dates are ~ 140 – 129 Ma, recording prolonged elevated temperatures associated with repeated pulses of pluton emplacement until magmatism ended and the area cooled through 310 – 345°C at ~ 129 Ma. Ar system dates for the Las Tazas and Sierra Dieciocho plutons along the central El Salado segment (~ 131 Ma and ~ 126 Ma, hornblende and biotite, respectively) overlap the zircon U-Pb dates (~ 131 Ma and 127 Ma), which indicates rapid post-emplacement cooling through 310 – 345°C . Ductile deformation was spatially and temporally associated with the sustained Early Cretaceous magmatic peak, and ended soon after the emplacement of the youngest Early Cretaceous plutons (~ 119 Ma). Brittle faults overprint mylonitic fabrics (Figure 1.11c) and record a transition from ductile to brittle deformation, which we attribute to cooling of the arc during progressive sinistral deformation along the AFS. These results refute the idea that distinct stages of motion within the arc are only loosely related to pluton emplacement (e.g., Scheuber and Andriessen, 1990; Scheuber and Gonzalez, 1999) and instead suggest that repeated emplacement of high temperature-low pressure Early Cretaceous plutons produced a high geothermal gradient in the arc that significantly thermally weakened the crust and played a critical role in facilitating the development of an intra-arc fault system (e.g., Beck, 1983; de Saint Blanquat et al., 1998; Scheuber and Reutter, 1992; Cao et al., 2015).

As the frequency and volume of intrusions waned and the magmatic peak tailed off, ductile deformation transitioned to brittle deformation as elevated geothermal gradients and crustal isotherms relaxed. The youngest pulse of Coastal Cordillera magmatism spans from 120 – 104 Ma and is found primarily along the central El Salado segment. Field relationships clearly show that slip along the AFS was in its final stages by ~ 110 Ma, just before the intrusion of the last arc plutons (~ 109 – 104 Ma). The similarity of zircon U-Pb, hornblende Ar system, and biotite Ar system in the post- 120 Ma plutons such as the La Borracha suggests elevated intra-arc gradients relaxed as magmatism waned. Our cooling dates most likely record the relaxation of elevated isotherms as

geothermal gradients went from $\geq 50^\circ\text{C}/\text{km}$ in plutons at ~ 130 Ma to a more standard $\sim 30^\circ\text{C}/\text{km}$ gradient by 100 Ma as magmatism waned. As it is unlikely that the geothermal gradient fell below $30^\circ\text{C}/\text{km}$, 180°C at 100 Ma implies a depth of 5–6 km. This value is in line with maximum pluton emplacement depths derived from Al-in-hbl barometry (Dallmeyer et al., 1996; González, 1996; Kurth, 2002). Published 113–100 Ma apatite fission track dates (Maksaev, 1990; Gana and Zentilli, 2000) and our ~ 116 –96 Ma ZHe dates (Figure 1.14) postdate the crystallization age of the youngest intrusion at all sites and indicate cooling of the arc was coeval with the end of slip along the AFS (e.g., Brown et al., 1993). In addition, the cessation of slip along the AFS broadly corresponds with a shift to transpressive crustal shortening recorded by a regional unconformity (Scheuber et al., 1994), the transition to slip along NW-striking fault systems such as the Taltal fault (Arabasz, 1971; Mavor et al., 2020), and westward acceleration of the South American plate due to the final breakup of South American and Africa during the opening of the South Atlantic (Seton et al., 2012; Maloney et al., 2013; Granot and Dymant, 2015). Together this suggests the end of slip along the AFS may be related to changing plate motion that resulted in a shift from SE-directed to NE-directed convergence (e.g., Seton et al., 2012; Maloney et al., 2013), uplift and erosion of the continental margin, eastern migration of the magmatic arc, and development of both a wide forearc and continental foreland basin (Coira et al., 1982). We propose that this plate motion reorganization at the end of the Early Cretaceous is linked to both abandonment of the Coastal Cordillera arc and cessation of slip along the AFS.

1.5.3 Thermal Weakening of the Crust due to Arc Magmatism

Increased geothermal gradients in and around Early Cretaceous plutons facilitated ductile strain by thermally weakening the crust (Figure 1.15). The peak strength of the crust, where the highest differential stresses are supported, occurs at the brittle-plastic transition (BPT; e.g., Sibson, 1983; Handy and Brun, 2004), typically defined as the intersection between frictional sliding criteria (Byerlee, 1978) and dislocation creep flow laws (e.g., Hirth et al., 2001). The depth to the BPT is highly dependent on temperature and strain rate, which ranges from 10^{-11} to 10^{-15} s^{-1} in most

shear zones (e.g., Pfiffner and Ramsay, 1982; Carter and Tsenn, 1987; Behr and Platt, 2014). We calculated a crustal strength profile for the AFS assuming quartz-controlled rheology based on the Hirth et al. (2001) quartzite flow law, hydrostatic fluid pressure Sibson (1992) and water fugacity (values calculated using Pitzer and Sterner, 1994, and Withers, 2013), and typical frictional sliding criteria (Byerlee, 1978) for a strike-slip faulting regime with a stress ratio of 0.5 (that is, neither transpressional nor transtensional with σ_2 halfway between σ_1 and σ_3). While some of these assumptions may not be entirely correct in detail, our aim is to evaluate the relative magnitude of stress change associated with geothermal gradients rather than accurately predicting peak stresses. At typical shear zone strain rates of 10^{-13} s^{-1} to 10^{-14} s^{-1} and a geothermal gradient of $30^\circ\text{C}/\text{km}$, the BPT occurs at depths of 9.5–12 km with maximum differential stresses of 120–170 MPa (Figure 1.15). However, when the geothermal gradient is increased to conditions typical of magmatic arcs ($50^\circ\text{C}/\text{km}$), the BPT shallows to 6–7 km and the maximum differential stress drops to 75–125 MPa, a $\sim 38\%$ reduction in peak crustal strength. Even a more moderate increase in geothermal gradient to $35^\circ\text{C}/\text{km}$ produces a 12–16% reduction in strength, with the BPT at 8–10 km and 100–150 MPa. These values agree with data from the Tonale shear zone that record a peak strength of $139 \pm 31 \text{ MPa}$ at $\sim 9 \text{ km}$ depth in the thermal aureole of a pluton with a geothermal gradient of $\sim 32^\circ\text{C}/\text{km}$ (Stipp and Kunze, 2008). Al-in-hbl barometry along the southern Paposito segment and El Salado segment gives maximum pluton emplacement depths of 6–10 km. Cooling dates indicate the plutons were at a minimum depth of 5 km at $\sim 100 \text{ Ma}$ assuming the geothermal gradient relaxed to $30^\circ\text{C}/\text{km}$ (Figure 1.15) and that AFS dip-slip motion was relatively minor, which matches the predicted $\sim 5\text{--}7 \text{ km}$ depth to the Early Cretaceous BPT for a geothermal gradient of $50^\circ\text{C}/\text{km}$. These gradients are similar to those documented along the Caleta Coloso fault at the northern end of the Paposito segment, where previous geothermobarometric, dating, and fluid inclusion studies suggest pluton emplacement as well as ductile and brittle deformation occurred prior to 118 Ma in a thinned intra-arc crustal zone with a geothermal gradient in excess of $50^\circ\text{C}/\text{km}$ (Herrera et al., 2005; Arancibia et al., 2014; González, 1999; Mitchell et al., 2017).

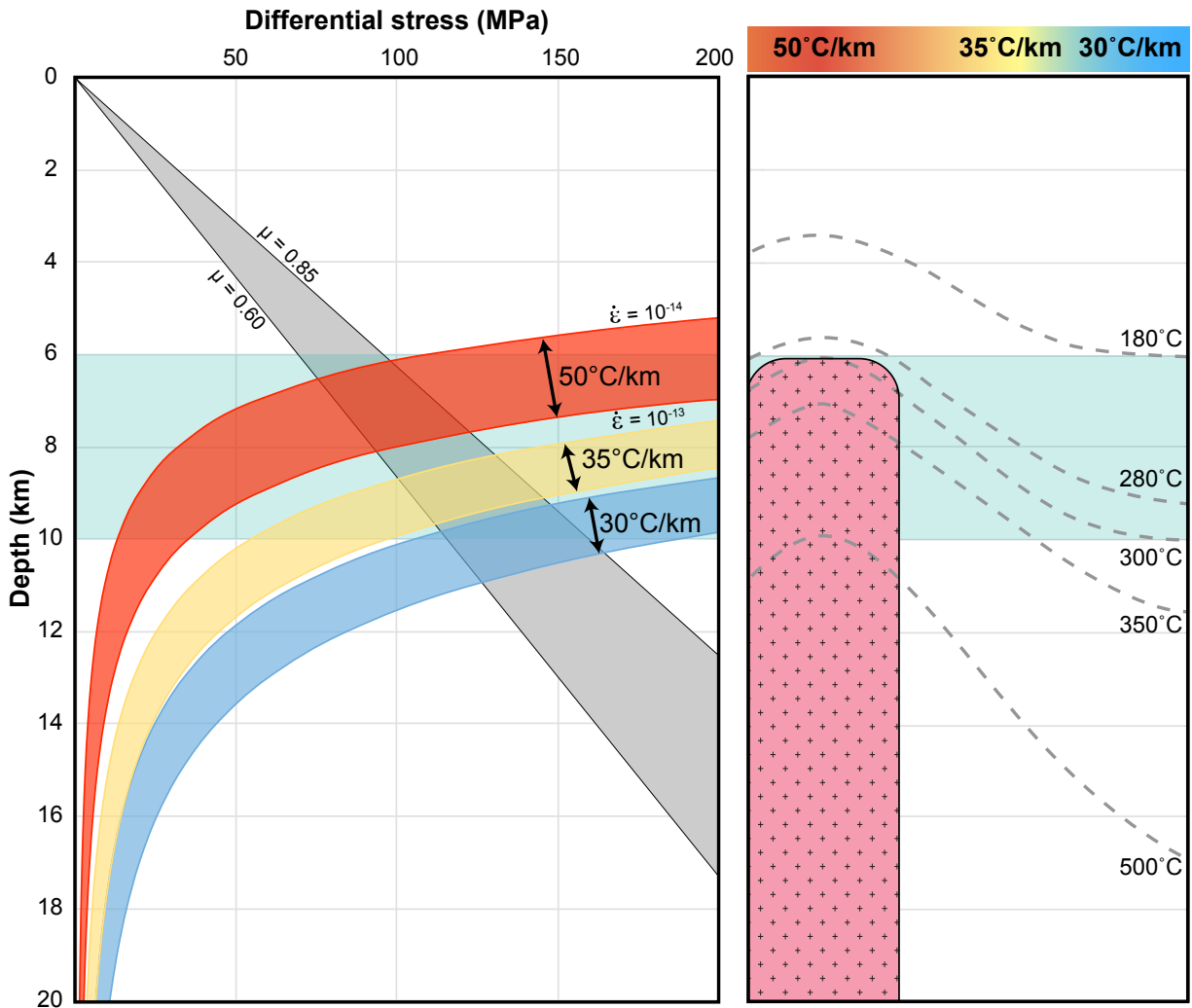


Figure 1.15: Left: Crustal strength profile showing the thermal softening effects of 50°C/km (red) and 35°C/km (yellow) geothermal gradients compared to a 30°C/km (blue) geothermal gradient. An envelope of values is presented for each geothermal gradient by varying the strain rate within typical values from 10^{-13} s^{-1} to 10^{-14} s^{-1} . Shaded gray envelope shows the range of brittle frictional sliding behavior. Green bar represents the 6–10 km depth of emplacement of Early Cretaceous plutons (Dallmeyer et al., 1996; González, 1996; Kurth, 2002). Right: Schematic diagram showing the deflection of isotherms around a tabular pluton with geothermal gradients of 50°C/km, 35°C/km, and 30°C/km. Note the shallowing and compression of isotherms due to heat flow from pluton emplacement (e.g., Murray et al., 2018).

Crustal strength may also be greatly reduced by fluid-rock reactions that alter and break down feldspar into secondary phyllosilicates or fine-grained polyphase mixtures of quartz and clays (e.g., Janecke and Evans, 1988; Wintsch et al., 1995; O'Hara, 2007; Marsh et al., 2009; Collettini et al., 2019; Stenvall et al., 2019). Fluid-rock interactions are promoted by the release of magmatic fluids exsolved from crystallizing plutons, converting strong phases such as feldspar to fine-grained phyllosilicates, introducing intragranular water-related defects, and resulting in hydrolytic weakening (e.g., Tullis and Yund, 1989; Hirth and Tullis, 1992; Post et al., 1996). The extensive alteration of the Jurassic plutons and local alteration of Early Cretaceous plutons indicates significant fluid flow through the Coastal Cordillera, and support the idea that reaction softening and hydrolytic weakening could have played a role in reducing the strength of the crust along the AFS corridor. Considering these effects together, we suggest the spatially heterogeneous Early Cretaceous pluton emplacement facilitated significant along-strike variations in crustal strength.

In such a rheologically heterogeneous crust, strain would more easily localize in thermally weakened areas (e.g., Jaquet and Schmalholz, 2018), thereby setting up a highly segmented fault system. Individual segments of the El Salado segment do not run the full length between Taltal and La Serena. Rather, the lengths of mapped fault traces at 1:100,000-scale approximately correlate to the percentage of Early Cretaceous plutons: >160 km along the southern Paposo segment (~23% Early Cretaceous plutons; Escribano et al., 2013; Álvarez et al., 2016), ~130 km and ~180 km traces of the eastern and western branches along the northern El Salado segment (~32% and ~49% Early Cretaceous plutons, respectively; Godoy and Lara, 1998; Lara and Godoy, 1998; Escribano et al., 2013; Espinoza et al., 2014), and a ~30 km continuous trace along the Mantoverde segment (~76% Early Cretaceous plutons; Lara and Godoy, 1998). Fault segments linked as strain along these initial segments propagated out into the cooler, stronger crust surrounding the Early Cretaceous plutons. Segments with a greater volume of synkinematic plutons record more distributed strain and evolved to brittle fault zones later in their history; however, the AFS never evolved to a mature fault system where slip was concentrated along one regional-scale fault.

1.6 Conclusions

Mapping and structural measurements along the southern Paposo segment and northern and central El Salado segments of the Atacama fault system (AFS) document mylonitic shear zones spatially and temporally associated with Early Cretaceous plutons that transition to brittle behavior during progressive strain. Sinistral ductile shear along the AFS initiated with the emplacement of synkinematic Early Cretaceous plutons between ~ 139 Ma and ~ 131 Ma. Ductile deformation was spatially and temporally associated with sustained Early Cretaceous magmatism and ended soon after the emplacement of the youngest synkinematic plutons (~ 119 Ma). Areas along the AFS with a greater volume of Early Cretaceous plutons record wider mylonite zones and evolved to brittle faults later in their history. Postmylonitic intrusions range in age from 119–107 Ma, and a ~ 110 Ma andesitic dike records the end of the brittle slip on the AFS.

New zircon U-Pb and (U-Th)/He dates coupled with previously published data demonstrate that magmatism in the Coastal Cordillera occurred in three primary pulses: a minor Late Jurassic pulse (195–175 Ma), broad Early Cretaceous pulse from 150–120 Ma, and a younger pulse at 120–105 Ma. Ar system dates in Jurassic and Early Cretaceous rocks are systematically younger than zircon U-Pb dates, indicating the background temperature of the Coastal Cordillera crust was $< 350^\circ\text{C}$ prior to Early Cretaceous arc magmatism. Strain gradients in the rheologically weak Paleozoic metasedimentary rocks surrounding shallowly-intruded Early Cretaceous plutons indicate arc magmatism thermally weakened the crust by locally elevating geothermal gradients, facilitating AFS deformation by enabling mylonitization to occur at ~ 5 – 7 km depths and low differential stress. Reaction softening and hydrolytic weakening could have further reduced the strength of the crust along the AFS corridor, creating significant along-strike variations in crustal strength that set up a segmented system that never evolved into a single regional-scale fault.

The cessation of slip along AFS was broadly coeval with the abandonment of the magmatic arc and cooling of the Coastal Cordillera below $\sim 180^\circ\text{C}$ as plate motion reorganization at the end of the Early Cretaceous likely resulted in a shift in convergence direction. 116–96 Ma ZHe cooling dates most likely record the relaxation of elevated isotherms from $\geq 50^\circ\text{C}/\text{km}$ at ~ 130 Ma

to $\sim 30^{\circ}\text{C}/\text{km}$ gradient by 100 Ma as magmatism migrated eastward and the effects of thermal weakening along the Coastal Cordillera subsided.

Chapter 2

Early Cretaceous Magnitude, Timing, and Rate of Slip along the El Salado Segment

Summary

The Atacama fault system (AFS) is a crustal-scale sinistral structure that accommodated oblique convergence in the Early Cretaceous Coastal Cordillera arc. Displacement estimates along this ~1,000 km-long fault system vary widely due to a lack of clear piercing points. We mapped the northern ~70 km of the El Salado segment, documenting the distribution of arc plutons and kinematics of deformation to establish the slip history of the AFS. Petrology, geochemistry, and geo/thermochronology were used to characterize and correlate pre-, syn-, and post-kinematic plutons, and structural data were analyzed to understand progressive changes in the style of deformation. Mylonitic fabrics uniquely associated with the synkinematic ~134–132 Ma Cerro del Pingo Plutonic Complex are sinistrally separated by 32–38 km along the eastern branch, whereas mylonites associated with a synkinematic ~119 Ma tonalite are sinistrally separated by 22–24 km. We propose that the synkinematic plutons and associated mylonites are offset markers that record ductile to brittle displacement along the eastern branch of the El Salado segment. A chain of leucocratic granites and hypabyssal intrusions are sinistrally separated across the western branch of the AFS by ~14–18 km, giving a total slip magnitude of $\sim 50 \pm 6$ km across the El Salado segment. Brittle fault slip indicators across all branches consistently record sinistral shear with a minor dip-slip component, and a latest-kinematic dike captures the ending stages of AFS slip at ~110 Ma. Displacement along the El Salado segment occurred almost entirely between ~133 and ~110 Ma at an average slip rate of ~2.0–2.5 km/Myr. This slip rate is low compared to other modern intra-arc strike-slip faults, suggesting the segmented nature of the AFS inhibited efficient

slip localization, or plate convergence rates or obliquity may have been significantly lower than previously modeled.

2.1 Introduction

Plate motion across most subduction zones is oblique ($>22^\circ$ from normal to the plate boundary) and partitioned between slab underthrusting and upper-plate lateral transport (Jarrard, 1986; Woodcock et al., 1986)². Lateral transport of forearc slivers may be achieved through oblique underthrusting or partitioned between underthrusting, distributed forearc deformation, and/or along crustal-scale strike-slip faults, with strike-slip faults dominating at margins where interplate coupling between a subducting oceanic slab and overriding continental plate is strong (Fitch, 1972; Jarrard, 1986). While the dynamics of oblique convergence have been studied from a modeling perspective (e.g., Tikoff and Teyssier, 1994; Teyssier et al., 1995), there are relatively few studies that have provided detailed slip histories of intra-arc strike-slip fault systems in the upper plate of a subduction zone.

The regional tectonic history of an area is of foremost importance when studying oblique convergence, as changes in convergence angles over time will directly affect the distribution of strain (e.g., Scheuber et al., 1994). In particular, the absolute motion of the overriding plate with respect to the trench—which includes the magnitude and rate of slip along trench-parallel strike-slip faults—must be known to understand subduction zone processes such as slip partitioning (Jarrard, 1986). There are significant variations and uncertainties in estimates of slip partitioning from modern subduction zones based on geodesy and strain modeling. For example, the Median Tectonic Line of Japan accommodates $\sim 25\%$ trench-parallel motion (Loveless and Meade, 2010), the Sumatran fault system accommodates $\sim 33\%$ (Tikoff and Teyssier, 1994) to $\sim 66\%$ (McCaffrey et al., 2000) of trench-parallel motion, and the Liquiñe-Ofqui fault system accommodates $\sim 75\%$ of modern trench-parallel motion (Wang et al., 2007). Recent work by Bradley et al. (2017) suggests

²This chapter will be submitted for publication: N.M. Seymour, J.S. Singleton, R. Gomila, S.P. Mavor, G. Heuser, G. Arancibia, S. Williams, and D.F. Stockli, Early Cretaceous magnitude, timing, and rate of slip along the Atacama fault system, northern Chile, in preparation.

oblique underthrusting is important across the Sumatran trench, with up to 40% of interseismic trench-parallel motion occurring on slab interface. While active displacement on modern intra-arc strike-slip faults may be known from geodesy, these major structures have poorly constrained total displacement estimates and geologic (Myr scale) slip rates. Detailed slip histories on these modern systems are hindered by a lack of exposure, as structures such as the Sumatran fault and Liquiñe-Ofqui fault are in heavily vegetated areas where clear bedrock piercing points are difficult to identify. Although direct slip rates on fossil fault systems cannot be gleaned from geodetic data, erosion to deeper levels in fossil strike-slip systems can expose piercing points, and the identification of crosscutting relationships marking the relative timing of slip along a fault system can be used to estimate slip rates.

The Atacama fault system (AFS), one of the best and most accessible examples of a major intra-arc fault system, runs for $\sim 1,000$ km through the Coastal Cordillera along the western margin of northern Chile (Figure 2.1). The AFS is a sinistral strike-slip, trench-linked structure that formed as a result of slip partitioning during Mesozoic SE-directed oblique subduction. Unparalleled exposure and the presence of pre-, syn-, and post-tectonic intrusions cutting both brittle and ductile features along the AFS provide an excellent opportunity to reconstruct slip history. Previous estimates of slip along this system are poorly constrained because no clear piercing points have been identified across the fault system. Using detailed geologic mapping, we identify offset markers along the AFS and use crosscutting relationships, geo-/thermochronology, and geochemistry to provide robust constraints on the timing, magnitude, and rate of slip along the El Salado segment of the AFS. We compare these data to slip rates and partitioning estimates from other major intra-arc strike-slip faults to understand the role of the AFS in accommodating oblique subduction.

2.2 Geologic Setting

2.2.1 Atacama fault system

Mesozoic SE-directed subduction of the Aluk (Phoenix) plate below the N-S trending South American plate margin produced a long-lived period of arc magmatism now preserved in the

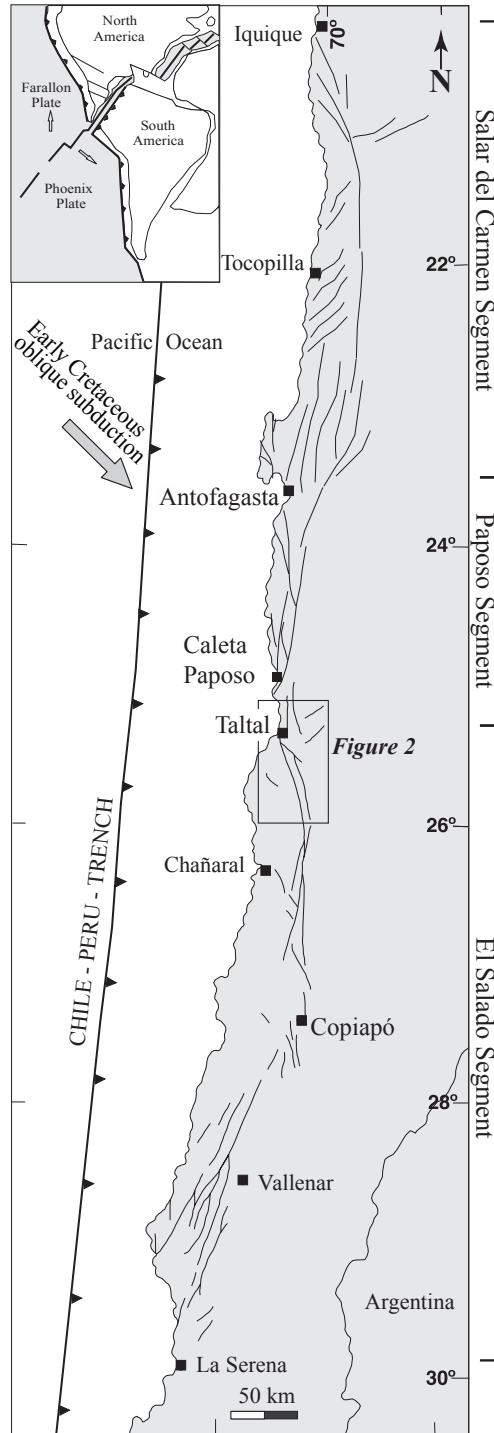


Figure 2.1: Regional scale geometry northern Chile showing the three segments of Atacama fault system (AFS). Gray arrow shows the Mesozoic convergence vector. Boxes show the location and name of the three areas studied in this work. Inset map shows approximate plate configuration coeval with Mesozoic sinistral strike-slip deformation along the AFS from Jaillard et al. (1990). Modified from Cembrano et al. (2005)

Coastal Cordillera (Scheuber and Andriessen, 1990; Dallmeyer et al., 1996; Scheuber and Gonzalez, 1999; Parada et al., 2007). Lateral strain from the obliquely descending slab was partitioned between the subducting plate and overriding South American plate along the sinistral AFS, which is exposed in the Late Jurassic to Early Cretaceous magmatic arc for $\sim 1,000$ km between Iquique (20.5°S) and La Serena (30°S) (e.g., Naranjo et al., 1984; Scheuber and Andriessen, 1990; Brown et al., 1993; Grocott et al., 1994; Scheuber et al., 1995; Grocott and Taylor, 2002). The timing of AFS deformation has been tied to Coastal Cordillera magmatism and is broadly constrained to ~ 140 – 110 Ma by crystallization and cooling ages of Coastal Cordillera granitoids (Grocott et al., 1994; Scheuber et al., 1995; Dallmeyer et al., 1996; Ruthven et al., 2020, Chapter 1).

The AFS is comprised of three distinct fault segments: the northern Salar del Carmen, central Paposo, and southern El Salado segment (e.g., Naranjo et al., 1984; Scheuber and Andriessen, 1990; Brown et al., 1993; Grocott and Taylor, 2002, Figure 2.1). The Paposo and El Salado segments record a progression from ductile (mylonitic) to brittle strain (e.g., Scheuber and Andriessen, 1990; Brown et al., 1993; Ruthven et al., 2020, Chapter 1). Studies of deformation along the Paposo segment document steeply dipping sinistral strike-slip duplexes developed in a transtensional regime near Antofogasta (Cembrano et al., 2005; Veloso et al., 2015) and steeply dipping sinistral mylonitic fabrics overprinted by brittle faults developed in a transpressional regime near Paposo (Ruthven et al., 2020). The variation in geometry and deformation style is likely due to the NNW to NNE variation in fault orientation relative to the SE-directed Cretaceous subduction direction (Ruthven et al., 2020). Overall, the fault system is highly segmented, with the Salar del Carmen, Paposo, and El Salado segments each comprised of several parallel branches rather than a single regional-scale fault (e.g., Godoy and Lara, 1998; Lara and Godoy, 1998; Escribano et al., 2013; Espinoza et al., 2014; Álvarez et al., 2016). Of the three major segments, we focused on the northern El Salado segment to take advantage of the excellent exposure of pre-, syn-, and post-kinematic igneous units available for constraining the slip history of the AFS.

2.2.2 The El Salado Segment

The El Salado segment represents half of the total AFS length, extending ~ 490 km along the Coastal Cordillera between Taltal (25.4°S) and La Serena (29.9°S). The AFS goes offshore for ~ 28 km, defining the separation between the El Salado and Pajoso segments, and comes back onshore at 25.1°S where southern end of the NNE-striking Pajoso fault intersects the coastline. This study focused on the northern half of the El Salado segment between 25.36°S and 26.00°S , a well-defined segment where kilometer-scale zones of steeply dipping, sinistral mylonitic fabrics are exposed and overprinted by brittle structures (e.g., Chapter 1). Rocks exposed along the El Salado segment are dominantly plutons ranging in age from 210 Ma to 107 Ma, Jurassic to Early Cretaceous La Negra and Aeropuerto volcanic and volcanoclastics, and lesser volumes of Paleozoic phyllites and quartzites (Godoy and Lara, 1998; Lara and Godoy, 1998; Godoy and Lara, 1999; Godoy et al., 2003; Arévalo, 2005a; Contreras et al., 2013; Escribano et al., 2013; Espinoza et al., 2014; Álvarez et al., 2016). Deformation along the El Salado segment is tied to activity of the Coastal Cordilleran arc between 140–110 Ma, with Early Cretaceous plutons spatially and temporally associated with AFS deformation. Elevated geothermal gradients thermally weakened the crust and enabled ductile strain at shallow crustal levels, facilitating mylonitization along the margins of Early Cretaceous plutons and surrounding metasedimentary rock. Ductile deformation transitioned to brittle deformation with waning arc magmatism, and the cessation of slip occurred as the arc cooled and migrated eastward at ~ 116 –99 Ma (Chapter 1).

The brittle Atacama fault system is composed of two well-defined, well-exposed branches that are regionally continuous for at least 130–180 km (Lara and Godoy, 1998; Godoy and Lara, 1999; Escribano et al., 2013; Espinoza et al., 2014), referred to as the eastern and western branches. The eastern branch is mapped for ~ 180 km along a ~ 170 – 350° trend as a discontinuous trace of two main strands each with several subsidiary faults (Lara and Godoy, 1998; Godoy and Lara, 1999; Escribano et al., 2013; Espinoza et al., 2014), locally represented by meter- to decameter-scale chlorite- and epidote-rich cataclasite fault cores. The eastern branch appears to be the major strand based on its continuity to the south, and separates Jurassic and Early Cretaceous plutons of

the Coastal Cordilleran arc and Paleozoic metasedimentary rocks of the Devonian-Carboniferous Chañaral Complex east of the eastern branch from Lower Jurassic to Lower Cretaceous deposits west of the eastern branch (Lara and Godoy, 1998; Godoy and Lara, 1999; Escribano et al., 2013; Espinoza et al., 2014). The western branch is mapped for ~ 130 km along a ~ 350 – 355° trend on 1:100,000-scale geologic maps (Lara and Godoy, 1998; Godoy and Lara, 1999; Escribano et al., 2013; Espinoza et al., 2014) and primarily separates Jurassic La Negra Formation volcanic and intercalated marine deposits on the west from Lower Cretaceous Aeropuerto Formation volcanic and volcanoclastic deposits on the east. The El Muelle fault splays off the western branch at 25.78°S and curves from a 340 – 345° trend at the point of divergence to a 325 – 330° trend as it enters the Pacific Ocean at 25.41°S . Brittle fault relays along the El Salado segment provided the fluid pathways for many of the Chilean Iron Belt ore deposits such as the NW-trending stepover at the Mantoverde IOCG mine (Vila et al., 1996; Rieger et al., 2010).

The AFS has been recognized as a regional-scale structure since at least 1960 (St. Amand and Allen, 1960), yet no clear geologic offset has been identified. Estimates of sinistral displacement magnitude along this segment range from ~ 70 km to <20 km. Brown et al. (1993) proposed ~ 70 km of brittle sinistral displacement along the AFS by correlating broad zones of ductile deformation north of Taltal with ductile shear zones located near Quebrada Pan de Azúcar. This interpretation relies on the original continuity of the Paposo and El Salado segments, and does not provide an estimate of slip during ductile deformation. More recent studies by Grocott and Taylor (2002) and Chapter 1 identified AFS mylonite zones in between these segments, casting doubt on the Brown et al. (1993) mylonite zone offset markers. Grocott and Taylor (2002) argue that the displacement is unlikely to exceed 20 km total with no more than a few km across any individual strand due to the discontinuous, overstepping nature of AFS fault branches. Hervé (1987b) documents ~ 34 km of Early Cretaceous sinistral slip along the Izcuña fault, a subsidiary branch along the Paposo segment, based on the offset and correlation of a ~ 144 Ma granodiorite body; however, no similar offset markers have been documented along the El Salado segment even though the entire segment has been mapped at 1:100,000 scale (Arévalo, 1995; Godoy and Lara, 1998;

Lara and Godoy, 1998; Blanco et al., 2003; Godoy et al., 2003; Arévalo, 2005a; Welkner et al., 2006; Arévalo and Welkner, 2008; Arévalo et al., 2009; Creixell et al., 2012; Contreras et al., 2013; Escribano et al., 2013; Espinoza et al., 2014; Álvarez et al., 2016).

The end of slip along the AFS is most likely related to changing plate motion that resulted in a transition to \sim E-W crustal shortening across the Taltal and Chivato fault systems and migration of arc magmatism inboard (e.g., Arabasz, 1971; Scheuber et al., 1994; Haschke et al., 2006; Ramos and Folguera, 2009), broadly coeval with the westward advance of the South American plate and onset of seafloor spreading in the South Atlantic (e.g., Matthews et al., 2012; Seton et al., 2012; Maloney et al., 2013; Granot and Dymant, 2015; Kirsch et al., 2016). The northern El Salado segment is cut by NW-striking sinistral faults such as the Taltal fault system that offset the main AFS strands by a total of \sim 11 km (Naranjo and Puig, 1984; Espinoza et al., 2014; Mavor et al., 2020). Near Taltal, unstrained dikes postdate slip along the eastern branch of the AFS (Mavor et al., 2020, Chapter 1). One dacite dike with a 107 ± 9 Ma zircon (U-Th)/He cooling date crosscuts AFS-related cataclasite derived from the Matancilla pluton and is cut by the Taltal fault (Mavor et al., 2020). An andesitic dike with a $\sim 110 \pm 4$ Ma zircon U-Pb date crosscuts both cataclasite and the main brittle fault strands of the eastern branch of the El Salado segment, but is sinistrally offset by \sim 147 m by one strand of the eastern branch (Chapter 1). This dike is also cut by the Quebrada de la Peineta fault, a subsidiary strand of the NW-striking Taltal fault system (Mavor et al., 2020). Neogene E-side-down motion has been documented along the AFS (Hervé, 1987a; González and Carrizo, 2003; González et al., 2006; Allmendinger and González, 2010); however, this motion is absent or limited to meter-to-decimeter scale dip-slip along parts of the northern El Salado segment (Arabasz, 1971) and does not obscure structures related to Cretaceous sinistral slip.

2.3 Methods

2.3.1 Field Mapping & Petrography

We expand upon the study area of Chapter 1 to include 70-km-long, 5 km-wide swath across the El Salado segment from the Pacific Ocean at 25.36°S to the C-119 highway at 26.00°S in order to identify potential offset markers across the AFS. Detailed 1:25,000-scale geologic mapping was undertaken to understand the distribution of ductile and brittle structures related to the AFS. We documented lithologies, and the geometry and kinematics of mylonitic fabrics and brittle faults (Table 2.1). Classifications of plutons were determined via petrographic analysis of both hand samples and thin sections. Samples of plutons deemed potential offset markers in the field were collected for geochemistry and geochronology. Offset features, R- and T-fractures, and mineral growth steps were used to determine slip sense (e.g., Petit, 1987).

Faults were classified based first on their association with either the western or eastern branch of the El Salado segment, then their proximity to the mapped trace of the fault. Faults listed with "Western Branch" or "Eastern Branch" include principal slip planes and parallel faults that occur within 50 m of the mapped trace of the major AFS branches; faults labeled "AFS Parallel" occur >50 m away from but strike $\leq \sim 30^\circ$ of the average orientation of the principal slip plane structures. Structural data were analyzed using Stereonet 10.1.1 (Allmendinger et al., 2011; Cardozo and Allmendinger, 2013) and FaultKin 7.7.4 (Allmendinger et al., 2011). Maximum eigenvectors were used to determine average orientations, and incremental shortening and extension (P- and T-) axes were determined from paired fault plane and slickenline lineation measurements (Marrett and Allmendinger, 1990). We present fault plane solutions derived from linked Bingham P- and T-axes of faults with a known slip sense. In addition, we present fault plane solutions for all of the AFS classifications assuming a sinistral slip sense on all \sim N-S-striking slickensided faults with unclear kinematics. Given the consistent sinistral kinematics along the AFS, this assumption is likely to be largely accurate and allows us to evaluate kinematic patterns that are not influenced by incomplete slip sense determination.

Table 2.1: Summary of U-Pb sample lithology and degree of strain.

Sample	UTM Coordinates ¹		Lithology	Deformation
	Easting (m)	Northing (m)		
161-74	374810	7131131	Bt-Hbl Tonalite	Protomylonitic
181-N154	375287	7125806	Hbl Tonalite	Unstrained w/ Discrete Zones
188-S142	366809	7161211	Granite	Unstrained
191-N46	366333	7138242	Granite	Unstrained

¹Coordinates in Universal Transverse Mercator (UTM) World Geodetic System 1984 (WGS84),

2.3.2 Analytical Methods

For U-Pb analysis, zircon grains separated from samples 161-74, 181-N154, 191-N46, and 188-S142 were mounted in epoxy, polished to expose the center of the grains, and imaged using cathodoluminescence (CL) to document internal zoning patterns (Appendix 3.6). Laser ablation inductively coupled plasma mass spectrometry spot analyses targeted individual growth domains determined from CL imagery. Additional euhedral, unpolished zircon grains were mounted on double-sided tape parallel to the c-axis and depth profiled according to the methods outlined in Marsh and Stockli (2015) to resolve fine-scale growth domains too small for a spot analysis. Full U-Pb methodology is given in Chapter 1. The combined internal and external error is reported for individual grains. Grains were filtered to <10% discordance to eliminate the effects of disturbance due to Pb loss and/or inheritance. Weighted $^{206}\text{Pb}/^{238}\text{U}$ average dates with 2σ error calculated in Isoplot 4.15 (Ludwig, 2003) are reported (Table 2.2).

(U-Th)/He analyses were conducted on samples 161-74 and 181-N154 according to the methods outlined in Wolfe and Stockli (2010). Aliquots were assigned an 8% analytical error based on the long-term laboratory reproducibility of the Fish Canyon Tuff zircon standard (e.g., Reiners et al., 2002, 2004). Dates are reported based on the average of 3–6 single grains per sample and two times the larger of either the traditional or alternative standard error of the average calculation (Table 2.2). Full (U-Th)/He methodology is given in Chapter 1.

Whole-rock sample volumes of relevant plutons were pulverized for geochemical analyses. Samples were sent to ALS Minerals in Reno, Nevada for major element composition according to the ME-MS61m analytical package. In this procedure, 0.250 g of prepared initial sample is decomposed with a hydrofluoric, nitric, perchloric acid digestion and HCl leach. The solution is made up to a final volume of 12.5 mL with 11% hydrochloric acid, homogenized, and analyzed by inductively coupled plasma atomic-emission-spectrometry or mass-spectrometry. Values are reported as weight percent oxides for major elements (Table 2.3).

Table 2.2: Summary of geo/thermochronometric data.

Sample	Date Range	U-Pb			(U-Th)/He				
		Mean Date $\pm 2\sigma$ (Ma)	n ¹	MSWD	Mean Date $\pm 1\sigma$ (Ma)	n	SE ²	Alt SE	Max SE
161-74 - cores	122.8–141.4	131.9 \pm 1.3	51	6.7	99 \pm 8.2	5/6	3.7	2.8	7.3
161-74 - rims	114.9–121.7	119.5 \pm 1.8	10	2.4	99 \pm 8.2	5/6	3.7	2.8	7.3
181-N154	125.6–140.7	134 \pm 0.8	62/69	6.5	99.1 \pm 1.1	3/4	0.6	2.8	5.6
188-S142	133.2–151.1	140.9 \pm 1.1	52/67	8.6	-	-	-	-	-
191-N46	135.9–153.1	143 \pm 1.8	27/40	7.7	-	-	-	-	-

¹Number of grains used to calculate average date. ²SE denotes Standard Error. See Table 1.2 for details.

Table 2.3: Whole-rock geochemical data.

Sample	SiO ₂	Al ₂ O ₃	Fe ₂ O ₃	CaO	MgO	Na ₂ O	K ₂ O	TiO ₂	MnO	P ₂ O ₅	SrO	BaO	LOI	Total
161-62	63.8	16.45	5.47	5.15	2.47	3.81	2.16	0.63	0.12	0.1	0.04	0.04	0.7	100.94
161-74	62.1	16.55	5.62	5.56	2.51	4.60	1.12	0.63	7.0E-2	0.19	0.05	0.03	1.16	100.19
Difference	1.70	0.10	0.15	0.41	4.00E-2	0.79	1.04	0	0	5.0E-2	0.09	1.0E-2	1.0E-2	0.46

Sample	Ba	Ce	Cr	Cs	Dy	Er	Eu	Ga	Gd	Hf	Ho	La	Lu	Nb	Nd	Pr	Rb	Sm	Sn	Sr
161-62	398	35.7	10	2.4	3.9	2.3	1.0	19.1	3.9	3.6	0.8	17	0.4	4.4	18.5	4.6	59.9	4.5	2	401
161-74	298	39.2	20	1.4	3.1	1.9	1.4	19.3	3.4	4.7	0.6	18.8	0.3	5.5	19.9	5.0	40.5	4.2	3	490

Sample	Ta	Tb	Th	Tm	U	V	W	Y	Yb	Zr
161-62	1.4	0.6	5.5	0.4	1.3	141	207	22	2.4	126
161-74	2.2	0.5	3.7	0.3	0.8	114	332	17.3	1.8	191

2.4 Results

Here we present map relationships along a ~ 70 km stretch of the northern El Salado segment from the Pacific Ocean at 25.36°S to the C-119 highway at 26.00°S (Figure 2.1, Figure 2.2), including and expanding upon mapping presented in Chapter 1 and Mavor et al. (2020). We document the occurrence of mylonitic shear zones in two distinct areas across the eastern branch. These mylonites are overprinted by brittle faults, and clasts within cataclasite along the eastern branch contain mylonitic metasedimentary rocks. We identified a suite of pre- and synkinematic intrusions that bear striking resemblances to one another during mapping and occur on opposite sides of the eastern branch of the northern El Salado segment, which presents the opportunity to use the plutons as offset markers recording sinistral separation. Across the western branch, we note the similarity in composition of two belts of leucocratic igneous bodies. We present a description of the petrography and textures of each potentially correlative igneous body as well as whole-rock geochemistry, zircon U-Pb crystallization dates, and (U-Th)/He cooling dates (Table 2.2).

2.4.1 Eastern Branch

Mylonite zone east of the eastern branch of the AFS (25.61°S and 25.78°S)

Along the east side of the eastern branch of the AFS a ~ 18 km-long mylonite zone occurs between 25.61°S and 25.78°S where the Cerro del Pingo Plutonic Complex is adjacent to the eastern branch and extending along-strike into the neighboring Chañaral Complex (Figure 2.3; Espinoza et al., 2014, Chapter 1). Fresh, medium-grained mesocratic hornblende biotite granodiorite to biotite hornblende tonalite with 47–56% plagioclase, 21–28% quartz, 4–15% potassium feldspar, 3–10% biotite, and 6–13% hornblende locally crosscut by adularia+quartz veinlets comprise the main body of the Cerro del Pingo Complex in this zone (Figure 2.4). Chapter 1 presents 132.6 ± 0.9 Ma and 132.3 ± 1.3 Ma zircon U-Pb dates for this body (samples 181-S55 and 181-S158). Protomylonitic fabrics within the tonalite are locally developed in the central ~ 14 km long portion of the shear zone that ranges from ~ 200 – 800 m wide where the Cerro del Pingo Complex intrudes Chañaral Complex metasedimentary rocks, extending up to ~ 300 – 400 m into the pluton itself.

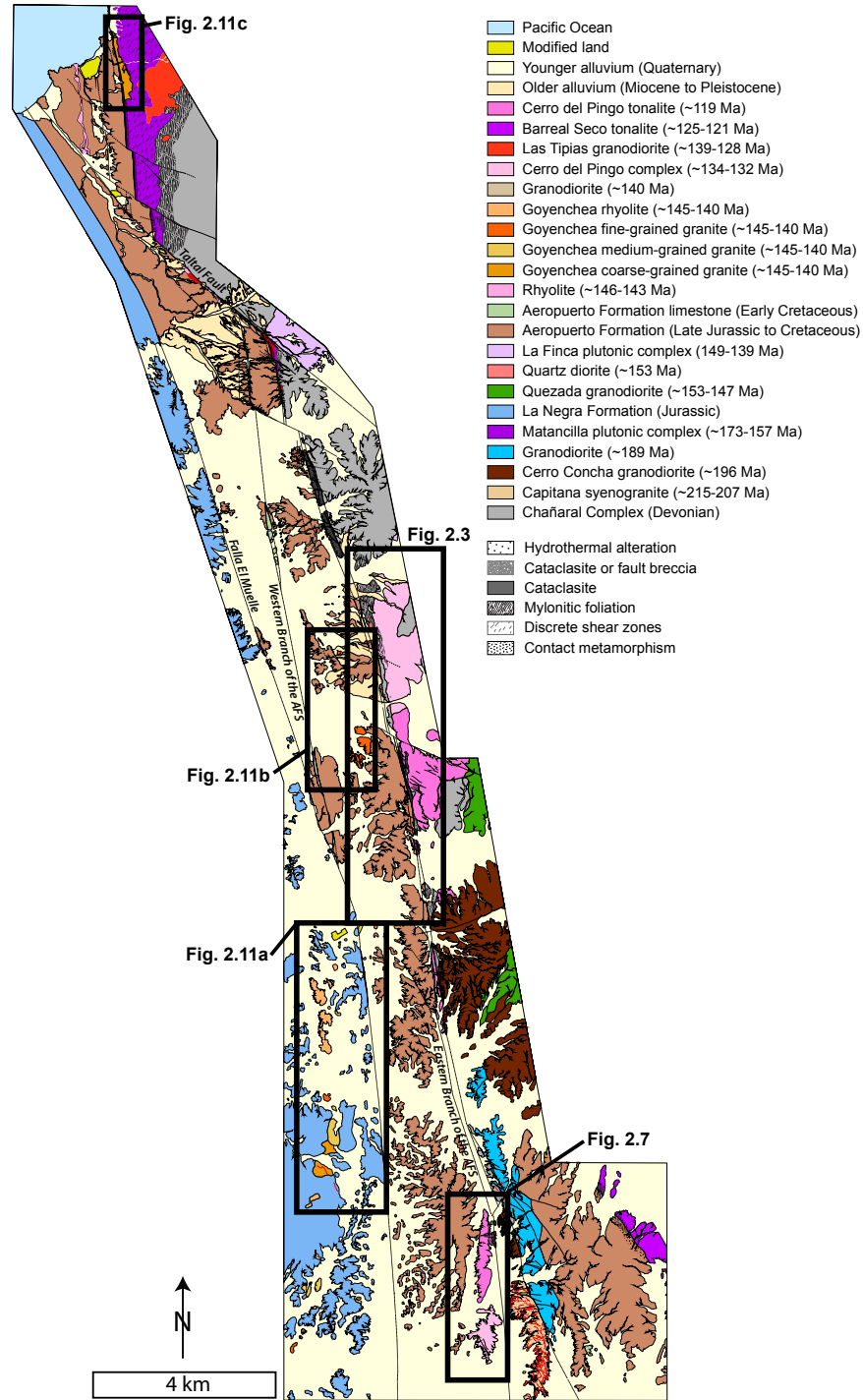


Figure 2.2: Simplified map of the northern El Salado segment study area compiled from our new mapping, Escribano et al. (2013), and Espinoza et al. (2014). The Cerro del Pingo Complex is shown in pink, the Jurassic plutons are shown in purple and blue, and the Chañaral Complex is shown in gray. Bold black lines show the major strands of the AFS and mylonites are shown by the wavy pattern. Yellow stars show new U-Pb samples from this study. Black boxes show the location of the inset maps in Figure 2.3, Figure 2.7, and Figure 2.11.

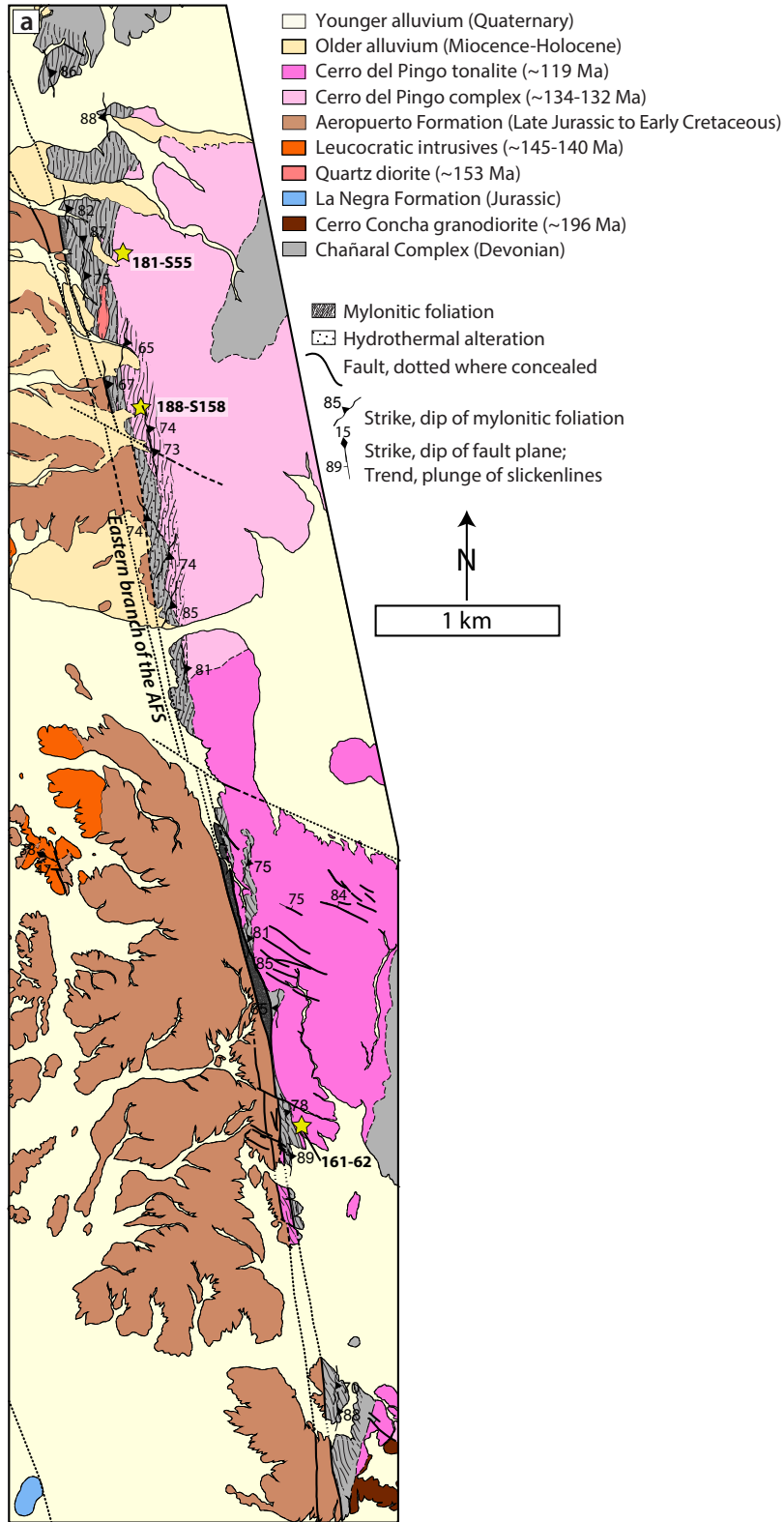


Figure 2.3: Inset map of the northern mylonite zone and Cerro del Pingo Complex east of the eastern branch of the AFS. Yellow stars show U-Pb samples from Chapter 1.

Metasedimentary rocks are pervasively highly strained: metasedimentary rocks in the central part of the shear zone are completely dynamic recrystallized, and mylonitic foliation defined by mica-rich bands and lineations defined by stretched quartz are well developed in both quartz-rich and phyllosilicate-rich lithologies. The quartzite mylonites between the tonalite and the eastern AFS branch have an average foliation of 000/81 E and are dominantly S-plunging (average lineation 179/15; Figure 2.5). Within the Cerro del Pingo Complex, protomylonitic fabrics are defined by recrystallized tails on feldspar porphyroclasts, fine-grained mixtures of altered feldspar and sericite, aligned chloritized biotite and hornblende, and pockets of recrystallized quartz (Figure 2.6). The degree of strain increases with proximity to the eastern branch, and some samples are mylonitic rather than protomylonitic (e.g., sample 181-S456). The average orientation of the ductile foliations within the pluton is 356/81 E. A strain gradient within the metasedimentary rocks records the northern limit of mylonitization where the AFS juxtaposes the Chañaral Complex against Aeropuerto Formation (Chapter 1). Quartzites grade from platy mylonites to statically recrystallized but unstrained within a ~ 1.5 –2 km distance along strike of the eastern branch. The brittle core of the eastern branch cuts mylonitic and protomylonitic fabrics, and is oriented $\sim 14^\circ$ counterclockwise of the average mylonitic foliation.

Between 25.70°S and 25.78°S , the ~ 132 Ma Cerro del Pingo Complex is intruded by a mesocratic tonalite. Near this contact, the ~ 132 Ma pluton is highly altered with silicification and adularia veining. The younger intrusive rock is fresher and distinctly black and white compared to other plutons in the area, which often present as a medium gray. Mineralogically, the younger phase is a hornblende-biotite tonalite composed of 50–62% plagioclase, 19–30% quartz, 6–17% biotite, 6–21% hornblende, and 0–2% apatite, zircon, and oxide phases (Figure 2.4). Dark enclaves of quartz diorite are common. Cathodoluminescence imagery of zircons show core and rim relationships (Appendix 3.6). Cores have igneous textures and a weighted mean date of 128.1 ± 0.5 Ma ($n = 59$, MSWD = 1.8; sample 161-62) derived from spots on polished mounts. Rims are too thin to analyze in polished mounts, so additional grains were depth-profiled. Dates younger than the cores were interpreted to capture rim growth. Th/U values for the overgrowths are 0.68–

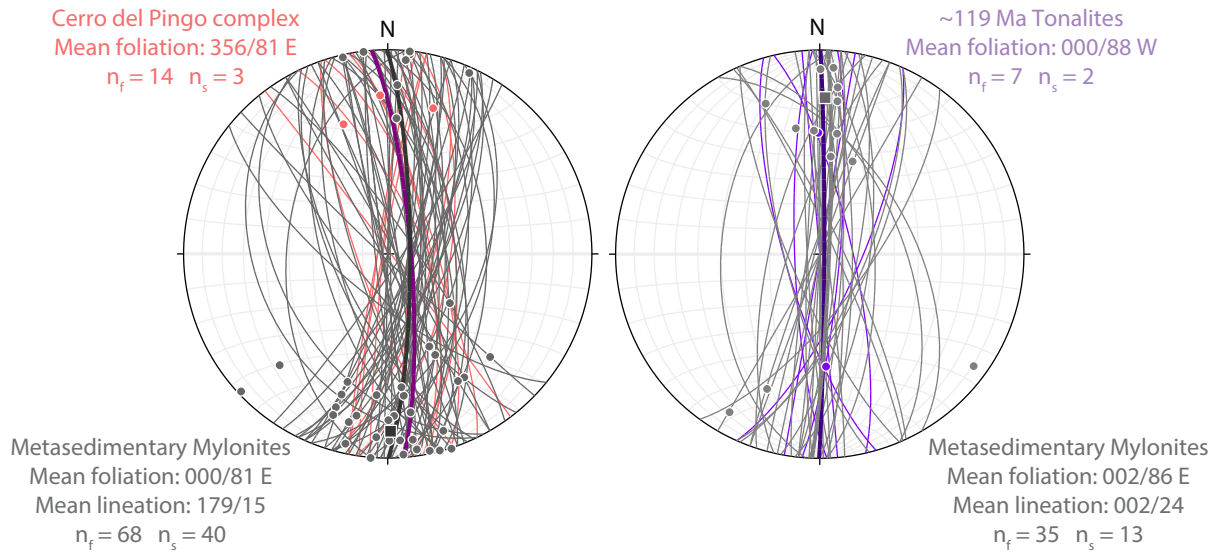


Figure 2.4: Equal-area stereograms of mylonitic foliations from the ~132 Ma Cerro del Pingo Complex (left, pink), ~119 Ma tonalites (right, purple) and adjacent metasedimentary mylonites for each pluton (both plots, gray). Individual measurements are shown with great circles (foliations) and dots (lineations). Average orientations are given by bold great circle and bold dots.

1.89, supporting igneous growth rather than metamorphic growth (e.g., Kirkland et al., 2015). The weighted mean date of rims is 118.6 ± 2.1 Ma ($n = 11$, MSWD = 3.5) and the (U-Th)/He zircon cooling date is 100.2 ± 12.9 Ma (Chapter 1). A sinistral shear zone up to ~220 m wide with a subvertical, NNE-striking foliation (002/86 E) and N-plunging lineation (001/24) is developed in Chañaral Complex metasedimentary rocks and the western margin of this pluton (Figure 2.5). The brittle eastern branch is oriented $\sim 13^\circ$ counterclockwise of the average mylonitic foliation. Strain in the quartzites and phyllites is record by bulging and subgrain rotation recrystallization of quartz grains, oblique grain shape fabrics, and asymmetric intrafolial folds (Figure 2.6). Within the tonalite, protomylonitic fabrics are defined by biotite, dynamically recrystallized quartz, and fractured feldspar porphyroclasts (average foliation 000/88 E). The highest degree of strain in the tonalite is found in a mylonitized ~1 m wide tonalite sill within the metasedimentary rocks. Strain in the ~119 Ma tonalite decreases with increasing distance from the eastern branch, grading from protomylonitic to unstrained with locally-developed magmatic fabrics defined by aligned biotite and hornblende ~50 m into the pluton. The mafic phases and plagioclase in these mylonites are

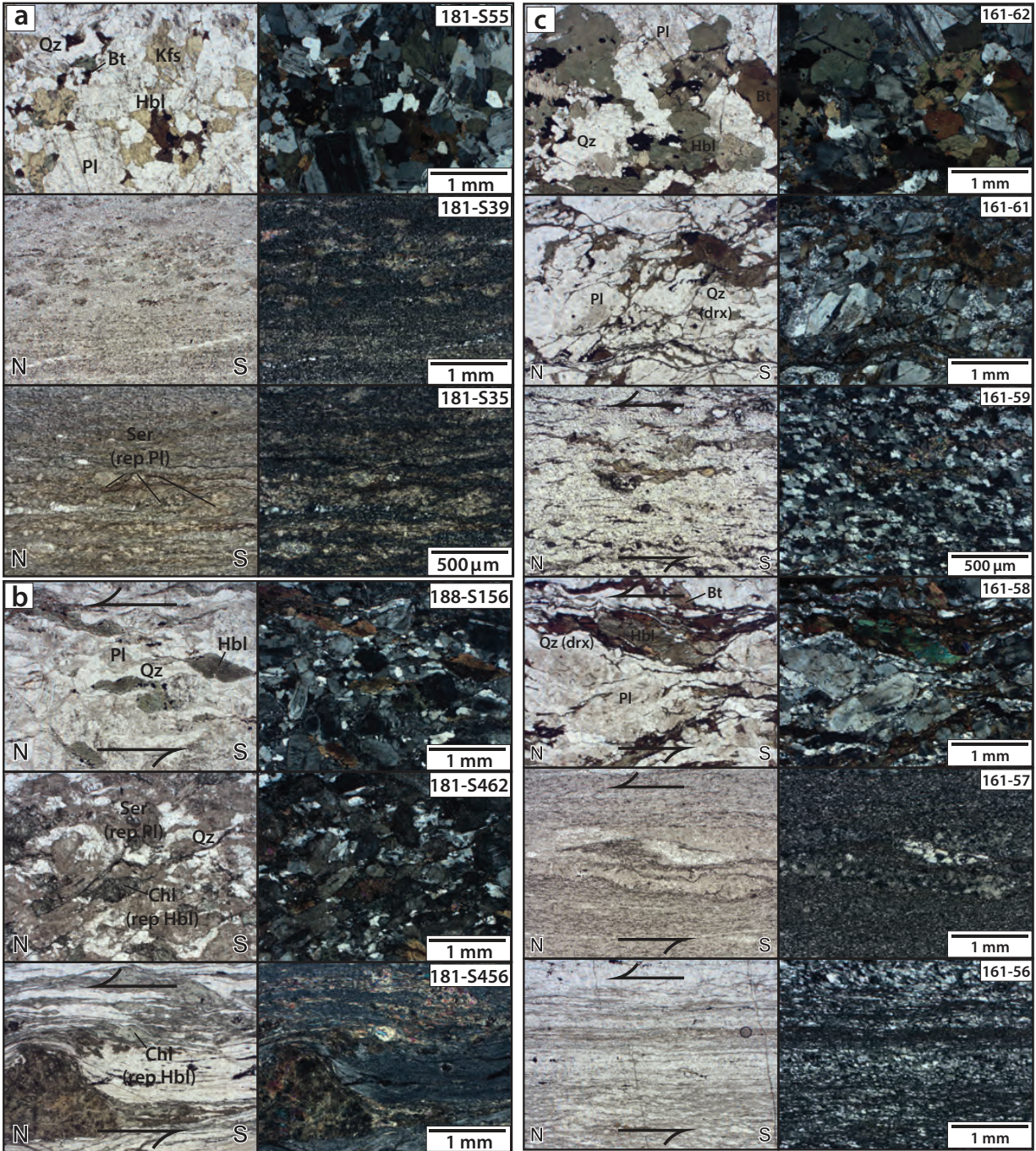


Figure 2.5: Photomicrographs in plane-polarized (left column) and cross-polarized (right column) light that correspond to the northern mylonite zone near (a) U-Pb sample 181-S55, (a) U-Pb sample 188-S156, and (c) U-Pb sample 161-62. Abbreviations are as follows: Bt = biotite; Chl = chlorite; drx = dynamically recrystallized; Hbl = hornblende; Kfs = potassium feldspar; Qz = quartz; Pl = plagioclase; rep = replaced; Ser = sericite. Samples with fabrics were cut perpendicular to foliation and parallel to lineation. Orientations and shear sense are noted where present.

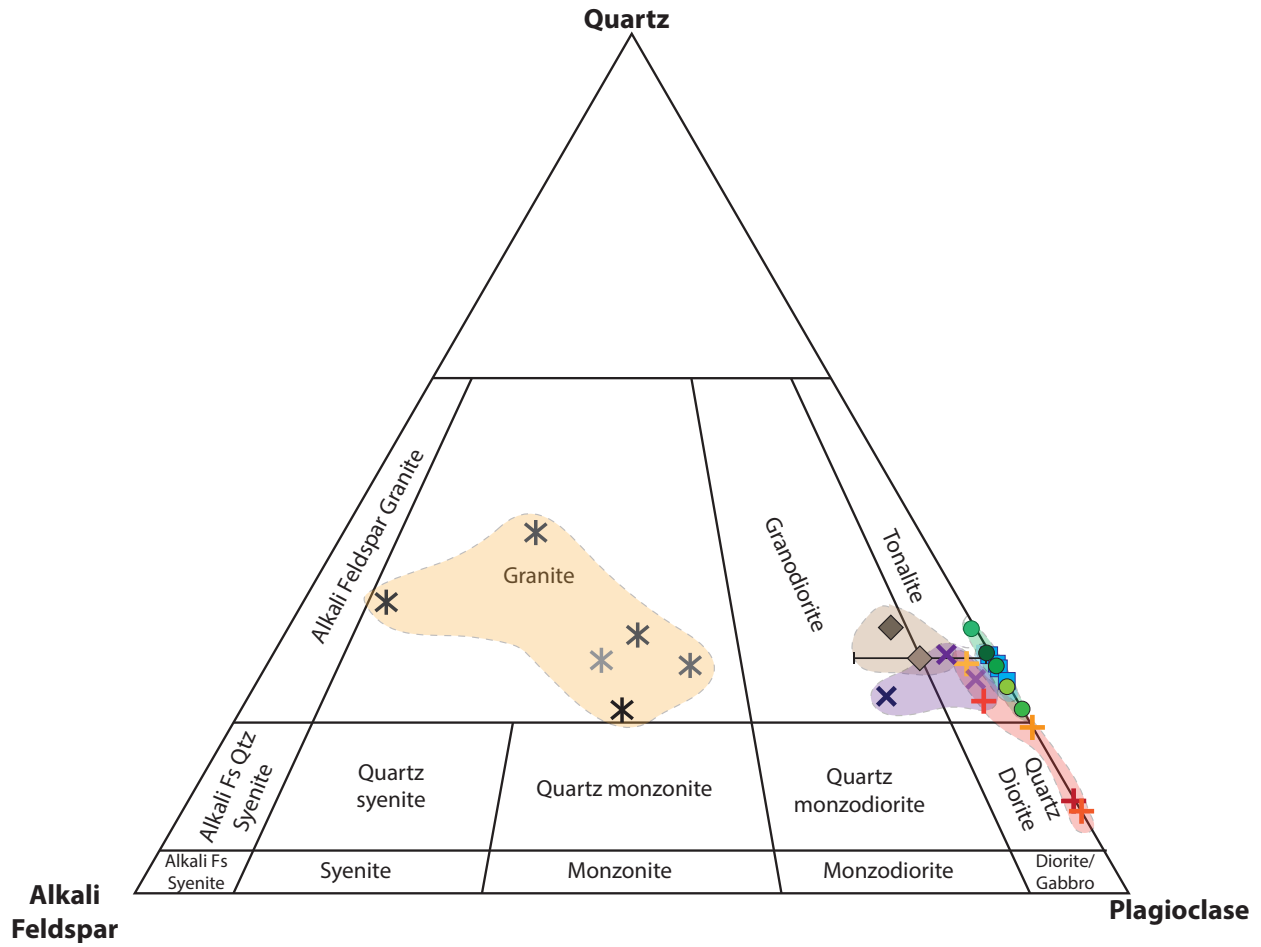


Figure 2.6: Ternary diagram showing the compositions of the Cerro Concha granodiorite (brown diamonds), northern ~132 Ma Cerro del Pingo Complex (purple x's), northern ~119 Ma tonalites (blue squares), southern ~134 Ma Cerro del Pingo Complex (red and orange crosses), southern ~119 Ma tonalites (green circles), and leucocratic intrusives (gray six-pointed stars). Compositions were determined by point counts.

fresher than those of the ~ 134 – 132 Ma pluton, both within the protomylonitic and unstrained portions of the pluton. A strain gradient is developed to the south where the eastern branch juxtaposes the Jurassic Cerro Concha granodiorite against Aeropuerto Formation, and quartzites again grade from platy mylonites to statically recrystallized but unstrained <1 km south of the ~ 119 Ma tonalite along the eastern branch.

Mylonite zone west of the eastern branch of the AFS (25.92°S and 25.99°S)

In this study we document another mylonite zone within metasedimentary rocks and synkinematic tonalitic plutons located ~ 22 km south of the previously described mylonite zone, exposed for ~ 6.3 km along strike of the western margin of the eastern branch between 25.92°S and 25.99°S (Figure 2.2, Figure 2.7). The subvertical eastern branch trends ~ 175 – 177° at this location. The pluton exposed at the northern end of this mylonite zone is a fresh hornblende biotite tonalite composed of 47–59% plagioclase, 16–27% quartz, 11–18% biotite, 6–20% hornblende, and 4–5% oxide phases and accessory minerals (Figure 2.4). As with the mesocratic tonalite to the north on the eastern side of the fault, the rock is distinctly black and white and is crosscut by sub-parallel adularia+quartz veinlets that incorporate clasts from the surrounding pluton. Similar to the northern mylonite zone, the shear zone is ~ 200 m wide and extends up to ~ 120 m into a mesocratic pluton that intrudes the metasedimentary mylonites along the western margin. Protomylonitic fabrics within the pluton are defined by the aligned long axes of hornblende, aligned biotite, and recrystallized tails of feldspar and have an average foliation orientation of $015/85$ E (Figure 2.8). Silicification of the tonalite and the metasedimentary mylonites occurs within 400 m of the eastern branch, and intensifies with proximity to the fault. Cathodoluminescence imagery of zircons shows igneous textures as well as core and rim relationships (Appendix 3.6). The weighted mean date of the cores derived from spot analyses is 131.9 ± 1.8 Ma ($n = 51$, MSWD = 6.7, sample 161-74; Figure 2.9) and the weighted mean date of rims derived from depth profiles is 119.5 ± 1.8 Ma ($n = 10$, MSWD = 2.4). Th/U values for the overgrowths are 0.75–1.29, reflecting igneous petrogenesis (e.g., Kirkland et al., 2015). The average (U-Th)/He zircon cooling date is 99.0 ± 7.3 Ma (Table 2.2). Metasedimentary rocks at this location are more arkosic than the northern re-

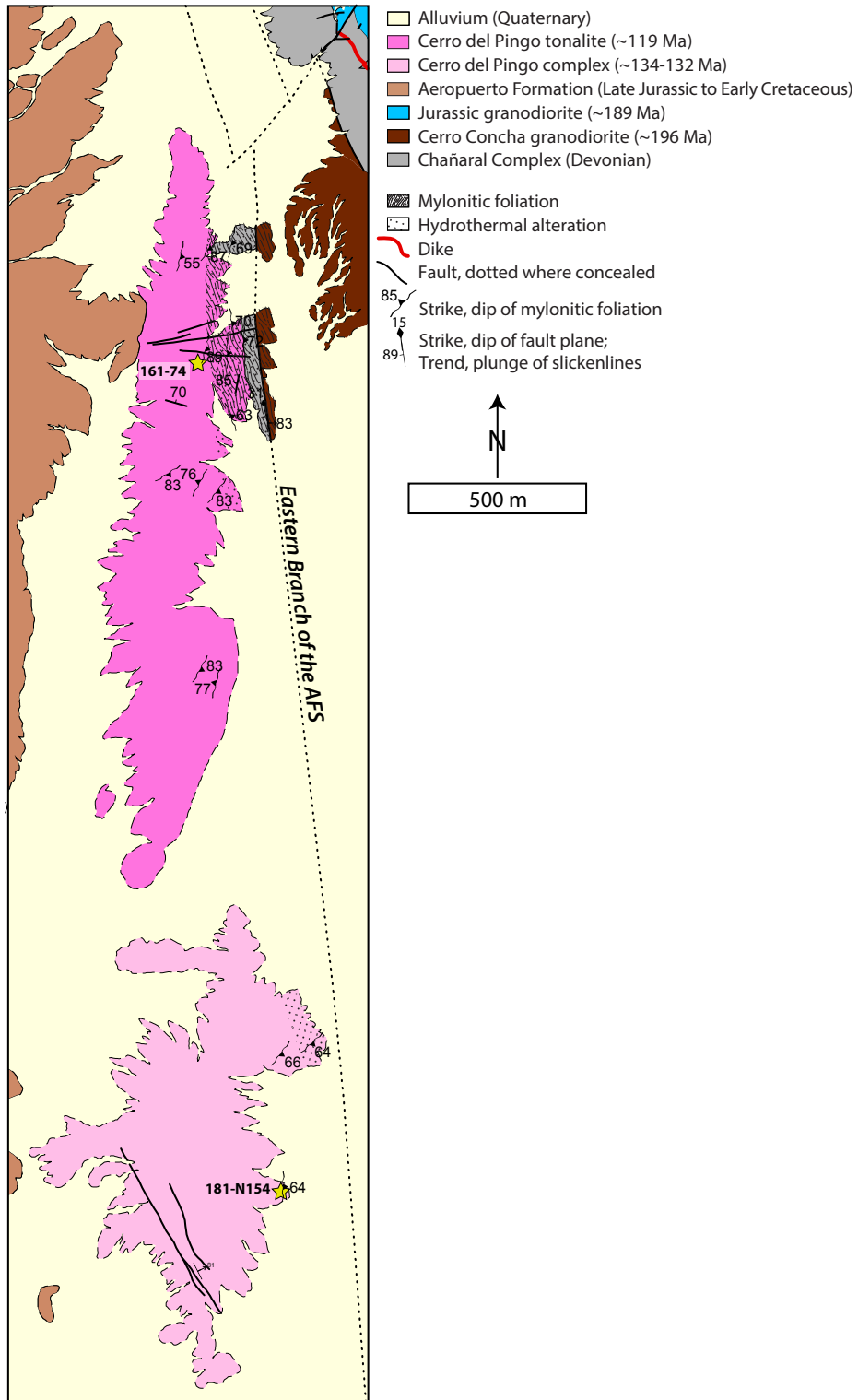


Figure 2.7: Inset map of the southern mylonite zone and Cerro del Pingo Complex west of the eastern branch of the AFS. Yellow stars show new U-Pb samples from this study.

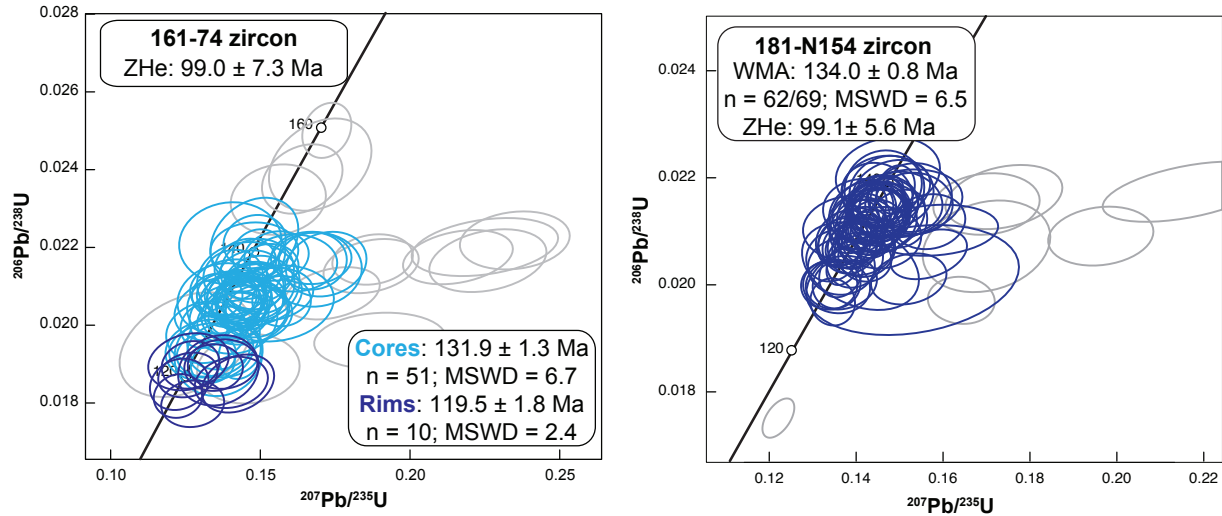


Figure 2.8: U-Pb concordia diagrams for plutons associated with the southern mylonite zone. Data have been filtered to 10% discordance and grains with >10% discordance are shown in gray. Uncertainties are reported at 2σ .

gion, and fine-grained recrystallized feldspar defines foliations in addition to recrystallized quartz. The average orientation of mylonitic foliation within the metasedimentary mylonites is 000/81 E, and lineations rake shallowly (177/14) from the south (Figure 2.8). The brittle eastern branch is oriented $\sim 10^\circ$ counterclockwise of the average mylonitic foliation, consistent with sinistral shear, and clasts of mylonitic quartzite are abundant within the cataclastic damage zone of the AFS.

Exposure of the quartzite mylonite screen and the eastern branch of the AFS is covered by alluvium to the south, and the shear zone narrows to ~ 15 m with variable degrees of protomylonitic fabric development with more localized distinct cm- to m-scale shear zones as the lithology transitions to an older mesocratic hornblende tonalite to quartz diorite with 52–74% plagioclase, 16–37% hornblende, 7–25% quartz, 1–5% oxides, titanite, and trace zircon, apatite, and other accessory minerals (Figure 2.4). The pluton, which is intruded by the ~ 119 Ma phase described above, is crosscut by adularia+quartz veinlets with selvages defined by potassium alteration of surrounding phases. Hornblende is often chloritized and individual portions of the pluton have up to 6–19% chlorite developed at the expense of hornblende. Plagioclase crystals are generally fresh, though some have deuteric alteration in cores. Extensive sericitization of plagioclase is associated with discrete zones of steep N- to NE-striking mylonitic foliation defined by recrystallized

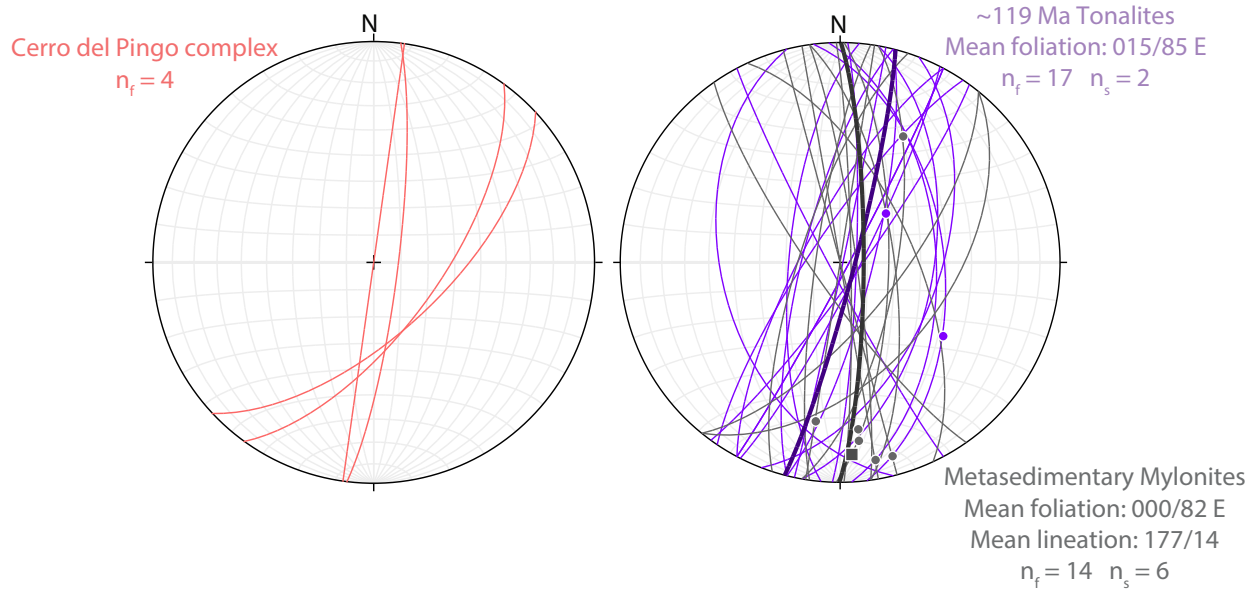


Figure 2.9: Stereograms of structural data from the ~134 Ma Cerro del Pingo Complex (left, pink), ~119 Ma tonalites (right, purple) and adjacent metasedimentary mylonites (gray). Individual measurements are shown with lines (faults, foliations) and dots (slickenlines, lineations). Average orientations are given by bold line (faults, foliations) and bold dots (slickenlines, lineations).

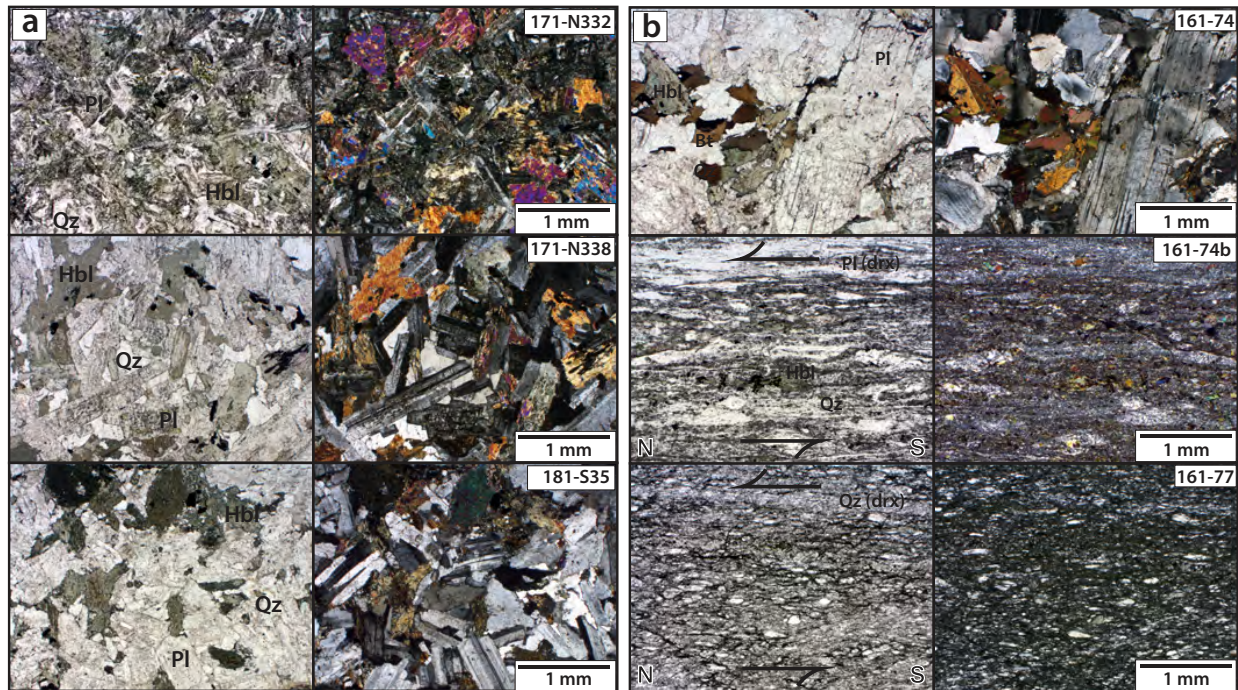


Figure 2.10: Field photos and photomicrographs in plane-polarized (left column) and cross-polarized (right column) light of the (a) ~134 Ma Cerro del Pingo Complex and (b) ~119 Ma tonalites and associated metasedimentary mylonites of the southern mylonite zone. Abbreviations are as follows: Bt = biotite; Chl = chlorite; drx = dynamically recrystallized; Hbl = hornblende; Qz = quartz; Pl = plagioclase; rep = replaced.

feldspar and fine-grained minerals and is concentrated along the eastern exposures of the pluton (Figure 2.8). No lineations were noted. We note that the eastern branch is located up 300 m away from most of this exposure under alluvial cover, and most of the exposure of the pluton retains unstrained magmatic textures with no mineral alignment. This pluton has a zircon U-Pb date of 134.0 ± 0.8 Ma (sample 181-N154, $n = 62/69$; MSWD = 6.5, Figure 2.9) and a ZHe date of 99.1 ± 1.2 Ma with a tight cluster of individual grain dates at 97.8–99.7 Ma (Table 2.2).

Non-mylonitized lithologies across the eastern branch

Our 1:25,000-scale mapping indicates that there are no other occurrences of significant AFS-related mylonite zones along the ~ 70 km length of the El Salado presented here. Pre-kinematic Jurassic plutons along the eastern branch include the ~ 196 Ma Cerro Concha granodiorite and an ~ 189 Ma Jurassic granodiorite (Figure 2.2, Chapter 1). Of these, only the Cerro Concha granodiorite occurs on both sides of a major structure – in this case, a NW-trending splay off the eastern branch, interpreted as a Riedel structure. The main eastern branch is located west of both of Cerro Concha exposures. The Cerro Concha pluton is a mesocratic hornblende biotite granodiorite composed of dominantly plagioclase and quartz with $<10\%$ potassium feldspar (Figure 2.4). Biotite is the dominant mafic phase, with common hornblende, and rare pyroxene with trace oxides, zircon, and apatite. On the western side of the NW-striking fault sinistrally separated by ~ 11 – 15 km, the Cerro Concha pluton is leucocratic due to extensive alteration. The along-strike strain gradient from high-strain mylonites in and adjacent to the Early Cretaceous Cerro del Pingo Complex to brittle fracturing and faulting in the Early Jurassic Cerro Concha granodiorite and adjacent Chañaral Complex metasedimentary rocks at the same structural level indicate the Cerro Concha intruded before the onset of AFS-related strain and was relatively cold compared to Early Cretaceous plutons during AFS deformation (Chapter 1). Their zircon U-Pb and (U-Th)/He dates also overlap within error (195.8 ± 1.0 Ma and 103.0 ± 16.0 Ma, sample 171-J250; 194.3 ± 2.2 Ma and 107.9 ± 4.8 Ma, sample 171-N235, Chapter 1). Together, these data suggest both outcrops were part of the originally continuous Cerro Concha granodiorite, and we therefore suggest that

they can be used to estimate $\sim 11\text{--}15$ km of slip across the NW-trending Riedel to the AFS since ~ 195 Ma.

At the northern end of the El Salado segment, an ~ 1.5 km-wide zone within the Jurassic Matancilla pluton (175–158 Ma; Escibano et al., 2013) and surrounding Chañaral Complex have distributed NE-striking discrete cm- to m-scale shear zones (Figure 2.2, Figure 2.11). These shear zones are protomylonitic granodiorite with dominantly sinistral shear sense indicators and marked by a "bleached" or "pinstriped" appearance due to localized hydrothermal alteration and high strain. Unstrained granodiorite separates the discrete mylonites. These shear zones are oriented at an oblique angle ($\sim 35\text{--}37^\circ$ on average) to the $175\text{--}177^\circ$ -trending AFS and do not have overprinting brittle faults, which indicates they did not form in a progressive ductile-to-brittle shearing event. Furthermore, the geometry of these shear zones is incompatible with AFS-related deformation, as the $\sim 35\text{--}37^\circ$ angle with the AFS is much greater than the angles between mylonitic foliations and the brittle fault documented along the northern and southern Cerro del Pingo mylonite zones ($\sim 13\text{--}14^\circ$ and $\sim 10^\circ$, respectively). As such, the discrete shear zones in the Matancilla plutonic complex are interpreted to predate AFS shear.

Mylonites are also not developed in the Jurassic La Negra Formation volcanics, Cretaceous Aeropuerto Formation volcanics and volcanoclastics, nor in the Devonian Chañaral Complex where it is not adjacent to synkinematic plutons. In between the two mylonite zones described above, metasedimentary rocks occur in two narrow slivers bound by fault strands between $25.82^\circ\text{S}\text{--}25.83^\circ\text{S}$ and $25.89^\circ\text{S}\text{--}25.92^\circ\text{S}$ (Figure 2.2). The northern sliver is 130–170 m wide and contains mylonitic metasedimentary rocks in contact with an altered granodiorite, interpreted here as an altered exposure of the Cerro del Pingo Complex based on its association with metasedimentary mylonites. The average orientation of the metasedimentary mylonites is $188/75$ W. The northern sliver is bound to the west by cataclastic volcanics of the Aeropuerto Formation and to the east by highly fractured but internally unstrained metasedimentary rocks and a highly altered granitoid, most likely the southern extent of the Cerro Concha granodiorite. The southern sliver is up to ~ 300 m wide and bound by the main eastern branch of the AFS to the west and a subsidiary NW-

trending splay to the east. The lithology west of the eastern AFS branch is covered by alluvium and the lithology west of the splay is a ~189 Ma altered granitoid (Figure 1.4 of Chapter 1). The metasedimentary rocks in this sliver are entirely unstrained and retained original detrital textures or are statically recrystallized. Additional reconnaissance work between the southern map boundary and 26.30° S (~33 km south of the map area) did not identify mylonites along the eastern branch, and mylonites are not represented in this area at the 1:100,000 scale (Godoy and Lara, 1998; Espinoza et al., 2014).

Finally, we note that an Early Cretaceous Las Tipias pluton located ~300–600 m east of the AFS between 25.3–25.4° S does not have an associated mylonite zone, despite its overlap in timing of emplacement with the mylonitic Cerro del Pingo Plutonic Complex (Figure 2.12). Therefore, we suggest the two occurrences of mylonite zones in synkinematic plutons and ductilely deformed metasedimentary rocks at 25.61–25.78° S and 25.92–25.98° S can be used as an offset marker along the eastern branch of the El Salado segment, provided the synkinematic plutons can be correlated.

2.4.2 Western Branch

At the northern end of the El Salado segment at the coastline, a uniquely felsic porphyritic stock with a fine-grained (1–2 mm) matrix of intergrown potassium feldspar and quartz is exposed east of the eastern branch (Figure 2.2, Figure 2.11). The character of the intrusion is variable within a single outcrop and ranges from mesocratic with ~30% 2–7 mm moderately sericitized plagioclase, ~18–20% chloritized hornblende and biotite to a purely leucocratic matrix of ~50% potassium feldspar and ~30–34% quartz with ~7–10% 2–7 mm sericitized plagioclase and <10% altered mafic phases (Figure 2.12). Potassium feldspar occasionally shows perthitic texture and often mantles sericitized plagioclase. Rarely, myrmekitic texture is found in smaller (2–3 mm) plagioclase crystals. These feldspar textures are indicative of intrusion at low pressures, likely recording shallow emplacement. Quartz is entirely unstrained in both textural varieties.

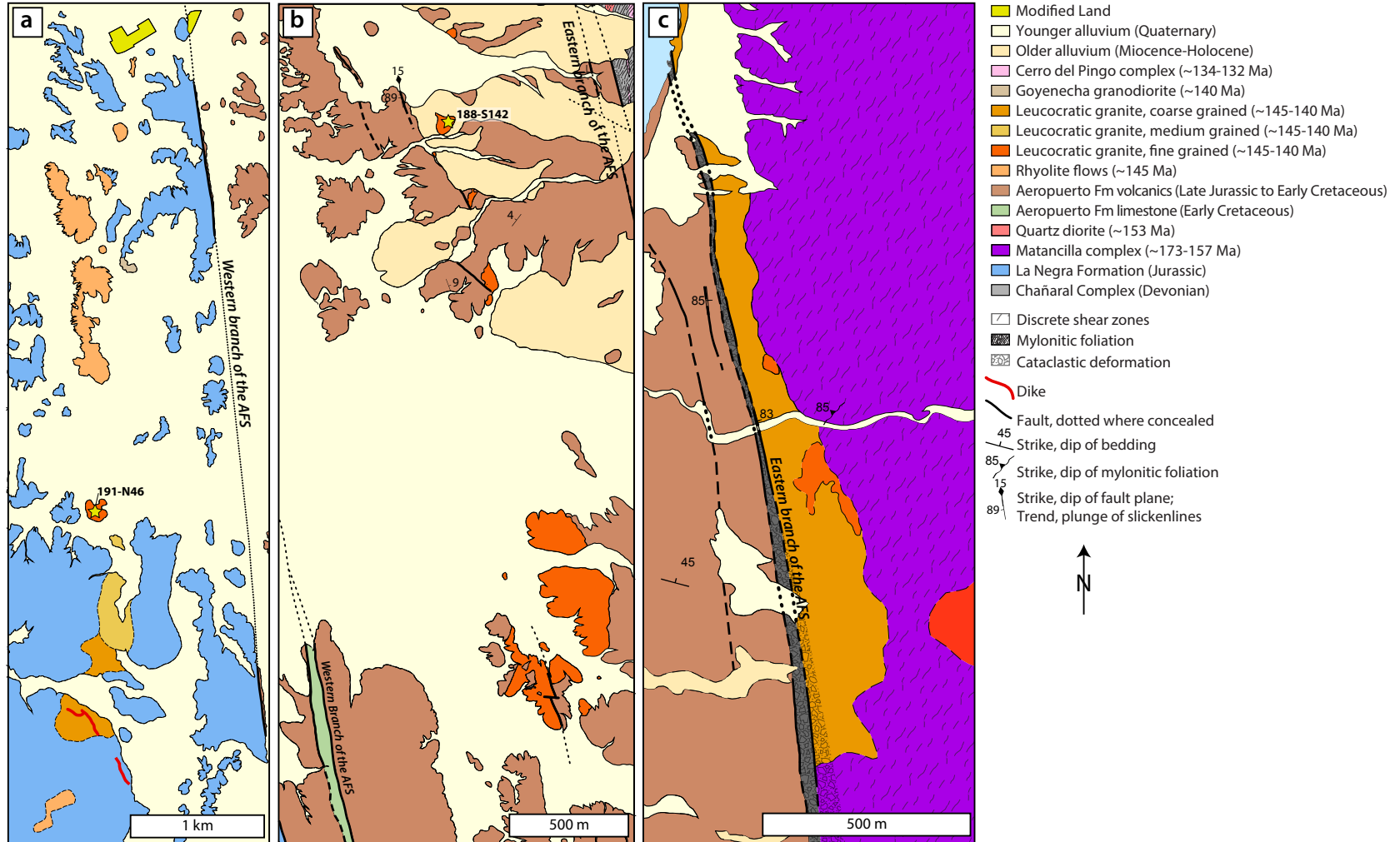


Figure 2.11: Inset map of the chain of leucocratic igneous bodies (a) west of the western branch of the AFS, (b) between the western and eastern branches, and (c) east of the eastern branch. Colors and map symbols are the same as Figure 2.2. Yellow stars show new U-Pb samples from this study.

A similar series of unstrained leucocratic granites with pervasive orange-brown oxidation intrude the Aeropuerto Formation as a NNE-SSW trending chain of low hills west of the eastern branch of the El Salado segment ~20–30 km south of the coastal exposure (Figure 2.11). Mafic phases are rare, and are completely altered to chlorite where present. Exposures located between the eastern and western branches intruding the Aeropuerto Formation between 25.65°S and 25.71°S are granites 19–33% 2–3 mm plagioclase, 29–36% 0.5–2 mm potassium feldspar and 30–43% modal quartz, with spherulitic to granophyric intergrowths and spherical bodies of intergrown quartz and epidote (Figure 2.2, Figure 2.12). Potassium feldspar mantling plagioclase is present, as are granophyric textures. Variations in these textures reflect an increase in emplacement depth moving north to south from very finely intergrown potassium feldspar and quartz that form spherulites (Figure 2.12a) to a coarser grained granophyric intergrowth with defined 0.5–1 mm quartz, plagioclase, and potassium feldspar crystals and cavities or spheres filled with quartz and epidote, interpreted as miarolitic cavities (Figure 2.12b). Granophyric textures represent segregation of the eutectic melt composition and miarolitic cavities indicate intrusion at very shallow levels (<4 km of the surface) that resulted in degassing of volatiles into bubbles and undercooling of the magma (e.g., Lowenstern et al., 1997). The zircon $^{206}\text{Pb}/^{238}\text{U}$ date on one of the felsic plutons between the eastern and western branches of the AFS is 140.9 ± 1.1 Ma (sample 188-S142, $n = 52/67$, MSWD = 8.6, Figure 2.13). Single grain dates with <10% discordance range from 133.2–151.1 Ma, with one young (120.5 Ma) and one older (161.7 Ma) grain.

Leucocratic plutons with pervasive orange oxidation also intrude the La Negra Formation in a NE-SW sub-linear belt west of the western branch of the AFS between 25.79°S and 25.95°S, 8–23 km south of the leucocratic plutons between the two branches (Figure 2.11). Texturally, these felsic bodies range from extrusive spherulitic rhyolite flows and very fine-grained quartz and feldspar mixtures (<0.2 mm) with phenocrysts of quartz and sanidine at the northern end of the belt to porphyritic intrusive bodies with coarse (2–9 mm) plagioclase and uncommon 2–4 mm clots of epidote, chlorite, and oxide phases interpreted to be replaced mafic phases at the southern end of the belt (Figure 2.12). Several outcrops have interlocking 1–2 mm quartz and potassium feldspar

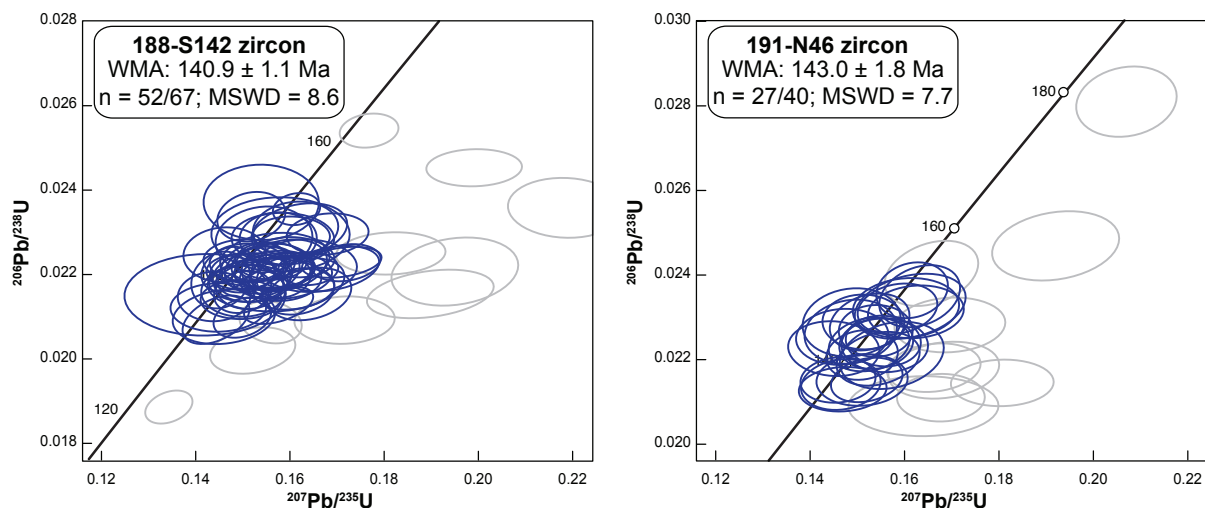


Figure 2.12: U-Pb concordia diagrams for the leucocratic plutons. Data have been filtered to 10% discordance and grains with >10% discordance are shown in gray. Uncertainties are reported at 2σ .

grains between sericitized plagioclase crystals, sometimes with granophyric texture indicative of shallow emplacement. The composition of these outcrops range from 34–35% plagioclase, 24–44% potassium feldspar, and 27–28% quartz (Figure 2.6). These plutons do not come into direct contact with the AFS and do not record ductile strain. Sample 191-N46 has single grain dates with <10% discordance ranging from 135.9–153.1 Ma that give a weighted $^{206}\text{Pb}/^{238}\text{U}$ average date of 143.0 ± 1.8 Ma ($n = 27/40$, $\text{MSWD} = 7.7$, Figure 2.13) and several older grains ranging from 178.6–659.1 Ma.

The dates of the felsic bodies on either side of the western branch are very similar to zircon U-Pb dates from Espinoza et al. (2014) on a fresh pluton that also intrudes the Aeropuerto Formation called the Goyenechea granodiorite (140.1 ± 6.0 Ma) and a spherulitic rhyolite (145 ± 2 Ma). Although the dates do not overlap within error, the high MSWD values indicate that the weighted mean dates do not necessarily represent the emplacement age of these shallow plutons and indicate there may be a high degree incorporation of either antecrysts or xenocrysts from the Aeropuerto Formation wall rock. Furthermore, the overlapping spread in single-grain dates across either side of the western branch and abnormally felsic composition compared to the other Coastal Cordillera arc-related plutons and volcanic rocks (21–43% quartz and 22–50% potassium feldspar in the

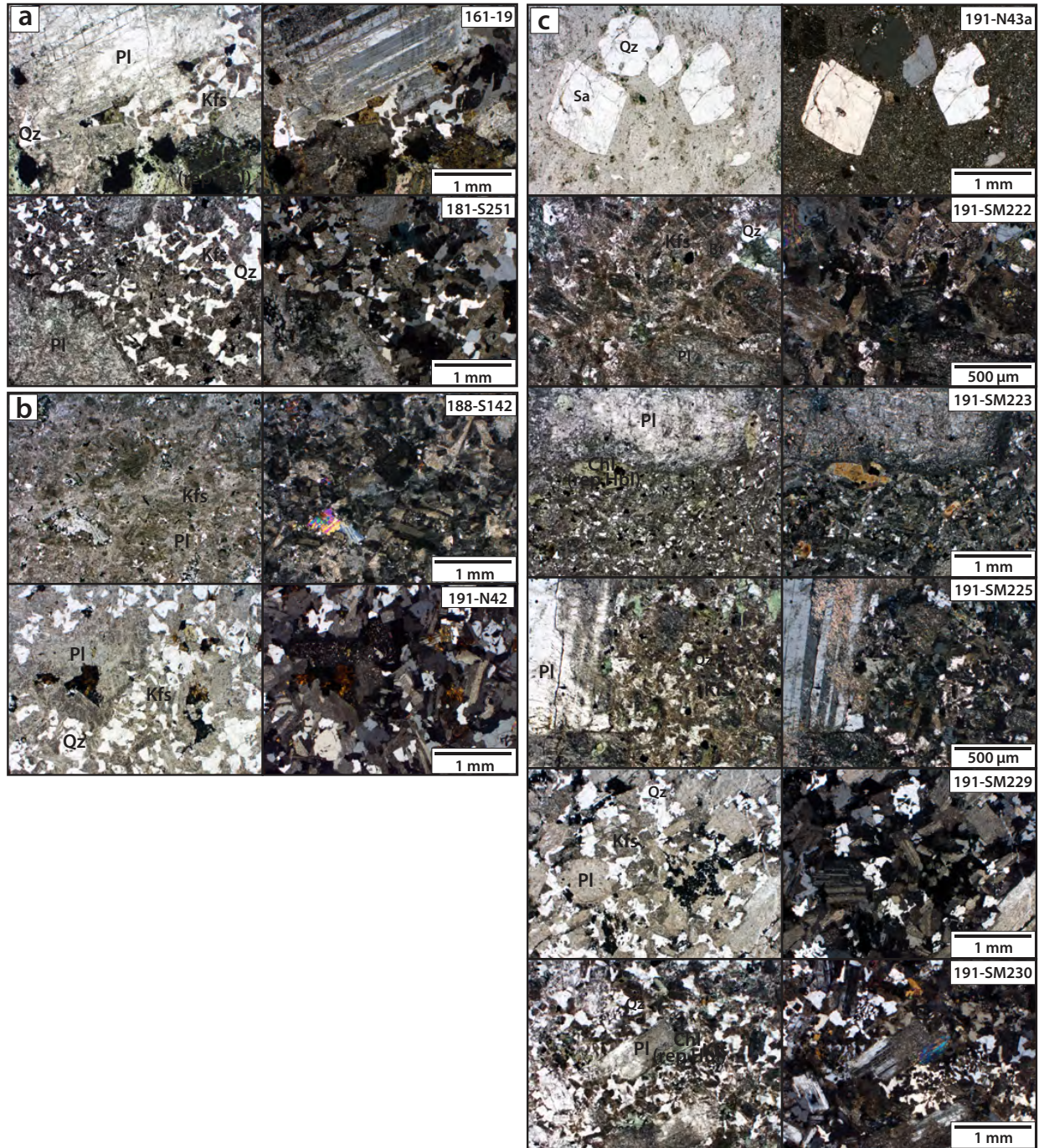


Figure 2.13: Photomicrographs in plane-polarized (left column) and cross-polarized (right column) light of the leucocratic igneous bodies (a) east of the eastern branch, (b) between the eastern and western branches, and (c) west of the western branch. Abbreviations are as follows: Bt = biotite; Chl = chlorite; Kfs = potassium feldspar; Hbl = hornblende; Qz = quartz; Pl = plagioclase; rep = replaced, Sa = sanidine.

leucocratic granite versus 15–30% quartz and 0–15% potassium feldspar in the Cerro Concha and Cerro del Pingo Complex, Figure 2.6) supports the idea that these intruded as a geochemically unique chain in an arc dominated by more mafic dioritic to tonalitic plutons. We suggest that the unique composition of the chain of felsic plutons is distinctive enough to provide constraints on the magnitude of slip across the western branch, thereby allowing us to estimate the total displacement magnitude across the entire El Salado segment of the AFS.

2.4.3 Brittle Fault Kinematics

The kinematics of AFS deformation given from the orientation of brittle fault planes, slickenlines, and slip sense indicators are dominantly sinistral strike-slip, with evidence of minor dip-slip motion. Most fault planes strike NNW and are near vertical (Figure 2.14). The orientation of eastern branch is similar to that of the mylonitic foliations: both are NNW-SSE striking and steeply dipping with slickenlines that plunge shallowly from the north. The average eastern branch brittle fault plane is oriented 13° counterclockwise from the average mylonitic foliation, which serves as an additional shear sense indicator for sinistral slip. The eastern branch has an average slickenline orientation of 354/11 on a subvertical N-trending fault (173/89 W). The average principal slip surface within the damage zone is oriented 352/88 E with slickenlines oriented 357/07, and the average fault gouge foliation is 15° clockwise of the average principal slip plane, consistent with sinistral shear (Figure 2.14). These orientations are very similar north and south of the Taltal fault system. Altogether 79% of slickenlines rake shallowly, with 50% of slickenlines raking $<45^\circ$ from the north and 29% raking $<45^\circ$ from the south). 21% of slickenlines rake steeply ($>45^\circ$). Together, these kinematics record a regime that was dominantly sinistral strike-slip motion with a minor component of dip-slip motion. When only faults with a field-determined sense of slip are included, the sinistral fault plane solution is 354/81 E and the slip vector is 355/06. When sinistral slip on unknown faults is assumed, the sinistral fault plane solution is 355/89 E with a 356/06 slip vector (Table 2.4).

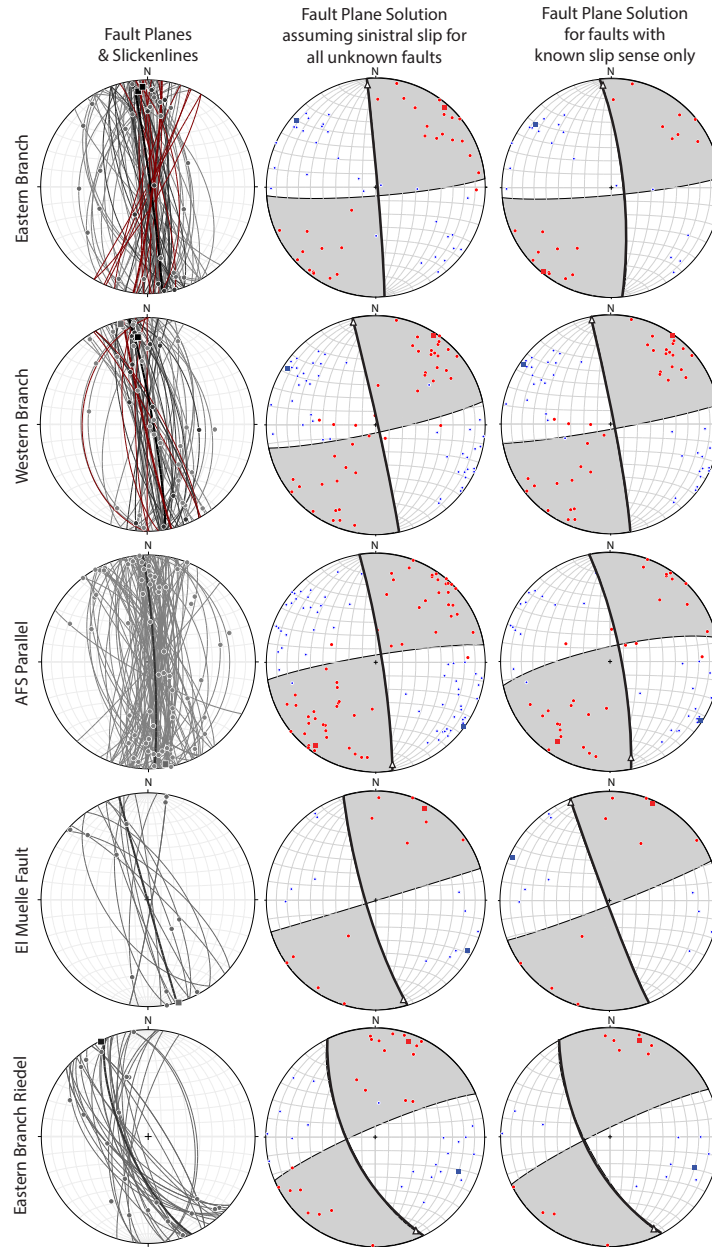


Figure 2.14: Equal-area stereograms of brittle faults along the northern El Salado segment. Top row for each fault category shows fault plane measurements (great circles) and slickenline lineation measurements (dots). Principal slip plane measurements for the eastern and western branches are shown in dark gray and measurements of foliated gouge in fault cores are shown in maroon. Note fault gouge measurements are parallel or slightly oblique clockwise to principal slip surfaces and serve as a sinistral kinematic indicator. Average measurements are shown in bold and denoted in the corresponding color to the fault type. The center column shows P-axes (blue) and T-axes (red) for fault planes with a measured slickenline lineation and an assumed sinistral slip sense, and the right column shows P- and T-axes (blue and red, respectively) for faults with a field-determined slip sense only. The solution fault plane is shown in bold and the average P- and T- axis are shown by bold squares.

The average fault plane orientation of faults in the damage zone of the western branch is 353/82 E with 345/03 slickenlines (Figure 2.14). All planes strike NNW and dip steeply east. The principal slip plane is oriented 350/85 E with 354/19 slickenlines. Altogether 72% of slickenlines rake shallowly (43% within 45° of north and 28% within 45° of south), and 28% are relatively steep (>45°). These data yield a sinistral fault plane solution of 350/88 E with a slip vector 350/04 when only faults with a field-determined sense of slip are included, and a sinistral fault plane solution of 348/89 E with a slip vector 348/06 when a sense of slip is assumed for all faults (Table 2.4).

Faults parallel to (strike $\leq 30^\circ$ from the average AFS principal slip planes) but not located within the damage zones of either major branch are also N-trending and steeply-E-dipping (average plane 357/85 E), with an average slickenline orientation of 171/04 (Figure 2.14). Similar to the major fault branches, 77% of slickenlines rake shallowly (39% rake <45° from the north and 39% rake <45° from the south) and 23% rake >45°. The sinistral fault plane solution is 349/82 E with a 167/11 slip vector for faults with a field-determined slip sense. When sinistral slip is assumed for faults with unknown slip sense, the fault plane solution is 351/85 E with a slip vector of 171/05 (Table 2.4). The El Muelle fault, which splays off the western branch and most likely continued to slip as a part of the Taltal fault system after AFS motion ceased (Mavor et al., 2020), is NW- to NNW-trending and subvertical (average plane 164/90), and is dominated by sinistral strike-slip motion with an average slickenline of 164/00 (Figure 2.14). Altogether 40% of slickenlines rake <45° from the north and 40% rake <45° from the south, and 20% rake >45°. For faults with a known slip sense in the field, the sinistral fault plane solution is 159/78 W and the slip vector is 339/03. When sinistral slip sense is assumed for unknown faults, the fault plane solution is oriented 163/83 W with a 165/07 slip vector. For all fault categories, the data consistently indicate a subhorizontal NW-SE-trending linked Bingham P-axis and subhorizontal NE-SW trending linked Bingham T-axis (Table 2.4).

We note that each of these fault populations record 20–28% steep (>45°) dip-slip slickenlines. Map patterns indicate a component of E-side-up motion on the eastern branch and a component of W-side-up motion on the W branch, creating a shallow graben between the two branches that

Table 2.4: Summary of brittle fault kinematic data. Eigenvalues are the maximum, intermediate, and minimum eigenvalues for each fault plane and slickenline dataset. P- and T-axes are linked Bingham eigenvalues.

	Eastern Branch	Western Branch	AFS Parallel	Falla El Muelle
Principal Slip Plane	352/88 E	350/85 E	-	-
Measurements	20	16	-	-
Eigenvalues	0.93, 0.05, 0.02	0.91, 0.06, 0.03	-	-
Average Slickenline	357/07	354/19	-	-
Measurements	9	15	-	-
Eigenvalues	0.64, 0.22, 0.13	0.71, 0.24, 0.05	-	-
Average Fault Plane	173/89 W	353/82 E	357/85 E	164/90
Measurements	51	39	99	15
Eigenvalues	0.81, 0.13, 0.06	0.83, 0.12, 0.05	0.85, 0.09, 0.06	0.87, 0.1, 0.03
Average Slickenline	354/11	345/03	171/04	164/00
Measurements	25	31	63	12
Eigenvalues	0.64, 0.22, 0.13	0.56, 0.35, 0.09	0.64, 0.26, 0.10	0.67, 0.22, 0.11
Average Fault Gouge	008/86 E	167/88 W	-	-
Measurements	13	6	-	-
Eigenvalues	0.92, 0.06, 0.02	0.91, 0.07, 0.01	-	-
Field-Determined Slip Sense Only				
Measurements	17	36	30	9
Fault Plane Solution	354/81 E	350/88 E	349/82 E	159/78 W
Slip Vector	355/06	350/04	167/11	339/03
P-Axis	310/10	305/04	123/02	115/11
T-Axis	219/02	035/01	213/14	023/06
All Faults Assumed Sinistral				
Measurements	30	44	57	11
Fault Plane Solution	355/89 E	348/89 E	351/85 E	163/83 W
Slip Vector	356/06	348/06	171/05	165/07
P-Axis	310/06	303/05	126/01	118/05
T-Axis	041/04	033/03	216/07	028/06

localized deposition of and preserves the Aeropuerto Formation (Figure 2.2). The Aeropuerto Formation is Late Jurassic to Early Cretaceous in age and is in part the same age at the Cerro del Pingo Complex exposed east of the eastern branch, implying a component of E-side up slip. However, kinematic data suggest mostly strike-slip motion with a component of E-side down motion on the eastern branch. It is possible that emplacement of the Cerro del Pingo Complex was initially associated with a E-side up component of shear along the eastern branch, similar to relationships documented in the Las Tazas pluton further south (Grocott and Taylor, 2002), and record of this motion has been largely overprinted by sinistral shear. The magnitude of dip-slip motion is <2 km based on the shallow rake of slickenlines plunging both north and south across the main branches of the El Salado segment, and ZHe dates do not appear to vary across the eastern strand of the AFS. The similarity in the range of single-aliquot ZHe dates in lithologies with different U-Pb crystallization dates on either side of the fault points to a shared low-temperature cooling history. Taken together, these results show the Earth's surface represents a plane that is largely perpendicular to the motion of the fault, and any correlation of horizontally separated markers represents the majority of slip magnitude.

2.5 Discussion

2.5.1 Correlation of Synkinematic Plutons and Mylonite Zones

Our data suggest six localities can be correlated across the eastern branch of the AFS to represent three distinct plutons: the unstrained ~195 Ma Cerro Concha granodiorite, strained ~134–132 Ma Cerro del Pingo Complex, and strained ~119 Ma Cerro del Pingo tonalite (Figure 2.15). The two exposures of the older phase of the Cerro del Pingo Complex are both fresh, medium-grained hornblende biotite granodiorite to biotite hornblende tonalite and quartz diorite crosscut by adularia+quartz veinlets (Figure 2.4). We note the degree of silicification, adularia+quartz veining, and chloritization of mafic phases is significantly more pronounced in the southern mylonite zone on the western side of the eastern branch. This may be due to fluid exsolution in a slightly higher structural level in the pluton, which would be consistent with a component of E-side-up motion across

the eastern branch. Their zircon U-Pb dates (132.6 ± 0.9 Ma and 132.3 ± 1.3 Ma, Chapter 1; 134.0 ± 0.8 Ma, this work, Figure 2.9) overlap within error, and both feature variable development of mylonitic fabrics that are concordant with AFS-related brittle fault kinematics, recording synkinematic intrusion during AFS shear. Contact metamorphism is present in the Chañaral Complex metasedimentary rocks that surround the Cerro del Pingo Complex, indicating shallow or epizonal emplacement. Sinistral separation of the older phase of the Cerro del Pingo Complex across the eastern branch is 32–38 km (Figure 2.15).

The younger hornblende biotite tonalite described above and the ~ 119 Ma hornblende biotite tonalite described in Chapter 1 also have several strong similarities. The two tonalites have zircon U-Pb dates that overlap within error (118.6 ± 2.1 Ma, sample 161-62 of Chapter 1, and 119.5 ± 1.8 Ma, sample 161-74, this work, Figure 2.9). Both exposures also have a similar distribution of Early Cretaceous zircons with cores ranging from ~ 124 – 137 Ma (sample 161-62) and ~ 123 – 141 Ma (161-74), and magmatic overgrowths ranging from ~ 115 – 123 Ma (sample 161-62) and ~ 115 – 122 Ma (sample 161-74). Results of geochemical analyses show the strong similarities between the ~ 119 Ma tonalites, with whole-rock geochemical analyses that match to within 1.7 wt% for all major oxides (Table 2.3), and zircon (U-Th)/He cooling dates that overlap within error (Table 2.2). The development of mylonitic fabrics in both outcrops further indicates the pluton intruded during active shear along the AFS. Therefore, we suggest that these tonalite exposures originated as one pluton emplaced ~ 119 Ma as a younger phase of the Cerro del Pingo Plutonic Complex, and that the mylonite zones developed in both the ~ 134 – 132 Ma and ~ 119 Ma phases of the Cerro del Pingo Complex provide information on the magnitude of displacement during Early Cretaceous ductile shear and brittle slip. The ~ 119 Ma tonalites are sinistrally separated by 22–24 km across the eastern branch (Figure 2.15).

2.5.2 Displacement Magnitude

Based on the correlation of plutons and the kinematic compatibility of both the mylonitic fabrics and brittle faults, we present a new estimate of the magnitude of slip along the El Salado seg-

ment of the AFS. Across the eastern branch, the synkinematic ~ 119 Ma Cerro del Pingo tonalites are separated by 22–24 km along the eastern branch, and the synkinematic ~ 134 – 132 Ma Cerro del Pingo Complex are separated by 32–38 km (Figure 2.15). The ~ 119 Ma tonalites occur between exposures of the older Cerro del Pingo Complex, and coupled with the development of shear zones in both phases of this Early Cretaceous plutonic complex, indicate that ~ 8 – 16 km of sinistral shear occurred prior to ~ 119 Ma. We further note that the two exposures of the prekinematic ~ 195 Ma Cerro Concha plutons are sinistrally separated by 11–15 km of slip along a subsidiary, NW-trending splay of the eastern branch. The higher degree of alteration in the exposure of the Cerro Concha on the western side of the splay may represent a higher structural level of the pluton, indicating a degree of E-side-up motion on the fault. The lower magnitude of sinistral separation combined with the lack of mylonitic shear zones developed in the Cerro Concha granodiorite further suggests the eastern branch does not record a prior Jurassic history of slip, as we would expect the sinistral separation of Jurassic plutons to exceed the sinistral separation of Early Cretaceous plutons if there had been a protracted pre-Cretaceous slip history.

The leucocratic granites exposed near the coastline east of the eastern branch are sinistrally separated by ~ 20 – 30 km from a set of leucocratic granites intruded into the Aeropuerto Formation with very similar textures on the western margin of the eastern branch, and that another set of leucocratic granites are exposed west of the western branch of the AFS (Figure 2.11). These granites are anomalously felsic for the Coastal Cordillera, and have a very distinct mineralogy compared to both the Jurassic granodiorites and the Early Cretaceous diorites and tonalites (Figure 2.4). Therefore, we propose this belt of felsic intrusions can be used to constrain the approximate displacement magnitude across the western branch of the El Salado segment. Determining the displacement magnitude is complicated by the uncertainty in the original geometry of emplacement of these felsic bodies. Exposures across the western branch both include fine-grained rhyolite and hypabyssal porphyritic intrusions with miarolitic cavities and granophyric textures. The presence of miarolitic cavities and spherical bodies filled with fine-grained epidote within the felsic pluton between the two major fault branches near 25.70°S indicate shallow-level (<4 km) emplacement

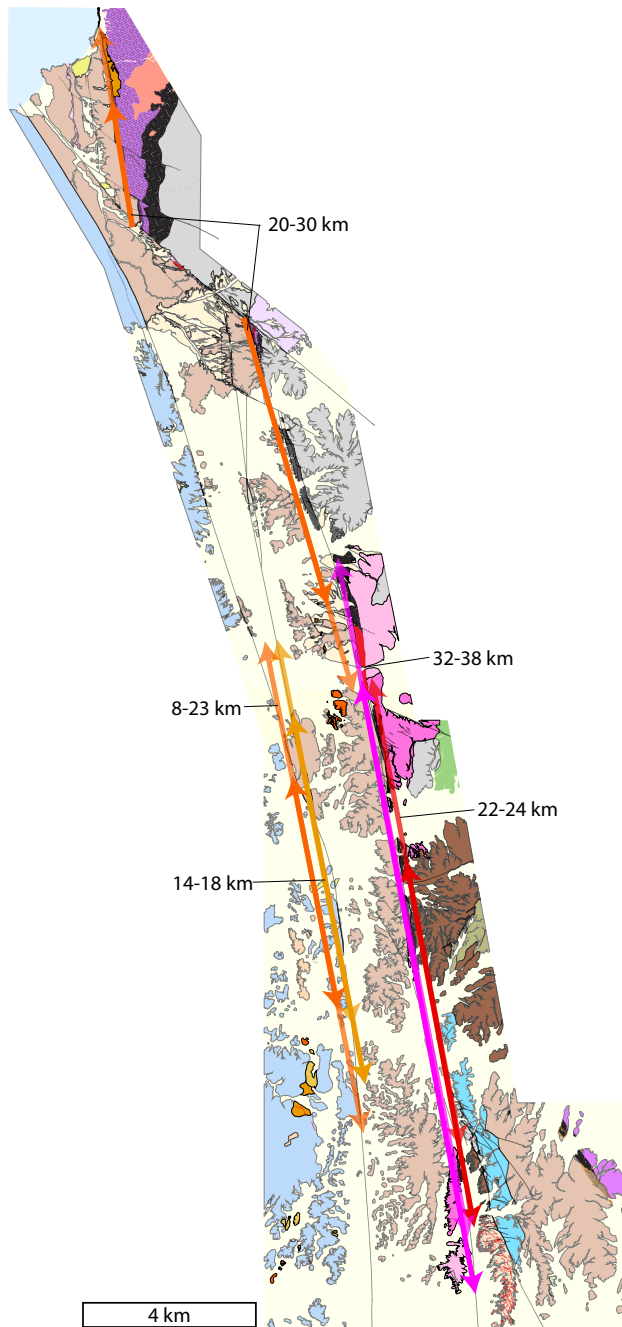


Figure 2.15: Correlation of offset markers along the AFS. Pink shows the 32–38 km sinistral separation of the ~134–132 Ma Cerro del Pingo Complex, red shows the 22–24 km sinistral separation of the ~119 Ma tonalites, and orange shows 20–30 km sinistral separation across the eastern branch and 8–23 km sinistral separation across the western branch for the leucocratic plutons. Inset arrow shows the 14–18 km of sinistral separation across the western branch when textural domains of the leucocratic plutons are correlated. Units are as shown in Figure 2. Note units not correlated across the AFS are shown at 50% opacity.

that allowed for the exsolution of fluids into bubbles which then crystallized into the fine-grained epidote spheres preserved in the intrusion (Lowenstern et al., 1997). Epidote is not present within the intrusion outside of these spheres. Textures of the leucocratic granites intruding the La Negra Formation west of the AFS include fine-grained mixtures of quartz and potassium feldspar with quartz and sanidine phenocrysts to porphyritic intrusions with 2–9 mm sericitized plagioclase crystals surrounded by interlocking grains of 1–2 mm potassium feldspar and quartz with occasional granophyric texture indicative of shallow emplacement. Coupled with the similar mineralogical composition, these textural observations suggest that leucocratic granites intruded as a continuous chain of epizonal and hypabyssal plutons along a 190–195° trend. Restoring the separation of this trend results in a minimum sinistral separation of ~8 km and maximum sinistral separation of ~23 km across the western branch, whereas the sinistral separation based on correlation of similar textural domains is ~14–18 km (Figure 2.15). As both sets of leucocratic lithologies show a N-S progression from fine-grained intergrowths of quartz and potassium feldspar with ~2–3 mm crystals of quartz and sanidine to coarser porphyritic plagioclase surrounded by interlocking 1–2 mm quartz and feldspar with granophyric textures, we prefer to correlate textural domains as a horizontal separation marker across both branches of the AFS and therefore report ~20–30 km of sinistral slip along the eastern branch and ~14–18 km of sinistral slip along the western branch, for a total displacement magnitude of ~34–48 km.

We note that the displacement magnitude estimate across the eastern branch based on these felsic plutons is less than that estimated from the displacement of the ~134–132 Ma Cerro del Pingo Complex, which may suggest slip decreases at the north end of the El Salado segment. The displacement estimate determined from the leucocratic plutons is not as clear as the correlation of the Cerro del Pingo Complex and associated metasedimentary mylonites partially due to less clear correlation relationships, the occurrence of the leucocratic plutons in a chain rather than a single intrusion, and the lack of direct interaction between the leucocratic plutons and the eastern branch. Therefore, we prefer the displacement magnitude estimate determined from the offset of the Cerro del Pingo Complex (~32–38 km) for the eastern branch. Altogether, our data provides

a displacement magnitude of $\sim 50 \pm 6$ km for slip on both branches of the El Salado segment between ~ 133 – 110 Ma (Figure 2.15, Figure 2.16). The lack of mylonitic deformation along the eastern branch in the leucocratic granite near the coast indicates the pluton had cooled below the brittle-plastic transition prior to the initiation of AFS shear, and therefore constrains the onset of slip to <140 – 145 Ma. Ruthven et al. (2020) document the initiation of AFS slip along the major branch of the Paposo segment at ~ 139 Ma. The timing presented here for the northern El Salado segment agrees with previous work by Taylor et al. (1998) and Grocott and Taylor (2002) that documents the initiation of the eastern branch of the AFS corresponded with the emplacement of Las Tazas pluton along the central El Salado segment at ~ 132 Ma. We did not identify any other offset markers along the ~ 70 km mapped length of the northern El Salado segment. The displacement magnitudes across the western and eastern branches of the El Salado segment are compatible with the Hervé (1987b) estimate of ~ 34 km of slip on the Izcuña fault, a parallel strand of the main Paposo fault along the Paposo segment of the AFS based on the identification of an offset granodioritic pluton and post-mylonitic granite.

2.5.3 Timing & Rate of Slip

Field relationships provide key insights into the timing of AFS slip. Jurassic plutons along the El Salado segment mapped here do not show evidence for ductile deformation and are prekinematic with respect to AFS sinistral shear (Chapter 1). The Cerro Concha granodiorite is sinistrally separated by 11–15 km along the major NW-trending splay of the eastern branch, consistent with 32–38 km of total slip across the entire eastern branch. The ~ 140 – 145 leucocratic granites lack mylonitic fabrics and are also prekinematic, supporting an initiation of AFS deformation in the Early Cretaceous.

Mylonitic tonalites bracket the onset of ductile deformation along the El Salado segment. The oldest pluton to record ductile deformation in the Taltal area is the ~ 134 – 132 Ma Cerro del Pingo Plutonic Complex. Metasedimentary rocks that are spatially associated with this phase of the Cerro del Pingo Complex have undergone contact metamorphism but are undeformed where they are not

adjacent to the AFS, and record increasing ductile strain with increasing proximity to the eastern branch of the AFS. Strain in the metasedimentary rocks is concentrated in phyllitic layers along the margins of the Cerro del Pingo Complex, and both phyllitic layers and quartz-rich, mica-poor beds are penetratively strained near the center of the Cerro del Pingo Complex. This spatial relationship between mylonites and the Cerro del Pingo Complex indicates ductile deformation and sinistral motion along the AFS had initiated by $\sim 134\text{--}132$ Ma.

Intrusion of the ~ 119 Ma tonalite between the exposures of the $\sim 134\text{--}132$ Ma plutons and the development of high-strain mylonite zones within the tonalites indicates the heat from sustained intrusions of the Cerro del Pingo Complex elevated the geothermal gradient high enough to allow for ductile deformation. The metasedimentary rocks spatially associated with both the ~ 119 Ma tonalite and AFS are highly strained in both phyllitic and quartz-rich layers, with both lithologies forming ultramylonites, indicating temperatures must have been in excess of the quartz brittle-plastic transition for strike-slip regimes ($\sim 280\text{--}310^\circ\text{C}$; Stöckhert et al., 1999; Stipp et al., 2002). Rapid cooling of the Cerro del Pingo Complex east of the eastern branch through $310\text{--}345^\circ\text{C}$ is recorded by $\sim 130\text{--}129$ Ma biotite $^{40}\text{Ar}/^{39}\text{Ar}$ dates (Espinoza et al., 2014) indicating elevated temperatures that produced ductile deformation are directly tied to pluton emplacement and the duration of mylonitic deformation along the eastern branch occurred over a relatively short time interval ($\sim 3\text{--}4$ Myr). If the mapped $\sim 8\text{--}14$ km of sinistral separation determined from restoring the northern and southern contacts of the $\sim 134\text{--}132$ Ma plutons and ~ 119 Ma tonalite occurred at a constant rate of $\sim 0.6\text{--}1$ km/Myr, then $\sim 3\text{--}4$ Myr of mylonitic shearing would produce $1.8\text{--}4.0$ km of sinistral displacement and the remaining $\sim 4\text{--}12$ km of separation would have occurred in the brittle regime. A separate, time-independent estimate of displacement accommodated by mylonitic shearing overlaps with the estimate derived from cooling dates: assuming simple shear across the $\sim 500\text{--}800$ m wide shear zone constrained by our mapping (Figure 2.3, Figure 2.7), the angle between the average mylonitic foliation and the average orientation of the brittle eastern branch ($\sim 10\text{--}14^\circ$, Figure 2.4, Figure 2.9) records the average shear strain ($\gamma = 3.8\text{--}5.5$; e.g., Ramsay, 1980). This shear strain corresponds to $\sim 1.9\text{--}4.4$ km of sinistral displacement across the

500–800 m-wide zone in the ductile regime, leaving 3.6–12.1 km of displacement in the brittle regime. A component of pure shear across the mylonite zone would reduce the magnitude of sinistral displacement accommodated by ductile shearing. The presence of mylonites and a brittle fault core associated with the ~ 119 Ma tonalites indicate a second punctuated period of mylonitic deformation that transitioned from ductile shear to brittle slip as the plutons cooled. Cooling through 180°C in the both Cerro Concha granodiorite and the two phases of the Cerro del Pingo Complex occurred at 108–99 Ma (Chapter 1; this work), indicating the entire duration of ductile and brittle AFS slip at the exposed structural levels occurred at temperatures $>180^\circ\text{C}$.

Post-kinematic dikes constrain the latest stages of slip along the brittle AFS. The end of AFS slip is recorded by a 10-m-wide andesitic dike that clearly cuts across most strands of the main eastern branch of the AFS and is sinistrally offset ~ 148 m along a fault parallel to the eastern AFS branch (Chapter 1; Mavor et al., 2020). Interpretation of the age of the latest-kinematic dike ($\sim 109.9 \pm 4.0$ Ma, Chapter 1) is complicated by low zircon yield and a significant spread in single-grain dates, but can be used to document the ending stages of AFS slip at 114–105 Ma. This timing is corroborated by a dacitic dike located $\sim 25.5^\circ\text{S}$ that cuts cataclasite of the AFS and has a zircon (U-Th)/He cooling date of ~ 107 Ma (Mavor et al., 2020), further supporting brittle slip and the development of AFS-related cataclasite had ceased by the end of the Early Cretaceous. Both the ~ 110 Ma andesitic and ~ 107 Ma dacitic dikes and the AFS are cut by NW-striking sinistral faults parallel to the younger Taltal fault system (Mavor et al., 2020). Based on the spatial offsets discussed above, we can couple these timing estimates with displacement magnitudes to calculate slip rates along the El Salado segment. We suggest that the entire ~ 46 – 56 km of slip along the El Salado segment occurred between ~ 133 – 110 Ma, resulting in a time-averaged slip rate of ~ 2.0 – 2.5 km/Myr across the entire northern El Salado segment. The slip rates for each branch are ~ 1.4 – 1.7 km/Myr for ~ 32 – 38 km of displacement along the eastern branch and ~ 0.6 – 0.8 km/Myr for ~ 14 – 18 km of displacement along the western branch.

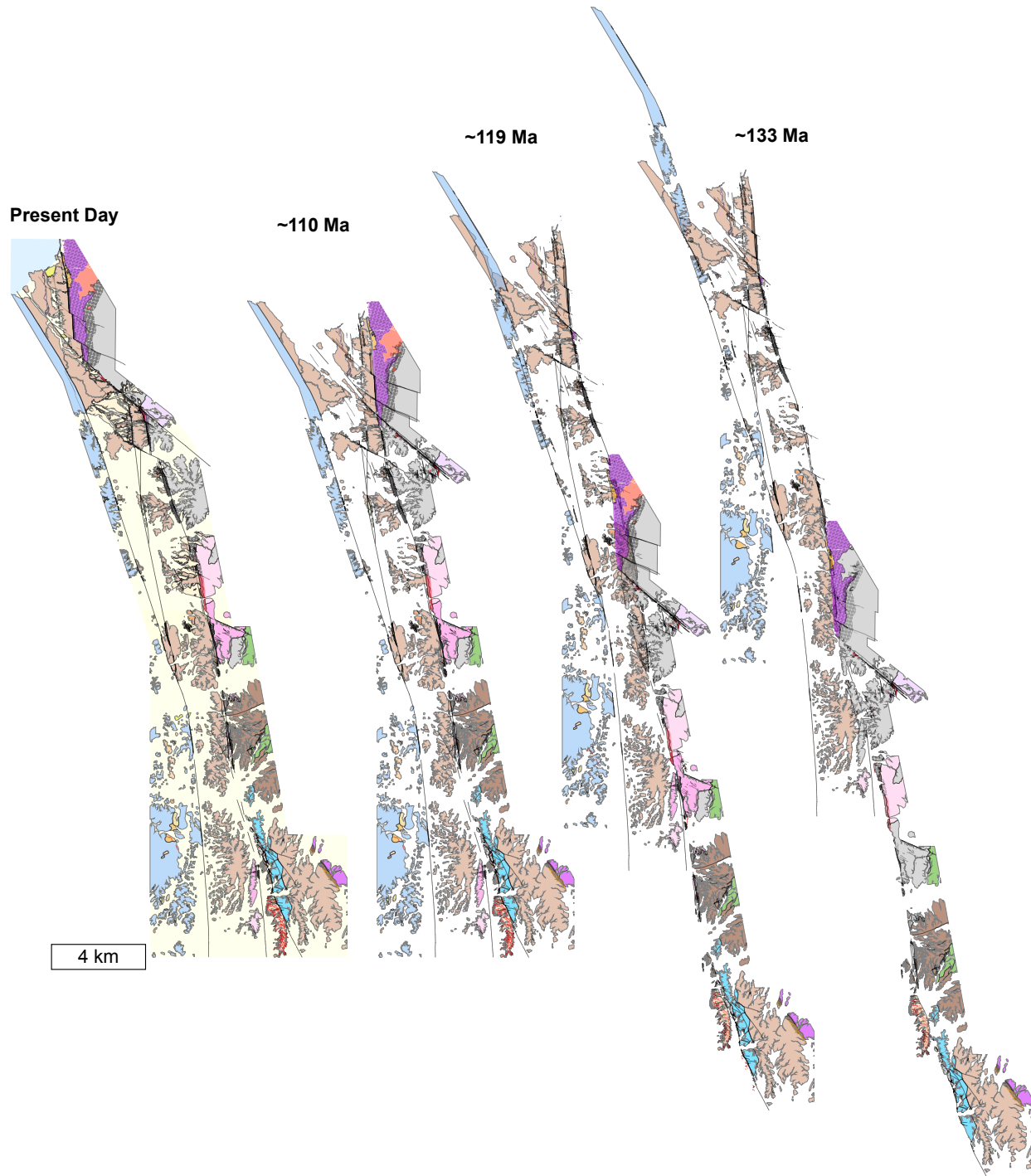


Figure 2.16: Proposed slip history of the El Salado segment from present day (far left) to ~133 Ma (far right) with intermediate steps for restoration of slip along the Taltal fault system (see Mavor et al., 2020) and intrusion of the ~119 Ma tonalites. See Plate 2 for a 1:100,000-scale version.

2.5.4 Fault Scaling Relationships & Comparison to other Fault Systems

Typical fault displacement:length scaling relationships predict a displacement magnitude will be $\leq 10\%$ of the fault length with a d_{max}/L of ~ 0.4 for strike-slip faults (Kim and Sanderson, 2005). Recent work by Stanton-Yonge et al. (2020) on subsidiary NW-striking second- and higher-order faults of the Caleta Coloso Duplex along the Paposo segment demonstrated a self-similar displacement:length scaling relationship over five orders of magnitude described by the equation $d_{max} = 0.0337L^{1.02}$, where d_{max} is the maximum displacement and L is the total fault length, for faults with 0.001–100 m of displacement. According to these relationships, the expected displacement magnitudes along the $\sim 1,000$ -km-long AFS as a whole is ~ 39 – 47 km and the ~ 480 -km-long El Salado segment is 18–22 km. Our results documenting $\sim 50 \pm 6$ km of slip across the El Salado segment are comparable to the magnitude of displacement predicted by displacement:length relationship for the entire AFS at a d_{max}/L of 0.05 and exceeds the expected displacement:length ratio for the El Salado segment ($d_{max}/L = 0.10$ from our data versus a $d_{max}/L = 0.4$; Kim and Sanderson, 2005). The average d_{max}/L for individual segments of strike-slip faults is generally larger than d_{max}/L for the fault zone as a whole, and is typically larger than the d_{max}/L for dip-slip faults due to the parallelism of measured length and slip direction (Peacock and Sanderson, 1996). This relationship is clearly seen along the AFS. Our documented displacement magnitudes of ~ 32 – 38 km (maximum $d_{max}/L = 0.20$) along the eastern branch and ~ 14 – 18 km (maximum $d_{max}/L = 0.12$) along the western branch significantly exceed the estimates for individual strike-slip faults ($d_{max}/L = 0.04$). These results may suggest slip was more effectively localized along the major branches of the AFS compared to the higher-order faults documented by Stanton-Yonge et al. (2020). We note that these d_{max}/L values are likely overestimated, as the true lengths of the fault segments are incompletely known given that the north end goes offshore and the southern ends are not precisely located. Furthermore, it is unlikely displacement along the northern end of the El Salado segment decreases to zero before it intersects or interacts with the southern Paposo segment, which also goes offshore. However, in order to achieve a d_{max}/L value of 0.04 as predicted by the Kim and Sanderson (2005) scaling relationship with our documented displacement magnitudes, the western

branch would have to be $\sim 350\text{--}450$ km long and the eastern branch would have to be $\sim 800\text{--}950$ km long. As no individual fault along the El Salado or Paposo segment reaches that length and neither our mapping nor previous 1:100,000 scale mapping document an additional major branch of the AFS throughout this region, an alternative explanation is necessary.

Ratios of d_{max}/L are also often high for interacting segments and linked faults (Kim and Sanderson, 2005). The fault segments that evolve without obvious connection—termed soft linkage by Peacock and Sanderson (1996)—may build up displacement with restricted propagation through the interaction with adjacent faults, producing higher d_{max}/L ratios (e.g., Willemsse, 1997), while hard linkages produce a drop in d_{max}/L as the fault length abruptly increases while displacement remains the same. A transition from soft to hard linkage is expected for mature fault systems (Peacock and Sanderson, 1996). An example of a strike-slip soft-linked fault system is the 80-km-long Dasht-e Bayaz fault of Iran, which is composed of several interacting strands (Fossen and Hesthammer, 1997). The highly segmented nature of the El Salado segment with multiple fault branches each individually comprised of more than one fault strand suggests it is a soft-linked system, as opposed to more hard-linked strike-slip duplexes developed along the northern Paposo segment (e.g., Cembrano et al., 2005; Veloso et al., 2015). In some areas, the El Salado segment developed hard linkages between individual fault strands, such as the NW-striking fault that hosts the Mantoverde iron oxide-copper-gold deposit (Vila et al., 1996). A linkage between the southern Paposo and northern El Salado segments is possible, as is a linkage between the Paposo and Salar de Carmen segments. Soft linkage of El Salado fault branches is a possible result of fault segment nucleation along the margins of Early Cretaceous plutons due to thermal weakening of the crust and subsequent propagation out into cooler country rocks (Chapter 1), where the individual branches may begin to interact and limit continued fault tip propagation while still accommodating the displacement magnitude expected of an $\sim 1,000$ km long system.

An alternative explanation for the relatively low displacement magnitude and high d_{max}/L values along the El Salado segment is a low slip rate (e.g., Kim and Sanderson, 2004). Slip rates of $\sim 2.0\text{--}2.5$ km/Myr for the El Salado segment are low compared to modern intra-arc systems: the $\sim 1,200$

km Liquiñe-Ofqui fault of southern Chile has modern slip rates of 6.5 mm/yr (Wang et al., 2007), the ~1,650 km long Sumatran fault has slip rates ~15–16 mm/yr (Bradley et al., 2017), the ~300 km Median Tectonic Line has strike-slip rates of 0.8–9.1 mm/yr, depending on the location along the fault system (Tsutsumi and Okada, 1996; Goto, 2018), and the ~1,250 km Philippine fault has strike-slip rates ranging from 7.7–31.4 mm/yr on individual fault branches (Hsu et al., 2016). The Liquiñe-Ofqui and Sumatran faults are mature, hard-linked systems with major throughgoing faults mapped along the entire length of the arc, whereas the Philippine fault is a complex system comprised of several interacting, hard-linked strands with differing slip rates. The 6.5 mm/yr of motion along Liquiñe-Ofqui fault system accommodates 30% of the 23–28 mm/yr margin-parallel motion across the southern Peru-Chile trench at an angle of ~20° from normal to the plate boundary (DeMets et al., 1994; Angermann et al., 1999; Kendrick et al., 2003; Wang et al., 2007). At a rate of 15–16 mm/yr, the Sumatran fault accommodates 60% of the plate motion between the Sunda and Australian plates along a margin with an obliquity of ~35–50° (Bradley et al., 2017). The Philippine fault is 40–55° from normal to the convergence vector across the Philippine Sea-Sunda plate boundary, and accommodates roughly half of the margin-parallel motion (Hsu et al., 2016). Finally, the Median Tectonic Line of Japan accommodates ~25% of the ~30 mm/yr trench-parallel motion across a margin with ~67° angle between the plate convergence direction and normal to the trench (Loveless and Meade, 2010).

2.5.5 Implications for Mesozoic Slip Partitioning & Plate Convergence

It is unclear why the slip rates and displacement magnitude along the AFS are comparatively low for such a long-lived, regionally extensive fault system. One possibility is the soft-linked, highly segmented nature of the AFS prevented the effective localization of trench-parallel motion in the upper plate. A second possibility is that the convergence rate was slower than rates at modern margins, or the convergence direction was less oblique than previously thought. Convergence vectors for modern intra-arc faults are well known from geodetic data, and therefore the percentage of margin-parallel motion along modern margins can be readily determined. In contrast, the con-

vergence vector across the Early Cretaceous Peru-Chile margin is not as well constrained due to the lack of Mesozoic oceanic crust. Plate motion reconstructions over the time period of AFS slip suggest Pacific-South America trench-normal convergence of $\sim 20\text{--}50$ km/Myr and trench-parallel motion of $\sim 0\text{--}20$ km/Myr between 140–110 Ma based on ocean basin seafloor-spreading histories and continental motion anchored to true-polar wander corrected paleomagnetic data for 200 to 100 Ma (Seton et al., 2012). These plate motion reconstructions result in a convergence obliquity normal to the plate margin that decreased from $>60^\circ$ before 135 Ma to a range of $22\text{--}36^\circ$ between 130–110 Ma (Maloney et al., 2013). Additional modeling of the Seton et al. (2012) plate reconstruction data by Butterworth et al. (2016) demonstrate that the obliquity of convergence varied strongly with position along the margin with proximity to the pole of rotation, and may suggest the pole of rotation of the Phoenix plate subducted beneath the AFS at $\sim 135\text{--}130$ Ma. These models as a whole suggest highly oblique subduction along the AFS at ~ 130 Ma transitioned to significantly more orthogonal subduction by ~ 120 Ma. The opening of a new oceanic ridge to the south of the AFS potentially concurrent with the abandonment of the Pacific-Phoenix ridge in these models at ~ 120 Ma produces a period of N-directed oblique convergence that coincides with the end of mylonitization documented along the El Salado segment here and in Chapter 1, followed by a period of relatively orthogonal convergence as the South Atlantic begins to open and South America advances westward at ~ 110 Ma (Seton et al., 2012; Maloney et al., 2013; Butterworth et al., 2016).

Obliquity estimates derived from these reconstructions are comparable to the angles of obliquity and trench-parallel motion rates of modern systems. If this reconstruction is accurate, our estimate of $2.0\text{--}2.5$ km/Myr of slip over that time interval suggests only $\sim 10\text{--}12.5\%$ of trench-parallel motion was accommodated along the AFS between 130–110 Ma. The remaining $87.5\text{--}90\%$ of trench-parallel motion must have been accommodated outside of the AFS, or may reflect significant uncertainties in the direction and magnitude of relative plate motion across the Mesozoic margin. These uncertainties are reflected in work by Maloney et al. (2013), which compares convergence rates and absolute plate motion from the Seton et al. (2012) reconstruction to geo-

logic features in the upper plate. Overall, low degrees of correlation between deformation and major magmatic events are found. Periods of high magmatic flux such as the development of the Coastal Cordilleran arc do not correlate with subducting slab age, absolute overriding plate velocity, or convergence velocity. High trench-normal (>4 cm/yr) convergence rates correlate with the development of fold and thrust belts along the Andean margin and may contribute to shortening in the upper plate, but does not uniquely initiate or control the development of high plateaus and fold and thrust belts (Maloney et al., 2013). The lack of correlation between the geologic record of the upper plate and plate motion reconstructions, in conjunction with the need to accommodate an anomalously high proportion of trench-parallel motion outside of a major intra-arc strike-slip fault system compared to modern systems, may suggest that the convergence rates and absolute plate motion produced by the model is not entirely correct.

Alternatively, the remaining trench-parallel motion may have been accommodated either along the slab interface or distributed through forearc rather than fully concentrating in the magmatic arc. It is difficult to evaluate the role of distributed forearc deformation as long-lived subduction erosion has removed the western portion of the Late Jurassic–Early Cretaceous arc (e.g., Rutland, 1971; Stern, 1991; Charrier et al., 2007; Ramos and Folguera, 2009; Contreras-Reyes et al., 2014). Subduction erosion of the upper plate has been tied to a lack of sediments on the subducting plate, which previous models related to high (>60 mm/yr) convergence rates (e.g., Von Huene and Scholl, 1991; Clift and Vannucchi, 2004; Stern, 2011). In northern Chile, a transition to contraction in the upper plate during the Late Cretaceous resulted in the inversion and closure of back-arc basins as well as subduction erosion that removed the western portion of the Late Jurassic–Early Cretaceous arc (Kay and Mahlburg-Kay, 1991; Stern, 1991; Charrier et al., 2007; Ramos and Folguera, 2009). Long-lived sediment starvation could promote the high degree of plate coupling between the subducting oceanic slab and overriding continental plate to produce crustal-scale strike-slip faults (e.g., Fitch, 1972; Jarrard, 1986). Recent work by Behr and Becker (2018) has suggested that sparse sediments on the subducting plate result in increased viscosities along the plate-mantle interface and reduced subduction plate speeds. Therefore, the combination of low slip rates along

the AFS and evidence for long-lived subduction erosion may record a high rate of coupling and low convergence obliquity or convergence rate across the Early Cretaceous Peru-Chile trench compared to modern oblique margins.

2.6 Conclusions

Through detailed field mapping and geo/thermochronology, we have identified pre-, syn-, and post-tectonic intrusions that document the timing, magnitude, and rate of slip along two major branches the El Salado segment of the Atacama fault system during Early Cretaceous convergence. The ~ 134 – 132 Ma Cerro del Pingo Complex, ~ 119 Ma tonalite and surrounding Chañaral Complex metasedimentary rocks are mylonitic along the eastern margin of the eastern branch of the AFS, as reported in Chapter 1. Here we document another zone of mylonitic lithologies along the western margin of the eastern branch, sinistrally separated from the northern occurrences by 32–38 km (~ 134 – 132 Ma phase) and 22–24 km (~ 119 Ma phase). This separation yields a slip rate of ~ 1.4 – 1.7 km/Myr over the ~ 23 Myr duration of deformation. Structural data from within 50 m of the principle slip surface of the eastern branch document dominantly sinistral motion on a N-trending, steeply-E-dipping fault.

We also document a chain of leucocratic felsic igneous bodies across the western branch of the El Salado segment. The exact restoration of these bodies is complicated by differences in grain size and texture, but allows ~ 8 – 23 km to restore them to a single continuous trend and ~ 14 – 18 km to restore textural domains. Kinematics derived from structural data are very similar to the eastern branch, with dominantly sinistral motion on a N-trending, steeply-E-dipping fault with an average slickenline orientation plunging shallowly N. Assuming the western branch was active over the same time period as the eastern branch, the slip rate between ~ 133 – 110 Ma was ~ 0.6 – 0.8 km/Myr.

In summary, the AFS was active between ~ 133 – 110 Ma at an average rate of ~ 2.0 – 2.5 km/Myr, resulting in $\sim 50 \pm 6$ km of sinistral displacement. This slip rate is lower than other modern intra-arc strike-slip faults and suggests plate convergence rates or obliquity may have been

significantly lower than previously modeled. If the convergence vector derived from previous plate reconstruction models is correct, the low slip rate along the AFS suggests the vast majority of trench-parallel slip was accommodated along the slab interface or within the forearc.

Chapter 3

Sodic-calcic alteration along the ductile Atacama fault system near Copiapó

Summary

The Chilean Iron Belt hosts world-class iron oxide-copper-gold deposits that are spatially associated with the Atacama fault system (AFS). Near Copiapó, clear regional-scale branches no longer define the AFS, and mineralization in the Punta del Cobre district occurs east of the main system. The main branch of AFS near Copiapó is defined by a ~200–500-m-thick steeply NW-dipping shear zone that lacks brittle overprint. Zircon U-Pb dates document synkinematic emplacement of a tonalite in the shear zone at ~122 Ma. NW-dipping mylonitic foliation in the tonalite is oriented at a low angle to the shear zone boundary, and most lineations plunge shallowly NE. Kinematic indicators record both sinistral and reverse shear and locally coaxial fabrics dominate, indicating an overall transpressional regime.

Original mineralogy of the mylonitic shear zone is entirely replaced or annealed by a synkinematic sodic-calcic actinolite+epidote+titanite assemblage as well as postkinematic secondary plagioclase. Replacement by hydrothermal alteration assemblages is most likely due to exsolution of fluids from the intrusion of the unstrained ~115 Ma Sierra Atacama diorite that cuts the shear zone. The Sierra Atacama diorite is also pervasively altered by a sodic-calcic plagioclase+actinolite+titanite (\pm andradite) assemblage. Finally, the annealed shear zone is cut by a late andradite+epidote+calcite+quartz (\pm magnetite \pm apatite) vein with a ~96 Ma andradite U-Pb date. Stable isotope analyses yield $\delta^{18}\text{O}$ values of +11.1‰ (qz), +5.4‰ (grt), and +5.7‰ (ep), indicating alteration by magmatic fluids at 400°C. Together, these relationships document three pulses of hydrothermal alteration over a ~25 Myr period. The oldest is synkinematic with Early Cretaceous sinistral shear that overlaps in age with other sections of the AFS. Sodic-calcic mineralization was

roughly coeval with andradite vein mineralization in the Las Pintadas deposit of the Punta del Cobre district based on new $\sim 113\text{--}115$ Ma Re-Os and garnet U-Pb geochronology. Focused fluid flow resulting in mineralization along the shear zone utilized the prominent steeply-dipping anisotropy of the AFS during ductile transpression and did not require coeval brittle transtension along the AFS, unlike other portions of the Chilean Iron Belt. The lack of brittle faulting in the shear zone is likely related to continued magmatism associated with the Copiapó batholith complex, which is younger than most arc plutons in the Coastal Cordillera and most likely sourced the magmatic fluids responsible for alteration.

3.1 Introduction

The Atacama fault system (AFS) played an important role in controlling major copper deposits of the Chilean Iron Belt³. Major N-striking fault branches and NNW- and WNW-striking second-order faults along the AFS provided a focused pathway for fluids, giving rise to some of the largest iron oxide-copper-gold (IOCG) and iron oxide-apatite (IOA) deposits in Chile (e.g., Espinoza, 1990; Grocott et al., 1994; Vila et al., 1996; Wilson and Grocott, 1999; Grocott and Taylor, 2002; Arévalo et al., 2006; Cembrano et al., 2009; Marquardt et al., 2009; Rieger et al., 2010, Figure 3.1). IOA deposits are located along the central and southern portions of the El Salado segment of the AFS and include El Romeral, Algarrobo, Los Colorados, Cerro Imán, and Cerro Negro Norte (Bookstrom, 1977; Pimentel and Vega, 1979; Espinoza, 1996; Raab, 2001; Vidal et al., 2001). IOCG deposits including Las Luces, Casualidad, Santo Domingo, Buena Aventura, Manto Verde, Candelaria, Carrizal Alto, and Productora are also located along the El Salado Segment, but notably extend farther north than the IOAs and also occur to the east and west of the main branches of the fault system (Vila et al., 1996; Marschik and Fontboté, 2001a; Mathur et al., 2002).

³This chapter will be submitted for publication: N.M. Seymour, J.S. Singleton, R. Gomila, J. Ridley, M.L. Gevedon, H. Stein, G. Yang, G. Arancibia, S.M. Seman, and D.F. Stockli, Sodic-calcic alteration along a Cretaceous transpressional shear zone near Copiapó, Chile: Implications for IOCG mineralization in the Chilean Iron Belt, in preparation.

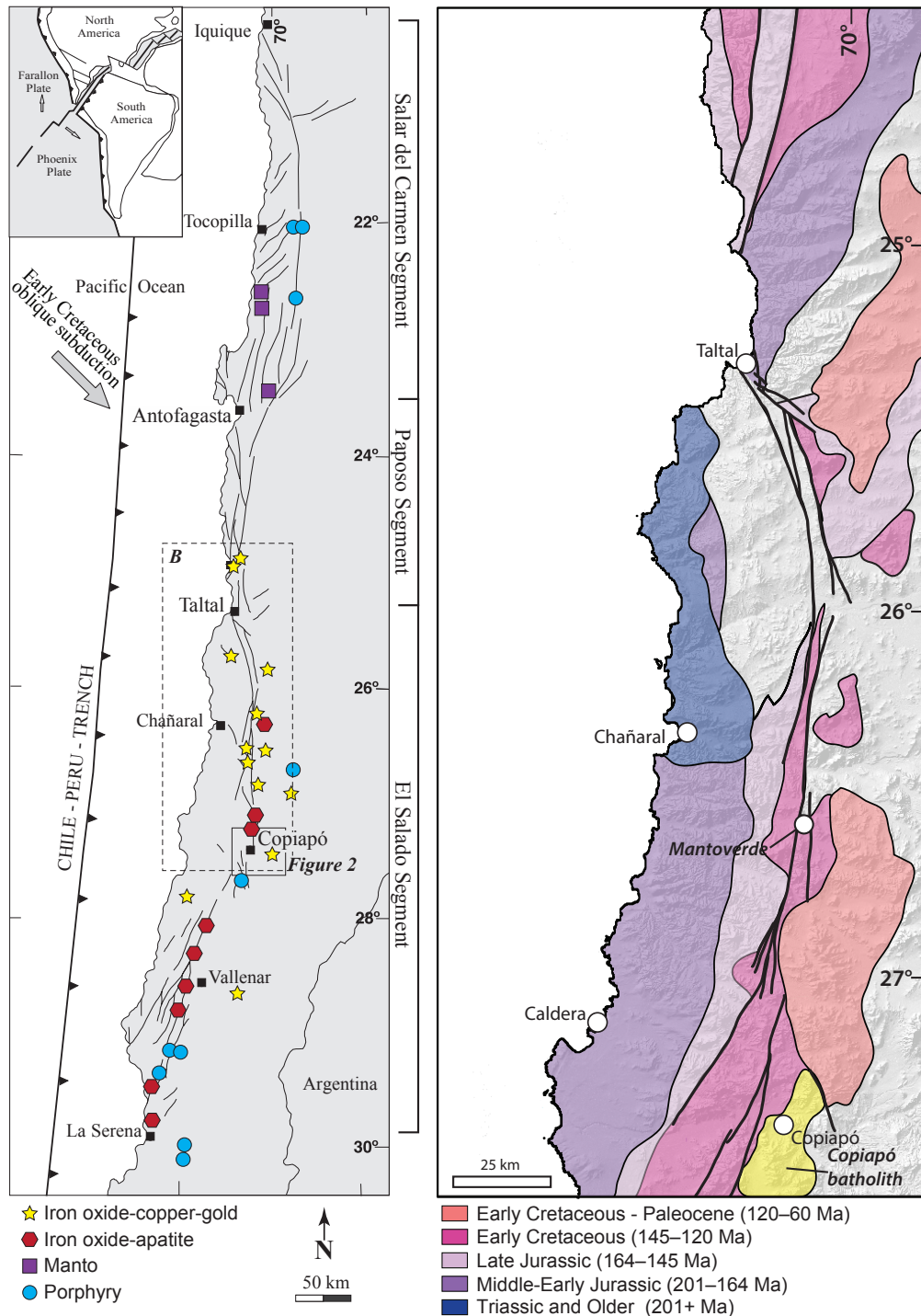


Figure 3.1: Left: Map of the regional geometry and strand of the Atacama fault system (AFS) with the locations and types of Chilean Iron Belt deposits plotted. Note the strong spatial correlation between the AFS and deposits. Modified from Cembrano et al. (2005). Location of Figure 3.2 is shown by the black box, and right panel is shown by the dashed box. Right: Distribution of Coastal Cordilleran pluton ages. Note the strong N-S trend of each belt. Post-Coastal Cordillera plutons (peach) cut these N-S belts. The Capiapó batholith (yellow) is one of these post-Coastal Cordillera intrusions.

Near Copiapó, the Punta del Cobre IOCG mining district hosts deposits formed by multiple hydrothermal alteration and mineralization events. Studies on individual deposits in the Punta del Cobre district have focused on the extent and style of hydrothermal alteration and mineralizing processes including the timing and style of mineralization, and composition and source of mineralizing fluids (Barton and Johnson, 1996; Marschik and Fontboté, 2001a; Mathur et al., 2002; Sillitoe, 2003; Gelcich et al., 2005; Tornos et al., 2010; Daroch and Barton, 2011; Rieger et al., 2012; Lopez et al., 2014; Marschik and Kendrick, 2015; Veloso et al., 2017). Despite this large body of work, fluid sources responsible for mineralization and genetic relationships between IOCG/IOA mineralization and plutonic rocks remain debated (Hitzman et al., 1992; Barton and Johnson, 2000; Marschik and Fontboté, 2001a; Mathur et al., 2002; Barton et al., 2005; Arévalo et al., 2006; Chiaradia et al., 2006). Two end-member hypotheses exist to explain IOCG ore genesis in the Chilean Iron Belt: (1) metal- and sulfur-bearing magmatic fluids exsolve from a crystallizing pluton and deposit ore in overlying country rocks (Marschik and Fontboté, 2001a; Sillitoe, 2003; Pollard, 2006; Tornos et al., 2020), and (2) evaporite-derived, thermally-driven oxidized brines leach and redeposit metals from the Jurassic and Cretaceous back-arc basin deposits (Barton and Johnson, 1996, 2000; Hitzman, 2000). Other authors advocate for a hybrid model with mineralization produced by mixed magmatic fluids and evaporite brines (Williams et al., 2003; Chiaradia et al., 2006). Some authors have suggested that IOCG and IOA deposits may be genetically related (Espinoza, 1996; Sillitoe, 2003; Knipping et al., 2015; Corriveau et al., 2016; Reich et al., 2016; Barra et al., 2017; Ootes et al., 2017). Textural and mineralogical evidence from Gawler Province in South Australia, the Great Bear district in Northwest Canada, and Los Colorados in northern Chile suggest IOA deposits are the deeper roots of IOCG systems, with an early IOA stage transitioning to a later, shallower IOCG stage (Oreskes and Einaudi, 1990; Davidson et al., 2007a,b; Corriveau et al., 2016; Reich et al., 2016; Ootes et al., 2017). Some models also suggest calcic skarns serve as feeders for manto-style deposits (e.g., Barra et al., 2017).

Recent work has documented the spatial and temporal association of Coastal Cordilleran arc magmatism and sinistral strike-slip AFS deformation in northern Chile (Chapter 1). Along parts of

the AFS mylonitic zones associated with Early Cretaceous plutons are overprinted by brittle faults, indicating deformation initiated in the ductile regime as the plutons intruded and progressed to brittle behavior as the plutons cooled. Mineralization in the Punta del Cobre district near Copiapó occurs east of the main AFS, perhaps because the fault system in this region is a ductile shear zone with no major regional-scale brittle fault. The shear zone is associated with plutons of the Early Cretaceous Copiapó batholith, which postdated the main phase of Coastal Cordillera magmatism. We incorporate geologic mapping, petrography, geo/thermochronometry, and geochemistry on the ductile shear zone overprinted by sodic-calcic alteration mapped as the main branch of the El Salado segment of the AFS (Arévalo, 2005a) to determine (1) why the AFS did not evolve to a brittle fault in this area, (2) the conditions and fluid sources responsible for alteration. We compare these data to new Re-Os, U-Pb, and stable isotope data a mineralized andradite vein from the Las Pintadas deposit and published data from the wider Punta del Cobre belt to evaluate how alteration relates to spatial and temporal patterns of AFS deformation, Coastal Cordillera arc magmatism, and Chilean Iron Belt mineralization.

3.2 Geologic Setting

Subduction along the Peru-Chile margin has been ongoing since the initial breakup of Pangaea at ~ 200 Ma (Parada et al., 2007; Ramos and Folguera, 2009). The calc-alkaline Late Jurassic–Early Cretaceous Coastal Cordillera arc and related back-arc basin volcanic deposits developed above an obliquely convergent margin as the Phoenix (Aluk) plate subducted southeastward below the N-S trending margin of the South American plate (Coira et al., 1982). Two primary phases of arc magmatism are documented along the Coastal Cordillera: Jurassic and Early Cretaceous (195–175 Ma and 150–120 Ma, respectively) with local pluton emplacement occurring until ~ 104 Ma (Naranjo et al., 1984; Dallmeyer et al., 1996; Parada et al., 2007; Oliveros et al., 2010, Chapter 1 and references therein). In northern Chile thermal weakening associated with the shallow (<10 km) intrusion of arc plutons facilitated trench-parallel sinistral motion along the intra-arc Atacama fault system (AFS), a $\sim 1,000$ km long structure between Iquique (20.5°S) and La Serena (30°S)

comprised of overstepping branches that each have several fault strands. The fault system is divided into three major segments from north to south: Salar del Carmen, Paposo, and El Salado (Thiele and Pinchiera, 1984; Naranjo, 1987; Brown et al., 1993; Marinovic et al., 1995; Arévalo et al., 2003). The El Salado segment of the AFS runs ~480 km from near Taltal to La Serena and features mylonitic zones developed along the margins of Early Cretaceous plutons that are overprinted by brittle faults. The volume of Early Cretaceous plutons roughly correlates to the width of these shear zones, with more voluminous magmatism producing wider shear zones and a later transition to brittle slip (Chapter 1). The El Salado segment records a transition from mylonitic sinistral shear coeval with the shallow emplacement of Early Cretaceous plutons to brittle sinistral strike-slip deformation during a progressive deformation event as the arc migrated eastward and the upper crust cooled (Brown et al., 1993; Scheuber et al., 1995; Dallmeyer et al., 1996; Scheuber and Gonzalez, 1999; Grocott and Taylor, 2002, Chapter 1). Eastward migration of the arc and abandonment of the AFS correlates with a shift in plate motion during final breakup of South America and Africa as seafloor spreading initiated in the South Atlantic, producing E-directed contraction across the Andean margin (Royden, 1993; Scheuber et al., 1994; Amilibia et al., 2008; Ramos, 2009).

3.2.1 Geology of the Copiapó Region

Studies in the Copiapó region have focused on Candelaria and the local deposits of the Punta del Cobre district (Segerstrom and Ruiz, 1962; Camus, 1980; Ryan et al., 1995; Marschik et al., 1997; Díaz et al., 1998; Lledó, 1998; Marschik and Fontboté, 2001a; Marschik and Söllner, 2006; del Real Contreras et al., 2018) as well as batholith- to regional-scale studies on the development of Early Cretaceous magmatism and the Copiapó batholith (Tilling, 1976; Zentilli, 1974; Arévalo, 1999). Compiled published data record a broad magmatic peak between ~140–100 Ma due to the areally extensive Cerro Morado (140–137 Ma), La Borracha (~107 Ma) pluton, and Copiapó batholith (119–97 Ma) which together dominate the volume of exposed rock in the region (Figure 3.2, Farrar et al., 1970; Arévalo, 1995, 1999; Ullrich et al., 2001; Marschik and Söllner,

2006; Girardi, 2014). The Copiapó batholith is an Early Cretaceous composite plutonic complex of broadly dioritic composition with local two-pyroxene diorite, monzodiorite, and tonalite emplaced into Jurassic and Cretaceous volcanic and marine sedimentary rocks (Marschik and Söllner, 2006). Individual phases of the Copiapó batholith defined by Tilling (1976); Arévalo (1999); Marschik and Söllner (2006) include the La Brea diorite (~118 Ma), San Gregorio monzodiorite (~115), Los Lirios complex (~110), and associated dacite and diorite dikes.

Sedimentary units in the Copiapó region include the Punta del Cobre Formation and the contemporaneous Chañarcillo and Bandurrias Groups (Figure 3.2, Segerstrom, 1960; Segerstrom and Ruiz, 1962; Moscoso et al., 1982). The Lower Cretaceous Punta del Cobre Formation is the basal unit in the region and includes the Lower Andesite, Dacite, Volcanic-sedimentary, and Upper Andesite members (Marschik and Fontboté, 2001b). Zircon U-Pb data indicate deposition of this unit between ~135–132 Ma (del Real Contreras et al., 2018). Mixed sedimentary rocks of the Early Cretaceous Chañarcillo Group and the interfingering volcanic rocks of the Bandurrias Group stratigraphically overlie the Punta del Cobre Formation (Segerstrom and Ruiz, 1962; Marschik and Fontboté, 2001b; Arévalo et al., 2006). The Chañarcillo Group varies from basal mudstones and arkoses of the Abundancia Formation, through mudstones and calcareous breccias with an evaporitic matrix in the Nantoco Formation, calcareous siltstones of the Totaralilo Formation to the uppermost cherts, limestones and calcareous sandstones of the Pabellón Formation (Segerstrom and Parker, 1959; Segerstrom and Ruiz, 1962). The Bandurrias Group interfingers with the Chañarcillo Group to the north and represents a lateral transition to andesitic volcanics mixed with continental volcanoclastic strata, tuffs, and intercalated shallow marine limestones and sandstones (Segerstrom, 1960, 1967). Coarse clastic alluvial strata and coeval subaerial volcanics of the early Albian–Cenomanian Cerrillos Formation (~111–100 Ma; Maksaev et al., 2009; del Real Contreras et al., 2018) unconformably overlie the Chañarcillo and Bandurrias Groups (Zentilli, 1974).

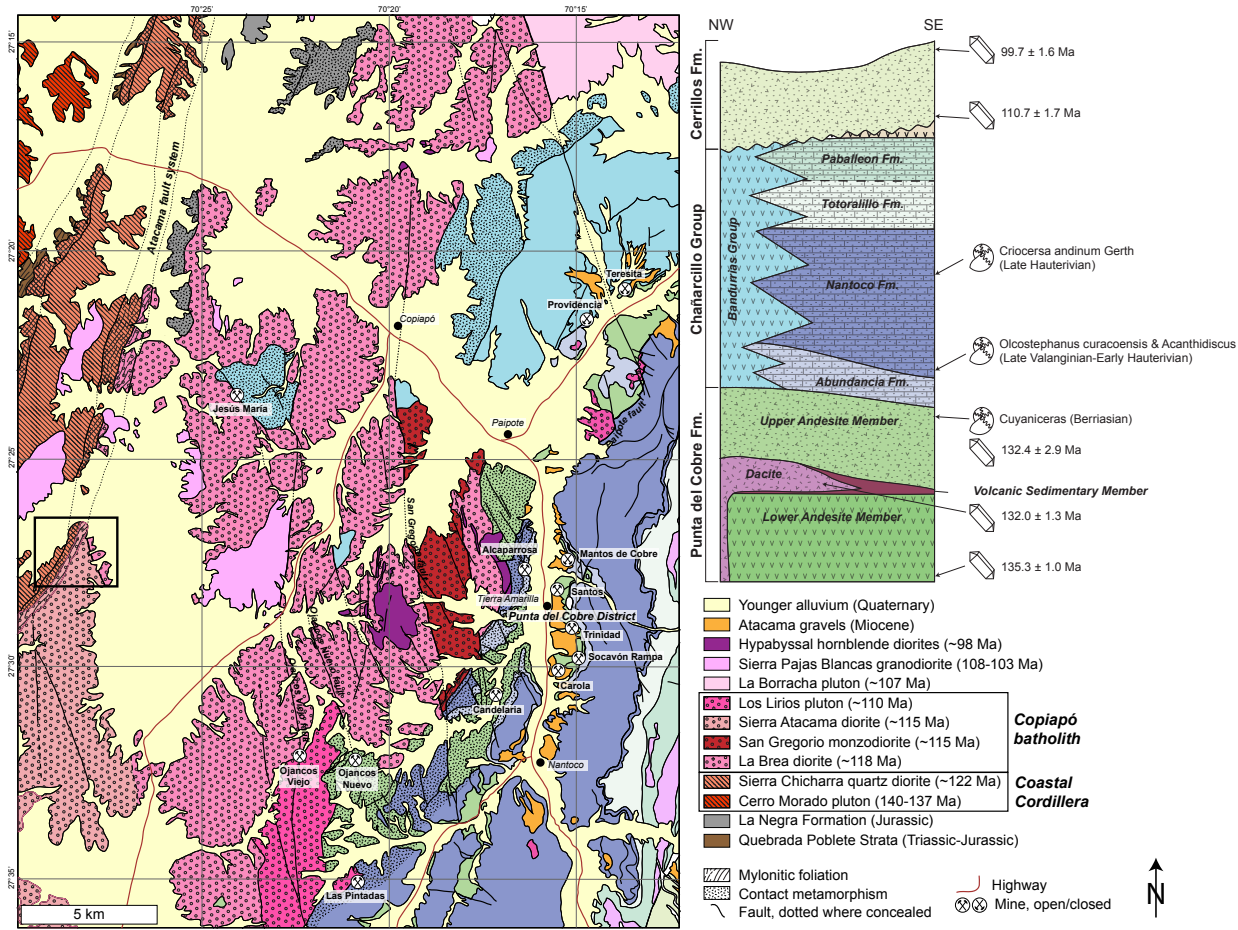


Figure 3.2: Regional map of bedrock geology in the Copiapó region including the location of Punta del Cobre district deposits and stratigraphic column of sedimentary sequence. Modified and compiled from Arévalo (2005a,b); Sillitoe (2003); Marschik and Söllner (2006); del Real Contreras et al. (2018). Location of Figure 3.3 is shown in the black box.

In the Copiapó region, the El Salado segment of the AFS turns from dominantly N-S to an overstepping set of NE-striking faults. This NE-striking orientation continues to the southern end of the El Salado segment at La Serena. Unlike other portions of the El Salado segment, no brittle fault is present through this area (Figure 3.2). Instead, the AFS is mapped at 1:100,000-scale as a subvertical 300–600-m-wide NE-striking ductile shear zone juxtaposing the Sierra Chicharra Quartz Diorite (128–125 Ma, K-Ar biotite) to the west against Sierra Atacama Diorite (104–117 Ma, K-Ar hornblende) to the east (Arévalo, 2005a). Other significant faults in the region with ductile fabrics include the Ojanco Nuevo fault and San Gregorio fault. The Ojancos Nuevo fault is major N-striking, steeply W-dipping structure that is continuous for 5–7 km. This fault juxtaposes shallow volcanic rocks against mylonitic plutonic rocks, indicating up to 1 km of normal-sense dip-slip motion (Arévalo et al., 2006; Kreiner, 2011). The San Gregorio fault marks the contact between the San Gregorio monzodiorite and La Brea diorite and is also NNW-striking and steeply W-dipping with mylonitic fabrics present along much of the strike length (Arévalo et al., 2006). The development of these large regional faults post-dates the emplacement of the La Brea diorite and may be coeval with the emplacement of the San Gregorio pluton at ~115 Ma (Arévalo, 2005a,b). Near these larger faults, a smaller-scale conjugate set of faults dipping 50–90° NNW and 60–90° WSW with up to 10s of meters of normal-sense slip served as fluid pathways that resulted in the development of mineralized vein systems (Kreiner, 2011).

The regional angular unconformity between the underlying Chañarcillo and Bandurrias Groups and overlying Cerrillos Formation together with Albian (113–100 Ma) apatite fission track dates (Maksaev, 1990; Gana and Zentilli, 2000) and zircon (U-Th)/He dates (116–96 Ma; Chapter 1) record compression and basin inversion. Sinistral slip along the AFS transitioned to E-W shortening that was accommodated across the district by the W-vergent Paipote thrust fault, NNE-trending upright Tierra Amarillo anticlinorium, and N-striking, steeply dipping faults reactivated in a reverse sense. These shortening structures cut both the Copiapó batholith and overlying sedimentary units (Scheuber et al., 1994; Arévalo, 2005a,b; Maksaev et al., 2009; Martínez et al., 2013; del Real Contreras et al., 2018). Two younger magmatic peaks (~95–80 Ma and ~60 Ma) in the

easternmost part of the Copiapó region are unrelated to the Coastal Cordillera arc and Copiapó batholith (Arévalo, 2005a,b).

3.2.2 Mineralization in the Punta del Cobre District

Candelaria and other Punta del Cobre deposits lie ~17–23 km east of the AFS in the thermal aureole of the Coastal Cordillera arc plutonic suite (Figure 3.2, Arévalo et al., 2006) and are the most significant cluster of actively-mined IOCG deposits along the Peru-Chile margin (Sillitoe, 2003). Reserves at Candelaria for both the open pit and underground workings exceed 400 Mt at 0.53–0.94% Cu (Couture et al., 2017), mineral reserves at Las Pintadas were 4 Mt at 1.0–1.5% Cu as of 2001 (Marschik and Fontboté, 2001a), and reserves at other deposits in the district range from 15–180 Mt and 0.8–1.5% Cu (Ichii et al., 2007; del Real Contreras et al., 2018, and references therein). Two vein systems mineralized over strike lengths of 4–10 km, the Tigresa and San Francisco systems, contain an estimated resource of ~1 Mt with an average grade of 1.5% Cu (Kreiner, 2011). Together, the Candelaria-Punta del Cobre district has a combined past production, mineral reserves, and mineral resources exceeding 13 Mt of contained Cu, ranking it among the largest IOCG districts worldwide (del Real Contreras et al., 2018).

Dioritic-granodioritic to quartz monzonitic Coastal Cordilleran arc and Copiapó batholith plutons intrude the back-arc sequence and serve as potential fluid and/or metal sources (Arévalo, 2005a,b). Each phase of the batholith produced an associated hydrothermal system (Barton et al., 2005, 2011). District-scale alteration associated with these hydrothermal systems is generally magnetite-destructive and characterized by sodic-calcic assemblages of oligoclase+actinolite with accessory titanite, rutile, apatite, epidote, and clinopyroxene (Barton et al., 2011). Other types of alteration present at the district-scale include sodic alteration characterized by albite+pyrite and chlorite+albite (\pm hematite \pm carbonate), several types of potassic alteration, and chloritic, sericitic, and advanced argillic assemblages (Kreiner, 2011).

Alteration related to vein systems is similar, if not identical, to the district-scale assemblages (Barton et al., 2005, 2011). An important difference is the stability of magnetite in sodic-calcic

styles of alteration related to the vein systems, as opposed to the magnetite-destructive character of district-scale alteration. Mineralization within the district-scale alteration occurs in two main styles: (1) disseminated, patchy sulfide mineralization hosted by stratigraphically-controlled replacement and breccia-hosted ore bodies, and (2) vein, manto bodies, and breccia-hosted mineralization formed along zones of faulting and fracturing in the batholith and supracrustal rocks (Camus, 1980; Ryan et al., 1995; Marschik and Fontboté, 2001a). Stratabound deposits are primarily concentrated in the Punta del Cobre Formation and lower Chañarcillo and Bandurrias Groups.

Iron oxide-dominated associations composed of magnetite or hematite within the vein systems or breccias are the primary ore targets. Ore mineralogy at Candelaria consists mainly of magnetite, chalcopyrite, and pyrite, with Au commonly associated with chalcopyrite and pyrite (Ryan et al., 1995). Ore bodies a close spatial and temporal relationship with texturally destructive, iron oxide- and sulfur-poor calcic amphibole alteration in the surrounding wall rock that overprints earlier biotite-quartz-magnetite alteration (Ryan et al., 1995; Ullrich and Clark, 1999; Marschik et al., 2000; Marschik and Fontboté, 2001a; Barton et al., 2011). Throughout the district, calcic assemblages consist of epidote+quartz(\pm actinolite) and locally include euhedral, granular epidote+actinolite+pyrite+chalcopyrite (Kreiner, 2011). Mineralized calcic veins in the form of andradite skarns at Atacama Kozan and Las Pintadas are found structurally below stratabound manto deposits, and may represent deeper levels of the same mineralizing system (e.g., Barra et al., 2017).

Three primary generations of vein formation have been documented in the Copiapó region: (1) an early stage hosted by the Early Cretaceous volcanic-sedimentary sequence and cut by \sim 127 Ma dikes, (2) a main stage related to emplacement of La Brea diorite at \sim 117 Ma, and (3) a late stage at \sim 115 Ma hosted in the San Gregorio monzodiorite (Zentilli, 1974; Marschik et al., 1997; Ullrich and Clark, 1999; Kreiner, 2011). $^{40}\text{Ar}/^{39}\text{Ar}$ dates on hydrothermal biotite at Candelaria constrain the timing of alteration to 116–110 Ma (Ullrich and Clark, 1998, 1999; Marschik and Fontboté, 2001a), and Re-Os dates of 115.2–114.2 Ma on molybdenite (Mathur, 2002) indicate Cu-Au mineralization was contemporaneous with nearby Copiapó batholith emplacement. Ore textures and

steeply-dipping brittle faults that grade downward into gently dipping ductilely deformed rocks suggest mineralization occurred during the transition from ductile to brittle deformation in the presence of a cooling hydrothermal system (Arévalo et al., 2006). Early iron oxide mineralization occurred at 500–600°C based on biotite-garnet thermometry on pre-chalcopyrite alteration at Candelaria (Ullrich and Clark, 1997), followed by main-stage sulfide mineralization at 400–500°C based on mineralogic evidence at the Carola mine (Hopf, 1990).

Fluid inclusion homogenization temperatures from across the Copiapó region vary with depth and range from 350–450°C at the deepest levels to 200–250°C at shallower levels (Rabbia et al., 1996; Marschik et al., 1997; Kreiner, 2011). Salinities range from 12–59 wt% NaCl_{eq} and contain up to 13–23 wt% CaCl₂ (Marschik et al., 1997; Kreiner, 2011). Oxygen isotope values for quartz associated with main-stage chalcopyrite mineralization at Candelaria are +11.2 to +12.6‰ $\delta^{18}\text{O}_{\text{SMOW}}$, and fluid inclusions in the Candelaria quartz homogenize at 370–440°C corresponding to an equilibrium fluid composition of +5.9 to +8.9‰ $\delta^{18}\text{O}_{\text{SMOW}}$ (Marschik et al., 2000). Sulfur isotopes ($\delta^{34}\text{S}$) in sulfides ranges from -3.2 to +7.2‰ with an average near 0‰ (Rabbia et al., 1996; Marschik et al., 1997; Ullrich and Clark, 1999; Marschik and Fontboté, 2001a; Kreiner, 2011), which has been interpreted by some workers to indicate a magmatic source for sulfur (e.g., Marschik et al., 2000; Marschik and Fontboté, 2001a) while others favor a mixed magmatic-evaporite source (Ullrich and Clark, 1999; Marschik and Söllner, 2006) or partial reduction of sulfate in sedimentary evaporites with no magmatic component as the sulfur source (Kreiner, 2011). Initial Os isotopic values in the Punta del Cobre district and the magmatic magnetite in the surrounding plutons are very similar (0.36 ± 0.1 at Candelaria, 0.33 at Bronce, and 0.21–0.41 in regional plutons, respectively), suggesting a magmatic metal source in the Candelaria–Punta del Cobre district (Mathur et al., 2000, 2002). However, none of these studies have established a direct link between the mineralizing fluid and a causative pluton, and the discussion regarding a purely magmatic versus evaporite-derived fluid source is ongoing.

In all Punta del Cobre deposits, late stage calcite post-dates both iron oxide and sulfide mineralization. Oxygen isotope ratios of calcite at Candelaria deposit are between +11.7 to +11.9‰

(Marschik et al., 2000), the Carola mine ranges from +15.4 to +15.9‰ (Rabbia et al., 1996), and the Santos and Socavón Rampa mines range from +14.3 to +15.3‰ (Marschik et al., 2000). Fluids in equilibrium with the late-stage calcite at these mines correspond to compositions of -5.4 and +1.3‰ $\delta^{18}\text{O}_{\text{SMOW}}$ at temperatures of 100–180°C (Candelaria deposit, Marschik et al., 2000), +4.6 and +7.7‰ $\delta^{18}\text{O}_{\text{SMOW}}$ at 175–235°C (Carola deposit, Rabbia et al., 1996), and -2.8 and +4.7‰ $\delta^{18}\text{O}_{\text{SMOW}}$ (Santos and Socavón Rampa deposits, Marschik et al., 2000). The low oxygen isotope ratios and low equilibrium temperatures suggest mixing between a magmatic fluid and basinal brine or meteoric water in the final stage of a cooling hydrothermal system (Marschik and Fontboté, 2001a).

3.3 Methods

3.3.1 Mapping & Structural Data

This study area is centered on an AFS ductile shear zone located ~17 km SW of Copiapó, ~20 km WNW of Candelaria, and ~19 km NW of the Las Pintadas deposit. Previous bedrock mapping was conducted at 1:100,000 scale by Arévalo (1995, 2005a,b), and alteration has been mapped at a regional scale by Kreiner (2011), Barton et al. (2013), and others. We conducted 1:10,000-scale field mapping to understand and resolve the relationships between the AFS ductile shear zone and plutons. We documented lithologies, degree of ductile strain, geometry of fabrics, crosscutting relationships, and alteration and collected samples for thin section petrography and geo/thermochronometric analyses from syn- and post-kinematic plutons (Table 3.1). Alteration, spacing of foliation, quartz strain, and presence of shear bands were used to distinguish mylonitic fabrics from magmatic fabrics in the field. Observations were confirmed in thin section by characterizing the presence or absence of deformation within individual mineral phases. Shear sense indicators including asymmetric porphyroclasts, asymmetric folds, foliation patterns, and shear bands were used to determine the kinematics of mylonitic fabrics. Average structural orientations were determined using maximum eigenvectors in the program Stereonet (Allmendinger et al., 2011; Cardozo and Allmendinger, 2013).

3.3.2 Geochronology

U-Pb Geochronology

U-Pb geochronology was used to directly date both the garnet and surrounding plutons in order to understand the timing of vein formation and its relationship to arc magmatism. Internal garnet fragments from samples 161-13 and 181-N144 were mounted in epoxy, polished, and analyzed with energy dispersive spectroscopy on a Phillips/FEI XL30 environmental scanning electron microprobe to determine garnet end-member composition and look for growth zonation prior to U-Pb analysis. Zircon grains were separated from igneous samples 161-2, 161-9, and 191-N116 via standard crushing, magnetic, and density separation procedures. A subset of zircon grains were mounted in epoxy and polished for cathodoluminescence (CL) imaging to document the internal textures of grains (Appendix 3.6). In order to capture thin zonation domains imaged in CL too small for spot analysis on polished mounts, additional whole, unpolished zircon grains from samples 161-2 and 161-9 were mounted parallel to the c-axis on double-sided tape for depth-profile analysis (e.g., Marsh and Stockli, 2015). Zircon grains and garnet fragments were analyzed for U-Pb with a Photon Machines Analyte G.2 Excimer laser paired with a ThermoScientific Element II magnetic sector inductively coupled plasma mass spectrometer (ICP-MS) at the University of Texas at Austin using the methods of Seman et al. (2017) for andraditic garnet and the methods outlined in Chapter 1 for zircon. Weighted $^{206}\text{Pb}/^{238}\text{U}$ average dates with 2σ error calculated in Isoplot 4.15 (Ludwig, 2003) are reported (Table 3.2).

(U-Th)/He Thermochronology

Zircon (U-Th)/He analyses were conducted on samples 161-2 and 161-9 according to the methods outlined in Wolfe and Stockli (2010). Aliquots were assigned an 8% analytical error based on the long-term laboratory reproducibility of the Fish Canyon Tuff zircon standard (e.g., Reiners et al., 2002, 2004). Dates are reported based on the average of 3–6 single grains per sample and two times the larger of either the traditional or alternative standard error of the average calculation (Table 3.2). Full (U-Th)/He methodology is given in Chapter 1.

Table 3.1: Summary of sample lithology.

Sample	UTM Coordinates ¹		Mineral	Unit Name
	Easting (m)	Northing (m)		
161-2	352915	6961489	zircon	Sierra Chicharra qtz diorite
161-9	353490	6960937	zircon	Sierra Atacama diorite
191-N116	353908	6962863	zircon	Sierra Pajas Blancas granodiorite
161-14	353369	6961503	andradite	AFS Andradite Vein
181-N144	366414	6947441	andradite	Las Pintadas Andradite Vein
181-N144	366414	6947441	pyrite	Las Pintadas Andradite Vein
181-N144	366414	6947441	chalcopyrite	Las Pintadas Andradite Vein

¹Coordinates in Universal Transverse Mercator (UTM) World Geodetic System 1984 (WGS84).

Re-Os Geochronology

Pyrite and chalcopyrite powders from the Las Pintadas andradite vein were acquired using a diamond-tipped drill on targeted occurrences within hand samples under the binocular microscope, weighed, and loaded into cleaned Carius tubes. Powders were combined with isotopic spike solutions of single ¹⁸⁵Re and ¹⁹⁰Os (LL Runs) or a ¹⁸⁵Re-¹⁸⁸Os-¹⁹⁰Os mixed double spike (MD Runs; Markey et al., 2003) while sitting in a dry ice-acetone cold slush. Spike designations are given under the AIRIE Run designation in Table 3.3. About 4–6 mL or 12–15 mL concentrated HNO₃ was added for LL and MD sample digestions, respectively. Carius tubes were sealed and placed in an oven at 230°C for 12 hours. After sample digestion, Os was isolated using CHCl₃ solvent extraction and back extracted with HBr. Two micro-distillations using Cr(VI)-H₂SO₄ into HBr were used to further purify the Os separate. Rhenium was then separated by anion exchange resin column chromatography using 0.18 g Eichrom 1×8 100-200 mesh Cl-form resin. Further purification of Re was made using a resin bead clean-up step (Yang et al., 2020). Additional analytical protocol details are given in Zimmerman et al. (2014) and Georgiev et al. (2018).

Purified Re and Os were loaded onto outgassed Pt filaments along with Ba(NO₃)₂ and Ba(OH)₂ as activators, respectively. Both Re and Os isotopic ratios were measured by negative thermal ionization mass spectrometry (N-TIMS) on Triton machines at the AIRIE Program, Colorado State University. Re isotopic ratios were measured simultaneously on Faraday cups with 11-Å am-

plifiers, and Os isotopic ratios were acquired in peak-jumping mode by SEM. Measured isotopic ratios of Re and Os were corrected for isobaric oxygen interferences, mass fractionation of Os ($^{192}\text{Os}/^{188}\text{Os} = 3.08271$), and blank contributions. In all cases, Re and Os blanks are very low and at maximum constitute <0.018% of the Re measurement, and <0.32% of the Os measurement (Table 3.3). Except for one maximum sample, all Re blank contributions are <0.01%, and except for one maximum sample, all Os blank contributions are <0.24%. Re-Os isochrons were obtained using Isoplot 4.15 3.0 (Ludwig, 2003) with a ^{187}Re decay constant of $1.666 \times 10^{11}/\text{year}$ (Smoliar et al., 1996).

Table 3.2: Summary of U-Pb and (U-Th)/He data.

Sample	Date Range	U-Pb			(U-Th)/He				
		Mean Date $\pm 2\sigma$ (Ma)	n	MSWD	Mean Date $\pm 1\sigma$ (Ma)	n	SE ¹	Alt SE	Max SE
161-2	116.0-131.9	122 \pm 1.2	31/33	4.9	69 \pm 0.5	3/6	0.2	2.7	4.7
161-9	104.3-136.1	115 \pm 0.7	9	0.3	87.1 \pm 4.6	6/6	1.9	2.6	5.2
191-N116 ³	100.6-143.1	103.2 \pm 4.2	3	1.6	-	-	-	-	-
161-14 ³	-	96.1 \pm 2.3	38	1.3	-	-	-	-	-
181-N144 ³	-	115.7 \pm 1.2	55	1.4	-	-	-	-	-

¹SE denotes Standard Error (see Table 1.2). ²Date based on youngest 3 grains. ³Date calculated from Tera-Wasserburg lower intercept.

Table 3.3: Summary of Re-Os geochronometric data. Letter designation refers to spatially unique mineral separations within sample 181-N144.

AIRIE Run #	Mineral Fraction	Model Date (Ma) ¹	Error ²	Common Os (ppb)	Error (2 σ)	Re Blank (%) ³	Os Blank (%) ³
LL-1103	Pyrite (B)	122.7	1.9	0.6	2.5E-3	4.7E-5	3.2E-4
LL-1104	Pyrite (C)	114.7	1.7	0.1	8.9E-4	5.4E-5	9.9E-4
LL-1105	Chalcopyrite (D)	105.1	2.9	8.0E-3	2.8E-4	8.3E-5	3.3E-3
LL-1106	Chalcopyrite (E)	109.2	1.5	3.6E-2	3.4E-4	8.3E-5	2.4E-3
LL-1120	Pyrite (F)	115.2	1.3	0.3	3.8E-4	9.2E-5	1.1E-3
LL-1121	Pyrite (G)	114.1	1.3	0.3	3.1E-4	1.0E-4	1.0E-3
LL-1122	Chalcopyrite (H)	114.3	1.3	0.1	2.0E-4	1.8E-4	2.1E-3

¹Model date calculations assume $^{187}\text{Os}/^{188}\text{Os}_{\text{initial}} = 0.50 \pm 0.01$. ²Includes uncertainty on decay constant. ³Blank contributions as a percentage of the total Re and Os in each run.

AIRIE Run #	Mineral Fraction ¹	Model Date (Ma) ²	Error ³	$^{187}\text{Re}/^{188}\text{Os}$	Error (2 σ)	$^{187}\text{Os}/^{188}\text{Os}$	err (2 σ)	ρ^4
MD-1820	Pyrite (A)	153.5	6.7	1078.3	15.8	3.0	0.2	1.2E-5
MD-1856	Chalcopyrite (D)	114.8	0.7	22070.3	370.7	42.5	0.8	0.8

¹(D) refers to the same separate as LL-1105. ²Model date calculations assume $^{187}\text{Os}/^{188}\text{Os}_{\text{initial}} = 0.20$. ³Includes uncertainty on decay constant. ⁴Error correlation between $^{187}\text{Re}/^{188}\text{Os}$ and $^{187}\text{Os}/^{188}\text{Os}$.

3.3.3 Geochemistry

Whole-Rock Geochemistry

Altered samples 191-N90 and 191-N81 and their unaltered plutonic equivalents 191-N88 and 191-N124 were pulverized and sent to Activation Laboratories, Ltd. for major and trace element whole-rock geochemistry. Samples were subjected to a four-acid leach according to the 4E-Exploration analytical package and analyzed by inductively coupled plasma mass-spectrometry. Values are reported as weight percent oxides for major elements and ppm for trace elements (Table 3.4).

Stable Isotope Analysis

Stable isotope analyses were performed in order to understand the composition, temperature, and potential source of fluids responsible for andradite vein formation. Silicate mineral separates were washed in dilute HCl to remove carbonate, rinsed in deionized water, and hand-picked under a binocular microscope to avoid pieces with visible mineral inclusions. Iron oxides and mineral fragments with iron oxide inclusions were removed with a hand magnet. Approximately 2.0 mg of mineral separates were analyzed on a BrF₅ laser fluorination extraction line coupled with a Thermo MAT253 stable isotope ratio mass spectrometer at the University of Texas at Austin according to the methods presented in Sharp (1990). Garnet and quartz standards UWG-2 ($\delta^{18}\text{O} +5.8\text{‰}$, Valley et al., 1995) and Lausanne-1 ($\delta^{18}\text{O} +18.1\text{‰}$; in-house standard) were run as a part of the analytical session to track precision and accuracy of measurements. Analytical error is $\pm 0.1\text{‰}$ and silicate isotopic values are reported relative to Standard average Ocean Water (SMOW). For calcite $\delta^{18}\text{O}$ analyses, 0.25–0.5 mg of calcite was loaded into Exetainer vials, flushed with ultra-high purity He, and reacted with 103% H₃PO₄ at 50°C for ~2 hours following methods modified from Spötl and Vennemann (2003). Headspace CO₂ was analyzed on a Thermo Gasbench II coupled to a Thermo-Electron 253 mass spectrometer. Samples were calibrated to standards NBS-18 ($\delta^{18}\text{O}_{\text{PDB}} -23.01\text{‰}$, Verkouteren and Klinedinst, 2004), NBS-19 ($\delta^{18}\text{O}_{\text{PDB}} -2.2\text{‰}$, Verkouteren and Klinedinst, 2004), and UT-Marble (in-house). Analytical error is $\pm 0.13\text{‰}$ based on the long-term reproducibility of

Table 3.4: Whole-rock geochemistry data. Major elements are given in weight percent and trace elements are given in parts per million (ppm).

Element ¹	191-N90	191-N81	191-N88	191-N124
SiO ₂	63.42	66.96	63.66	51.38
TiO ₂	1.44	0.79	0.53	1.01
Al ₂ O ₃	14.59	17.70	17.32	18.92
Fe ₂ O ₃	3.18	0.92	4.41	9.92
MnO	0.04	0.02	0.09	0.14
MgO	3.79	0.99	1.78	4.59
CaO	6.95	4.89	4.84	10.11
Na ₂ O	5.55	7.08	4.75	3.74
K ₂ O	0.37	0.32	2.41	0.29
P ₂ O ₅	0.37	0.02	0.12	0.12
As	3	-	-	-
S	100	120	60	140
Rb	-	-	30	-
Ba	42	47	300	117
Sr	246	326	337	426
Cr	36	20	5	
Ni	13	6	6	8
V	165	64	79	312
Sc	21.6	3.3	12.3	34.7
Zn	6	7	21	53
U	6.3	-	1.4	-
Zr	408	146	123	56
Hf	12.1	-	-	-
Y	48	29	18	15
Th	5.8	4.4	6	-
La	19.5	6.7	15.4	6.3
Ce	68	26	31	31
Nd	48	23	16	10
Sm	10.7	5.4	3.2	2.5
Eu	2.9	0.8	0.9	0.9
Gd	-	-	-	-
Tb	1.7	-	-	-
Yb	7.3	3.7	2.8	2
Lu	0.88	0.31	0.28	0.12

¹Cs, Li, Pb, Ga, Ge, Bi, Nb, Ta, Tl, Pr, Gd, Dy, Ho, Er, and Tm were included in the analysis but fell below limits of detection.

Table 3.5: Oxygen stable isotope data.

Sample	Mineral	Mass (mg)	Pressure	$\delta^{18}\text{O}$	$\delta^{17}\text{O}$	$^{17}/^{18}\text{O}$	$\delta^{18}\text{O}_{\text{corr}}$
161-14	quartz	2.07	9.9	11.05	5.84	0.53	11.1
161-14	quartz	1.86	9.0	11.10	6.00	0.54	11.1
161-14	garnet	2.14	7.9	5.44	2.96	0.54	5.4
161-14	garnet	2.04	7.3	5.33	2.91	0.55	5.3
161-14	epidote	1.87	7.4	5.67	3.09	0.55	5.7
161-14	epidote	1.88	7.5	5.64	3.05	0.54	5.6
181-N144	actinolite	1.26	4.6	7.90	3.99	0.51	7.8
181-N144	garnet-dark	1.97	6.6	7.94	4.06	0.51	7.9
181-N144	garnet-light	2.14	7.1	8.45	4.46	0.53	8.4
181-N144	quartz	2.05	8.9	11.64	5.82	0.50	11.6

Temperature Calculations			
Mineral Pair	Temperature (°C)	+ (1 σ)	- (1 σ)
qtz-andr	431	24	27
qtz-epi	319	49	61
qtz-light andr	828	72	87
qtz-dark andr	691	53	61
qtz-act	559	46	54
cal-act	505	96	134

Fluid Composition Calculations			
Mineral	$\delta^{18}\text{O}_{\text{mineral}}$	Temperature (°C)	$\delta^{18}\text{O}_{\text{water}}$
andradite	5.4	430	8.1
quartz	11.1	430	7.1
quartz	11.1	320	4.6
epidote	5.7	320	5.0
light andradite	8.5	830	10.5
dark andradite	7.9	830	11.0
quartz	11.6	830	10.6
quartz	11.6	560	9.1
actinolite	7.9	560	9.7
actinolite	7.9	505	9.6
calcite	11.1	505	9.9

UT-Marble. Calcite isotopic values are reported relative to Pee Dee Belemnite (PDB). Thermometry calculations were performed utilizing ThermoOx 1.0.1 and the DBOXYGEN 2.0.3 database (Vho et al., 2020).

3.4 Results

3.4.1 Map relationships

Here we present crosscutting relationships determined via mapping and the timing of those relationships as determined by U-Pb geochronology. Exposures west of the AFS shear zone (Figure 3.3) consist of a medium-grained mesocratic biotite quartz diorite mapped by Arévalo (2005a,b) as the Sierra Chicharra pluton. Plagioclase is the dominant phase (55–65%) and is found as 2–4 mm euhedral- to subhedral crystals with oscillatory zoning, polysynthetic twins, Carlsbad twins, and rare deformation twins (Figure 3.4). Quartz occurs as anhedral ~1 mm crystals, is a lesser (10–15%) component of the rock, and does not display undulose extinction or dynamic recrystallization. Potassium feldspar is absent. Mafic phases include subequal proportions of 0.5–1 mm brown biotite and green hornblende, locally with apatite inclusions. Magmatic foliation defined by aligned biotite with an average orientation of 219/79 W is pervasive throughout the exposure of the pluton (Figure 3.5). Outcrop exposures are recessive, and the pluton is weathered to grus (Figure 3.6).

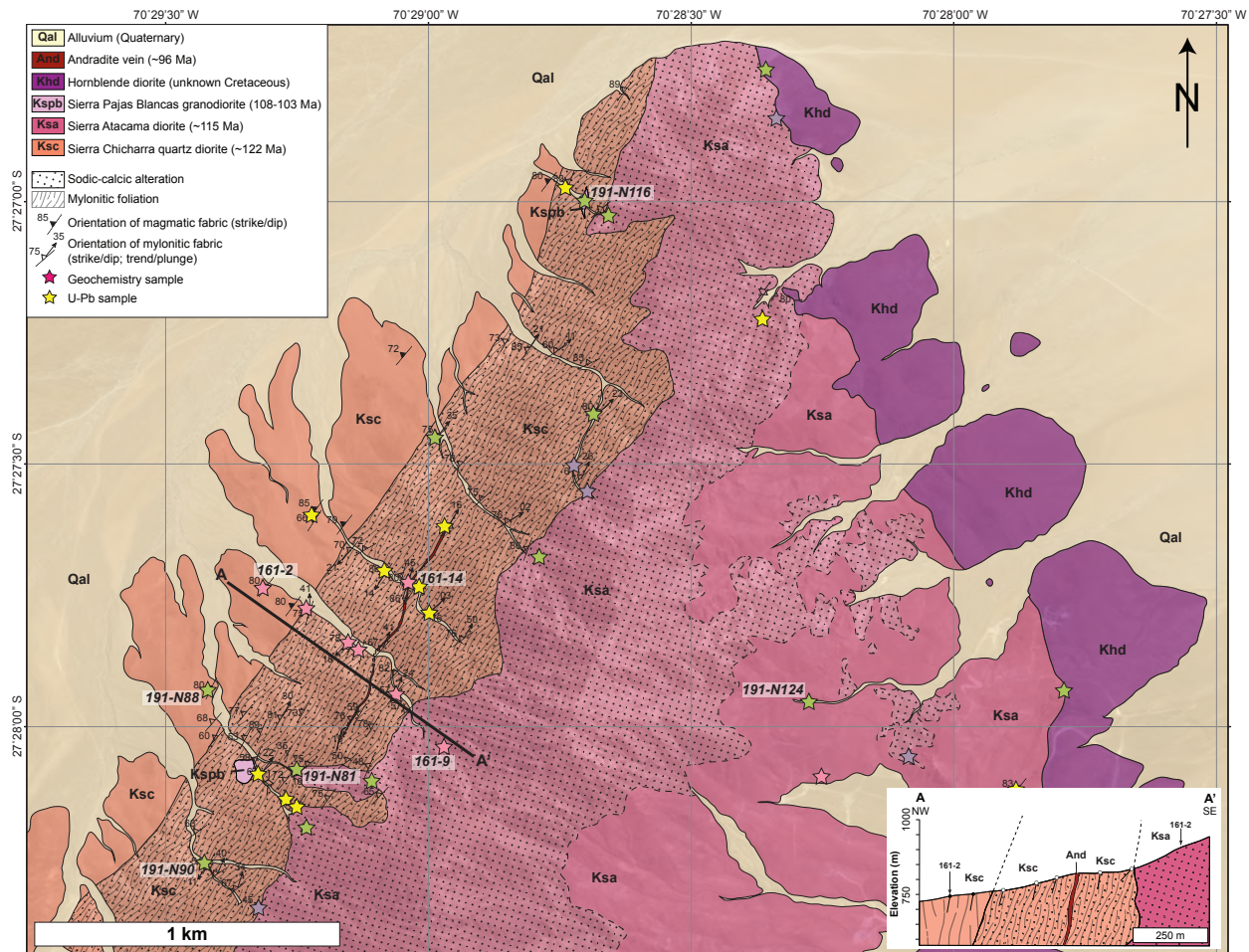


Figure 3.3: Detailed mapping of the ductile shear zone that defines the AFS in the Copiapó region. Yellow stars show the locations of new U-Pb dates, pink stars show the location of geochemical samples. See Plate 3 for 1:10,000-scale version of this map.

The Sierra Chicharra pluton is generally unaltered, with the exception of sausseritization in the Ca-rich cores of some plagioclase and local development of chlorite and titanite with increasing proximity to the shear zone. Near the margin of the shear zone, the magmatic fabric transitions to a zone of hydrothermally-altered protomylonitic and mylonitic fabrics described below. The Sierra Chicharra quartz diorite has a 122.0 ± 1.2 Ma zircon U-Pb date ($n = 31/33$; MSWD = 4.9, Figure 3.7) with a population of 7 older grains (~ 126 – 132 Ma) and 5 younger grains (~ 116 – 118 Ma). Decreasing the discordance threshold to $<5\%$ gives an a weighted mean date of 122.6 ± 1.2 Ma ($n = 27/33$, MSWD = 5.9). Th/U values consistently cluster around ~ 1 (0.95 ± 0.15 ; range 0.69–1.29) except for a few grains with a Th/U of ~ 0.23 – 0.28 . Grains with low Th/U are not restricted to a particular date range. Individual zircon (U-Th)/He aliquot dates cluster around 69 Ma (68.6–69.5 Ma) with one aliquot at 84.4 Ma (sample 161-2; Table 3.2).

The transition to protomylonites and mylonites correlates with the edge of a bleached zone of hydrothermal alteration trending $\sim 212^\circ$. Pinstripe ultramylonites with a "sugary" texture and well developed, distinctly green and white banding characterize the shear zone (Figure 3.6). Compositional banding is much more strongly developed than in the magmatic fabrics of the Sierra Chicharra quartz diorite, and spacing of foliation varies from the cm to mm-scale (Figure 3.4). Although the fabrics in the shear zone appear mylonitic at the outcrop scale, petrographic analysis reveals these fabrics are completely annealed. Dark green foliation planes are defined by aligned actinolite, epidote, and titanite. Locally, rutile mantled by elongate titanite is also present and actinolite shows undulose extinction. White bands are coarse, blocky plagioclase, which are grown around the mafic phases in a chessboard pattern in samples with closely spaced foliation and pinned between foliation planes where spacing is on the order of ~ 1 mm (Figure 3.7). Igneous plagioclase textures such as oscillatory zoning and polysynthetic twins are absent, and crystals are large (3 to >10 mm) compared to other phases (<1 mm, with most ≤ 0.5 mm). Together these observations indicate the plagioclase is a secondary alteration phase rather than an original igneous phase. Samples with very finely spaced foliation planes hosted in secondary feldspar are concentrated near the center of the shear zone.

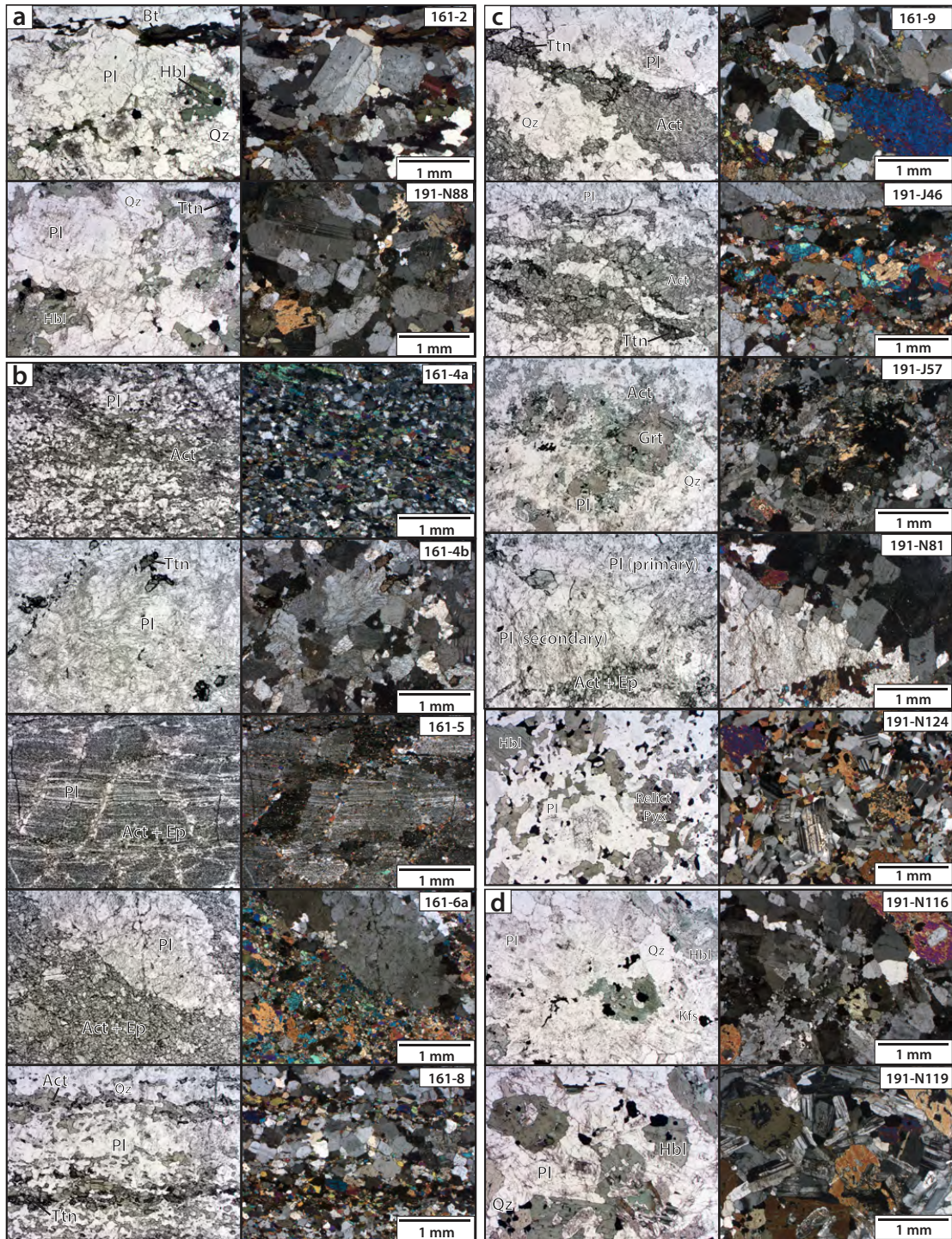


Figure 3.4: Photomicrographs of (a) the Sierra Chicharra quartz diorite west of the shear zone, (b) hydrothermally altered mylonitic shear zone defining the AFS, (c) bleached white appearance of the altered, unstrained Sierra Atacama diorite, and (d) the unstrained, unaltered Sierra Atacama diorite, hornblende granodiorite dike, and hornblende diorite. Abbreviations are as follows: Act = actinolite; Bt = biotite; Ep = epidote; Hbl = hornblende; Kfs = potassium feldspar; Qz = quartz; Pl = plagioclase; Pyx = pyroxene; Ttn = titanite.

The average mylonitic foliation orientation is 218/74 NW (Figure 3.5). Lineations are relatively rare and occur in ~37% of outcrops, dominantly plunging <45° from the NE. Lineations have an average orientation of 033/20. Kinematic indicators in the shear zone such as interactions between foliation planes and shear bands record sinistral shear as well as apparent reverse motion, but ϕ -clasts and the symmetric warping of foliation around boudinaged layers appear to record a high degree of coaxial strain. Near the center of this ~200–500-m-wide shear zone, foliation-parallel breccia zones up to 10 cm wide locally cut mylonites; however, a map-scale brittle fault is not present in this area. Breccias within the mylonite zone have angular clasts of the green-and-white banded ductile fabrics in a matrix of actinolite and epidote and do not show evidence of internal strain (Figure 3.4). Locally, the long axes of the actinolite and epidote in the breccia matrix are aligned, but the long axes of clasts do not have a preferred orientation and often display a jigsaw pattern in outcrop (Figure 3.6).

Within the shear zone a ~2–3 m wide andradite vein extends ~775 m along a NNE-SSW (~023°) trend. Vein mineralogy is dominantly (90–95%) euhedral brown garnet up to 0.5 cm with lesser euhedral green epidote up to 1 cm long, euhedral quartz up to 0.5 cm long, magnetite, and calcite. Quartz, epidote, and calcite are interstitial to garnet, indicating garnet crystallized before other phases. Locally, mineralogy varies to include anhedral masses of 0.5–1 mm apatite. Where this occurs, anastomosing veins of iron oxide often cut grain boundaries of the apatite. No sulfides are present. The margins of the vein are relatively sharp and lined with massive anhedral garnet grading into bleached wallrock over ~1–2 mm, which together with euhedral crystals within the vein indicates precipitation in an open space rather than replacement of country rock. There is no evidence for ductile or brittle deformation within the andradite vein.

The eastern margin of the shear zone is cut by an intrusive contact with a bleached but internally unstrained pluton with similar alteration mineralogy to that of the mylonites within the shear zone, containing abundant actinolite and epidote concentrated in veinlets surrounded by fractured plagioclase. Locally, veinlet-hosted actinolite is full of cleavage-parallel, sub- μm mineral inclusions, indicative of the presence of hydrothermal fluids during crystallization. Titanite and local sub-

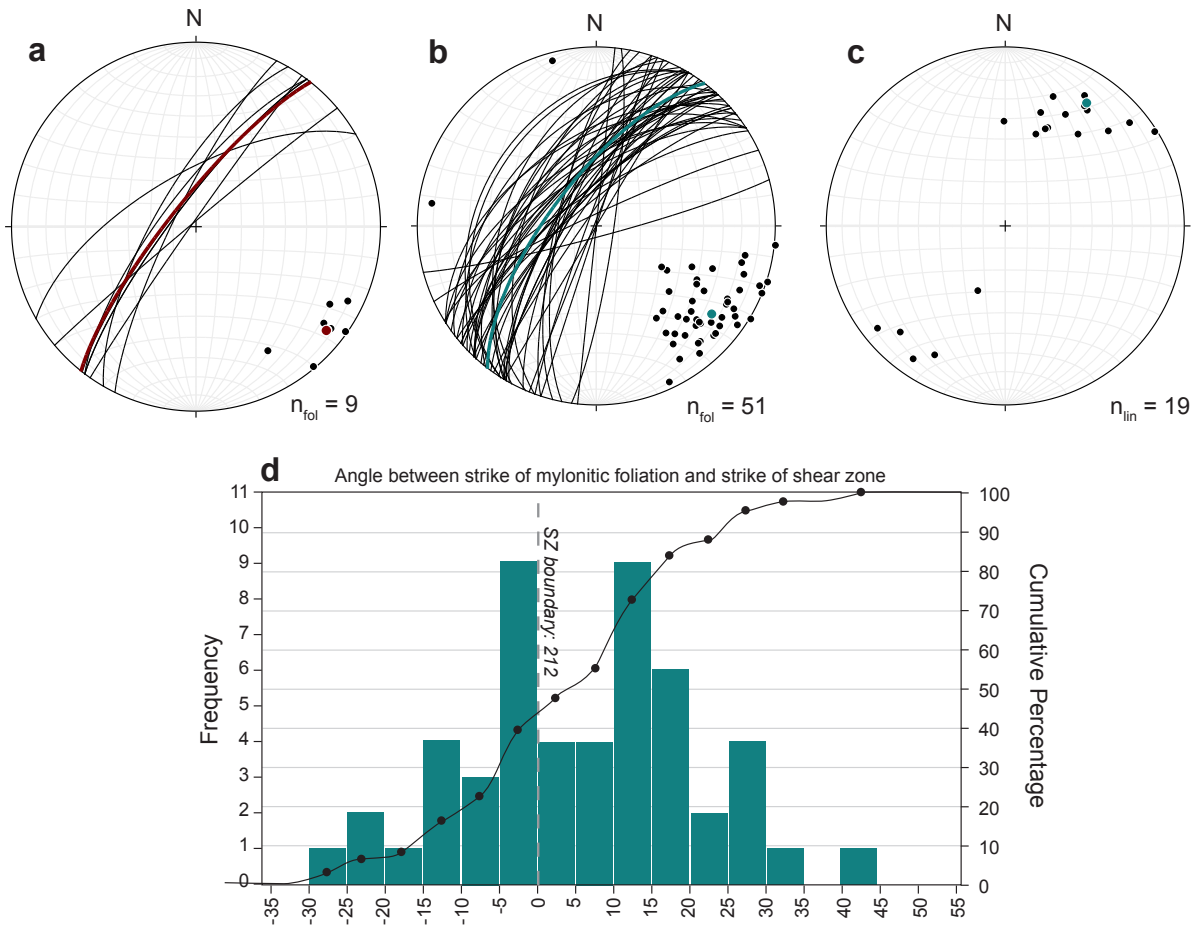


Figure 3.5: Stereograms of (a) planes and poles to the magmatic foliation within the Sierra Chicharra quartz diorite, (b) planes and poles to the mylonitic foliation within the shear zone, (c) mylonitic lineations in the shear zone. The angle between the shear zone boundary and mylonitic foliations is given in (d).

to anhedral brown garnet with rims of actinolite and titanite occur distributed within the pluton, not connected to obvious veins or fluid pathways, indicating alteration was pervasive throughout the pluton and not concentrated solely along veins. Textures within the bleached pluton are locally igneous rather than secondary, and alteration is incomplete as evidenced by the preservation of 1–2 mm subhedral plagioclase with original igneous textures including oscillatory zoning and polysynthetic twinning and the presence of large (>10 mm), cloudy, anhedral secondary feldspar with abundant fluid inclusions and no zoning or twinning (Figure 3.4). The igneous texture is subhedral granular, with quartz and plagioclase displaying straight, polygonal grain boundaries. Locally, bands of titanite and actinolite define compositional bands sub-parallel to zones of secondary feldspar development; however, undulose extinction and other evidence of internal mineral strain are lacking. The altered portion of this pluton is resistant and forms the ridgeline of the range. Moving farther to the east away from the shear zone, alteration is less pervasive, and the unaltered pluton appears to be a mesocratic medium-grained hornblende diorite. Some larger (0.75–1 mm) plagioclase crystals have relatively high-relief fractured cores with well-developed black-and-white polysynthetic twins with rims of lower-relief, dominantly gray and black twinned plagioclase, reflecting a change in composition. Most plagioclase consists of this outer composition and forms an anhedral granular texture of 0.25–0.75 mm interlocking crystals. Quartz is a minor phase and forms 0.05–0.25 mm anhedral crystals. Green hornblende and iron oxide phases form clusters that occasionally have ~0.5–1.5 mm relict cores of clinopyroxene with embayed edges. As with the altered portion of the pluton, there is no alignment of minerals, and the igneous textures do not record strain.

Zircon textures and U-Pb dates of the altered pluton are complex and show evidence of interaction with fluids. Cathodoluminescent imagery of the zircons from sample 161-9 shows complex internal textures with overgrowths (Figure 3.7). Cores retain oscillatory zoning, but the zones are often blurred. Other cores have convolute zoning patterns with complex patches of bright and dark CL response. Irregular dissolution/recrystallization fronts cut internal domains and are typically medium to bright gray. Overgrowths are typically medium gray and patchy, and in some grains

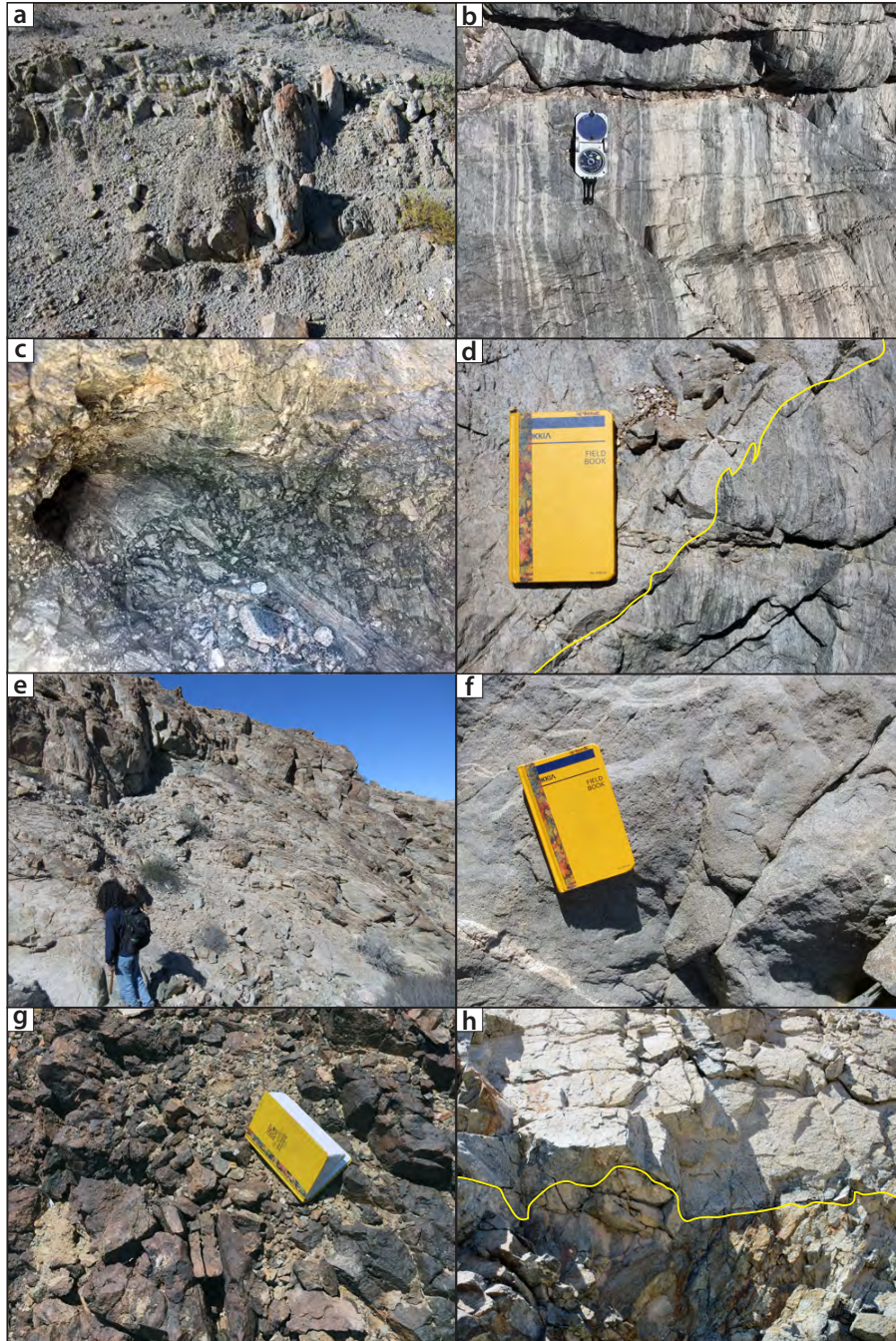


Figure 3.6: Field photographs showing (a) the magmatic foliation in the Sierra Chicharra quartz diorite west of the shear zone, (b) green and white banding in the hydrothermally altered mylonitic shear zone defining the AFS, (c) clasts of altered mylonite in a jigsaw breccia, (d) the unstrained, altered Sierra Atacama diorite cutting the mylonitic shear zone (yellow line), (e) bleached white appearance of the altered, unstrained Sierra Atacama diorite, (f) outcrop appearance of the unaltered, unstrained Sierra Atacama diorite, (g) outcrop of the ~2-3-m-wide andradite vein within the mylonitic shear zone, and (h) the fresh, unstrained hornblende diorite cutting the altered mylonite zone (yellow line).

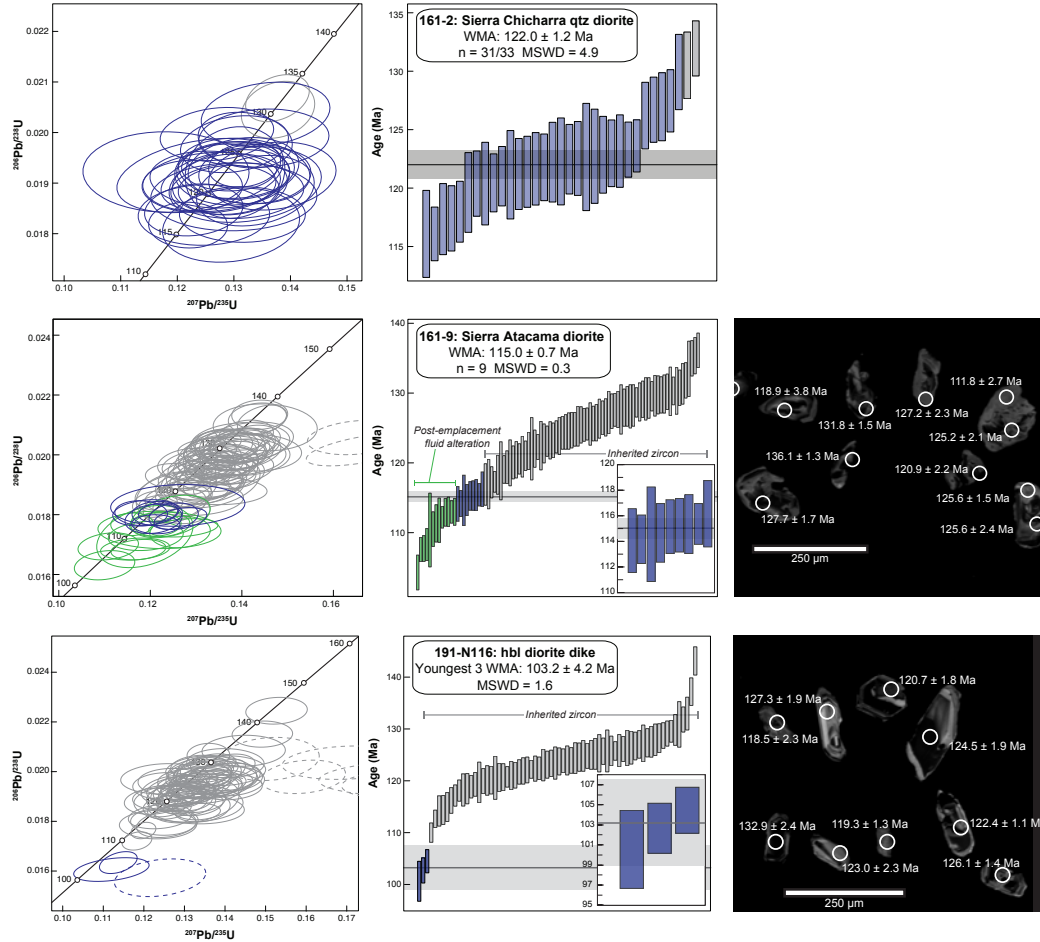


Figure 3.7: U-Pb concordia diagrams (left column) and weighted mean dates (right column) for zircon from the Sierra Chicharra quartz diorite, Sierra Atacama diorite, and hornblende granodiorite dike. Grains used to determine the weighted mean date are shown in blue, grains affected by hydrothermal alteration are shown in green, and inherited grains are shown in gray. Data have been filtered to 10% discordance and grains with >10% discordance are shown with dashed ellipses. Uncertainties are reported at 2σ .

this texture has almost completely replaced original internal textures. Complex internal zonation is reflected in the spread of U-Pb dates on the internal domains of single grains in polished mounts, which range from 118.9–136.1 Ma and lack a coherent single population of dates. This may indicate a significant component of inherited and/or antecrystic zircons, consistent with petrographic evidence for the inheritance of clinopyroxene and plagioclase cores into the magma. External domains documented in polished mounts range from 110.3–116.2 Ma, and may record a significant degree of recrystallization in the presence of fluids. Depth-profile analysis of additional zircons from this sample documented single grain dates ranging from 104.3–130.3 Ma. Grains of all ages have Th/U values ranging from 0.15–1.69 (average 1.03 ± 0.42) and do not show systematic variations in Th/U, [U], or degree of discordance with date. Coupled with petrographic evidence for a phase of syn-emplacement alteration and zircon U-Pb evidence from a hornblende diorite dike (discussed below), we interpret a 115 ± 0.7 Ma zircon U-Pb emplacement date for the pluton ($n = 9$, MSWD = 0.3, Figure 3.7). Increasing the discordance threshold to $<5\%$ for this set of grains yields a weighted mean date of 115.2 ± 1.9 Ma ($n = 8/9$, MSWD = 0.3). Zircon (U-Th)/He analysis produced an average date of 87.1 ± 5.2 Ma with individual grain aliquots ranging from 81.2–93.3 Ma.

A small intrusive body of unstrained medium-grained hornblende granodiorite and a hornblende granodiorite dike intrude the shear zone. These bodies are unaltered and have sharp contacts with the surrounding altered mylonite zone (Figure 3.6). The dike is dominantly subhedral plagioclase with Carlsbad, polysynthetic, and minor deformation twins with lesser amounts of ~ 0.5 mm quartz, 0.25–0.75 mm potassium feldspar, and 2–3 mm subhedral green hornblende with irregular grain boundaries (Figure 3.4). Locally there are finer-grained zones of feldspar (0.05–0.20 μm). These phases do not show undulose extinction or a preferential orientation. Alteration is limited to incipient development of sericite within plagioclase. Zircon grains from the hornblende diorite dike (sample 191-N116) are euhedral and have complex internal textures with igneous zoning and overgrowths, including core and rim relationships, convoluted zoning, and recrystallization fronts similar to those documented in the altered Sierra Atacama diorite (Figure 3.7). Cores are often

bright, with dark inner rims and medium-gray outer rims. Oscillatory zoning is almost entirely destroyed and replaced by mixed bright and black domains. Where oscillatory zoning remains, the zones have been blurred. Overgrowths are patchy in CL and uniformly medium-gray, and in some grains this patchy, medium-gray texture has replaced the entire zircon structure. Recrystallization fronts are irregular and crosscut other internal textures. U-Pb analyses of these grains yielded a range of single-grain dates between 114.2–132.9 Ma and two slightly older dates (137.2 Ma and 143.1 Ma) for grains with <10% discordance. Additional depth-profile analyses yielded a range of single-grain dates from 100.6–132.9 Ma. The range of dates for both analysis types overlaps with both the western Sierra Chicharra quartz diorite (125–128 Ma, biotite K-Ar; ArÁvalo, 2005a) and the eastern Sierra Atacama diorite (104–117 Ma; Arévalo, 2005a,b), including a population that overlaps the overgrowth dates in sample 161-9 (Figure 3.7). This overlapping range of dates is in conflict with field relationships documenting the intrusion of this dike after the alteration of the ~115 Ma Sierra Atacama diorite, and as such we interpret the majority of zircon grains from this dike to be inherited xenocrysts and/or antecrysts from the surrounding plutons. We note the absence of single-grain dates younger than ~114 Ma, and together with field evidence for the lack of alteration further supports an intrusion age of the Sierra Atacama diorite by ~115 Ma with continued hydrothermal alteration producing the ~114–104 Ma range of dates seen in sample 161-9. The youngest three depth-profile analyses give a weighted average of 103.2 ± 4.2 Ma (MSWD = 1.6) and are younger than single-grain dates documented in the other plutons. We note that the youngest grain is ~15% discordant, and removing this analysis gives a date of 103.7 ± 10.6 Ma. As such, we interpret the dike and small hornblende granodiorite intrusion to be no older than ~103 Ma.

Finally, a medium- to coarse-grained melanocratic hornblende diorite cuts both the annealed shear zone and the bleached Sierra Atacama diorite at the northern end of the study area and continues to the southeast. Mineralogically, this body is 30–55% 1–4 mm plagioclase with well-developed oscillatory zoning, Carlsbad twins, and polysynthetic twins, ~5–10% <1 mm anhedral quartz, and ~35–65% eu- to subhedral green hornblende, locally up to cm-scale (Figure 3.4).

All phases are unaltered with minimal development of sausserite within plagioclase and limited replacement of hornblende by biotite, and there is no alignment of grain long axes. Undulose extinction is locally present in quartz, but there is no evidence of dynamic recrystallization. The contact with the Sierra Atacama diorite is intrusive rather than faulted. This contact becomes hard to trace in the field due to the similarity of the color index and mineralogy, but is likely defined by mine workings on the eastern side of the study area. Workings are associated with the development of hydrothermal actinolite at $\sim 103\text{--}99$ Ma (102.7 ± 1.4 Ma and 99.3 ± 1.3 Ma, Díaz et al., 2003) but lack the characteristic bleaching of the western margin of the Sierra Atacama diorite where it cuts the shear zone.

3.4.2 Geochemistry

Whole-rock Geochemistry of Plutons & the Shear Zone

Whole-rock geochemistry of the ~ 122 Ma Sierra Chicharra pluton (sample 191-N88) west of the shear zone has a major element composition of 63.7% SiO₂, 17.3% Al₂O₃, 4.8% CaO, 4.8% Na₂O, 4.4% Fe₂O₃, 2.4% K₂O, 1.8% MgO, 0.5% TiO₂, and minor MnO and P₂O₅ (Table 3.4). These values are consistent with the petrographic description of the pluton as a quartz diorite composed of plagioclase, quartz, biotite, hornblende, minor oxide phases, and trace apatite, zircon. Relative to the Sierra Chicharra quartz diorite, the annealed mylonitic fabrics (sample 191-N90) have a similar percentage of SiO₂ (63.4%), less Al₂O₃ (14.6%), K₂O (0.4%), and Fe₂O₃ (3.2%) and more Na₂O (5.6%), CaO (7.0%), MgO (3.8%), and TiO₂ (1.4%). The gain in CaO and TiO₂ is documented by the presence of calcic minerals like titanite, epidote, and actinolite, and loss of Al₂O₃, K₂O, and Fe₂O₃ is consistent with the absence of biotite and oxide phases.

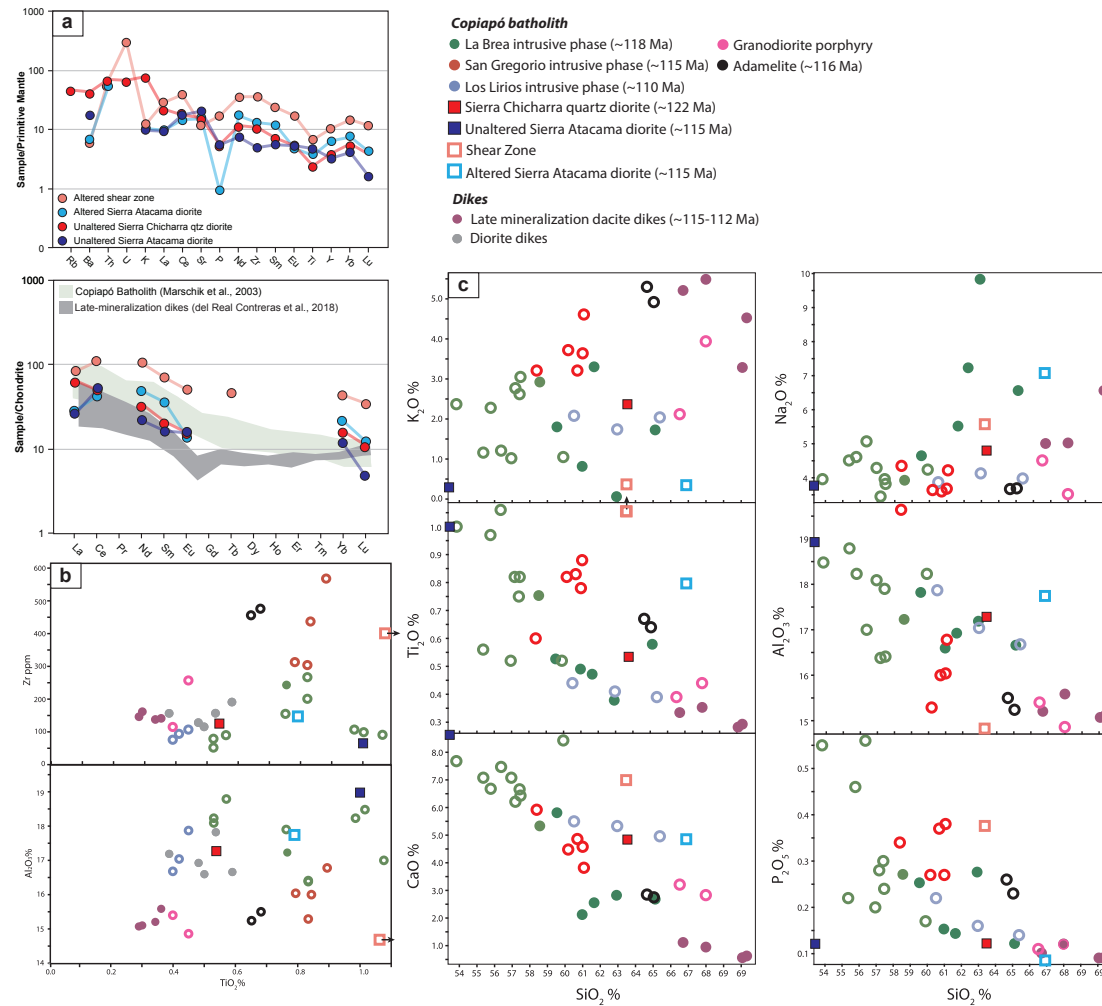


Figure 3.8: Plots of whole-rock geochemistry data including (a) trace element concentrations relative to primitive mantle and chondrite (Sun and McDonough, 1989). (b) Immobility comparison to other phases of the Copiapó batholith. (c) Harker diagrams showing mobile and immobile element evolution with regard to SiO₂. Open circles are data from Marschik et al. (2003), closed circles are from del Real Contreras et al. (2018), and squares are from this study. Modified from del Real Contreras et al. (2018).

A sample of the altered portion of the Sierra Atacama pluton collected immediately east of the intrusive contact with the shear zone (sample 191-N81) is composed of 67.0% SiO₂, 17.7% Al₂O₃, 7.1% Na₂O, 4.9% CaO, 1.0% MgO, 0.9% Fe₂O₃, 0.8% TiO₂, with minor K₂O, MnO, P₂O₅. The low values of MnO, MgO, and Fe₂O₃ is reflected in the absence of biotite, hornblende, pyroxene, and oxide phases. Secondary plagioclase, titanite, actinolite, epidote, and local andradite account for the abundances of SiO₂, Al₂O₃, CaO, Na₂O, and TiO₂. The freshest possible sample of the Sierra Atacama pluton (sample 191-N124) was collected about 1.5 km east of the shear zone for comparison to the unstrained but hydrothermally-altered pluton that cuts the shear zone. This pluton is composed of 51.4% SiO₂, 18.9% Al₂O₃, 10.1% CaO, 9.9% Fe₂O₃, 4.6% MgO, 3.7% Na₂O, 1.0% TiO₂, and minor K₂O, MnO, P₂O₅ (Table 3.4). This indicates the Sierra Atacama diorite is geochemically a gabbro, though the presence of anhedral hornblende with relict cores of clinopyroxene supports the petrographic description as a diorite.

Both altered phases are enriched in large ion lithophile elements (LILEs) and rare earth elements (REEs) relative to their assumed protolith. REE patterns between the three unstrained plutons (Samples 191-N81, 191-N88, and 191-N124) all show enrichment in the LREEs over the HREEs. Using an alternative set of trace elements (Rb, Ba, Th, U, K, La, Ce, Sr, P, Nd, Zr, Sm, Eu, Ti, Y, Yb, and Lu), similar patterns are present: the altered lithologies are more enriched than their respective protoliths. The Sierra Chicharra quartz diorite shows higher LILE concentrations of Rb, Ba, Th, U, and K than the Sierra Atacama diorite (Figure 3.8). The lack of an Eu anomaly within the shear zone may reflect complete replacement of the original assemblage, liberating Eu for incorporation into replacement phases, or suggest the two samples are not derived from the same magma. Exact HREE patterns are hard to discern due to most elements falling below levels of detection during analysis, but [Sm]>[Yb]>[Lu] for all samples, indicating the HREE pattern is most likely slightly negatively sloped. The rocks in the shear zone are the most enriched in LILEs and REEs relative to all other lithologies, and is 2.5–3.5 times enriched relative to the Sierra Chicharra quartz diorite (Figure 3.8).

We acknowledge the significant uncertainty in comparing two geochemical samples separated by >1 km. This sample separation was necessary due to the extensive distribution of alteration, which ranged from complete near the shear zone boundary to partial with increasing distance from the contact. The contact between altered and unaltered pluton is both irregular and gradational; however, there is no clear contact across that distance and we believe sample 191-N124 is a representative sample of the Sierra Atacama diorite based on mapping. While map relationships suggest both outcrops are part of the same pluton, many arc plutons within the Coastal Cordillera record significant zonation (e.g., Rodríguez et al., 2019), and the possibility remains that these two outcrops of the Sierra Atacama diorite may have had significantly different unaltered compositions.

In order to test the original similarity of these samples and compare them to the wider Copiapó batholith, we compared these data to published results from Marschik et al. (2003) and del Real Contreras et al. (2018). The Sierra Chicharra quartz diorite and both the altered and unaltered domains of the Sierra Atacama diorite plot within the immobile element array of the La Brea, San Gregorio, and Los Lirios phases of the Copiapó batholith (Figure 3.8). The Sierra Chicharra quartz diorite, although categorized as a part of the Coastal Cordillera arc, is most similar to the youngest Los Lirios phase of the Copiapó batholith and late diorite dikes in the region in terms of both Al_2O_3 and TiO_2 versus SiO_2 and Zr and Al_2O_3 versus TiO_2 . The unaltered domain of the Sierra Atacama diorite is most similar to the mafic end-member of the La Brea pluton. The altered domain of the Sierra Atacama diorite also shows the strongest similarity to the La Brea pluton in terms of Zr and Al_2O_3 versus TiO_2 , but shows a relative enrichment in TiO_2 versus SiO_2 , and a very strong enrichment in Al_2O_3 versus SiO_2 . Enrichment in TiO_2 is reflected in the presence of titanite in the altered domain of the pluton, but the large difference in SiO_2 relative to Al_2O_3 may be more easily explained by original geochemical differences in a zoned pluton. We further note that while the shear zone does plot in the Copiapó batholith array for Al_2O_3 versus SiO_2 , it is significantly different from the intrusive phases in terms of TiO_2 versus SiO_2 , Zr versus TiO_2 , and Al_2O_3 versus TiO_2 . This strong difference in immobile element values may suggest this part of the shear zone

is derived from a different protolith entirely, or that sodic-calcic alteration of the Sierra Chicharra quartz diorite significantly affected the values of typically immobile elements.

U-Pb Geochronology & Stable Isotope Geochemistry of the Andradite Vein

Energy-dispersive X-ray spectroscopy analysis of garnet yielded a dominantly andraditic composition, which is favorable for U-Pb analysis due to its ferric Fe content (Table 3.6 Seman et al., 2017). U concentrations range between 0.23–5.3 ppm and some domains include significant proportions of non-radiogenic or common Pb (Pb_c) in the garnet lattice. Andradite dates were plotted in Tera-Wasserburg space to account for the presence of Pb_c and record a $^{238}U/^{206}Pb$ lower intercept date of 96.1 ± 2.1 Ma (MSWD = 1.3, n = 38, Figure 3.9). While some individual analyses have high analytical error, the lower intercept is tightly constrained with no evidence of spread along concordia. Petrography indicates euhedral garnet was an early-crystallizing mineral within the vein, and therefore this date records crystallization of the andradite vein. Oxygen isotope ($\delta^{18}O_{SMOW}$) values for quartz, epidote, and garnet mineral separates from within the vein are strongly positive, ranging from +5.7‰ for epidote, +5.4‰ for garnet, and +11.1‰ for quartz (Table 3.5). The low degree of scatter between duplicated analyses and linear trend of $\delta^{17}O$ versus $\delta^{18}O$ values suggests all three minerals grew in equilibrium, allowing for the calculation of temperatures and fluid $\delta^{18}O$ values. Andradite-quartz thermometry calculations yield crystallization temperatures of $431 \pm 27/-24^\circ C$ in the presence of +6.8‰ to +7.0‰ $\delta^{18}O$ fluids and epidote-quartz thermometry calculations yield temperatures of $\sim 319 \pm 61/-49^\circ C$ in the presence of +6.8‰ to +6.9‰ $\delta^{18}O$ fluids.

3.4.3 Las Pintadas Andradite Vein

The Las Pintadas deposit is located ~ 19 km SE of the AFS study area described above. Mineralization occurs as a series of stacked manto horizons near the contact between the Upper Andesite of the Punta del Cobre Formation and base of carbonate-rich Abundancia Formation (Chañarcillo Group), stratigraphically above the Candelaria deposit, and is cut by unmineralized dikes from the adjacent ~ 110 Ma Los Lirios pluton (Arévalo, 2005b; del Real Contreras et al., 2018). Ore

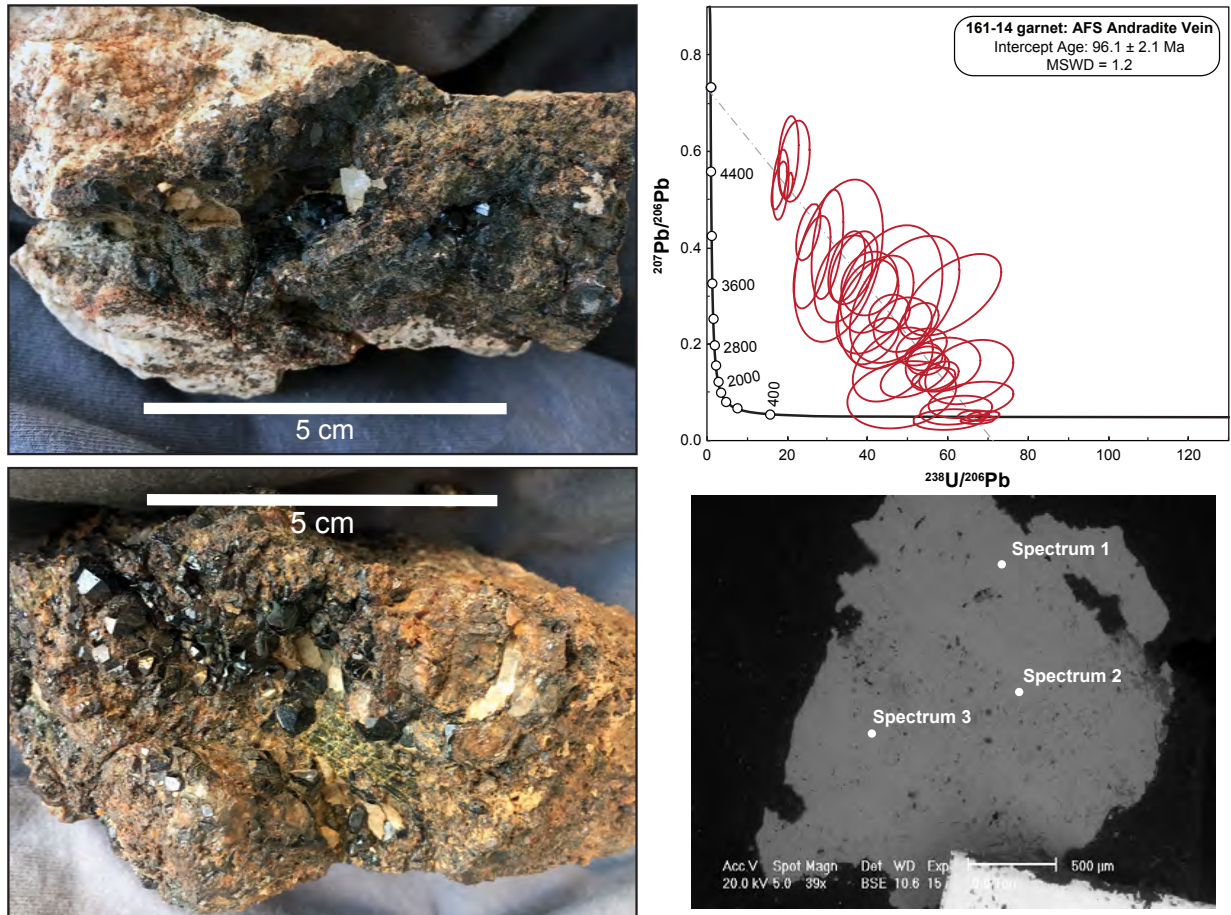


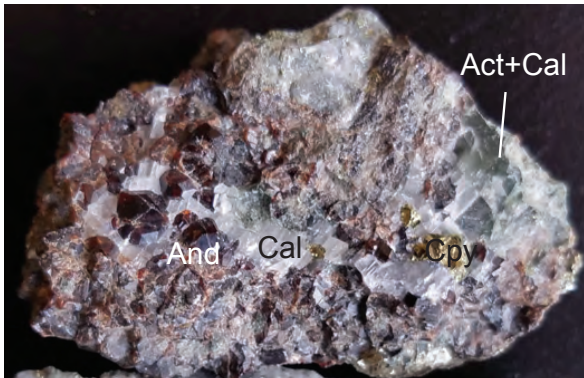
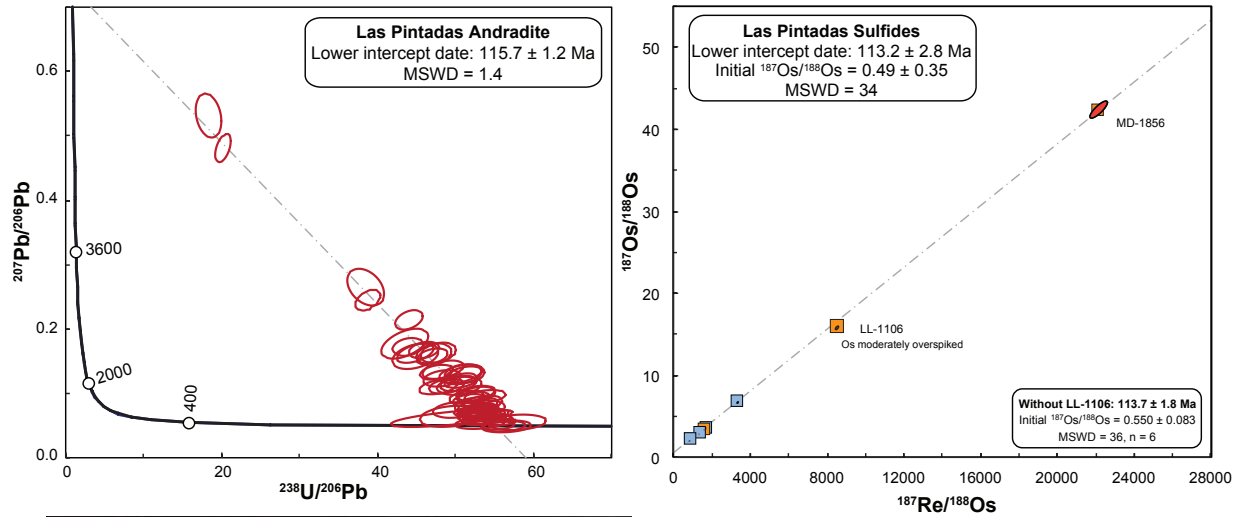
Figure 3.9: Photographs (left), U-Pb Tera-Wasserburg concordia diagram, and backscatter electron image showing points of EDS composition of garnet from the AFS andradite vein. U-Pb uncertainties are reported at 2σ , and EDS values for the 3 spectra points are given in Table 3.6.

Table 3.6: Garnet compositions from EDS data from the AFS Vein.

Spectrum 1			Spectrum 2			Spectrum 3		
Element	Wt%	1σ	Element	Wt%	1σ	Element	Wt%	1σ
Ca	32.18	0.60	Ca	33.94	0.62	Ca	30.47	0.62
Mn	1.12	0.33	Mn	0.00	0.00	Mn	0.00	0.00
Fe	20.86	0.70	Fe	23.34	0.74	Fe	23.37	0.74
Al	4.13	0.24	Al	2.89	0.22	Al	3.20	0.21
Si	20.25	0.45	Si	19.95	0.46	Si	19.92	0.44
O	21.47	0.66	O	21.47	0.65	O	23.05	0.66
Total	100.01		Total	101.59		Total	100.01	

mineralogy includes a supergene assemblage of atacamite+malachite+bronchantite+azurite copper oxides and hypogene chalcopyrite+pyrite that is both disseminated and concentrated within veins below the level of oxidation. The veins are composed of euhedral brown andraditic garnet up to 0.5 cm in diameter, anhedral chalcopyrite and pyrite, and massive transparent calcite up to 0.5 cm with intergrown acicular actinolite (Figure 3.10). The calcite surrounds the euhedral garnet. All phases are fresh with no evidence of retrogression. Pyrite and chalcopyrite mostly occur in distinct patches on other mineral phases including calcite and garnet. The sulfides are minimally intergrown, and there is no visual indication that pyrite and chalcopyrite are paragenetically distinct. Magnetite is locally present, but apatite is entirely absent from this assemblage.

We report new dates for mineralization at Las Pintadas: two separate 3- and 4-point isochrons comprised of chalcopyrite and pyrite, a single-aliquot Re-Os date on highly radiogenic chalcopyrite, and an andradite U-Pb date (Figure 3.10). Pyrite and chalcopyrite have distinct Re-Os concentration data and Re-Os isotopic data suggesting that any contamination of one sulfide by another during mineral separation was minimal. All concentrations are in the low ppb range, mostly in the tens of ppb range. Pyrites have systematically higher Re (76–129 ppb) compared to chalcopyrites (38–62 ppb). Interestingly, pyrites also have systematically higher Os (207–749 ppb) than chalcopyrites (58–165 ppb). The $^{187}\text{Re}/^{188}\text{Os}$ ratios for pyrites (851–3350) are generally lower than for chalcopyrites (1628–39,275), and the $^{187}\text{Os}/^{188}\text{Os}$ ratios for pyrites (2.24–6.91) are correspondingly lower than chalcopyrites (3.6–69). Isochrons for each sulfide are determined separately: a pyrite-only isochron yields an age of 112.9 ± 8.8 Ma ($\text{Os}_{\text{initial}} = 0.58 \pm 0.28$, MSWD = 64, $n = 4$) and a chalcopyrite-only isochron yields an age of 114 ± 30 ($\text{Os}_{\text{initial}} = 0.2 \pm 6.5$, MSWD = 43, $n = 3$). There is no difference in the ages or $\text{Os}_{\text{initial}}$ for each of these sulfides at the 2σ level; however, we acknowledge this statement is limited by the low number of data points. We further acknowledge the high degree of uncertainty in the $\text{Os}_{\text{initial}}$ value derived from the isochron containing all seven analyses (0.49 ± 0.35). The role of $\text{Os}_{\text{initial}}$ was investigated with double-spiked analyses. One of the analyses, chalcopyrite MD-1856, is a true low level, highly radiogenic sample (LLHR) and is insensitive to $\text{Os}_{\text{initial}}$. LLHR samples yield the most accurate and precise Re-Os



MD-1856 (chalcopyrite)				Os isotopic composition LLHR		
$^{187}\text{Re}/^{188}\text{Os}$	2σ abs err	$^{187}\text{Os}/^{188}\text{Os}$	2σ abs err	rho	assumed Os initial	Model Age (Ma)
22070.3	370.7	42.451	0.847	0.8246	0.2	114.80
22070.3	370.7	42.451	0.847	0.8246	0.5	113.98
22070.3	370.7	42.451	0.847	0.8246	0.9	112.90

Re-Os model ages are highly insensitive to initial $^{187}\text{Os}/^{188}\text{Os}$ ratio in age calculation

MD-1820 (pyrite)				Os isotopic composition is NOT LLHR		
$^{187}\text{Re}/^{188}\text{Os}$	2σ abs err	$^{187}\text{Os}/^{188}\text{Os}$	2σ abs err	rho	assumed Os initial	Model Age (Ma)
1078.3	15.8	2.960	0.237	1.22E-05	0.2	153.47
1078.3	15.8	2.960	0.237	1.22E-05	0.5	136.81
1078.3	15.8	2.960	0.237	1.22E-05	0.9	114.59

Re-Os model ages are sensitive to assumed initial $^{187}\text{Os}/^{188}\text{Os}$ ratio in age calculation

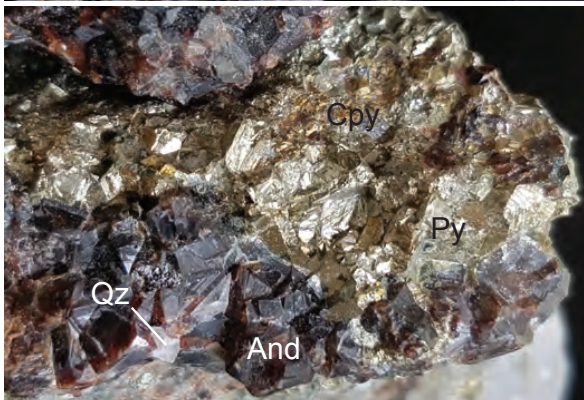


Figure 3.10: U-Pb Terra Wasserburg concordia diagram for garnet and Re-Os isochron diagram for sulfide phases at the Las Pintadas andradite vein. Uncertainties are reported at 2σ . 6 LL and 1 MD analyses are included in the Re-Os isochron and 2 unacceptably overspiked samples were omitted. An alternative age with sample LL-1106 (moderately overspiked) is also shown. Chalcopyrite is shown in orange and pyrite is shown in blue. Table below the Re-Os isochron shows the response of LLHR sample MD-1856 and non-LLHR sample MD-1820 to differing values of $\text{Os}_{\text{initial}}$, which does not have a strong influence on the date. Photographs show sample analyzed for geochronology and stable isotopes. Abbreviations are as follows: Act = actinolite; And = andradite; Cal = calcite; Cpy = chalcopyrite; Qz = quartz; Py = pyrite.

ages (Stein et al., 2000). The age of MD-1856 remains between 113–115 Ma based on a wide range of O_{Sinitial} isotope ratios (0.2, 0.5, 0.9), indicating these are the most robust Re-Os data. Another analysis, MD-1820, is not a LLHR sample, and is highly sensitive to the O_{Sinitial} value. Using the isochron-derived value of 0.5 yielded a model date of ~ 137 Ma, which is not in agreement with the isochronous data. An O_{Sinitial} value of 0.9 was necessary to produce a model date in agreement with other analyses (~ 115 Ma).

Re-Os dates are within error of our new andradite Tera-Wasserburg lower intercept $^{238}\text{U}/^{206}\text{Pb}$ date of 115.7 ± 1.2 Ma ($n = 55$, $\text{MSWD} = 1.4$, Figure 3.10). U concentrations range between 0.9–9.2 ppm and have a low contribution of non-radiogenic Pb_c compared to the andradite vein along the AFS. Euhedral garnet is petrographically determined to be an early-crystallizing phase, indicating this date records the inception of vein development. Light and dark garnet domains also do not show a difference in U-Pb date and the lower intercept is tightly clustered with no evidence of spread along concordia, suggesting this vein did not experience multiple distinct phases of garnet growth.

Silicate oxygen stable isotope values ($\delta^{18}\text{O}_{\text{SMOW}}$) are +7.8‰ for actinolite, +7.9‰ for dark garnet, +8.4‰ light garnet, and +11.6‰ for quartz (all values are ± 0.1 ‰; Table 3.5). Calcite has values of -7.7‰ $\delta^{13}\text{C}_{\text{PDB}}$ and -19.2‰ $\delta^{18}\text{O}_{\text{PDB}}$ (+11.1‰ $\delta^{18}\text{O}_{\text{SMOW}}$). Petrographic textures show euhedral garnet with interstitial quartz, and intergrown calcite and actinolite with patches of sulfide mineralization. While there is no fracture and infill of garnet and quartz domains with the intergrown calcite and actinolite, the calcite+actinolite is confined to the interstitial space between the euhedral garnet and is not intermixed with the quartz+garnet domain. We interpret these textures to reflect two separate equilibrium pairs: quartz and garnet, and calcite and actinolite. Thermometry calculations for quartz and garnet yield temperatures of 828–840°C for light garnet and 670–690°C for dark garnet in equilibrium with fluid compositions of +10.0 to +10.8‰, respectively. Thermometry calculations for calcite and actinolite yield crystallization temperatures of 505°C in the presence of fluids with $\delta^{18}\text{O}_{\text{SMOW}}$ values of +9.5 to +9.7‰.

3.5 Discussion

3.5.1 Pluton Emplacement and Evolution of the Shear Zone

Field relationships clearly outline the following series of events in this area: emplacement of the ~122 Ma Sierra Chicharra quartz diorite during AFS strain, post-kinematic emplacement of the ~115 Ma Sierra Atacama diorite and coeval sodic-calcic alteration, and post-kinematic crystallization of the andradite vein at ~96 Ma. The Sierra Chicharra quartz diorite has a K-Ar date of 128–125 Ma (Arévalo, 2005a) that is close to but older than our new ~122 Ma zircon U-Pb date. The older K-Ar date may have a component of excess Ar due to hydrothermal alteration of the host phase, which can be expected in open systems that extensively interact with fluids (e.g., Harrison and McDougall, 1980; Kelley et al., 1986; Kendrick et al., 2001a,b; Turner et al., 1993; McDougall and Harrison, 1999). Synkinematic emplacement of the Sierra Chicharra quartz diorite during AFS strain is suggested by field relationships including a transition from magmatic fabrics throughout the pluton to protomylonitic fabrics across the western margin of the shear zone, and ultimately to ultramylonites within the shear zone. The orientation of the magmatic fabrics (219/79 NW) and solid-state fabrics (218/74 NW) are concordant (Figure 3.5), and the contact between magmatic fabrics and solid-state fabrics is locally gradational with regards to original lithology. The NW shear zone boundary is well defined, and both high- and low-strain mylonitic foliations strike at a low angle to the shear zone strike (Figure 3.3, Figure 3.5). If the shear zone was only a product of sinistral simple shear, lower-strain fabrics should be systematically oriented more clockwise than the higher strain zones (e.g., Chapter 1). Both apparent sinistral and reverse-sense indicators are present at the outcrop scale in the mylonites. Together with NE-plunging lineations across the NW-dipping shear zone, these kinematics record a component of shortening in addition to sinistral lateral shear across the shear zone. Sinistral transpression is also consistent with the presence of S>L fabrics, which suggest a component shear-zone perpendicular flattening (Sanderson and Marchini, 1984; Fossen and Tikoff, 1993).

Post-kinematic plutonism indicates ductile deformation ended by ~115 Ma and lasted <8 Myr. The eastern margin of the hydrothermally-altered mylonites is cut by the Sierra Atacama diorite,

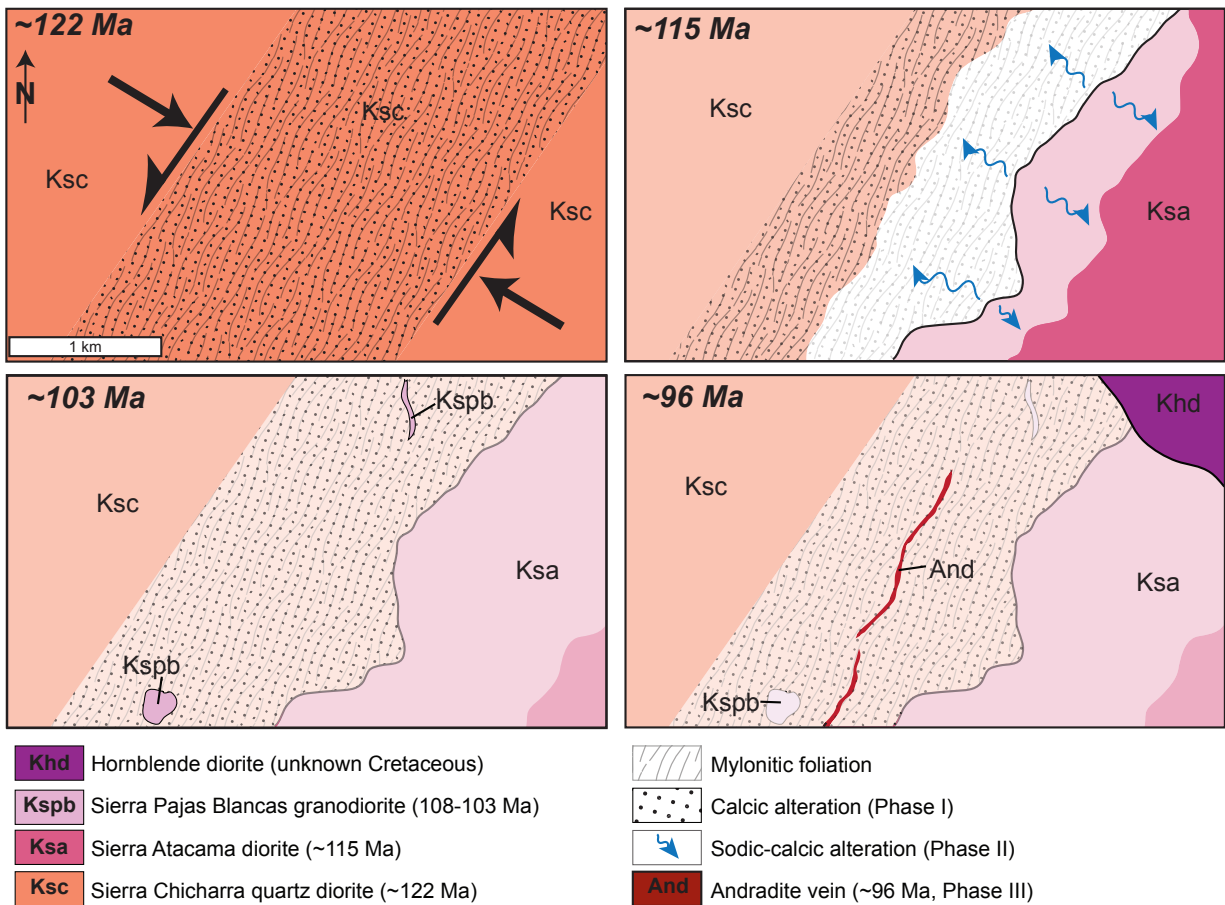


Figure 3.11: Temporal evolution of magmatism, deformation, and alteration along the AFS. Intrusion of the ~122 Ma Sierra Chicharra quartz diorite is associated with the development of a NW-dipping sinistral shear zone as documented by a progression from magmatic fabrics within the pluton to protomylonitic to ultramylonitic fabrics within a ~200–500-m-wide shear zone along the main branch of the AFS. An initial phase of alteration is associated with shearing, recorded by internally strained actinolite and elongate titanite aligned parallel to foliation planes. Deformation ceased by ~115 Ma, documented by the intrusion of the unstrained Sierra Atacama diorite that cuts all mylonitic fabrics. Annealing of mylonitic fabrics in the shear zone and sodic-calcic alteration of the western margin of the unstrained diorite record a post-kinematic phase of alteration associated with the intrusion of the Sierra Atacama diorite. Two phases of intrusions cut annealed shear zone fabrics: several small hornblende granodiorite bodies within the shear zone, and a larger unstrained hornblende diorite that intrudes both the shear zone and the unstrained Sierra Atacama diorite. A final phase of alteration is marked by the development of an ~775 m-long post-kinematic andradite vein through the center of the annealed shear zone at ~96 Ma.

which has a K-Ar date of 117–104 Ma (Arévalo, 2005a,b) that overlaps with the overgrowths on zircon used here to determine a \sim 115 Ma crystallization age. Locally, aligned actinolite defines a very weak fabric subparallel to the shear zone, and veinlets also often form in subparallel orientations. This may suggest that the pluton records the ending stages of deformation, or may alternatively reflect emplacement-related flow. Two exposures of \sim 103 Ma hornblende granodiorite also cut the shear zone and are entirely unstrained. Based on similar mineralogy and ages, we interpret these small intrusions to be part of the Sierra Pajas Blancas granodiorite (108–103 Ma; Arévalo, 2005a) that cuts the AFS shear zone to the north of the study area. Finally, the hornblende diorite that cuts the shear zone and Sierra Atacama diorite at the north end of the study area is mapped as the La Brea diorite faulted against the Sierra Atacama diorite; however, our mapping has demonstrated the contact is intrusive rather than faulted. Furthermore, this pluton is distinctly mafic and melanocratic compared to the Sierra Chicharra quartz diorite, Sierra Atacama diorite, and La Brea diorite, and may represent a late hornblende diorite such as the small \sim 98 Ma hornblende clinopyroxene diorites mapped \sim 18 km to the E near the town of Paipote (Arévalo, 2005a) and \sim 18 km to the SE of the shear zone along Quebrada Los Toros (Arévalo, 2005b). These outcrops occur along the trace of the Paipote fault, a NW-dipping reverse fault associated with the Late Cretaceous Chañarcillo thrust belt.

Zircon (U-Th)/He cooling dates in the unaltered Sierra Chicharra quartz diorite and altered phase of the Sierra Atacama diorite postdate crystallization of the skarn vein and record cooling through \sim 180°C. In the Sierra Atacama quartz diorite, individual grains range from 81.2–93.3 Ma. A single aliquot from the altered Sierra Chicharra diorite overlap with the range of the Sierra Atacama dates (84.4 Ma) while the rest of the aliquots form a tight cluster around \sim 69 Ma (68.6–69.5 Ma). Regionally, K-Ar and $^{40}\text{Ar}/^{39}\text{Ar}$ dates cluster at 121–128 Ma, \sim 116 Ma, and 104–110 Ma and are interpreted to represent the emplacement and cooling of the Sierra Chicharra, La Brea, and Sierra Pajas Blancas plutons through 310–345°C (Arévalo, 2005a, and references therein). Dikes within 1 km of the shear zone intruded between 101–80 Ma (K-Ar whole rock and amphibole, Lledó, 1998; Arévalo, 2005a). Both the \sim 69 Ma cooling date in the unaltered Sierra

Chicharra quartz diorite and ~ 87 Ma cooling date in the altered Sierra Atacama diorite post-date all Ar system cooling dates and therefore record regional cooling following the latest stages of magmatism recorded by dikes (~ 87 – 85 Ma). The difference in cooling dates across the sheared pluton could be consistent with a component of Late Cretaceous E-side-up dip-slip motion between the plutons; however, the lack of any significant brittle faults contradicts this hypothesis.

The single ~ 84 Ma zircon (U-Th)/He date from the unaltered Sierra Chicharra diorite and presence of ~ 87 Ma dates in the altered Sierra Atacama diorite alternatively suggest changes in the diffusivity of He within the zircon lattice as a result of hydrothermal fluid flow and alteration. Complex internal textures seen in the CL imagery of Sierra Atacama diorite zircons analyzed for U-Pb were most likely produced by extensive interaction with fluids during syn-emplacement hydrothermal alteration. These zones have extremely non-uniform CL response with some bright areas and some black areas as described above, reflecting variations in the zircon lattice that can change the diffusion domain size and diffusion pathways within individual crystals. Internal heterogeneities in parent isotope distribution are also likely based on differences in CL brightness. Variations or zonation in parent isotope are not accounted for in the calculation of (U-Th)/He dates, which assume a homogenous parent isotope distribution, and can significantly affect dates: zircon with U-Th enriched rims can be up to 40% inaccurate, and depleted rims can be up to $\sim 25\%$ inaccurate (Farley et al., 1996; Reiners et al., 2004; Hourigan et al., 2005). Our data show a difference of $\sim 20\%$ between the Sierra Chicharra quartz diorite and Sierra Atacama diorite which we attribute to the combination of complex, discordant internal textures produced by recrystallization in the presence of fluids and the resulting heterogeneous distribution of parent isotope concentrations throughout the zircon, together resulting in non-standard diffusion kinetics and anomalously old ages in the altered pluton.

3.5.2 Comparison to Regional Magmatism & Deformation

Ductile deformation in the Copiapó region is localized to the margins of Early Cretaceous plutons, and the timing of shear zone development (122–115 Ma) overlaps with activity of the AFS

elsewhere along the El Salado segment (Figure 3.12). The end of shear zone activity by ~ 115 Ma agrees with the relatively short duration of ductile deformation along the northern El Salado segment and is similar to the ending of slip documented by the ~ 110 Ma latest-kinematic dike that cuts the eastern branch of the AFS at 25.56°S (Chapter 1). These results are also in agreement with recent work documenting coeval main-stage mineralization and transpressional shearing along the intrusive contact of the San Gregorio intrusive with the Chañarcillo basin contemporaneous with batholith emplacement and the onset of basin inversion and folding (del Real Contreras et al., 2018) and precipitation of copper ores under a transpressional regime at the Dominga Fe-Cu deposit (Heuser et al., 2020). The SE-directed convergence vector beneath the N-striking Peru-Chile trench through the thermally weakened Early Cretaceous arc and Copiapó batholith produced a transpressional strain field across the NNE-striking shear zone recorded by component of coaxial flattening and oblique sinistral-reverse shear. Elsewhere along the AFS, Ruthven et al. (2020) document Early Cretaceous transpression along the southern Pajón segment where the Pajón fault strikes $\sim 020^\circ$ and dips steeply east. In contrast, Cembrano et al. (2005) and Veloso et al. (2015) document transtension along the northern end of the Pajón segment, where major faults strike NNW to NW. Along much of the northern and the central El Salado segment north of Copiapó where the dominant trend of the AFS is \sim N-S, sinistral shear dominates and with no evidence for widespread transpression nor transtension (Chapter 1). The patterns of AFS-related strain are regionally consistent with varying orientations of the branches and a uniform Early Cretaceous SE-directed convergence across the Coastal Cordillera.

A notable difference between the AFS near Copiapó compared to the rest of the El Salado segment is the distinct lack of brittle faults overprinting mylonitic fabrics and the failure of the shear zone to evolve to a large brittle fault. Several small brittle faults and foliation-parallel cataclasite zones are present; however, we interpret the lack of a major brittle fault across this portion of the AFS to reflect the influence of the younger age of magmatism in this area compared to the rest of the El Salado segment. Our dates are consistent with published data recording magmatic peaks at 140–105 Ma, 96–76 Ma, and 65–58 Ma (Farrar et al., 1970; Arévalo, 1995, 1999, 2005a; Ullrich

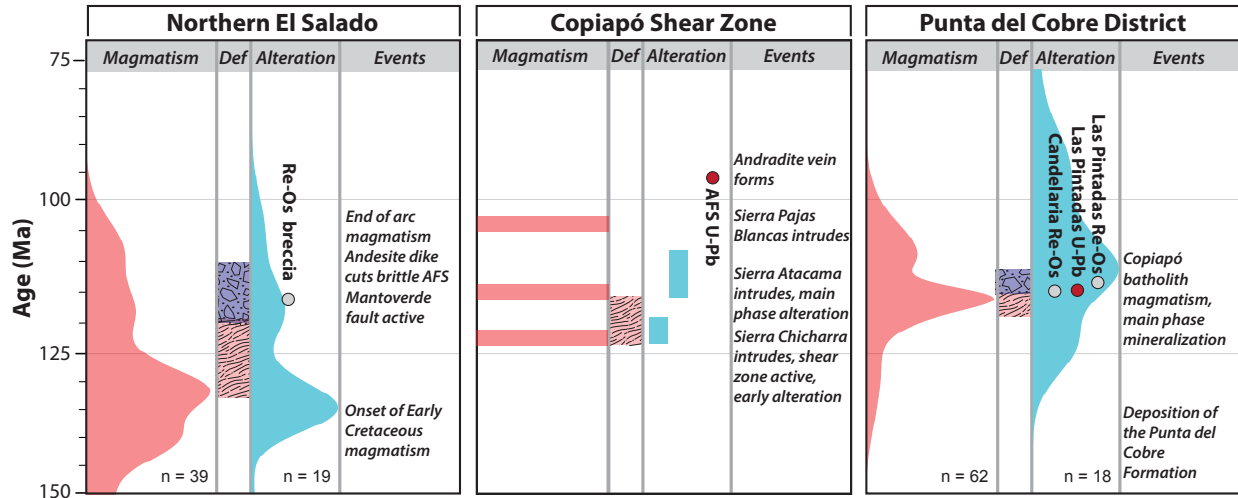


Figure 3.12: Time (vertical axis) vs. N-S trend (horizontal axis) diagram summarizing magmatism, deformation, alteration and tectonic events along the northern El Salado segment, Copiapó shear zone, and Punta del Cobre district. In the Magmatism column, kernel density estimate plots of our new dates compiled with published plutonic and volcanic zircon U-Pb data are shown in red. Plots were constructed with a bandwidth of 3 and a bin width of 5. In the Deformation column (Def), duration of deformation determined by field relationships is shown in the red bar, with ductile deformation noted by the wavy pattern and brittle deformation noted by the block pattern. In the Alteration column, curves are actinolite, adularia, and sericite K-Ar and $^{40}\text{Ar}/^{39}\text{Ar}$ from published literature. Individual data points in the Alteration column are sulfide Re-Os and andradite U-Pb dates. Sources of published data are given in Appendix 3.6.

et al., 2001; Marschik and Söllner, 2006; Girardi, 2014). The oldest peak overlaps with documented Early Cretaceous magmatism along the northern El Salado segment, but the two younger pulses postdate the eastward migration of the arc during the Paleogene, and are not recorded along the rest of the Coastal Cordillera. However, unlike the northern portion of the El Salado segment, magmatism continued beyond ~ 105 Ma with the emplacement of the polyphase Copiapó batholith until ~ 97 Ma (Farrar et al., 1970; Arévalo, 1995, 1999; Ullrich et al., 2001; Girardi, 2014). The continued intrusions of magmatic bodies maintained elevated geothermal gradients in this area beyond the end of slip along the El Salado segment, and therefore slip never progressed into the brittle regime prior to the shift from SE-directed oblique convergence to E-directed shortening, which began in this area in the earliest Albian (Maksaev, 1990; Gana and Zentilli, 2000). Furthermore, the annealing of mylonitic fabrics and coarse grain sizes of secondary plagioclase formed during alteration indicates high temperatures outlived deformation.

Table 3.7: Classification of alteration types based on mineralogy and textures. Abbreviations are as follows: act = actinolite, alb = albite, all = allanite, ap = apatite, bt = biotite, ca-amp = calcic amphibole, carb = carbonate, chl = chlorite, cpx = clinopyroxene, cpy = chalcopyrite, epi = epidote, grt = garnet, hem = hematite, ilm = ilmenite, kfs = potassium feldspar, mgt = magnetite, olig = oligoclase, py = pyrite, qtz = quartz, rt = rutile, scap = scapolite, tour = tourmaline, ttn = titanite.

Alteration Facies	Major Minerals	Accessory Minerals	Iron Oxides	Textures
Na(-Ca), Type A	act, olig	ttn, rt, ap, epi, cpx	none, mgt and ilm destructive	destructive
Na(-Ca), Type B	scap, ca-amp	ttn, epi, rt, ap	low-Ti mgt in veins, destructive regionally	can be destructive
Na	alb, py, chl	hem, carb	none, mgt destructive	destructive
K	qtz, tour, kfs, bt	not specified	none	kfs selvages
Ca	epi, grt	all, act, py, cpy	none	increased porosity

3.5.3 Sodic-calcic Hydrothermal Alteration

Repeated pulses of alteration associated with the intrusion of plutons have been documented across the Punta del Cobre district, with each intrusion producing its own hydrothermal system (e.g., Kreiner, 2011). Fresh outcrops of plutons weather to grus and are recessive, whereas altered rocks form the prominent outcrops. The Copiapó batholith is extensively altered to a variety of alkali-dominated assemblages including sodic-calcic, sodic, and potassium alteration assemblages occurring at a shallow crustal levels ($\leq 4-6$ km) along the margins of plutons and major structures (e.g., Kreiner, 2011; Barton et al., 2013).

Along the AFS, the sodic-calcic alteration assemblage that characterizes both the shear zone (plagioclase+actinolite+epidote+titanite+rutile) and the western portion of the undeformed Sierra Atacama diorite matches the mineralogy of widespread sodic-calcic alteration in the Punta del Cobre district. Elongate actinolite, epidote, and titanite are well aligned with the relict mylonitic fabric in the shear zone, suggesting they developed synkinematically. Undulose extinction in actinolite,

which is concentrated in compositional bands, mantling of rutile by titanite, and large, blocky plagioclase that envelops other phases and compositional bands in the annealed shear zone indicates multiple phases of alteration. Similar alteration of a mylonite zone is documented at Cerro Negro Norte (Raab, 2001). Geochemically, the shear zone records a loss of K_2O and Fe_2O_3 and enrichment of Na_2O , CaO , MgO , TiO_2 related to the development of sodic-calcic minerals like titanite, epidote, and actinolite, and loss of original mafic phases. The shear zone is 2.5–3.5 times enriched in trace elements relative to the Sierra Chicharra quartz diorite (Figure 3.8).

We attribute initial alteration and synchronous ductile deformation documented by actinolite and epidote within the shear zone to be related to synkinematic intrusion of the Early Cretaceous Sierra Chicharra quartz diorite at ~ 122 Ma and ending prior to the intrusion of the Sierra Atacama diorite at ~ 115 Ma. The annealed "sugary" macroscopic texture of the green-and-white banded shear zone and the chessboard texture of the plagioclase grown around the actinolite, epidote, and titanite indicate one phase of alteration of the shear zone was most likely coeval with the alteration of the Sierra Atacama diorite and therefore also post-dated ductile deformation. Cataclasite mineralization is dominantly epidote and chlorite and occurs as angular pockets within the shear zone. This suggests they may be a product of hydrothermal brecciation related to fluid flow and alteration of the shear zone rather than the brittle overprinting of a ductile shear zone during a progressive deformation event, as is the case for mylonite zones along the margins of Early Cretaceous plutons elsewhere along the El Salado segment (e.g., Chapter 1).

Extensive sodic-calcic alteration of western exposure Sierra Atacama diorite is documented by loss of mafic phases and presence of epidote, titanite, actinolite, and garnet within veinlets and represents a second phase of alteration associated with the intrusion of that pluton. The altered portion of the Sierra Atacama diorite is enriched in SiO_2 , Na_2O , and depleted in CaO , MgO , and Fe_2O_3 relative to the unaltered diorite, which is reflected in the absence of mafic phases. The lack of strain in the pluton indicates that phase of alteration post-dates ductile deformation (≤ 115 Ma). Local alteration of the eastern margin of the Sierra Atacama diorite unrelated to shear zone activity is recorded by actinolite $^{40}Ar/^{39}Ar$ dates (102.7 ± 1.4 Ma and 99.3 ± 1.3 Ma, Díaz et al.,

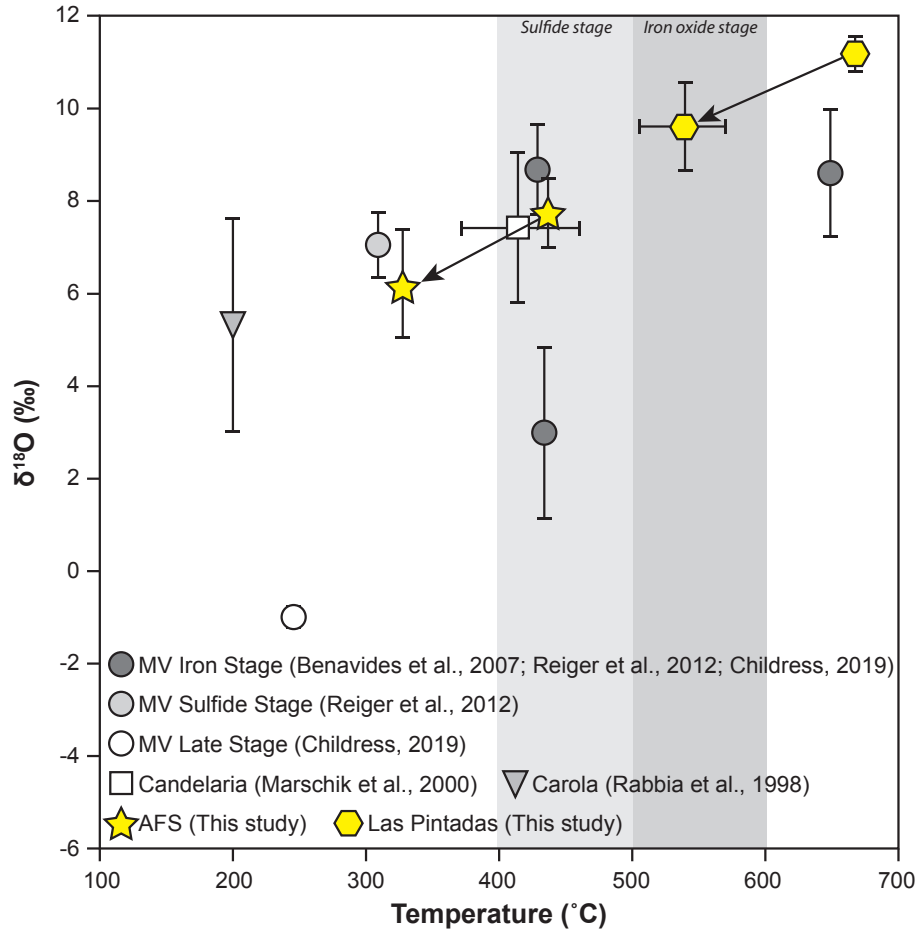


Figure 3.13: Comparison of equilibrium fluid $\delta^{18}\text{O}$ compositions and crystallization temperatures from this study to other deposits in the Chilean Iron Belt. Iron oxide and sulfide ore stages are based on data from Ullrich and Clark (1997) and (Hopf, 1990).

2003) in mine workings ~1–2 km to the east of the shear zone. The limited alteration footprint, spatial distance from the shear zone, differing alteration assemblage, and actinolite dates indicate this event was separate from the pulse that annealed the shear zone. Actinolite $^{40}\text{Ar}/^{39}\text{Ar}$ alteration dates overlap with the emplacement of the Sierra Pajas Blancas pluton, located north of the ductile shear zone. Formation of the unaltered, undeformed andradite vein at ~96 Ma documents yet another pulse of post-kinematic hydrothermal alteration. The ~17 Myr gap between the intrusion of the postkinematic Sierra Atacama diorite and formation of the vein that clearly cuts the annealed shear zone indicate these were distinct alteration events rather than a single, continuous event. The pervasive sodic-calcic alteration of the shear zone and margin of the Sierra Atacama diorite indicates fluids preferentially exploited the strong vertical anisotropy of foliation planes along the transcrustal AFS (e.g., Tornos et al., 2020) and pluton margins as fluid pathways. However, despite the coeval timing of alteration with the economic Punta del Cobre district, fluids along the AFS experienced a much higher degree of wallrock interaction without a central brittle fault to serve as a focused conduit that may have prevented the formation of an economic deposit.

Finally, the calcic andradite+epidote+magnetite+quartz+calcite+apatite mineralogy of the vein matches the sulfide-poor calcic epidote+quartz(\pm actinolite \pm andradite) ore assemblages seen elsewhere in the Punta del Cobre district (Ryan et al., 1995; Ullrich and Clark, 1999; Marschik et al., 2000; Marschik and Fontboté, 2001a; Kreiner, 2011; Barra et al., 2017). The vein clearly cuts the annealed fabrics of the shear zone, indicating the episode of fluid flow that produced the andradite vein post-dates both previous alteration events. In contrast with the diffuse alteration throughout the shear zone, the vein has sharp contacts with the wall rock indicate concentrated fluid flow along an opening-mode conduit that may have been a result of high fluid pressures as hydrothermal fluids exsolved from an underlying pluton. Petrographic textures showing interstitial quartz and epidote between euhedral garnet crystals indicate garnet was the first mineral to crystallize. Garnet records the composition of the fluid present during growth (e.g., Clechenko and Valley, 2003), and is expected to have $\delta^{18}\text{O}$ values between +5‰ and +8‰ when crystallized in equilibrium with magmatic fluids (Bowman, 1998). Therefore, strong positive $\delta^{18}\text{O}$ values for garnet (+5.4‰),

other mineral phases, and the calculated equilibrium fluid (+6.8‰ to +7.0‰) from the vein suggest fluids were magmatically derived. Petrography and stable isotope thermometry suggests crystallization of the andradite vein in an open conduit at ~400°C. The ~96 Ma andradite crystallization date only slightly postdates emplacement of a ~98 Ma hypabyssal hornblende clinopyroxene diorite mapped nearby (Arévalo, 2005a,b), and may indicate magmatically-derived hydrothermal fluids were sourced from the deeper reaches of that pluton. The strong magmatic signal recorded by the stable isotope signature of the minerals is not surprising given the lack of sedimentary rocks in the study area, and does not support the influence of evaporate-derived brines. A lack of sulfides may be an additional consequence of the presence of the andradite vein between two dioritic plutons rather than within a volcanoclastic sequence. The abundance of iron oxides, lack of sulfides, and ~400°C crystallization temperatures could indicate the vein formed as a part of the iron oxide stage of IOCG deposit genesis. The local presence of iron oxide-apatite domains in an otherwise typical IOCG-type sulfide-poor calcic assemblage may also suggest this vein represents a transition between IOA-type mineralization and IOCG-type mineralization (see below).

3.5.4 Comparison to Las Pintadas & the Punta del Cobre District

At Las Pintadas, andradite+actinolite+magnetite+quartz+calcite+pyrite+chalcopyrite mineralization does feature sulfide phases in high enough concentrations to make the deposit economic for Cu (Marschik and Fontboté, 2001a). Actinolite is present rather than epidote, and is intergrown with calcite that fills void spaces between other phases. Sulfides are also anhedral and occur on the surfaces of garnet and calcite in distinct patches with minimal intergrowth between pyrite and chalcopyrite. Iron oxides are locally present, but apatite is absent. This mineralization assemblage matches the main ore stage at Candelaria (Ryan et al., 1995). Temperatures and fluid compositions derived from oxygen stable isotope values agree with the petrographic determination of mineral paragenesis: quartz and garnet crystallized at 828–840°C (light garnet) and 670–690°C (dark garnet) in equilibrium with fluid compositions of +10.0 to +10.8‰ $\delta^{18}\text{O}_{\text{SMOW}}$, followed by crystallization of calcite and actinolite at ~505°C in the presence of fluids with $\delta^{18}\text{O}_{\text{SMOW}}$ values

of +9.5 to +9.6‰. The ages derived from both Re-Os and U-Pb overlap within error and agree with petrographic textures indicating early growth of garnet (115.7 ± 1.2 Ma) followed by crystallization of chalcopyrite (114 ± 30 from isochron, 114.8 ± 1.5 from LLHR analysis) and pyrite (112.9 ± 8.8 Ma).

Oxygen stable isotope values for dark and light garnet fractions and the calculated equilibrium fluids are higher than those along the AFS and are dominantly magmatic in signature. The temperature recorded by calcite+actinolite is also high, and falls at the top of the range proposed for the sulfide ore stage at the Carola deposit (400–500°C, Hopf, 1990). These temperatures are near the upper limit of magmatic-hydrothermal systems (Seedorff et al., 2005; Koděra et al., 2014; Weis et al., 2014), and likely reflect the formation Las Pintadas deposit at a shallow level proximal to its inferred source, the ~115 Ma San Gregorio pluton (Kreiner, 2011). Equilibrium fluid compositions $\delta^{18}\text{O}$ values in excess of +8‰ indicate magmatic fluids interacted with or mixed with another fluid source such as evaporite brines or fluids derived from metamorphic devolatilization in the thermal aureole during pluton emplacement (e.g., Bowman, 1998; Clechenko and Valley, 2003). Given the high temperatures recorded by stable isotope values, close proximity to coeval plutons, and volcanoclastic host sequence, we favor a component of metamorphic devolatilization over deeply circulating brines. These data combined with dates suggest the Las Pintadas andradite vein formed from a single pulse of magmatically derived fluids, and mineralization occurred during progressive crystallization in a cooling hydrothermal system.

Interaction with the sedimentary host sequence may also explain the presence of sulfides at Las Pintadas and elsewhere in the Punta del Cobre district, and correspondingly explain the lack of sulfides in the andradite vein along the AFS shear zone, which is hosted in igneous rocks. If elevated oxygen isotope values for equilibrium fluids record metamorphic devolatilization of the Punta del Cobre and Abundancia Formations, they may also be suggesting a degree of assimilation that could have pushed the fluid to sulfur saturation and triggered the precipitation of sulfide phases. Pyrite from Las Pintadas has 76–129 ppb Re and 207–749 ppb Os and chalcopyrite has 38–62 ppb Re and 58–165 ppb Os. These values are higher than concentrations recorded in pyrite

and chalcopyrite from the Candelaria, Mantoverde, Casualidad, Diego de Almagro, and Barreal Seco IOCG deposits (2–149 ppb Re and up to 49 ppt Os) and similar to the [Re] from pyrite at the Los Colorados, El Romeral and Carmen IOA deposits (10.8–214 ppb; Barra et al., 2017). Osmium concentrations at Las Pintadas are higher than [Os] reported for both IOCG and IOA deposits (Barra et al., 2017). Initial Os values at Las Pintadas (0.49 ± 0.35) are higher than those documented throughout the Punta del Cobre district (0.36 ± 0.1 at Candelaria, 0.33 at Bronce, and 0.21–0.41 in regional plutons, respectively; Mathur et al., 2000, 2002), and show a greater degree of uncertainty. The relatively low values of the district suggest ore was dominantly sourced from the relatively primitive regional plutons, and that the higher Os_{initial} value at Las Pintadas may reflect incorporation of crustal material (e.g., Stein, 2014). High uncertainty can also indicate a mixture of source material with differing initial ratios (e.g., Mathez and Kent, 2007; Martin et al., 2010; McLeod et al., 2012). Variations may be a product of magma mixing in a long-lived arc environment, incorporation of sedimentary rocks such as the Punta del Cobre and Abundancia Formations influenced by heterogeneous detrital materials or diagenetic processes, or interaction with fluids released by dehydration or decarbonation reactions (Stein, 2014). In the context of independent oxygen stable isotope data, we interpret the higher and more uncertain Os_{initial} values to be a result of interaction with fluids produced by devolatilization reactions of the sedimentary host sequence at Las Pintadas.

At the district scale, magnetite-destructive sodic-calcic alteration focused along the AFS shear zone matches regional alteration patterns including pervasive, texturally destructive alkali-calcic-iron replacement of igneous host rocks by fine- to medium-grained alkali feldspar, actinolite or diopside, magnetite, hydrothermal titanite with local rutile cores, and variable proportions of biotite, epidote, anhydrite, scapolite, tourmaline, and quartz (e.g., Camus, 1980; Ryan et al., 1995; Marschik and Fontboté, 2001a; Barton et al., 2005, 2011; Kreiner, 2011). The calcic andradite vein has an assemblage similar to the epidote+quartz(\pm actinolite) veins documented at the Tigresa and San Francisco deposits (Kreiner, 2011) and the mineralized andradite skarns at Atacama Kozan and Las Pintadas (e.g., Barra et al., 2017). Prograde garnet dominates the skarn-type IOCG

deposits such as San Antonio, Panulcillo, and Las Pintadas (Fréaut and Cuadra, 1994) and is paragenetically equivalent to potassium feldspar+albite+quartz and biotite+magnetite assemblages in contiguous andesitic volcanic rocks at Panulcillo at the southern end of the Chilean Iron Belt (Hopper and Correa, 2000). Our geochemical data indicate the shear zone and altered Sierra Atacama diorite are enriched in Na₂O, CaO, MgO, SiO₂, and TiO₂, relative to their unaltered protoliths (Figure 3.8), consistent with recent work by Tornos et al. (2020) suggesting residual melts enriched in Ca, Mg, Si, Ti, and volatiles are responsible for the development of regional assemblages. The timing of alteration is compatible with known alteration and mineralization events documented throughout the district, including an early stage associated with emplacement of an Early Cretaceous Coastal Cordillera pluton, a major stage related to emplacement of La Brea diorite at ~117 Ma, and a final stage at ~115 Ma hosted in the San Gregorio monzodiorite (Zentilli, 1974; Marschik et al., 1997; Ullrich and Clark, 1999; Kreiner, 2011). Development of the AFS andradite vein at ~96 Ma post-dates mineralization elsewhere in the district and represents a separate mineralization event. Though the vein developed after the latest widely recognized ~115 Ma mineralization event in the Punta del Cobre district, it shares many characteristics with Punta del Cobre deposits and likely formed as a result of the same processes.

Fluid flow along the shear zone was distributed throughout the strongly-anisotropic transpressional mylonitic shear zone rather than focused along brittle faults during a transition to brittle transtension, which may have prevented the development of an economic deposit along this portion of the AFS. Many IOA and IOCG deposits are located along AFS-related N-S to NNE-SSW subvertical structures such as dilatational jogs or pull apart structures (e.g., El Romeral, Algarrobo), at the intersection of NE-SW and NW-SE trending subsidiary faults (e.g., Tofo, Cristales, Fresia), or in extensional duplexes (Cerro Negro Norte, Dominga, Los Colorados; Bonson, 1998; Raab, 2001; Veloso et al., 2017) or transtensional stepovers (Mantoverde, Vila et al., 1996; Rieger et al., 2010). A few small deposits are related to subsidiary faults located as far as 27 km east of the main AFS (e.g., Carmen de Fierro, Maria Ignacia), similar to the position of the Las Pintadas deposit and Punta del Cobre district ~18–22 km east of the AFS in this region. The temporal association

between IOA and IOCG mineralization and sinistral slip suggests the formation of both deposit types requires the transcrustal faults such as the AFS to facilitate the rapid ascent of deeply generated melts and associated fluids to shallow depths along focused, strongly anisotropic pathways to minimize interactions with wallrock and maintain a strong magmatic to magmato-hydrothermal fluid signature (e.g., Tornos et al., 2020).

Our stable isotope results from the andradite vein overlap with the reported values for quartz associated with chalcopyrite at Candelaria (+11.2 to +12.6‰ and +5.9 to >+8.9‰, respectively) and fluid inclusions homogenization temperatures of 370° to >440°C (Marschik et al., 2000). Petrography and stable isotope support vein formation resulting from dominantly magmatic fluids that progressively cooled from 840–505°C (Las Pintadas) and 400°C (AFS). A magmatic origin of calcic skarns is proposed for other deposits in the area such as the Farola copper skarn, which is most likely derived from the Ojancos plutonic complex (Sillitoe, 2003). Magmatic fluids from this plutonic complex were likely involved in mineralization at Candelaria, which is <2 km from the complex (Sillitoe, 2003). Temperatures and conditions at Las Pintadas match as described for iron oxide mineralization at 500–600°C followed by sulfide stage mineralization at 400–500°C elsewhere in the district (Arévalo et al., 2006). Las Pintadas formed at higher temperatures than the andradite vein along the AFS, which is reflected in the presence of higher-temperature actinolite rather than epidote in the Las Pintadas alteration assemblage. The temperatures recorded along the AFS are more consistent with fluid inclusion homogenization temperatures from deeper (≤ 3 km) levels of Punta del Cobre deposits (350–450°C; Rabbia et al., 1996; Marschik et al., 1997; Marschik and Fontboté, 2001a; Kreiner, 2011). Zircon (U-Th)/He cooling dates of ~ 87 Ma and ~ 69 Ma recording cooling through $\sim 180^\circ\text{C}$ support andradite vein formation at >3 km depths in a cooling thermal aureole around the Copiapó batholith: assuming an average arc geothermal gradient of $\sim 40\text{--}50^\circ\text{C}/\text{km}$, the minimum depth of the Sierra Atacama diorite at 87 Ma is $\sim 3.4\text{--}4.3$ km (e.g., González, 1999; Herrera et al., 2005; Arancibia et al., 2014; Mitchell et al., 2017, Chapter 1). Kreiner (2011) documented the exposure of deeper structural levels west of the AFS, and stratigraphy constrains the depth of manto-type deposits to <3 km (Marschik and Fontboté, 2001a).

Relatively cool temperatures for the AFS andradite vein despite its position at a deeper structural level could suggest a much deeper source for the hydrothermal fluids compared to other Punta del Cobre andradite veins and other calcic skarns. We further note the vein along the AFS lacks sulfides and locally features zones of iron oxide+apatite, similar to IOA deposits from elsewhere in the Chilean Iron Belt. These characteristics, combined with the presence of calcic skarns at and below other Punta del Cobre deposits such as Las Pintadas and Atacama Kozan, may suggest andradite veins are an important link between deep IOA and shallow IOCG mineralization.

3.6 Conclusions

Our results document the timing of magmatism, sodic-calcic alteration, and Atacama fault system deformation near Copiapó. Intrusion of the ~122 Ma Sierra Chicharra quartz diorite is associated with the development of a NW-dipping sinistral shear zone as documented by a progression from magmatic fabrics within the pluton to protomylonitic to ultramylonitic fabrics within a ~200–500-m-wide shear zone along the main branch of the AFS. Petrography along the ductile AFS shear zone records an early phase associated with the synkinematic intrusion and shearing of the Sierra Chicharra quartz diorite recorded by internally strained actinolite and elongate titanite aligned parallel to foliation planes. Deformation ceased by ~115 Ma, documented by the intrusion of the unstrained Sierra Atacama diorite that cuts all mylonitic fabrics. A post-kinematic main phase of sodic-calcic alteration associated with the intrusion of the Sierra Atacama diorite is recorded by annealing of mylonitic fabrics in the shear zone by secondary plagioclase and sodic-calcic alteration of the western margin of the unstrained diorite. Two phases of intrusions cut annealed shear zone fabrics: several small ~103 Ma hornblende granodiorite bodies of the Sierra Pajas Blancas pluton within the shear zone, and a larger undated, unstrained hornblende diorite that intrudes both the shear zone and the unstrained Sierra Atacama diorite. Finally, a late phase of hydrothermal alteration is marked by the development of an ~775 m-long post-kinematic andradite vein through the center of the annealed shear zone at ~96 Ma.

The Sierra Atacama diorite and other late intrusions are part of the Early Cretaceous (119–97 Ma) Copiapó batholith, a pulse of magmatism that outlasted Early Cretaceous Coastal Cordillera magmatism documented elsewhere along the northern El Salado segment. AFS-related deformation ended both here and elsewhere along the El Salado segment by ~115–110 Ma, coeval with a shift from arc-parallel sinistral shear to E-directed contraction. Continuation of magmatism into the latest Albian near Copiapó kept geothermal gradients above the brittle-plastic transition during AFS shear and prevented the development of a major brittle fault. Kinematics and deformation geometry indicate ductile shear occurred in a transpressional regime that did not evolve to a brittle fault, due to protracted magmatism that outlasted AFS deformation in the Copiapó region. Notably, mineralization occurred in the absence of a transition to brittle transtension along the AFS. Geochronometric and oxygen stable isotope data indicate magmatic (+6.8 to +7.0‰ $\delta^{18}\text{O}_{\text{SMOW}}$), high-temperature (~400°C) fluids were responsible for andradite vein formation. The formation of this vein post-dated all documented intrusions along the shear zone, and a causative pluton is not recognized. In lieu of a brittle fault to provide a focused fluid pathway, fluid flow utilized the prominent subvertical anisotropy along the shear zone during ductile transpression, unlike other portions of the Chilean Iron Belt.

The strong spatial, structural, and geochemical similarities between the AFS and other deposits in the Punta del Cobre district including the andradite vein at Las Pintadas indicate they were formed by a very similar set of processes. New garnet U-Pb and sulfide Re-Os dates clearly document alteration and mineralization at ~115 Ma, coeval with emplacement of the unstrained Sierra Atacama diorite and resulting sodic-calcic alteration along the AFS. Stable isotope data show the Las Pintadas andradite vein formed at 505–840°C from dominantly magmatic fluids.

Bibliography

- Allmendinger, R. W., Cardozo, N., and Fisher, D. M. (2011). *Structural Geology Algorithms: Vectors and Tensors*. Cambridge University Press.
- Allmendinger, R. W. and González, G. (2010). Invited review paper: Neogene to Quaternary tectonics of the Coastal Cordillera, northern Chile. *Tectonophysics*, 495(1-2):93–110.
- Álvarez, J., Jorquera, R., Miralles, C., Padel, M., and Martínez, P. (2016). Cartas Punta Posallaves y Sierra Vicuña Mackenna, Región de Antofagasta. Servicio Nacional de Geología y Minería. *Carta Geológica de Chile, Geología Básica*.
- Amilibia, A., Sàbat, F., McClay, K. R., Muñoz, J. A., Roca, E., and Chong, G. (2008). The role of inherited tectono-sedimentary architecture in the development of the central Andean mountain belt: Insights from the Cordillera de Domeyko. *Journal of Structural Geology*, 30(12):1520–1539.
- Andronicos, C. L., Chardon, D. H., Hollister, L. S., Gehrels, G. E., and Woodsworth, G. J. (2003). Strain partitioning in an obliquely convergent orogen, plutonism, and synorogenic collapse: Coast Mountains Batholith, British Columbia, Canada. *Tectonics*, 22(2).
- Angermann, D., Klotz, J., and Reigber, C. (1999). Space-geodetic estimation of the Nazca-South America Euler vector. *Earth and Planetary Science Letters*, 171(3):329–334.
- Arabasz, W. J. J. (1971). Geological and geophysical studies of the Atacama fault zone in northern Chile.
- Arancibia, G., Fujita, K., Hoshino, K., Mitchell, T. M., Cembrano, J., Gomila, R., Morata, D., Faulkner, D. R., and Rempe, M. (2014). Hydrothermal alteration in an exhumed crustal fault zone: Testing geochemical mobility in the Caleta Coloso Fault, Atacama Fault System, Northern Chile. *Tectonophysics*, 623:147–168.

- Arévalo, C. (1995). Mapa Geológico de Copiapó, Región Atacama. Servicio Nacional de Geología y Minería. *Documentos de Trabajo*, 6.
- Arévalo, C. (1999). *The Coastal Cordillera/Precordillera Boundary in the Tierra Amarilla area (27° 20' 27 40'S/70° 05'–70 20'W), northern Chile, and the structural setting of the Candelaria Cu-Au ore deposit*. Thesis.
- Arévalo, C. (2005a). Carta Copiapó, Región de Atacama. Servicio Nacional de Geología y Minería. *Carta geológica de Chile, Serie Geología Básica*, 91:54.
- Arévalo, C. (2005b). Carta Los Loros, Región de Atacama. Servicio Nacional de Geología y Minería. *Carta Geológica de Chile, Serie Geología Básica, escala*, 1(100.000).
- Arévalo, C., Grocott, J., Martin, W., Pringle, M., and Taylor, G. (2006). Structural Setting of the Candelaria Fe Oxide Cu-Au Deposit, Chilean Andes (27° 30' S). *Economic Geology*, 101(4):819–841.
- Arévalo, C., Grocott, J., and Welkner, D. (2003). The Atacama fault system in the Huasco province, southern Atacama desert, Chile. *Proceedings of 10th Congreso Geológico Chileno*, pages 1–5.
- Arévalo, C., Mourgues, O., Amaro, F., and Chávez, M. (2009). Geología del área Vallenar-Domeyko, región de Atacama. *Carta Geológica de Chile, Serie Geología Básica*.
- Arévalo, C. and Welkner, D. (2008). Geología del área Carrizal Bajo-Chacritas, Región de Atacama. Servicio Nacional de Geología y Minería. *Carta Geológica de Chile, Serie Geología Básica*, 111:67.
- Avé Lallemant, H. G. and Oldow, J. S. (1988). Early Mesozoic southward migration of Cordilleran transpressional terranes. *Tectonics*, 7(5):1057–1075.
- Barra, F., Reich, M., Selby, D., Rojas, P., Simon, A., Salazar, E., and Palma, G. (2017). Unraveling the origin of the Andean IOCG clan: A Re-Os isotope approach. *Ore Geology Reviews*, 81:62–78.

- Barrier, E., Huchon, P., and Aurelio, M. (1991). Philippine fault: a key for Philippine kinematics. *Geology*, 19(1):32–35.
- Barton, M. D., Jensen, E. P., and Ducea, M. (2005). Fluid Sources for IOCG (Candelaria, Punta del Cobre) and Porphyry Cu-Style Mineralization, Copiapó batholith, Chile, Geologic and Sr Isotopic Constraints. *Geological Society of America Annual Meeting*.
- Barton, M. D. and Johnson, D. A. (1996). Evaporitic-source model for igneous-related Fe oxide–(REE-Cu-Au-U) mineralization. *Geology*, 24(3):259–262.
- Barton, M. D. and Johnson, D. A. (2000). Alternative brine sources for Fe-oxide (-Cu-Au) systems: Implications for hydrothermal alteration and metals. *Hydrothermal Iron Oxide Copper-Gold and related deposits: A global perspective*, 1:43–60.
- Barton, M. D., Johnson, D. A., Kreiner, D. C., and Jensen, E. P. (2013). Vertical zoning and continuity in Fe oxide (-Cu-Au-Ag-Co-U-REE) (or 'IOCG') systems: Cordilleran insights. *Proceedings of the 12th Biennial Meeting, Society for Geology Applied to Ore Deposits*, pages 1348–1351.
- Barton, M. D., Kreiner, D. C., Jensen, E. P., and Girardi, J. D. (2011). Multiple igneous-related hydrothermal systems and related IOCG mineralization, near Copiapó, Chile. *XI SGA Biennial Meeting, Actas*, pages 521–523.
- Beck, M. E. J. (1983). On the mechanism of tectonic transport in zones of oblique subduction. *Tectonophysics*, 93(1-2):1–11.
- Beck, M. E. J. (1991). Coastwise transport reconsidered: lateral displacements in oblique subduction zones, and tectonic consequences. *Physics of the Earth and Planetary Interiors*, 68(1-2):1–8.
- Behr, W. M. and Becker, T. W. (2018). Sediment control on subduction plate speeds. *Earth and Planetary Science Letters*, 502:166–173.

- Behr, W. M. and Platt, J. P. (2014). Brittle faults are weak, yet the ductile middle crust is strong: Implications for lithospheric mechanics. *Geophysical Research Letters*, 41(22):8067–8075.
- Berg, K. and Baumann, A. (1985). Plutonic and metasedimentary rocks from the Coastal Range of northern Chile: Rb-Sr and U-Pb isotopic systematics. *Earth and Planetary Science Letters*, 75(2-3):101–115.
- Berg, K. and Breitzkreuz, C. (1983). *Mesozoische Plutone in der nordchilenischen K ıjstenkordillere: petrogenese, geochronologie, Geochemie und Geodynamik mantelbetonter Magmatite*. E. Schweizerbart.
- Blackwell, D. D., Bowen, R. G., Hull, D. A., Riccio, J., and Steele, J. L. (1982). Heat flow, arc volcanism, and subduction in northern Oregon. *Journal of Geophysical Research: Solid Earth*, 87(B10):8735–8754.
- Blackwell, D. D., Steele, J. L., Kelley, S., and Korosec, M. A. (1990). Heat flow in the state of Washington and thermal conditions in the Cascade Range. *Journal of Geophysical Research: Solid Earth*, 95(B12):19495–19516.
- Blanco, N., Godoy, E., and Marquardt, C. (2003). Cartas Castilla y Totoral Bajo, Regi n de Atacama. Servicio Nacional de Geolog a y Miner a. *Serie Geolog a B sica*, (77).
- Bonson, C. (1998). *Fracturing, fluid processes and mineralisation in the Cretaceous continental magmatic arc of Northern Chile (25  15' -27  15'S)*. Thesis.
- Bookstrom, A. A. (1977). The magnetite deposits of El Romeral, Chile. *Economic Geology*, 72(6):1101–1130.
- Boric, R., D az, F., and MaksaeV, V. (1990). Geologia y yacimientos metaliferos de la region de Antofogasta.
- Bowman, J. R. (1998). Stable isotope systematics of skarns. *Mineralogical Association of Canada Short Course Series*, 26.

- Bradley, K. E., Feng, L., Hill, E. M., Natawidjaja, D. H., and Sieh, K. (2017). Implications of the diffuse deformation of the Indian Ocean lithosphere for slip partitioning of oblique plate convergence in Sumatra. *Journal of Geophysical Research: Solid Earth*, 122(1):572–591.
- Brown, M., Diaz, F., and Grocott, J. (1993). Displacement history of the Atacama fault system 25° 00' S–27° 00' S, northern Chile. *Geological Society of America Bulletin*, 105(9):1165–1174.
- Busby-Spera, C. J. and Saleeby, J. B. (1990). Intra-arc strike-slip fault exposed at batholithic levels in the southern Sierra Nevada, California. *Geology*, 18(3):255–259.
- Butterworth, N., Steinberg, D., Müller, R. D., Williams, S., Merdith, A. S., and Hardy, S. (2016). Tectonic environments of South American porphyry copper magmatism through time revealed by spatiotemporal data mining. *Tectonics*, 35(12):2847–2862.
- Byerlee, J. (1978). Friction of rocks. *Pure and Applied Geophysics*, 116(4):615–626.
- Camus, F. (1980). Posible modelo genético para los yacimientos de cobre del distrito minero Punta del Cobre. *Andean Geology*, (11).
- Cao, W., Paterson, S., Memeti, V., Mundil, R., Anderson, J. L., and Schmidt, K. (2015). Tracking paleodeformation fields in the Mesozoic central Sierra Nevada arc: Implications for intra-arc cyclic deformation and arc tempos. *Lithosphere*, 7(3):296–320.
- Cardozo, N. and Allmendinger, R. W. (2013). Spherical projections with OSXStereonet. *Computers & Geosciences*, 51:193–205.
- Carter, N. L. and Tsenn, M. C. (1987). Flow properties of continental lithosphere. *Tectonophysics*, 136(1-2):27–63.
- Cembrano, J., Garrido, I., and Marquardt, M. (2009). Tectonic setting of IOCG deposits in the Central Andes: Strike-slip-dominated deformation. *XII Congreso Geológico Chileno, Santiago*.

- Cembrano, J., González, G., Arancibia, G., Ahumada, I., Olivares, V., and Herrera, V. (2005). Fault zone development and strain partitioning in an extensional strike-slip duplex: A case study from the Mesozoic Atacama fault system, Northern Chile. *Tectonophysics*, 400(1-4):105–125.
- Cembrano, J., Hervé, F., and Lavenu, A. (1996). The Liquiñe Ofqui fault zone: a long-lived intra-arc fault system in southern Chile. *Tectonophysics*, 259(1-3):55–66.
- Cembrano, J. and Lara, L. (2009). The link between volcanism and tectonics in the southern volcanic zone of the Chilean Andes: a review. *Tectonophysics*, 471(1-2):96–113.
- Charrier, R., Pinto, L., and Rodríguez, M. P. (2007). *Tectonostratigraphic evolution of the Andean Orogen in Chile*.
- Charrier, R., Ramos, V. A., Tapia, F., and Sagripanti, L. (2015). Tectono-stratigraphic evolution of the Andean Orogen between 31 and 37 S (Chile and Western Argentina). *Geological Society, London, Special Publications*, 399(1):13–61.
- Chiaradia, M., Banks, D., Cliff, R., Marschik, R., and De Haller, A. (2006). Origin of fluids in iron oxide–copper–gold deposits: constraints from $\delta^{37}\text{Cl}$, $^{87}\text{Sr}/^{86}\text{Sr}$ i and Cl/Br. *Mineralium Deposita*, 41(6):565–573.
- Clechenko, C. C. and Valley, J. W. (2003). Oscillatory zoning in garnet from the Willsboro Wollastonite Skarn, Adirondack Mts, New York: a record of shallow hydrothermal processes preserved in a granulite facies terrane. *Journal of Metamorphic Geology*, 21(8):771–784.
- Clift, P. and Vannucchi, P. (2004). Controls on tectonic accretion versus erosion in subduction zones: Implications for the origin and recycling of the continental crust. *Reviews of Geophysics*, 42(2).
- Coira, B., Davidson, J., Mpodozis, C., and Ramos, V. (1982). Tectonic and magmatic evolution of the Andes of northern Argentina and Chile. *Earth-Science Reviews*, 18(3):303–332.

- Collettini, C., Tesei, T., Scuderi, M. M., Carpenter, B. M., and Viti, C. (2019). Beyond Byerlee friction, weak faults and implications for slip behavior. *Earth and Planetary Science Letters*, 519:245–263.
- Contreras, J. P., Espinoza, M., De la Cruz, R., Jorquera, R., Kraus, S., Ramírez, C., Naranjo, J. A., Escribano, J., and Martínez, P. (2013). Carta Cifuncho, Regiones de Antofagasta y Atacama. Servicio Nacional de Geología y Minería. *Carta Geológica de Chile, Serie Geología Básica*, 161(1):100–000.
- Contreras-Reyes, E., Becerra, J., Kopp, H., Reichert, C., and Díaz-Naveas, J. (2014). Seismic structure of the north-central Chilean convergent margin: Subduction erosion of a paleomagmatic arc. *Geophysical Research Letters*, 41(5):1523–1529.
- Corriveau, L., Montreuil, J. F., and Potter, E. G. (2016). Alteration facies linkages among iron oxide copper-gold, iron oxide-apatite, and affiliated deposits in the Great Bear magmatic zone, Northwest Territories, Canada. *Economic Geology*, 111(8):2045–2072.
- Couture, J., Cole, G., Zhang, B., Nilsson, J., Dance, A., Scott, C., and Vidal, M. (2017). Technical Report for the Candelaria Copper Mining Complex, Atacama Province, Region III, Chile. Report, Lundin Mining Corporation.
- Creixell, T., Ortiz, L., and Arévalo, V. (2012). Geología del área Carrizalillo-El Tofo, Regiones de Atacama y Coquimbo. Servicio Nacional de Geología y Minería. *Carta Geológica de Chile, Serie Geología Básica*.
- Dahl, P. S. (1996). The crystal-chemical basis for Ar retention in micas: inferences from interlayer partitioning and implications for geochronology. *Contributions to Mineralogy and Petrology*, 123(1):22–39.
- Dallmeyer, R. D., Brown, M., Grocott, J., Taylor, G. K., and Treloar, P. J. (1996). Mesozoic Magmatic and Tectonic Events within the Andean Plate Boundary Zone, 26°-27°30'S, North Chile: Constraints from $^{40}\text{Ar}/^{39}\text{Ar}$ Mineral Ages. *The Journal of Geology*, 104(1):19–40.

- Daroch, G. A. and Barton, M. D. (2011). Hydrothermal alteration and mineralization in Santo Domingo Sur iron oxide (-Cu-Au)(IOCG) deposit, Atacama Region, Chile. *11th SGA Biennial meeting*.
- Davidson, G. J., Paterson, H., Meffre, S., and Berry, R. F. (2007a). Characteristics and origin of the Oak Dam East breccia-hosted, iron oxide Cu-U-(Au) deposit: Olympic Dam region, Gawler craton, South Australia. *Economic Geology*, 102(8):1471–1498.
- Davidson, J., Turner, S., Handley, H., Macpherson, C., and Dosseto, A. (2007b). Amphibole "sponge" in arc crust? *Geology*, 35(9):787–790.
- de Saint Blanquat, M., Horsman, E., Habert, G., Morgan, S., Vanderhaeghe, O., Law, R., and Tikoff, B. (2011). Multiscale magmatic cyclicality, duration of pluton construction, and the paradoxical relationship between tectonism and plutonism in continental arcs. *Tectonophysics*, 500(1):20–33.
- de Saint Blanquat, M., Tikoff, B., Teyssier, C., and Vigneresse, J. L. (1998). Transpressional kinematics and magmatic arcs. *Geological Society, London, Special Publications*, 135(1):327.
- del Real Contreras, I., Thompson, J. F. H., and Carriedo, J. (2018). Lithological and structural controls on the genesis of the Candelaria-Punta del Cobre Iron Oxide Copper Gold district, Northern Chile. *Ore Geology Reviews*, 102:106–153.
- DeMets, C., Gordon, R. G., Argus, D. F., and Stein, S. (1994). Effect of recent revisions to the geomagnetic reversal time scale on estimates of current plate motions. *Geophysical research letters*, 21(20):2191–2194.
- Díaz, A., Lledó, H., and Vivallo, W. (1998). Yacimientos Metalíferos de la Hoja de Los Loros, Región de Atacama. *Servicio Nacional de Geología y Minería Mapa Recursos Mineral Chile*, 2:1–25.

- Díaz, A., Vivallo, W., Jorquera, R., and Pizarro, N. (2003). Depósitos de Fe, óxidos de Fe-Cu-Au y su relación con el magmatismo del Cretácico Inferior, III Región de Atacama, Chile. *Congreso Geológico Chileno*.
- Dodson, M. H. (1973). Closure temperature in cooling geochronological and petrological systems. *Contributions to Mineralogy and Petrology*, 40(3):259–274.
- Ehlers, T. A. and Farley, K. A. (2003). Apatite (U–Th)/He thermochronometry: Methods and applications to problems in tectonic and surface processes. *Earth and Planetary Science Letters*, 206(1):1–14.
- Elhlou, S., Belousova, E., Griffin, W. L., Pearson, N. J., and O'Reilly, S. Y. (2006). Trace element and isotopic composition of GJ-red zircon standard by laser ablation. *Geochimica et Cosmochimica Acta*, 70(18):A158.
- Emparan, C. and Pineda, G. (2000). Área La Serena-La Higuera, Región de Coquimbo. Servicio Nacional de Geología y Minería. *Mapas Geológicos*, 18(1).
- Emparan, C. and Pineda, G. (2005). Geología del Andacollo–Puerto Aldea, Región de Coquimbo. Servicio Nacional de Geología y Minería. *Carta Geológica del Chile, Serie Geología Básica*.
- Escribano, J., Martínez, P., Domagala, J., Padel, M., Espinoza, M., Jorquera, R., Contreras, J., De la Cruz, R., and Calderón, M. (2013). Cartas Bahía Isla Blanca y Taltal, Región de Antofagasta. Servicio Nacional de Geología y Minería. *Carta Geológica de Chile, Serie Geología Básica*, pages 164–165.
- Espinoza, M., Contreras, J. P., Jorquera, R., De La Cruz, R., Kraus, S., and Ramírez, C. (2014). Carta Cerro del Pingo, Regiones de Antofagasta y Atacama. Servicio Nacional de Geología y Minería. *Carta Geológica de Chile, Serie Geología Básica*, 169(1).
- Espinoza, S. (1990). *The Atacama-Coquimbo ferriferous belt, northern Chile*, pages 353–364. Springer.

- Espinoza, S. (1996). The cupriferous province of the Coastal Range, northern Chile. *Andean copper deposits: new discoveries, mineralization, styles and metallogeny*, pages 19–32.
- Farley, K. A., Wolf, R. A., and Silver, L. T. (1996). The effects of long alpha-stopping distances on (U-Th)/He ages. *Geochimica et Cosmochimica Acta*, 60(21):4223–4229.
- Farrar, E., Clark, A. H., Haynes, S. J., Quirt, G. S., Conn, H., and Zentilli, M. (1970). K-Ar evidence for the post-Paleozoic migration of granitic intrusion foci in the Andes of northern Chile. *Earth and Planetary Science Letters*, 10(1):60–66.
- Fitch, T. J. (1972). Plate convergence, transcurrent faults, and internal deformation adjacent to southeast Asia and the western Pacific. *Journal of Geophysical research*, 77(23):4432–4460.
- Fossen, H. and Hesthammer, J. (1997). Geometric analysis and scaling relations of deformation bands in porous sandstone. *Journal of Structural Geology*, 19(12):1479–1493.
- Fossen, H. and Tikoff, B. (1993). The deformation matrix for simultaneous simple shearing, pure shearing and volume change, and its application to transpression-transension tectonics. *Journal of Structural Geology*, 15(3-5):413–422.
- Fréaut, R. and Cuadra, W. (1994). Mineralización de Fe, Cu y Au en la franja cretácica de la Costa. Regiones III y IV de Chile. *Actas 7th Congr Geol Chileno*, 2:1046–1050.
- Gana, P. and Zentilli, M. (2000). Historia termal y exhumación de intrusivos de la Cordillera de la Costa de Chile central. *IX Congreso Geológico Chileno*, 2:664–668.
- Gelcich, S., Davis, D. W., and Spooner, E. T. C. (2005). Testing the apatite-magnetite geochronometer: U-Pb and $^{40}\text{Ar}/^{39}\text{Ar}$ geochronology of plutonic rocks, massive magnetite-apatite tabular bodies, and IOCG mineralization in Northern Chile. *Geochimica et Cosmochimica Acta*, 69(13):3367–3384.

- Georgiev, S. V., Zimmerman, A., Yang, G., Goswami, V., Hurtig, N. C., Hannah, J. L., and Stein, H. J. (2018). Comparison of chemical procedures for Re-isotopic measurements by N-TIMS. *Chemical Geology*, 483:151–161.
- Girardi, J. D. (2014). *Comparison of Mesozoic magmatic evolution and iron oxide (-copper-gold) ('IOCG') mineralization, Central Andes and western North America*. The University of Arizona.
- Glazner, A. F. (1991). Plutonism, oblique subduction, and continental growth: An example from the Mesozoic of California. *Geology*, 19(8):784–786.
- Godoy, E. and Lara, L. (1998). *Hojas Chañaral y Diego de Almagro, Región de Atacama. Servicio Nacional de Geología y Minería*.
- Godoy, E. and Lara, L. (1999). Hoja Puerto Flamenco, Región de Atacama. Servicio Nacional de Geología y Minería. *Carta Geológica de Chile, Serie Geología Básica*, 1:15.
- Godoy, P.-B., Marquardt, C., and Blanco, N. (2003). Carta Cifuncho, Región de Atacama. Servicio Nacional de Geología y Minería. *Carta Geológica de Chile, Serie Geología Básica*, page mapa escala 1:100.000.
- González, G. (1996). Evolución tectónica de la Cordillera de la Costa de Antofagasta (Chile): con especial referencia a las deformaciones sinmagmáticas del Jurásico-Cretácico Inferior. *Berliner Geowissenschaftliche Abhandlungen, Series A*, 181:1–111.
- González, G. (1999). Mecanismo y profundidad de emplazamiento del Plutón de Cerro Cristales, Cordillera de la Costa, Antofagasta, Chile. *Revista geológica de Chile*, 26(1):43–66.
- González, G. and Carrizo, D. (2003). Segmentación, cinemática y cronología relativa de la deformación tardía de la Falla Salar del Carmen, Sistema de Fallas de Atacama, (23°40'S), norte de Chile. *Revista geológica de Chile*, 30:223–244.

- González, G., Dunai, T., Carrizo, D., and Allmendinger, R. (2006). Young displacements on the Atacama Fault System, northern Chile from field observations and cosmogenic ^{21}Ne concentrations. *Tectonics*, 25(3).
- Goto, H. (2018). Late quaternary slip rates and vectors on the Median Tectonic Line active fault zone in eastern Shikoku, southwest Japan. *Quaternary International*, 471:267–277.
- Granot, R. and Dymant, J. (2015). The Cretaceous opening of the South Atlantic Ocean. *Earth and Planetary Science Letters*, 414:156–163.
- Grocott, J., Brown, M., Dallmeyer, R. D., Taylor, G. K., and Treloar, P. J. (1994). Mechanisms of continental growth in extensional arcs: An example from the Andean plate-boundary zone. *Geology*, 22(5):391–394.
- Grocott, J. and Taylor, G. K. (2002). Magmatic arc fault systems, deformation partitioning and emplacement of granitic complexes in the Coastal Cordillera, north Chilean Andes (25°30'S to 27°00'S). *Journal of the Geological Society*, 159(4):425–443.
- Grove, M. and Harrison, T. M. (1996). $^{40}\text{Ar}^*$ diffusion in Fe-rich biotite. *American Mineralogist*, 81(7-8):940–951.
- Handy, M. R. and Brun, J. P. (2004). Seismicity, structure and strength of the continental lithosphere. *Earth and Planetary Science Letters*, 223(3):427–441.
- Harrison, T. M. (1982). Diffusion of ^{40}Ar in hornblende. *Contributions to Mineralogy and Petrology*, 78(3):324–331.
- Harrison, T. M., Duncan, I., and McDougall, I. (1985). Diffusion of ^{40}Ar in biotite: Temperature, pressure and compositional effects. *Geochimica et Cosmochimica Acta*, 49(11):2461–2468.
- Harrison, T. M. and McDougall, I. (1980). Investigations of an intrusive contact, northwest Nelson, New Zealand. Thermal, chronological and isotopic constraints. *Geochimica et cosmochimica acta*, 44(12):1985–2003.

- Haschke, M., Günther, A., Melnick, D., Echtler, H., Reutter, K.-J., Scheuber, E., and Oncken, O. (2006). *Central and southern Andean tectonic evolution inferred from arc magmatism*, pages 337–353. Springer.
- Herrera, V., Cembrano, J., Olivares, V., Kojima, S., and Arancibia, G. (2005). Precipitación por despresurización y ebullición en vetas hospedadas en un dÃžplex de rumbo extensional: evidencias microestructurales y microtermométricas. *Revista geológica de Chile*, 32(2):207–228.
- Hervé, M. (1987a). Movimiento normal de la falla Paposo, Zona de Falla Atacama, en el Mioceno, Chile. *Andean Geology*, (31):31–36.
- Hervé, M. (1987b). Movimiento sinistral en el Cretácico Inferior de la Zona de Falla de Atacama al Norte de Paposo (24°S), Chile. *Andean Geology*, (31):37–42.
- Hervé, M. and Marinovic, N. (1989). Geocronología y evolución del Batolito Vicuña Mackenna, Cordillera de la Costa, sur de Antofagasta (24-25 S). *Andean Geology*, 16(1):31–49.
- Heuser, G., Arancibia, G., Veloso, E., Cembrano, J., Cordeiro, P., Nehler, M., and Bracke, R. (2020). The evolution of the Dominga Fe-Cu deposit (northern Chile): insights from mineral textures and micro-CT analysis. *Ore Geology Reviews*, page 103316.
- Hirth, G., Teyssier, C., and Dunlap, J. W. (2001). An evaluation of quartzite flow laws based on comparisons between experimentally and naturally deformed rocks. *International Journal of Earth Sciences*, 90(1):77–87.
- Hirth, G. and Tullis, J. (1992). Dislocation creep regimes in quartz aggregates. *Journal of Structural Geology*, 14(2):145–159.
- Hitzman, M. W. (2000). Iron oxide-Cu-Au deposits: What, where, when, and why. *Hydrothermal iron oxide copper-gold and related deposits: A global perspective*, 1:9–25.

- Hitzman, M. W., Oreskes, N., and Einaudi, M. T. (1992). Geological characteristics and tectonic setting of proterozoic iron oxide (Cu-U-Au-REE) deposits. *Precambrian research*, 58(1-4):241–287.
- Hopf, S. (1990). *The Agustina mine, a volcanic-hosted copper deposit in northern Chile*, pages 421–434. Springer.
- Hopper, D. and Correa, A. (2000). *The Panulcillo and Teresa de Colmo copper deposits: two contrasting examples of Fe-ox-Cu-Au mineralisation from the Coastal Cordillera of Chile.*, pages 177–189. Australian Mineral Foundation, Adelaide.
- Hourigan, J. K., Reiners, P. W., and Brandon, M. T. (2005). U-Th zonation-dependent alpha-ejection in (U-Th)/He chronometry. *Geochimica et Cosmochimica Acta*, 69(13):3349–3365.
- Hsu, Y.-J., Yu, S.-B., Loveless, J. P., Bacolcol, T., Solidum, R., Luis Jr, A., Pelicano, A., and Woessner, J. (2016). Interseismic deformation and moment deficit along the Manila subduction zone and the Philippine Fault system. *Journal of Geophysical Research: Solid Earth*, 121(10):7639–7665.
- Ichii, Y., Abe, A., Ichige, Y., Matsunaga, J., Miyoshi, M., Furuno, M., and Yokoi, K. (2007). Copper exploration of the Atacama Kozan Mine, Region III, Chile. *Shigen-Chishitsu*, 57(1):1–14.
- Jackson, S. E., Pearson, N. J., Griffin, W. L., and Belousova, E. A. (2004). The application of laser ablation-inductively coupled plasma-mass spectrometry to in situ U–Pb zircon geochronology. *Chemical Geology*, 211(1):47–69.
- Jaffey, A. H., Flynn, K. F., Glendenin, L. E., Bentley, W. C., and Essling, A. M. (1971). Precision Measurement of Half-Lives and Specific Activities of ^{235}U and ^{238}U . *Physical Review C*, 4(5):1889–1906.

- Jaillard, E., Soler, P., Carlier, G., and Mourier, T. (1990). Geodynamic evolution of the northern and central Andes during early to middle Mesozoic times: a Tethyan model. *Journal of the Geological Society*, 147(6):1009.
- Janecke, S. U. and Evans, J. P. (1988). Feldspar-influenced rock rheologies. *Geology*, 16(12):1064–1067.
- Jaquet, Y. and Schmalholz, S. M. (2018). Spontaneous ductile crustal shear zone formation by thermal softening and related stress, temperature and strain rate evolution. *Tectonophysics*, 746:384–397.
- Jarrard, R. D. (1986). Terrane motion by strike-slip faulting of forearc slivers. *Geology*, 14(9):780–783.
- Jensen, E., Cembrano, J., Faulkner, D., Veloso, E., and Arancibia, G. (2011). Development of a self-similar strike-slip duplex system in the Atacama Fault system, Chile. *Journal of Structural Geology*, 33(11):1611–1626.
- Kay, R. W. and Mahlburg-Kay, S. (1991). Creation and destruction of lower continental crust. *Geologische Rundschau*, 80(2):259–278.
- Kelley, S., Turner, G., Butterfield, A. W., and Shepherd, T. J. (1986). The source and significance of argon isotopes in fluid inclusions from areas of mineralization. *Earth and Planetary Science Letters*, 79(3-4):303–318.
- Kendrick, E., Bevis, M., Smalley Jr, R., Brooks, B., Vargas, R. B., LaurÁsa, E., and Fortes, L. P. S. (2003). The Nazca–South America Euler vector and its rate of change. *Journal of South American Earth Sciences*, 16(2):125–131.
- Kendrick, M. A., Burgess, R., Patrick, R. A. D., and Turner, G. (2001a). Fluid inclusion noble gas and halogen evidence on the origin of Cu-Porphyry mineralising fluids. *Geochimica et Cosmochimica Acta*, 65(16):2651–2668.

- Kendrick, M. A., Burgess, R., Patrick, R. A. D., and Turner, G. (2001b). Halogen and Ar–Ar age determinations of inclusions within quartz veins from porphyry copper deposits using complementary noble gas extraction techniques. *Chemical Geology*, 177(3-4):351–370.
- Kim, Y.-S. and Sanderson, D. J. (2004). Similarities between strike-slip faults at different scales and a simple age determining method for active faults. *Island Arc*, 13(1):128–143.
- Kim, Y.-S. and Sanderson, D. J. (2005). The relationship between displacement and length of faults: a review. *Earth-Science Reviews*, 68(3-4):317–334.
- Kirkland, C. L., Smithies, R. H., Taylor, R. J. M., Evans, N., and McDonald, B. (2015). Zircon Th/U ratios in magmatic environs. *Lithos*, 212:397–414.
- Kirsch, M., Paterson, S. R., Wobbe, F., Ardila, A. M. M., Clausen, B. L., and Alasino, P. H. (2016). Temporal histories of Cordilleran continental arcs: Testing models for magmatic episodicity. *American Mineralogist*, 101(10):2133–2154.
- Knipping, J. L., Bilenker, L. D., Simon, A. C., Reich, M., Barra, F., Deditius, A. P., Lundstrom, C., Bindeman, I., and Munizaga, R. (2015). Giant Kiruna-type deposits form by efficient flotation of magmatic magnetite suspensions. *Geology*, 43(7):591–594.
- Koděra, P., Heinrich, C. A., Wälle, M., and Lexa, J. (2014). Magmatic salt melt and vapor: Extreme fluids forming porphyry gold deposits in shallow subvolcanic settings. *Geology*, 42(6):495–498.
- Kreiner, D. C. (2011). Epithermal Style Iron Oxide(-Cu-Au) (=IOCG) Vein Systems and Related Alteration.
- Kurth, D. (2002). *Die Nordchilenische KÃijstenkordillere bei Taltal: Scherzonen und forearc-silver im Jurassischen und Unterkretazischen magmatischen Bogen: ein Verfahren zur Lautheitsskalierung bei Kindern*. Thesis.
- Lara, L. and Godoy, E. (1998). *Hoja Quebrada Salitrosa, Regi3n de Atacama*. Servicio nacional de geologÃa y minerÃa.

- Lledó, H. (1998). *Metalogenesis de los cuadrángulos Copiapó, Cerro Chamonate, y Nantoco, III region, Chile*. Thesis.
- Lopez, G., Hitzman, M., and Nelson, E. (2014). Alteration patterns and structural controls of the El Espino IOCG mining district, Chile. *Mineralium Deposita*, 49(2):235–259.
- Loveless, J. P. and Meade, B. J. (2010). Geodetic imaging of plate motions, slip rates, and partitioning of deformation in Japan. *Journal of Geophysical Research: Solid Earth*, 115(B2).
- Lowenstern, J. B., Clynne, M. A., and Bullen, T. D. (1997). Comagmatic A-type granophyre and rhyolite from the Alid volcanic center, Eritrea, northeast Africa. *Journal of Petrology*, 38(12):1707–1721.
- Lucassen, F. and Thirlwall, M. F. (1998). Sm–Nd ages of mafic rocks from the Coastal Cordillera at 24°S, northern Chile. *Geologische Rundschau*, 86(4):767–774.
- Ludwig, K. R. (2003). ISOPLOT 3.00: a geochronology toolkit for Microsoft Excel. *Berkeley Geochronological Center Special Publication, Berkeley*, 70.
- Maksaev, V. (1990). *Metallogeny, geological evolution, and thermochronology of the Chilean Andes between latitudes 21° and 26° south, and the origin of major porphyry copper deposits*. Thesis.
- Maksaev, V., Munizaga, F., Valencia, V., and Barra, F. (2009). LA-ICP-MS zircon U-Pb geochronology to constrain the age of post-Neocomian continental deposits of the Cerrillos Formation, Atacama Region, northern Chile: tectonic and metallogenic implications. *Andean geology*, 36(2):264–287.
- Maloney, K. T., Clarke, G. L., Klepeis, K. A., and Quevedo, L. (2013). The Late Jurassic to present evolution of the Andean margin: Drivers and the geological record. *Tectonics*, 32(5):1049–1065.
- Marinovic, S., Smoje, T., Maksaev, J., Hervé, A., and Mpodozis, M. (1995). Hoja Aguas Blancas, Región de Antofagasta. *Servicio Nacional de Geología y Minería*.

- Markey, R., Hannah, J. L., Morgan, J. W., and Stein, H. J. (2003). A double spike for osmium analysis of highly radiogenic samples. *Chemical Geology*, 200(3):395–406.
- Marquardt, M., Cembrano, J., Siña, A., and Garrido, I. (2009). IOCG-type Deposits in North-Central Chile: A Case Study and Implications for Exploration. *XII Congreso Geológico Chileno*.
- Marrett, R. and Allmendinger, R. W. (1990). Kinematic analysis of fault-slip data. *Journal of Structural Geology*, 12(8):973–986.
- Marschik, R. and Fontboté, L. (2001a). The Candelaria-Punta del Cobre iron oxide Cu-Au (-Zn-Ag) deposits, Chile. *Economic Geology*, 96:1799–1826.
- Marschik, R. and Fontboté, L. (2001b). The Punta del Cobre Formation, Punta del Cobre–Candelaria area, northern Chile. *Journal of South American Earth Sciences*, 14(4):401–433.
- Marschik, R., Fontignie, D., Chiaradia, M., and Voldet, P. (2003). Geochemical and Sr–Nd–Pb–Sm–O isotope composition of granitoids of the Early Cretaceous Copiapó plutonic complex (27° 30' S), Chile. *Journal of South American Earth Sciences*, 16(5):381–398.
- Marschik, R. and Kendrick, M. (2015). Noble gas and halogen constraints on fluid sources in iron oxide-copper-gold mineralization: Mantoverde and La Candelaria, Northern Chile. *Mineralium Deposita*, 50(3):357–371.
- Marschik, R., Leveille, R., and Martin, W. (2000). *La Candelaria and the Punta del Cobre district, Chile: Early Cretaceous iron oxide Cu-Au(-Zn-Ag) mineralization*, pages 163–175. Australian Mineral Foundation, Adelaide.
- Marschik, R., Singer, B. S., Munizaga, F., Tassinari, C., Moritz, R., and Fontboté, L. (1997). Age of Cu(-Fe)-Au mineralization and thermal evolution of the Punta del Cobre district, Chile. *Mineralium Deposita*, 32(6):531–546.

- Marschik, R. and Söllner, F. (2006). Early Cretaceous U–Pb zircon ages for the Copiapó plutonic complex and implications for the IOCG mineralization at Candelaria, Atacama Region, Chile. *Mineralium Deposita*, 41(8):785–801.
- Marsh, J. H., Johnson, S. E., Yates, M. G., and West Jr, D. P. (2009). Coupling of deformation and reactions during mid-crustal shear zone development: an in situ frictional-viscous transition. *Journal of Metamorphic Geology*, 27(8):531–553.
- Marsh, J. H. and Stockli, D. F. (2015). Zircon U–Pb and trace element zoning characteristics in an anatectic granulite domain: Insights from LASS-ICP-MS depth profiling. *Lithos*, 239:170–185.
- Martin, V. M., Davidson, J., Morgan, D., and Jerram, D. A. (2010). Using the Sr isotope compositions of feldspars and glass to distinguish magma system components and dynamics. *Geology*, 38(6):539–542.
- Martínez, F., Arriagada, C., Peña, M., Del Real, I., and Deckart, K. (2013). The structure of the Chañarcillo Basin: An example of tectonic inversion in the Atacama region, northern Chile. *Journal of South American Earth Sciences*, 42(C):1–16.
- Mathez, E. A. and Kent, A. J. R. (2007). Variable initial Pb isotopic compositions of rocks associated with the UG2 chromitite, eastern Bushveld Complex. *Geochimica et Cosmochimica Acta*, 71(22):5514–5527.
- Mathur, R. (2002). Age of Mineralization of the Candelaria Fe Oxide Cu-Au Deposit and the Origin of the Chilean Iron Belt, Based on Re-Os Isotopes. *Economic Geology*, 97(1):59–71.
- Mathur, R., Marschik, R., Ruiz, J., Munizaga, F., Leveille, R. A., and Martin, W. (2002). Age of Mineralization of the Candelaria Fe Oxide Cu-Au Deposit and the Origin of the Chilean Iron Belt, Based on Re-Os Isotopes. *Economic Geology*, 97(1):59–71.
- Mathur, R., Ruiz, J., and Munizaga, F. (2000). Relationship between copper tonnage of Chilean base-metal porphyry deposits and Os isotope ratios. *Geology*, 28(6):555.

- Matthews, K. J., Seton, M., and Müller, R. D. (2012). A global-scale plate reorganization event at 105–100 Ma. *Earth and Planetary Science Letters*, 355:283–298.
- Mavor, S. P., Singleton, J. S., Gomila, R., Heuser, G., Seymour, N. M., Williams, S. A., Arancibia, G., Johnston, S. M., Kylander-Clark, A. R. C., and Stockli, D. F. (2020). Timing, Kinematics, and Displacement of the Taltal Fault System, Northern Chile: Implications for the Cretaceous Tectonic Evolution of the Andean Margin. *Tectonics*, 39(2):e2019TC005832.
- McCaffrey, R., Zwick, P. C., Bock, Y., Prawirodirdjo, L., Genrich, J. F., Stevens, C. W., Puntodewo, S. S. O., and Subarya, C. (2000). Strain partitioning during oblique plate convergence in northern Sumatra: Geodetic and seismologic constraints and numerical modeling. *Journal of Geophysical Research: Solid Earth*, 105(B12):28363–28376.
- McCarthy, A. J. and Elders, C. F. (1997). Cenozoic deformation in Sumatra: oblique subduction and the development of the Sumatran Fault System. *Geological Society, London, Special Publications*, 126(1):355.
- McDougall, I. and Harrison, T. M. (1999). *Geochronology and Thermochronology by the $^{40}\text{Ar}/^{39}\text{Ar}$ Method*. Oxford University Press on Demand.
- McLeod, C. L., Davidson, J. P., Nowell, G. M., and de Silva, S. L. (2012). Disequilibrium melting during crustal anatexis and implications for modeling open magmatic systems. *Geology*, 40(5):435–438.
- Memeti, V., Krause, J., Anderson, J. L., and Paterson, S. R. (2009). Interpreting Al-in Hornblende and Hbl-Plag thermobarometry results from the Tuolumne batholith and magmatic lobes in conjunction with single mineral element distribution electron microprobe maps. *American Geophysical Union Fall Meeting*.
- Miller, J. S., Matzel, J. E. P., Miller, C. F., Burgess, S. D., and Miller, R. B. (2007). Zircon growth and recycling during the assembly of large, composite arc plutons. *Journal of Volcanology and Geothermal Research*, 167(1):282–299.

- Mitchell, T. M., Cembrano, J. M., Fujita, K., Hoshino, K., Faulkner, D. R., Perez-Flores, P., Arancibia, G., Rempe, M., and Gomila, R. (2017). Fluid Inclusion Evidence of Coseismic Fluid Flow Induced by Dynamic Rupture. *Fault Zone Dynamic Processes: Evolution of Fault Properties During Seismic Rupture*, pages 37–45.
- Moscoso, R., Nasi, C., and Salinas, P. (1982). Hoja Vallenar y parte norte de La Serena, Regiones de Atacama y Coquimbo. Servicio Nacional de Geología y Minería. *Carta geologica de Chile*, 55.
- Mpodozis, C. and Kay, S. M. (1992). Late Paleozoic to Triassic evolution of the Gondwana margin: Evidence from Chilean Frontal Cordilleran batholiths (28°S to 31°S). *GSA Bulletin*, 104(8):999–1014.
- Murray, K. E., Braun, J., and Reiners, P. W. (2018). Toward robust interpretation of low-temperature thermochronometers in magmatic terranes. *Geochemistry, Geophysics, Geosystems*, 19(10):3739–3763.
- Nadin, E. S., Saleeby, J. B., Wright, J. E., and Shervais, J. W. (2008). Disruption of regional primary structure of the Sierra Nevada batholith by the Kern Canyon fault system, California. *Geological Society of America Special Papers*, 438:429.
- Naranjo, J. A. (1987). Interpretación de la actividad cenozoica superior a lo largo de la Zona de Falla Atacama, Norte de Chile. *Revista geológica de Chile: An international journal on andean geology*, (31):43–55.
- Naranjo, J. A., Hervé, F., Prieto, X., and Munizaga, F. (1984). Actividad cretácica de la Falla de Atacama al este de Chañaral: Milonitización y plutonismo. *Comunicaciones*, 34:57–66.
- Naranjo, J. A. and Puig, A. (1984). Geología de las Hojas Taltal y Chañaral, Regiones de Antofagasta y Atacama. Servicio Nacional de Geología y Minería. *Carta Geológica de Chile*, (62-63):140.

- O'Hara, K. (2007). Reaction weakening and emplacement of crystalline thrusts: Diffusion control on reaction rate and strain rate. *Journal of Structural Geology*, 29(8):1301–1314.
- Oliveros, V., Morata, D., Aguirre, L., Féraud, G., and Fornari, M. (2010). Jurassic to Early Cretaceous subduction-related magmatism in the Coastal Cordillera of northern Chile (18° 30' -24° S): geochemistry and petrogenesis. *Andean Geology*, 34(2):209–232.
- Ootes, L., Snyder, D., Davis, W. J., Acosta-Góngora, P., Corriveau, L., Mumin, A. H., Gleeson, S. A., Samson, I. M., Montreuil, J.-F., Potter, E., and Jackson, V. A. (2017). A Paleoproterozoic Andean-type iron oxide copper-gold environment, the Great Bear magmatic zone, Northwest Canada. *Ore Geology Reviews*, 81(1):123–139.
- Oreskes, N. and Einaudi, M. T. (1990). Origin of rare earth element-enriched hematite breccias at the Olympic Dam Cu-U-Au-Ag deposit, Roxby Downs, South Australia. *Economic Geology*, 85(1):1–28.
- Parada, M. A., López-Escobar, L., Oliveros, V., Fuentes, F., Morata, D., Calderón, M., Aguirre, L., Féraud, G., Espinoza, F., and Moreno, H. (2007). *Andean magmatism, booktitle = The geology of Chile*, pages 115–146.
- Peacock, D. C. P. and Sanderson, D. J. (1996). Effects of propagation rate on displacement variations along faults. *Journal of structural geology*, 18(2-3):311–320.
- Petit, J. P. (1987). Criteria for the sense of movement on fault surfaces in brittle rocks. *Journal of structural Geology*, 9(5-6):597–608.
- Petrus, J. A. and Kamber, B. S. (2012). VizualAge: A Novel Approach to Laser Ablation ICP-MS U-Pb Geochronology Data Reduction. *Geostandards and Geoanalytical Research*, 36(3):247–270.
- Pfiffner, O.-A. and Ramsay, J. G. (1982). Constraints on geological strain rates: arguments from finite strain states of naturally deformed rocks. *Journal of Geophysical Research: Solid Earth*, 87(B1):311–321.

- Pimentel, B. and Vega, A. (1979). Los Colorados Norte, yacimiento ferrífero, Provincia del Huasco. *Actas Congreso Geológico Chileno*, 2:C361–C378.
- Pitzer, K. S. and Sterner, S. M. (1994). Equations of state valid continuously from zero to extreme pressures for H₂O and CO₂. *The Journal of Chemical Physics*, 101(4):3111–3116.
- Pollard, P. (2006). An intrusion-related origin for Cu–Au mineralization in iron oxide–copper–gold (IOCG) provinces. *Mineralium Deposita*, 41(2):179–187.
- Post, A. D., Tullis, J., and Yund, R. A. (1996). Effects of chemical environment on dislocation creep of quartzite. *Journal of Geophysical Research: Solid Earth*, 101(B10):22143–22155.
- Putirka, K. (2016). Amphibole thermometers and barometers for igneous systems and some implications for eruption mechanisms of felsic magmas at arc volcanoes. *American Mineralogist*, 101(4):841–858.
- Quebral, R. D., Pubellier, M., and Rangin, C. (1996). The onset of movement on the Philippine Fault in eastern Mindanao: A transition from a collision to a strike-slip environment. *Tectonics*, 15(4):713–726.
- Raab, A. K. (2001). *Geology of the Cerro Negro Norte Fe-Oxide (Cu-Au) District, Coastal Cordillera, northern Chile*. Masters thesis.
- Rabbia, O., Frutos, J., Pop, N., Isache, C., Sanhueza, V., and Edelstein, O. (1996). Características isotópicas de la mineralización de Cu (-Fe) de Mina Carola, distrito minero Punta del Cobre, norte de Chile. *Congreso Geológico Argentino—Actas*, pages 241–254.
- Ramos, V. (2009). Anatomy and global context of the Andes: Main geologic features and the Andean orogenic cycle. *Geological Society of America Memoirs*, 204:31–65.
- Ramos, V. A. and Folguera, A. (2009). Andean flat-slab subduction through time. *Geological Society, London, Special Publications*, 327(1):31–54.

- Ramsay, J. G. (1980). Shear zone geometry: a review. *Journal of structural geology*, 2(1-2):83–99.
- Reich, M., Simon, A. C., Deditius, A., Barra, F., Chryssoulis, S., Lagas, G., Tardani, D., Knipping, J., Bilenker, L., Sánchez-Alfaro, P., Roberts, M. P., and Munizaga, R. (2016). Trace element signature of pyrite from the Los Colorados iron oxide-apatite (IOA) deposit, Chile: A missing link between Andean IOA and iron oxide copper-gold systems? *Economic Geology*, 111(3):743–761.
- Reiners, P., L. Spell, T., Nicolescu, S., and A. Zanetti, K. (2004). *Zircon (U-Th)/He thermochronometry: He diffusion and comparisons with $^{40}\text{Ar}/^{39}\text{Ar}$ dating*, volume 68.
- Reiners, P. W., Farley, K. A., and Hickey, H. J. (2002). He diffusion and (U–Th)/He thermochronometry of zircon: initial results from Fish Canyon Tuff and Gold Butte. *Tectonophysics*, 349(1):297–308.
- Reiners, P. W., Zhou, Z., Ehlers, T. A., Xu, C., Brandon, M. T., Donelick, R. A., and Nicolescu, S. (2003). Post-orogenic evolution of the Dabie Shan, eastern China, from (U–Th)/He and fission-track thermochronology. *American Journal of Science*, 303(6):489–518.
- Rieger, A., Marschik, R., and Díaz, M. (2012). The evolution of the hydrothermal IOCG system in the Mantoverde district, northern Chile: new evidence from microthermometry and stable isotope geochemistry. *Mineralium Deposita*, 47(4):359–369.
- Rieger, A. A., Marschik, R., Díaz, M., Hölzl, S., Chiaradia, M., Akker, B., and Spangenberg, J. E. (2010). The hypogene iron oxide copper-gold mineralization in the Mantoverde district, northern Chile. *Economic Geology*, 105(7):1271–1299.
- Rodríguez, N., Díaz-Alvarado, J., Fernández, C., Fuentes, P., Breitzkreuz, C., and Tassinari, C. C. G. (2019). The significance of U–Pb zircon ages in zoned plutons: the case of the Flamenco pluton, Coastal Range batholith, northern Chile. *Geoscience Frontiers*, 10(3):1073–1099.

- Rogers, G. and Hawkesworth, C. J. (1989). A geochemical traverse across the North Chilean Andes: evidence for crust generation from the mantle wedge. *Earth and Planetary Science Letters*, 91(3):271–285.
- Rothstein, D. A. and Manning, C. E. (2003). *Geothermal gradients in continental magmatic arcs; constraints from the eastern Peninsular Ranges Batholith, Baja California, Mexico*, volume 374, page 0. Geological Society of America.
- Royden, L. (1993). The tectonic expression slab pull at continental convergent boundaries. *Tectonics*, 12(2):303–325.
- Ruthven, R., Singleton, J., Seymour, N., Gomila, R., Arancibia, G., Stockli, D. F., Ridley, J., and Magloughlin, J. (2020). The geometry, kinematics, and timing of deformation along the southern segment of the Paposo fault zone, Atacama fault system, northern Chile. *Journal of South American Earth Sciences*, 97:102355.
- Rutland, R. W. R. (1971). Andean orogeny and ocean floor spreading. *Nature*, 233(5317):252–255.
- Ryan, P., Lawrence, A., Jenkins, R., Matthews, J., Zamora, J., Marino, E., and Urqueta, I. (1995). The Candelaria copper-gold deposit, Chile. *Arizona Geological Society Digest*, 20:625–645.
- Sanderson, D. J. and Marchini, W. R. D. (1984). Transpression. *Journal of Structural Geology*, 6(5):449–458.
- Sato, H., Kato, N., Abe, S., Van Horne, A., and Takeda, T. (2015). Reactivation of an old plate interface as a strike-slip fault in a slip-partitioned system: Median Tectonic Line, SW Japan. *Tectonophysics*, 644-645:58–67.
- Scheuber, E. and Andriessen, P. A. M. (1990). The kinematic and geodynamic significance of the Atacama fault zone, northern Chile. *Journal of Structural Geology*, 12(2):243–257.

- Scheuber, E., Bogdanic, T., Jensen, A., and Reutter, K.-J. (1994). *Tectonic Development of the North Chilean Andes in Relation to Plate Convergence and Magmatism Since the Jurassic*, pages 121–139. Springer Berlin Heidelberg, Berlin, Heidelberg.
- Scheuber, E. and Gonzalez, G. (1999). Tectonics of the Jurassic-Early Cretaceous magmatic arc of the north Chilean Coastal Cordillera (22°–26°S): A story of crustal deformation along a convergent plate boundary. *Tectonics*, 18(5):895–910.
- Scheuber, E., Hammerschmidt, K., and Friedrichsen, H. (1995). $^{40}\text{Ar}/^{39}\text{Ar}$ and Rb/Sr analyses from ductile shear zones from the Atacama Fault Zone, northern Chile: the age of deformation. *Tectonophysics*, 250(1):61–87.
- Scheuber, E. and Reutter, K.-J. (1992). Magmatic arc tectonics in the Central Andes between 21° and 25°S. *Tectonophysics*, 205(1):127–140.
- Seedorff, E., Dilles, J., Proffett, J., Einaudi, M., Zurcher, L., Stavast, W., Johnson, D., and Barton, M. (2005). *Porphyry deposits: characteristics and origin of hypogene features*, pages 251–299. Society of Economic Geologists.
- Segerstrom, K. (1960). Cuadrángulo Quebrada Paipote, Provincia de Atacama. *Instituto de Investigaciones Geológicas, Chile*.
- Segerstrom, K. (1967). Geology and Ore Deposits of Central Atacama Province, Chile. *Bulletin of the Geological Society of America*, 78(3):305–318.
- Segerstrom, K. and Parker, R. (1959). Cuadrángulo Cerrillos, Provincia de Atacama. *Instituto de Investigaciones Geológicas, Chile*.
- Segerstrom, K. and Ruiz, C. (1962). Geología del Cuadrángulo Copiapó, Provincia de Atacama. *Instituto de Investigaciones Geológicas, Chile*.
- Seman, S., Stockli, D. F., and McLean, N. M. (2017). U-Pb geochronology of grossular-andradite garnet. *Chemical Geology*, 460:106–116.

- Seton, M., Müller, R. D., Zahirovic, S., Gaina, C., Torsvik, T., Shephard, G., Talsma, A., Gurnis, M., Turner, M., Maus, S., and Chandler, M. (2012). Global continental and ocean basin reconstructions since 200Ma. *Earth-Science Reviews*, 113(3):212–270.
- Seymour, N. M., Singleton, J. S., Mavor, S. P., Gomila, R., Stockli, D. F., Heuser, G., and Arancibia, G. (2020). The relationship between magmatism and deformation along the intra-arc strike-slip Atacama fault system, northern Chile. *Tectonics*, page e2019TC005702.
- Sharp, Z. D. (1990). A laser-based microanalytical method for the in situ determination of oxygen isotope ratios of silicates and oxides. *Geochimica et Cosmochimica Acta*, 54(5):1353–1357.
- Sibson, R. H. (1983). Continental fault structure and the shallow earthquake source. *Journal of the Geological Society*, 140(5):741.
- Sibson, R. H. (1992). Fault-valve behavior and the hydrostatic-lithostatic fluid pressure interface. *Earth-Science Reviews*, 32(1):141–144.
- Sieh, K. and Natawidjaja, D. (2000). Neotectonics of the Sumatran fault, Indonesia. *Journal of Geophysical Research: Solid Earth*, 105(B12):28295–28326.
- Sillitoe, R. (2003). Iron oxide-copper-gold deposits: an Andean view. *Mineralium Deposita*, 38(7):787–812.
- Sláma, J., Košler, J., Condon, D. J., Crowley, J. L., Gerdes, A., Hanchar, J. M., Horstwood, M. S. A., Morris, G. A., Nasdala, L., Norberg, N., Schaltegger, U., Schoene, B., Tubrett, M. N., and Whitehouse, M. J. (2008). Plešovice zircon – A new natural reference material for U–Pb and Hf isotopic microanalysis. *Chemical Geology*, 249(1):1–35.
- Smoliar, M. I., Walker, R. J., and Morgan, J. W. (1996). Re–Os ages of group IIA, IIIA, IVA, and IVB iron from meteorites. *Science*, 271(5252):1099.
- Spötl, C. and Vennemann, T. W. (2003). Continuous-flow isotope ratio mass spectrometric analysis of carbonate minerals. *Rapid Communications in Mass Spectrometry*, 17(9):1004–1006.

- St. Amand, P. and Allen, C. R. (1960). *Strike-Slip Faulting in Northern Chile*, volume 71.
- Stanton-Yonge, A., Cembrano, J., Griffith, W. A., Jensen, E., and Mitchell, T. M. (2020). Self-similar length-displacement scaling achieved by scale-dependent growth processes: Evidence from the Atacama Fault System. *Journal of Structural Geology*, 133:103993.
- Stein, H. J. (2014). *Dating and Tracing the History of Ore Formation*. Elsevier Ltd, second edition edition.
- Stein, H. J., Morgan, J. W., and Schersten, A. (2000). Re-Os Dating of Low-Level Highly Radiogenic (LLHR) Sulfides: The Harnas Gold Deposit, Southwest Sweden, Records Continental-Scale Tectonic Events. *Economic Geology*, 95(8):1657–1671.
- Stenvall, C. A., Fagereng, Å., and Diener, J. F. A. (2019). Weaker than weakest: on the strength of shear zones. *Geophysical Research Letters*, 46(13):7404–7413.
- Stern, C. R. (1991). Role of subduction erosion in the generation of Andean magmas. *Geology*, 19(1):78–81.
- Stern, C. R. (2011). Subduction erosion: rates, mechanisms, and its role in arc magmatism and the evolution of the continental crust and mantle. *Gondwana Research*, 20(2-3):284–308.
- Stipp, M. and Kunze, K. (2008). Dynamic recrystallization near the brittle-plastic transition in naturally and experimentally deformed quartz aggregates. *Tectonophysics*, 448(1-4):77–97.
- Stipp, M., Stünitz, H., Heilbronner, R., and Schmid, S. M. (2002). The eastern Tonale fault zone: a 'natural laboratory' for crystal plastic deformation of quartz over a temperature range from 250 to 700°C. *Journal of Structural Geology*, 24(12):1861–1884.
- Stöckhert, B., Brix, M. R., Kleinschrodt, R., Hurford, A. J., and Wirth, R. (1999). Thermochronometry and microstructures of quartz—a comparison with experimental flow laws and predictions on the temperature of the brittle-plastic transition. *Journal of Structural Geology*, 21(3):351–369.

- Stockli, D. F. (2005). Application of Low-Temperature Thermochronometry to Extensional Tectonic Settings. *Reviews in Mineralogy and Geochemistry*, 58(1):411–448.
- Tabei, T., Hashimoto, M., Miyazaki, S., and Ohta, Y. (2003). Present-day deformation across the southwest Japan arc: Oblique subduction of the Philippine Sea plate and lateral slip of the Nankai forearc, journal = *Earth, Planets and Space*. 55(10):643–647.
- Taylor, G. K., Grocott, J., Pope, A., and Randall, D. E. (1998). Mesozoic fault systems, deformation and fault block rotation in the Andean forearc: a crustal scale strike-slip duplex in the Coastal Cordillera of northern Chile. *Tectonophysics*, 299(1-3):93–109.
- Teyssier, C., Tikoff, B., and Markley, M. (1995). Oblique plate motion and continental tectonics. *Geology*, 23(5):447–450.
- Thiele, R. and Pinchiera, M. (1984). Las megafallas Los Colorados-Portezuelo Tatara y La Sosita-Huantemé, en la extensión sur de la Zona de Falla Atacama al noroeste de Vallenar. *Comunicaciones Departamento de Geología, Universidad de Chile, Santiago*, pages 67–70.
- Tikoff, B. and Teyssier, C. (1994). Strain modeling of displacement-field partitioning in transpressional orogens. *Journal of Structural Geology*, 16(11):1575–1588.
- Tilling, R. (1976). El Batolito andino cerca de Copiapó, Provincia de Atacama. *Andean Geology*, 3:1–24.
- Tornos, F., Hanchar, J. M., Munizaga, R., Velasco, F., and Galindo, C. (2020). The role of the subducting slab and melt crystallization in the formation of magnetite-(apatite) systems, Coastal Cordillera of Chile. *Mineralium Deposita*.
- Tornos, F., Velasco, F., Barra, F., and Morata, D. (2010). The Tropezón Cu–Mo–(Au) deposit, Northern Chile: the missing link between IOCG and porphyry copper systems? *Mineralium Deposita*, 45(4):313–321.

- Tsutsumi, H. and Okada, A. (1996). Segmentation and Holocene surface faulting on the Median Tectonic Line, southwest Japan. *Journal of Geophysical Research: Solid Earth*, 101(B3):5855–5871.
- Tullis, J. and Yund, R. A. (1989). Hydrolytic weakening of quartz aggregates: The effects of water and pressure on recovery. *Geophysical Research Letters*, 16(11):1343–1346.
- Turner, G., Burnard, P., Ford, J. L., Gilmour, J. D., Lyon, I. C., Stuart, F. M., Gruszczynski, M., and Halliday, A. (1993). Tracing Fluid Sources and Interactions. *Philosophical Transactions of the Royal Society: Physical and Engineering Sciences (1990-1995)*, 344(1670):127–140.
- Ullrich, T. and Clark, A. (1997). Paragenetic sequence of mineralization in the main orebody, Candelaria copper-gold deposit, Chile. Report, Phelps Dodge Exploration Corporation.
- Ullrich, T. and Clark, A. (1998). Evolution of the Candelaria Cu-Au deposit, III Region, Chile. *Geological Society of America Abstracts with Programs*.
- Ullrich, T. and Clark, A. (1999). *The Candelaria copper-gold deposit, Región III, Chile: Paragenesis, geochronology and fluid composition*, pages 201–204. Rotterdam.
- Ullrich, T., Clark, A., and Kyser, K. (2001). The Candelaria Cu-Au Deposit, III region, Chile: Product of Long-Term Mixing of Magmatic-Hydrothermal and Evaporite-Sourced Fluids. *GSA Annual Meeting Abstracts with Programs*.
- Uyeda, S. and Hôrai, K.-I. (1964). Terrestrial heat flow in Japan. *Journal of Geophysical Research*, 69(10):2121–2141.
- Valley, J. W., Kitchen, N., Kohn, M. J., Niendorf, C. R., and Spicuzza, M. J. (1995). UWG-2, a garnet standard for oxygen isotope ratios: Strategies for high precision and accuracy with laser heating. *Geochimica et Cosmochimica Acta*, 59(24):5223–5231.
- Van der Pluijm, B. and Marshak, S. (2004). *Earth Structure*. WW Norton & Company, New York, 2 edition.

- Veloso, E., Cembrano, J., Arancibia, G., Heuser, G., Neira, S., Siña, A., Garrido, I., Vermeesch, P., and Selby, D. (2017). Tectono-metallogenetic evolution of the Fe–Cu deposit of Dominga, northern Chile. *Mineralium Deposita*, 52(4):595–620.
- Veloso, E. E., Gomila, R., Cembrano, J., González, R., Jensen, E., and Arancibia, G. (2015). Stress fields recorded on large-scale strike-slip fault systems: Effects on the tectonic evolution of crustal slivers during oblique subduction. *Tectonophysics*, 664:244–255.
- Verkouteren, R. and Klinedinst, D. (2004). Standard reference materials. Report.
- Vermeesch, P. (2012). On the visualisation of detrital age distributions. *Chemical Geology*, 312-313:190–194.
- Who, A., Lanari, P., and Rubatto, D. (2020). Internally-consistent database for oxygen isotope fractionation between minerals. *Journal of Petrology*.
- Vidal, O., Parra, T., and Trotet, F. (2001). A thermodynamic model for Fe-Mg aluminous chlorite using data from phase equilibrium experiments and natural pelitic assemblages in the 100 degrees to 600 degrees C. *American Journal of Science*, 301(6):557–592.
- Vila, T., Richard, Z., and Lindsay, N. (1996). *Geology of the Manto Verde Copper Deposit, Northern Chile: A specularite-rich, Hydrothermal-Tectonic Breccia Related to the Atacama Fault Zone*, volume 5, page 0. Society of Economic Geologists.
- Von Huene, R. and Scholl, D. W. (1991). Observations at convergent margins concerning sediment subduction, subduction erosion, and the growth of continental crust. *Reviews of Geophysics*, 29(3):279–316.
- Wang, K., Hu, Y., Bevis, M., Kendrick, E., Smalley Jr, R., Vargas, R. B., and Lauría, E. (2007). Crustal motion in the zone of the 1960 Chile earthquake: Detangling earthquake-cycle deformation and forearc-sliver translation. *Geochemistry, Geophysics, Geosystems*, 8(10).

- Weis, P., Driesner, T., Coumou, D., and Geiger, S. (2014). Hydrothermal, multiphase convection of H²O-NaCl fluids from ambient to magmatic temperatures: a new numerical scheme and benchmarks for code comparison. *Geofluids*, 14(3):347–371.
- Welkner, D., Arévalo, C., and Godoy, E. (2006). Geología del área Freirina–El Morado, Región de Atacama. *Carta Geológica de Chile, Serie Geología Básica*, 44.
- Wiedenbeck, M., Allé, P., Corfu, F., Griffin, W. L., Meier, M., Oberli, F., Quadt, A. V., Roddick, J. C., and Spiegel, W. (1995). Three natural zircon standards for U-TH-PB, LU-HF, trace element and REE analyses. *Geostandards Newsletter*, 19(1):1–23.
- Willemsse, E. J. M. (1997). Segmented normal faults: Correspondence between three-dimensional mechanical models and field data. *Journal of Geophysical Research: Solid Earth*, 102(B1):675–692.
- Williams, P., Guoyi, D., Pollard, P., Broman, C., Martinsson, O., Wanhainen, C., Mark, G., Ryan, C., and Mernagh, T. (2003). The nature of iron oxide-copper-gold ore fluids: Fluid inclusion evidence from Norrbotten (Sweden) and the Cloncurry district (Australia). *7th Biennial SGA Meeting*, pages 1127–1130.
- Wilson, J. and Grocott, J. (1999). The emplacement of the granitic Las Tazas complex, northern Chile: the relationship between local and regional strain. *Journal of Structural Geology*, 21(11):1513–1523.
- Wintsch, R. P., Christoffersen, R., and Kronenberg, A. K. (1995). Fluid-rock reaction weakening of fault zones. *Journal of Geophysical Research: Solid Earth*, 100(B7):13021–13032.
- Wolfe, M. R. and Stockli, D. F. (2010). Zircon (U–Th)/He thermochronometry in the KTB drill hole, Germany, and its implications for bulk He diffusion kinetics in zircon. *Earth and Planetary Science Letters*, 295(1):69–82.
- Woodcock, N. H., Daly, M. C., Watson Janet, V., Reading, H. G., Watterson, J., White, S. J., and White, S. H. (1986). The role of strike-slip fault systems at plate boundaries. *Philosophical*

Transactions of the Royal Society of London. Series A, Mathematical and Physical Sciences, 317(1539):13–29.

Yang, G., Zimmerman, A., Hurtig, N., Georgiev, S., Goswami, V., Hannah, J., and Stein, H. (2020). Optimization of chemical methods for the extraction and purification of Re from sample solutions: Role of coarse anion resin beads. *Geostandards and Geoanalytical Research*.

Zentilli, M. (1974). Geological evolution and metallogenic relationships in the Andes of northern Chile between 26° and 29° south. (*PhD Thesis*). *Queen's University*.

Zimmerman, A., Stein, H. J., Morgan, J. W., Markey, R. J., and Watanabe, Y. (2014). Re–Os geochronology of the El Salvador porphyry Cu–Mo deposit, Chile: Tracking analytical improvements in accuracy and precision over the past decade. *Geochimica et Cosmochimica Acta*, 131(C):13–32.

Appendix

Here I provide 5 supplementary figures and 1 dataset for Chapter 1 representing a compilation of previously published geochronometric data. 3 plates and 5 datasets are included as separate files. U-Pb and (U-Th)/He data can be accessed at the Geochron.org database: https://www.geochron.org/dataset/html/geochron_dataset_2020_01_21_C9pPo.

Included here:

Figure A1. Distribution of locations visited for this study.

Figure A2. Cathodoluminescence imagery of zircon from Chapter 1.

Figure A3. Cathodoluminescence imagery of zircon from Chapter 2.

Figure A4. Cathodoluminescence imagery of zircon from Chapter 3.

Figure A5. Wetherill Concordia, field photograph, and kernel density estimate of age spectra for mylonitic sample 171-N37d.

Dataset A6. Compilation of published age data.

Included separately:

Plate 1. 1:20,000-scale map of the Mantoverde area.

Plate 2. 1:100,000-scale slip history reconstruction.

Plate 3. 1:10,000-scale map of the Copiapó shear zone.

Dataset 1. Zircon U-Pb data.

Dataset 2. Zircon (U-Th)/He data.

Dataset 3. Andradite U-Pb data.

Dataset 4. Sulfide Re-Os data.

Dataset 5. Oxygen stable isotope data.



Figure A1. Distribution of locations visited for this study.

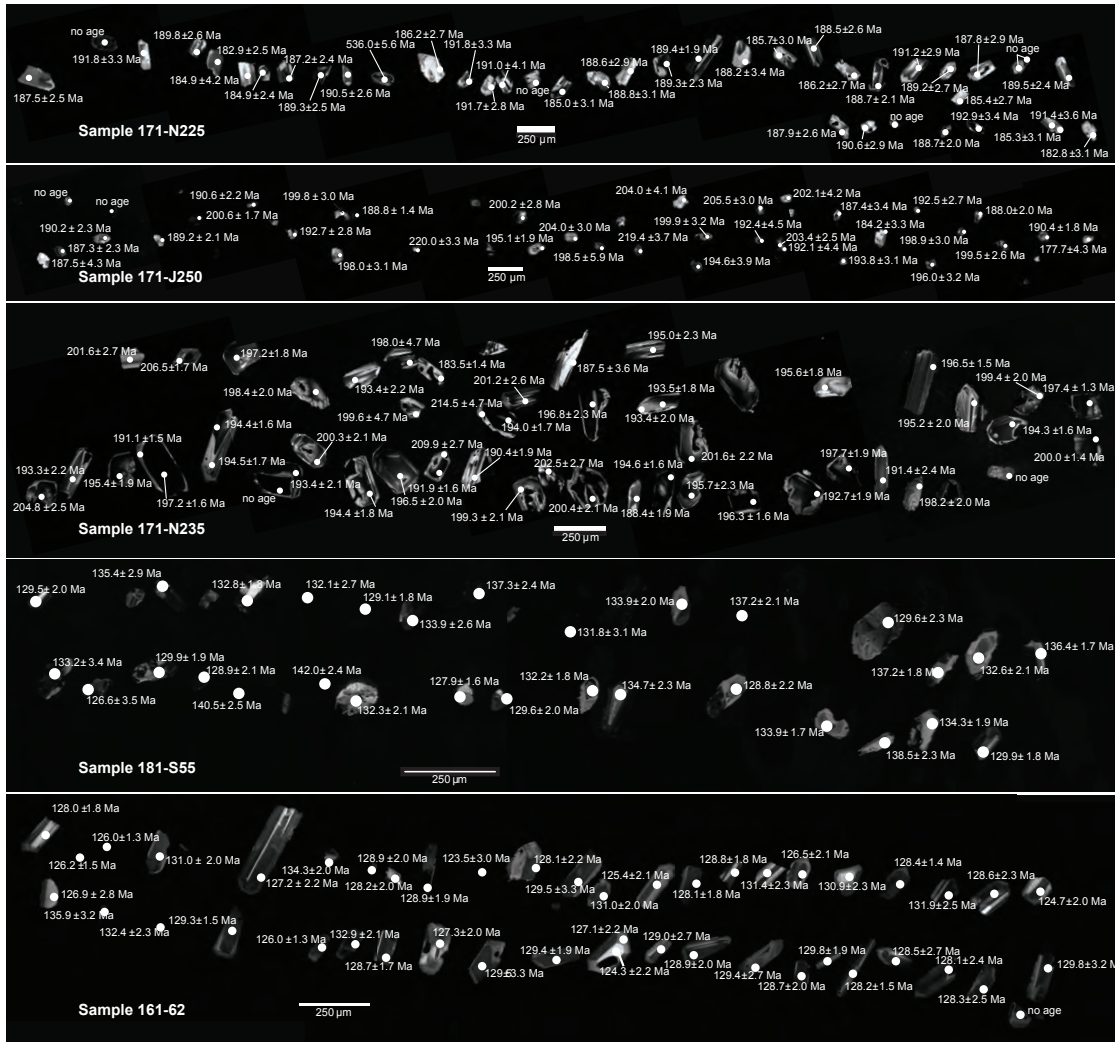


Figure A2. Cathodoluminescence imagery of zircon from Chapter 1.

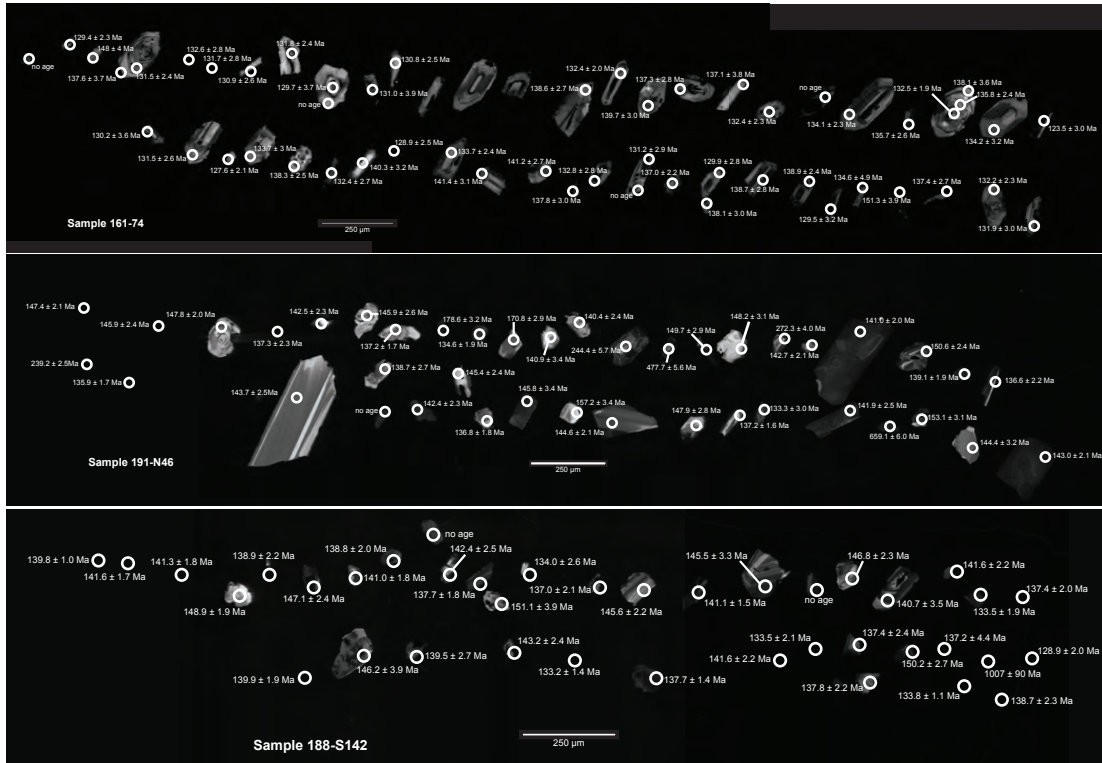


Figure A3. Cathodoluminescence imagery of zircon from Chapter 2.

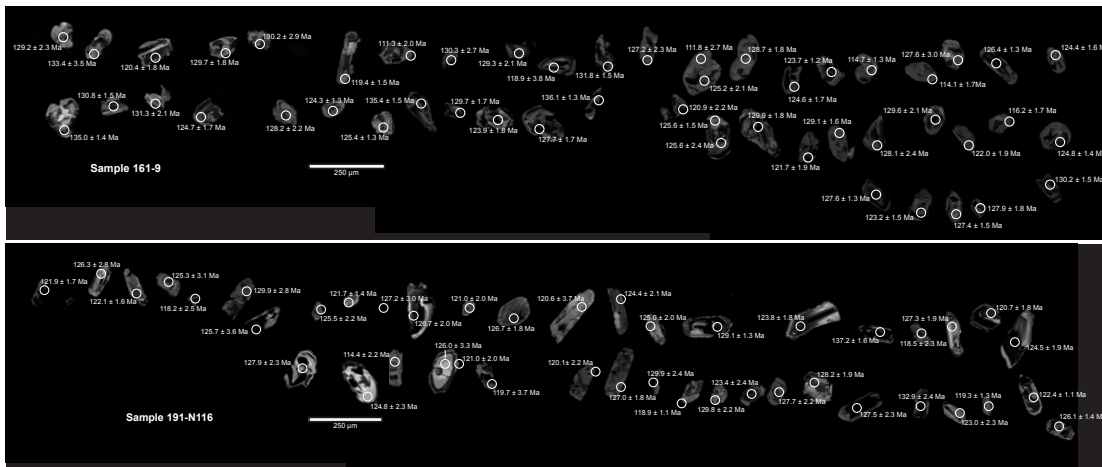


Figure A4. Cathodoluminescence imagery of zircon from Chapter 3.

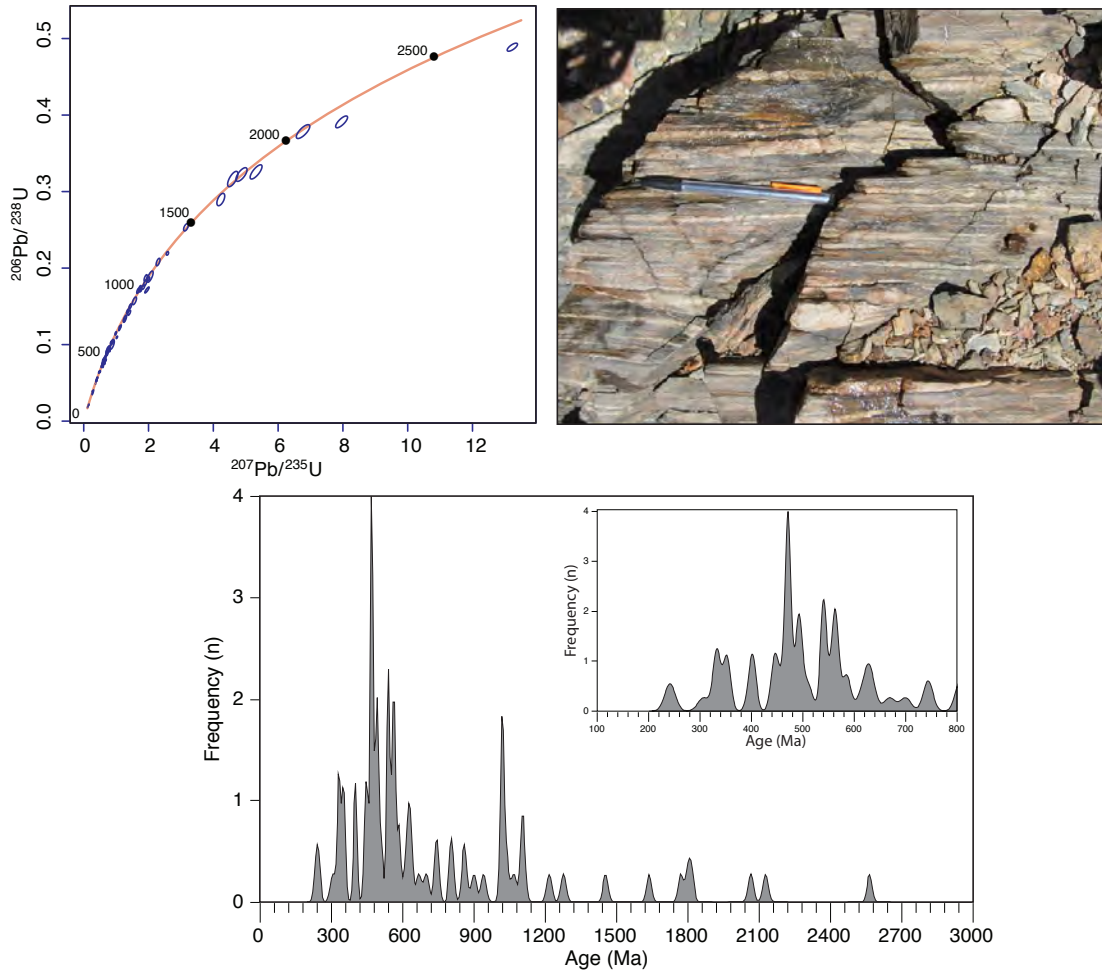


Figure A5. Wetherill Concordia, field photograph, and kernel density estimate of age spectra for mylonitic sample 171-N37d. Inset shows detailed peaks between 100–800 Ma. Note the spread in ages along Concordia and multiple peaks, which is consistent with a sedimentary protolith rather than an igneous protolith.

Dataset A6. Compilation of published age data.

Region	Easting (m)	Northing m)	Mineral	System	Age (Ma)	Source Publication
Paposo	369312	7275426	Zircon	U-Pb	135.6 ± 1.3	Álvarez et al., 2016
Paposo	358066	7275308	Biotite	K-Ar	156 ± 4	Álvarez et al., 2016
Paposo	364061	7274416	Hornblende	Ar-Ar	138.8 ± 1.7	Scheuber et al., 1995
Paposo	370490	7273616	Biotite	K-Ar	133 ± 3	Hervé and Marinovic, 1989
Paposo	349513	7272868	Zircon	U-Pb	147.1 ± 1.4	Álvarez et al., 2016
Paposo	347183	7272468	Zircon	U-Pb	151 ± 0.8	Álvarez et al., 2016
Paposo	351102	7272203	Zircon	U-Pb	147 ± 1.3	Álvarez et al., 2016
Paposo	348848	7270225	Zircon	U-Pb	150 ± 0.7	Álvarez et al., 2016
Paposo	349205	7269506	Biotite	K-Ar	144 ± 4	Hervé and Marinovic, 1989
Paposo	361187	7269413	Zircon	U-Pb	233.8 ± 2.1	Álvarez et al., 2016
Paposo	349926	7269298	Zircon	U-Pb	150.5 ± 0.9	Álvarez et al., 2016
Paposo	350313	7269015	Zircon	U-Pb	145.9 ± 1.2	Álvarez et al., 2016
Paposo	371568	7268713	Biotite	K-Ar	128 ± 3	Hervé and Marinovic, 1989
Paposo	358481	7268013	Biotite	K-Ar	155 ± 4	Hervé and Marinovic, 1989
Paposo	355489	7266310	Zircon	U-Pb	155.8 ± 0.7	Álvarez et al., 2016
Paposo	350271	7265654	Zircon	U-Pb	142.2 ± 1.3	Álvarez et al., 2016
Paposo	368397	7262624	Biotite	Ar-Ar	135.2 ± 0.1	Álvarez et al., 2016

Paposo	350408	7262334	Biotite	K-Ar	142 ± 3	Hervé and Marinovic, 1989
Paposo	357482	7261798	Biotite	K-Ar	144 ± 4	Hervé and Marinovic, 1989
Paposo	362278	7260236	Zircon	U-Pb	135.1 ± 1	Álvarez et al., 2016
Paposo	348149	7257576	Biotite	K-Ar	151 ± 4	Hervé and Marinovic, 1989
Paposo	363474	7255149	Biotite	K-Ar	155 ± 4	Hervé and Marinovic, 1989
Paposo	348950	7255145	Biotite	K-Ar	148 ± 4	Hervé and Marinovic, 1989
Paposo	361488	7252124	Biotite	K-Ar	133 ± 3	Álvarez et al., 2016
Paposo	353838	7251731	Zircon	U-Pb	225.6 ± 6.7	Álvarez et al., 2016
Paposo	360498	7248341	Biotite	K-Ar	128 ± 3	Hervé and Marinovic, 1989
Paposo	352609	7246588	Zircon	U-Pb	225.3 ± 4.5	Álvarez et al., 2016
Paposo	355961	7246090	Zircon	U-Pb	175.1 ± 1.3	Álvarez et al., 2016
Paposo	353920	7246055	Zircon	U-Pb	226.6 ± 2.5	Álvarez et al., 2016
Paposo	354261	7244639	Zircon	U-Pb	246.1 ± 1.3	Álvarez et al., 2016
Paposo	355324	7242687	Hornblende	Ar-Ar	165.6 ± 1.5	Álvarez et al., 2016
Paposo	355084	7241697	Biotite	K-Ar	165 ± 5	Hervé and Marinovic, 1989
Paposo	356717	7240775	Hornblende	K-Ar	131 ± 5	Hervé and Marinovic, 1989
Paposo	355099	7240576	Hornblende	K-Ar	176 ± 6	Hervé and Marinovic, 1989
Paposo	355866	7237641	Biotite	K-Ar	129 ± 3	Hervé and Marinovic, 1989
Paposo	354865	7232483	Zircon	U-Pb	146.5 ± 1.5	Ruthven et al., 2020

Paposo	353935	7232068	Zircon	U-Pb	136 ± 1.8	Ruthven et al., 2020
Paposo	353526	7231582	Zircon	U-Pb	177.9 ± 1.7	Ruthven et al., 2020
Paposo	354970	7231061	Zircon	U-Pb	138.5 ± 1.6	Ruthven et al., 2020
Northern El Salado	366366	7177135	Biotite	Ar-Ar	149.2 ± 0.6	Las Cenizas, 2007
Northern El Salado	366885	7176402	Hornblende	Ar-Ar	150.5 ± 1	Espinoza et al., 2014
Northern El Salado	364690	7176216	Biotite	Ar-Ar	146.8 ± 0.3	Espinoza et al., 2014
Northern El Salado	360586	7174559	Zircon	U-Pb	141.3 ± 0.1	Las Cenizas, 2007
Northern El Salado	372887	7172187	Zircon	U-Pb	128.2 ± 0.1	Las Cenizas, 2007
Northern El Salado	371902	7170388	Biotite	Ar-Ar	142 ± 0.6	Las Cenizas, 2007
Northern El Salado	353711	7166591	Zircon	U-Pb	173 ± 4	Espinoza et al., 2014
Northern El Salado	368319	7163693	Biotite	K-Ar	126 ± 3	Kurth, 2002
Northern El Salado	368386	7163527	Biotite	K-Ar	130 ± 3	Kurth, 2002
Northern El Salado	368710	7163268	Hornblende	Ar-Ar	127.5 ± 1.5	Kurth, 2002
Northern El Salado	368348	7163267	Biotite	K-Ar	128 ± 3	Kurth, 2002
Northern El Salado	368380	7162680	Hornblende	K-Ar	137 ± 5	Kurth, 2002
Northern El Salado	368378	7162669	Hornblende	K-Ar	137 ± 5	Kurth, 2002
Northern El Salado	365140	7162586	Zircon	U-Pb	138.2 ± 0.7	Espinoza et al., 2014
Northern El Salado	368344	7162347	Hornblende	K-Ar	148 ± 7	Kurth, 2002

Northern El Salado	368387	7162343	Hornblende	K-Ar	138 v 5	Kurth, 2002
Northern El Salado	369053	7161469	Biotite	K-Ar	125 ± 5	Kurth, 2002
Northern El Salado	369269	7161376	Hornblende	K-Ar	133 ± 5	Kurth, 2002
Northern El Salado	369301	7161373	Hornblende	K-Ar	136 ± 5	Kurth, 2002
Northern El Salado	373444	7161066	Hornblende	Ar-Ar	127.4 ± 1.1	Espinoza et al., 2014
Northern El Salado	369096	7161063	Hornblende	K-Ar	123 ± 3	Kurth, 2002
Northern El Salado	369107	7161036	Hornblende	K-Ar	90 ± 9	Kurth, 2002
Northern El Salado	371376	7160281	Hornblende	K-Ar	131 ± 5	Las Cenizas, 2007
Northern El Salado	365721	7160272	Zircon	U-Pb	139.1 ± 0.6	Espinoza et al., 2014
Northern El Salado	372348	7157218	Biotite	Ar-Ar	130 ± 0.3	Espinoza et al., 2014
Northern El Salado	370324	7155718	Hornblende	Ar-Ar	130.6 ± 1	Espinoza et al., 2014
Northern El Salado	370941	7152388	Biotite	Ar-Ar	128.7 ± 0.3	Espinoza et al., 2014
Northern El Salado	379838	7151926	Biotite	K-Ar	141 ± 8	Espinoza et al., 2014
Northern El Salado	376539	7144988	Zircon	U-Pb	153 ± 0.4	Espinoza et al., 2014
Northern El Salado	373559	7143208	Biotite	Ar-Ar	177.4 ± 0.4	Espinoza et al., 2014
Northern El Salado	379437	7143195	Hornblende	Ar-Ar	138.9 ± 1.4	Espinoza et al., 2014
Northern El Salado	366839	7142619	Zircon	U-Pb	140.1 ± 6	Espinoza et al., 2014
Northern El Salado	366236	7142339	Zircon	U-Pb	145 ± 2	Espinoza et al., 2014
Northern El Salado	379618	7132600	Biotite	K-Ar	120 ± 3	Ulriksen, 1979

Northern El Salado	379618	7132600	Biotite	Ar-Ar	124 ± 4	Ulriksen, 1979
Northern El Salado	381847	7131914	Biotite	Ar-Ar	125.4 ± 0.2	Espinoza et al., 2014
Northern El Salado	386497	7131222	Biotite	K-Ar	112 ± 4	Ulriksen, 1979
Northern El Salado	376056	7127711	Zircon	U-Pb	207.3 ± 1	Espinoza et al., 2014
Central El Salado	361719	7066348	Hornblende	Ar-Ar	131 ± 1.1	Dallmeyer et al., 1996
Central El Salado	365256	7064331	Zircon	U-Pb	130.2 ± 1.3	Berg and Bretkreutz, 1983
Central El Salado	355421	7062647	Hornblende	Ar-Ar	153 ± 1	Dallmeyer et al., 1996
Central El Salado	365068	7061153	Hornblende	Ar-Ar	196.5 ± 0.3	Wilson et al., 2000
Central El Salado	365068	7061153	Hornblende	Ar-Ar	133.3 ± 0.2	Wilson et al., 2000
Central El Salado	373863	7058842	Hornblende	Ar-Ar	127.2 ± 1	Dallmeyer et al., 1996
Central El Salado	373872	7058634	Zircon	U-Pb	126.8 ± 1.3	Berg and Bretkreutz, 1983
Central El Salado	375279	7055914	Hornblende	K-Ar	120 ± 4	Zentilli, 1974
Central El Salado	375277	7055895	Biotite	K-Ar	115 ± 3	Zentilli, 1974
Central El Salado	372610	7054122	Hornblende	Ar-Ar	125.5 ± 1.1	Dallmeyer et al., 1996
Central El Salado	370828	7036884	Biotite	K-Ar	104 ± 3	Lara and Godoy, 1998
Central El Salado	356012	7034987	Hornblende	Ar-Ar	140.1 ± 0.8	Dallmeyer et al., 1996
Central El Salado	365558	7030600	Hornblende	Ar-Ar	107.4 ± 0.5	Dallmeyer et al., 1996
Central El Salado	349552	7025020	Biotite	K-Ar	150 ± 4	Godoy and Lara, 1999

Central El Salado	349498	7020671	Hornblende	Ar-Ar	148.5 ± 1.1	Dallmeyer et al., 1996
Central El Salado	350688	7020294	Biotite	K-Ar	135 ± 4	Godoy and Lara, 1999